DEVELOPING NOVEL MATERIALS FOR SPIN TRANSFER TORQUE DEVICES

A THESIS SUBMITTED TO THE UNIVERSITY OF MANCHESTER
FOR THE DEGREE OF DOCTOR OF PHILOSOPHY
IN THE FACULTY OF SCIENCE AND ENGINEERING

2022

Author Name: Philip N. Thompson
Student id:10186530
Primary Supervisor: Thomas Thomson

Department of Computer Science

Table of Contents

4

Word Count: 50000

List of Tables

List of Figures

Abstract

Ferromagnetic thin films consisting of binary alloys with $L1_0$ crystallographic ordering are currently being used as the medium in heat assisted magnetic recording (HAMR) and have significant potential in spintronic devices and more generally as permanent magnets in electric machines. This research focuses on the formation of the $L1_0$ phase in FePt and MnAl thin films, which is motivated by their potential for use in energy assisted data storage devices. FePt and MnAl binary alloy magnetic properties in their $L1_0$ phase have highly desirable magnetic properties; FePt has a high magnetic moment and very high magnetic anisotropy, MnAl has a moment comparable to permalloy, high magnetic anisotropy and low spin orbit coupling in addition to being composed of relatively abundant elements. The research presented in this thesis details the development of fabrication procedures to achieve $L1_0$ ordered thin films of FePt and MnAl using magnetron sputtering.

Whilst the fabrication of $L1_0$ ordered thin films of FePt with either random or perpendicular magnetic anisotropy is well known, thin films with uniaxial in-plane magnetic anisotropy is unreported using sputter deposition. The fabrication of uniaxial in-plane FePt thin films is investigated as a foundation for their use in exchange spring structures. The growth of the $L1_0$ phase is controlled by seed layers and choice substrates, along with deposition and annealing temperatures. The phase formation within the films is characterised by X-ray diffraction, with a novel approach of using XRD with in-situ heating for feedback into the fabrication procedure. The optimised sputter fabrication procedure is shown to be comparable with literature values for MBE grown samples.

Fabrication of sputtered $L1_0$ ordered MnAl thin films was investigated using both an alloy target and Mn/Al co-deposition. Forming the desired phase is highly dependent on composition, where both methods show an unexpected substantial loss of Mn during fabrication, which it is proposed to be due to adhesion issues on the substrate surface. Further exploration of deposition and annealing conditions found key links between phase formation and film surface roughness, where reducing deposition pressure plays a key role in formation of low roughness films. However, the magnetic properties of the films fabricated fell short of the theoretical values for MnAl. This work moves the state-of-knowledge forward in the fabrication of $L1_0$ ordered MnAl thin films and details the challenges faced producing ferromagnetic $L1_0$ ordered MnAl film with key findings on compositional uncertainties.

Declaration

No portion of the work referred to in this thesis has been submitted in support of an application for another degree or qualification of this or any other university or other institute of learning.

Copyright

i. The author of this thesis (including any appendices and/or schedules to this thesis) owns certain copyright or related rights in it (the "Copyright") and s/he has given The University of Manchester certain rights to use such Copyright, including for administrative purposes.

ii. Copies of this thesis, either in full or in extracts and whether in hard or electronic copy, may be made **only** in accordance with the Copyright, Designs and Patents Act 1988 (as amended) and regulations issued under it or, where appropriate, in accordance with licensing agreements which the University has from time to time. This page must form part of any such copies made.

iii. The ownership of certain Copyright, patents, designs, trade marks and other intellectual property (the "Intellectual Property") and any reproductions of copyright works in the thesis, for example graphs and tables ("Reproductions"), which may be described in this thesis, may not be owned by the author and may be owned by third parties. Such Intellectual Property and Reproductions cannot and must not be made available for use without the prior written permission of the owner(s) of the relevant Intellectual Property and/or Reproductions.

iv. Further information on the conditions under which disclosure, publication and commercialisation of this thesis, the Copyright and any Intellectual Property and/or Reproductions described in it may take place is available in the University IP Policy (see http://documents.manchester.ac.uk/DocuInfo.aspx?DocID=487), in any relevant Thesis restriction declarations deposited in the University Library, The University Library's regulations (see http://www.manchester.ac.uk/library/aboutus/regulations) and in The University's policy on presentation of Theses

List of Publications

Published:

Characterisation of size distribution and positional misalignment of nanoscale islands by small-angle X-ray scattering, G. Heldt, P. Thompson, R. V. Chopdekar, J. Kohlbrecher, S. Lee, L. J. Heyderman, T. Thomson, Journal of Applied Physics, (2019), DOI: 10.1063/1.5050882.

Papers in preparation:

Fabrication of $L1_0$ ordered FePt films with Uniaxial in-plane anisotropy, P. Thompson, T. Thomson, Magnetism and Magnetic Materials in preparation.

Sputter deposition of MnAl thin films, P. Thompson, B. Spencer, T. Thomson, AIP advances in preparation.

Depth resolved magnetic response of Co/Pd multilayers interacting with magnetically soft Py layer, W. Griggs, P. Thompson, A. Lincoln, C. J. Kinane, A. Caruana, T. Thomson, APL materials in preparation.

Characterisation of buried interfaces using Ga Kα Hard X-ray Photoelectron Spectroscopy (HAXPES), B. Spencer, S. Maniyarasu, P. Thompson, S. A. Church, D. Cant, D. J. Binks, A. G. Thomas, T. Thomson, A. G. Shard, W. R. Flavell, Faraday Discussion in preparation.

Conference Participation

Exploration of new $L1_0$-ordered materials for their spintronic applications, IoP Magnetism Conference 2018 (Poster)

Characterisation of size distribution and positional misalignment of nanoscale islands by small-angle X-ray scattering with high statistical significance, IoP Magnetism Conference 2019 (Poster)

Rigaku Workshop on use of Smartlab diffractometer experimental work (Contributed work for invited Presentation), 2019

Fabrication of orientated ordered $L1_0$ thin films, York-Tohoku-Kaiserslautern Research Symposium 2019 (Poster)

Covid-19 Impact statement

This PhD relied on a feedback loop between the making and characterisation of thin films of L10 ordered alloys. Four main instruments were used for fabrication (AJA sputterer) and characterisation (VSM, Rigaku Smartlab and HAXPES). If any of these systems is out of commission for more than a short period then progress is hindered, but when the system is down for a long-time (two weeks or more) progress is halted. The various systems are housed in three separate university buildings and as such the Covid-19 guidelines had a severe impact on productivity, where intermixing between buildings was not allowed. During the closure period from March 2020 to September 2020 there was no access to any experimental facility and therefore no progress was possible. Given the stage of the research project when this happened, the impact was particularly severe with a serious loss in momentum just when an intense period of experimental activity had been planned. Although progress was possible from September 2020 it was necessarily at a much slower speed than previously achieved, especially as multiple users are playing catchup on each system. The HAXPES system was in the initial stages of being commissioned shortly before the closure and therefore steps to bring it online fully were delayed, without this system it would not have been possible to undertake the MnAl work reported in this thesis. Limited working hours have remained consistent at the university to help combat Covid-19 effects, thus slowing the possible progress in the final stages of this PhD.

The closure of facilities led to unexpected issues with equipment, where failures arose due to vacuum systems being at atmospheric pressure for prolonged periods of time. This includes, but is not limited to, issues with fabrication systems as they did not return to full functionality immediately after opening again in September. Alongside these issues the demand for systems increased and an equal opportunity system had to be put in place to allow all research to begin again in an equitable manner. This was a an entirely appropriate measure but due to limited hours access to laboratory equipment it meant productivity was less than half what it was pre-pandemic.

Acknowledgements

Firstly, I would like to thank my supervisor Professor Tom Thomson for the expert guidance and support throughout my PhD. I have learned so much from Tom during my time at the University of Manchester, where there have been many insightful conversations had whilst making the cups of tea that got me through the day. A special thanks goes to the technical staff for keeping the machines running throughout my PhD. I would especially like to thank Dr. Alex Lincoln for his technical support with the fabrication of films and for always being up for a debate on why the sputtering system wasn't working properly.

I also want to show my appreciation to the academic staff and fellow students of the NEST group for their warm welcome and technical expertise that has helped progress the work of this thesis. The ups and downs of IT109 will forever be remembered, where each student has their own unique stories of the joys and hurdles that is a PhD relying on experimental equipment. For making IT109 so enjoyable I would like to thank Will Griggs, Harry Warring, Charley Bull, Yu Li, Yuzhe Zhang, Michael Grimes, Adrian Peasey, Runze Chen, Cory Emmerson, Meg Smith and Aayush Chadha for making the best work environment possible, with both highly educational and humorous conversation.

I would also like to take this very rare occasion to thank my friends and family for their love and support throughout one of the most challenging parts of my life. I thank my mother Michelle and father Nicky for supporting me from afar with love and encouragement throughout every stage of my studies. I also thank my sisters Dawn, Ashley and their partners for always supporting me. Lastly I would like to give a huge thank you to Shannon McErlean for her love and support throughout this PhD, even if she never quite understood what I was doing she always supported me.

Chapter 1

Introduction

New materials and materials with specifically designed properties are a key enabler of technological advances [1]. In the electronics industry new and improved materials have allowed tremendous advances in functionality of microelectronics, data storage and sensors observed over the last 60+ years [2]. An example is the improvement in materials for semiconductor gate dielectrics and interconnects, which have played a crucial role in enabling the $x10^8$ increase [1] in transistor density achieved since the inception of the integrated circuit.

In magnetic data storage, which has undergone a similarly impressive increase in functionality, the increase in the number of bits that can be stored on a HDD or MRAM device has been driven by material innovation. The increased storage demand is accompanied by large and small scale hoarding of data associated with the digital age of society, which has enormous amounts (2 petabytes per minute [2]) of information being generated daily. Companies are now offering cloud storage to consumers with large scale data centres set up to store information. The normal civilian is expanding their storage needs through various sources such as the internet of things (IoT) devices which include sensors in our bodies, homes and cities, as well as high resolution 360°video and augmented reality and 5G communications [2]. This branch of data generation has now gained the new term of "digital transformation" as it shows mankind's transition to the new era. Within the next 5 years the transition of consumer storage from at home to cloud storage is set to flip, with the amount of information being stored globally projected to reach 175 zettabytes [3].

1.1 Magnetic Storage

The core storage device has remained the hard disk drive (HDD), made of spinning platters of magnetic layers with bits stored as magnetic structures on their surface, for many years since the first drives were shipped in 1956 [2]. However, the HDD has begun to reach a physical limit and therefore alternative media is highly sought to progress storage to its next breakthrough. The field of spintronics is beginning a new branch of devices that use energy assisted methods to overcome the HDD's problems. The areal storage density of these devices is shown in figure 1.1, where HDD can be seen progressing over the last few decades with the new heat assisted magnetic recording (HAMR) coming into play over the last decade. The HDD has progressed impressively at a 30% compound annual growth rate (CAGR) for five decades now but is reaching a plateau, whereas the energy assisted newcomers, such as HAMR, are seeing the same initial growth that HDD showed [2].
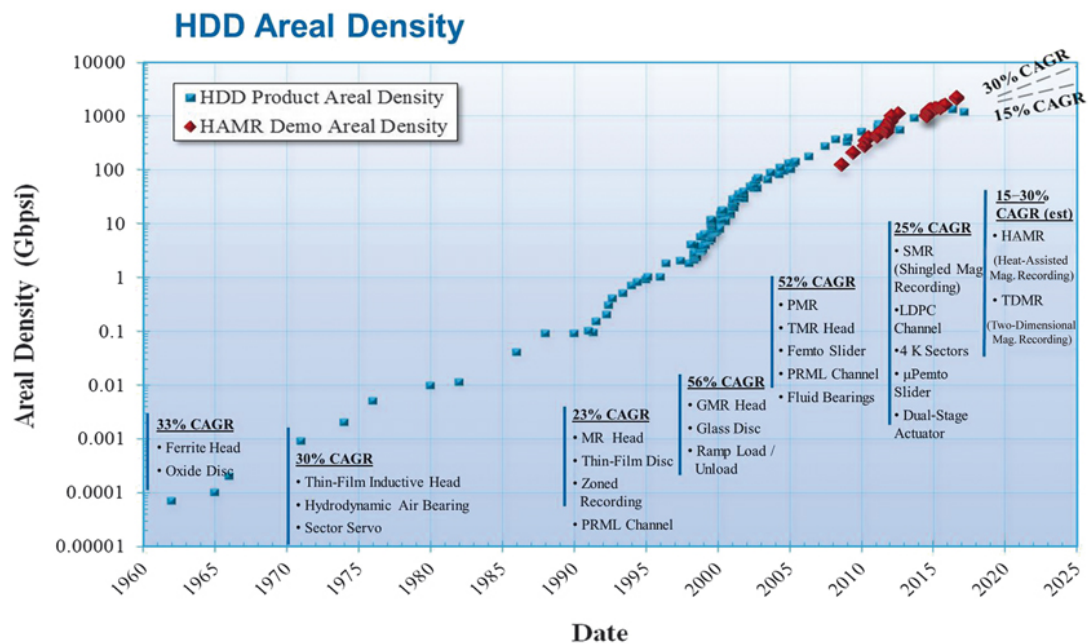
Figure 1.1: The areal density progression of HDD over the last six decades with HAMR beginning to emerge over the last decade [2].

At present there is a paradigm shift in the storage industry from conventional HDD towards spintronic devices. The burden the HDD has taken over the past few decades must be alleviated by some new device, where spintronic devices are set to be at the

forefront of this new storage device era. This change is mainly due to the magnetic storage "trilemma" limiting the storage capacity of HDD's [4]. This trilemma relates to how HDD write data, store information as bits and the corresponding magnetic stability of the written bits to thermally activated reversal. The HDD started by storing information in-plane and then later transitioned to perpendicular magnetic recording (PMR), where further advancements are limited due to physical restrictions. To achieve the difficult goals of upgrading computer storage devices there must first be a detailed understanding of material applicable, where numerous materials and alloys are set in a race to improve current storage limitations by allowing higher density storage.

Writing information on magnetic media uses the fact that a magnet has a north and south pole, where these poles point up and down representing a 1 and 0 respectively for bit storage. The write field used to change the magnetic bit state uses a write head, where bits are made of multiple grains of the storage media. These write heads have reached an upper limit in their magnetic field strength and cannot go higher by HDD standards. Therefore without a larger magnetic field strength it is not possible to change the state of strong anisotropy materials, which becomes troublesome as these materials have the ability to remain thermally stable for a smaller grain size thus increasing the storage capacity. The thermal energy barrier relates to the magnetic anisotropy of the storage material and the temperature of operation, normally taken as room temperature (20°C). The thermal energy that must be overcome is given by the equation:

$$EnergyBarrier \quad \Delta = \frac{K_U V}{k_B T} \tag{1.1}$$

where K_U is the anisotropy energy, V is the volume of the grain and $k_B T$ is the thermal energy with k_B being Boltzmann constant and T as temperature. The value of Δ must be above 60 for industry standards, this corresponds to storing information for at least 10 years without losses due to thermal effects. To help combat these thermal effects a larger anisotropy energy K_U material may be used, but this would need a larger field to switch bits. This brings back the write head limitation and so the trilemma circulates, therefore any break in this trend would lead to progression in storage capacity.

1.2 Spintronic Storage Devices

The use of energy assisted magnetic recording in the forms of microwave assisted magnetic recording (MAMR) and heat assisted magnetic recording (HAMR) are paving the way for greater storage capacities in HDD and future storage devices. Spin torque oscillators (STO) in MAMR allow increased storage capacity as the STO increases the effective field of the read/write head, which broadens the scope of materials used to store magnetic bits as the write fields have increased thus breaking the trilemma of HDD's. It is anticipated that MAMR drives could have a storage capacity of $4Tb/in^2$ [5]. Alternatively heat assisted magnetic recording (HAMR) uses focused heating to reduce field needed for switching and is projected to ultimately be capable of $10Tb/in^2$ [6], with a future plan to integrate bit patterned media into HAMR. These isolated bits would create heated dot magnetic recording (HDMR) and is projected to scale up to $100Tb/in^2$ [7].

HAMR is localised heating of nanoscale regions of media (bits), enabling higher anisotropy materials for storage media as the higher temperature allows field switching, shown in figure 1.2. The bit size can then be reduced, increasing the storage capacity without any loss in stability as at room temperature the high anisotropy materials are very stable. However, the manufacturing limitations of reliable localised heating mean full commercialisation of this technique has not yet been achieved.
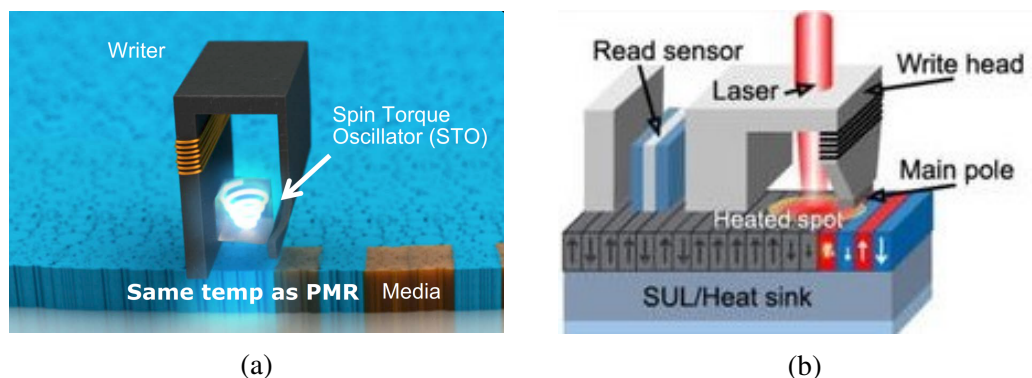
Figure 1.2: Current technological leaders in energy assisted magnetic recording, where $L1_0$ materials are used in spin torque oscillators (STO)(a) and as media in heat assisted magnetic recording (b) [6].

The write head in MAMR devices is equipped with a STO, described further in chapter 3, which increases the effective field, as shown in figure 1.2. This allows higher anisotropy materials to be used as storage media as the field can now overcome the energy barriers needed to switch the bit states. The bit size can be reduced as an effect of having a higher anisotropy and the areal storage density will therefore increase. Unlike HAMR, MAMR is not limited by the heating mechanism and has therefore been able to reach commercial market as of 2020.

1.3 $L1_0$ Ordered Binary Alloys for Spintronic and Data Storage Applications

Binary alloys in highly ordered crystallographic states are at the cutting edge of research into magnetic device applications such as; permanent magnets [8], storage media [9] and spintronic devices [10]. This is attributed to the $L1_0$ crystallographic state possessing a large uniaxial perpendicular magnetocrystalline anisotropy, present in materials such as FePt [11], FePd [12], CoPt [12, 13], MnGa [14] and MnAl [15]. Particular interest is given to FePt for its especially large magnetocrystalline anisotropy putting it at the forefront of high density storage [9] and MnAl for its simultaneous low magnetic damping and high uniaxial anisotropy making it a potentially valuable material for spin torque devices [16].

The optimised $L1_0$ state forms under refined fabrication conditions for various materials, where temperature plays a vital role in overcoming energy barriers [13,15,17]. The fabrication and annealing temperature is linked to chemical ordering through atomic diffusion, where added energy allows the atoms to move into a more stable state [17]. Structural and magnetic characterisation of materials like FePt and MnAl is vital for future device applications, where various approaches may be used for optimisation as will be covered in section 6 and 7.

1.4 Research Aim

My research focus is material development, specifically the fabrication and characterisation of highly ordered binary alloys in the $L1_0$ crystallographic phase. In particular, my focus is on MnAl and FePt, both of which have potential application in MAMR

and HAMR devices respectively. These materials have similarities in fabrication procedure, where energy control of arriving atoms is vital to controlling the disordered to ordered phase transition. The two alloys have narrow allowed compositional range and temperature plays a key role in the thermodynamics of phase formation.

The study of FePt transition to the $L1_0$ phase through heating has produced many papers, those of particular interest [4, 11, 18–21]. FePt potential use as a medium in HAMR has been responsible for its continued research, where the focus of this work is on highly ordered FePt thin films with perpendicular magnetic anisotropy. In comparison, work on $L1_0$ ordered FePt with in-plane uniaxial anisotropy is virtually unreported. An important goal of this work is to demonstrate that $L1_0$ ordered FePt with in-plane uniaxial anisotropy can be produced by sputtering. Such films are rare, as typically materials with in-plane anisotropy demonstrate cubic rather than uniaxial anisotropy [22] or at best weak uniaxial anisotropy, such as NiFe produced using forming field [23]. A thin film material with uniaxial in-plane anisotropy has applications as bias magnets in recording heads, and in exchange spring systems.

The developments of $L1_0$ ordered MnAl thin films is a key part of this work. The number of papers showing the successful fabrication of thin film MnAl in a highly ordered state is limited, leaving a large parameter space for optimisation. To achieve ordering the composition must be controlled within a small window of 10 atomic %, where temperature plays a key role in overcoming energy barriers for phase formation. This work aims to highlight key issues faced with fabricating the $L1_0$ phase, where the composition, magnetic and structural properties of films are evaluated.

1.5 Contribution Acknowledgement

possible.

In addition to the main focus, the work on understand the fabrication of $L1_0$ FePt and MnAl, I have contributed to several projects during my PhD studies and these together with their expected outcomes are briefly summarised below.

Characterisation of size distribution and positional misalignment of nanoscale islands by small-angle X-ray scattering [24]

The beamtime measurements and initial analysis were carried out by Georg Heldt, a previous PhD student at the University of Manchester. The work involved a large collaboration from Georg Heldt, myself and Thomas Thomson at the University of Manchester (UK), Rajesh V. Chopdekar and Joachim Kohlbrecher at the Paul Scherrer Institut (Switzerland), Stephen Lee at the University of St. Andrews (UK) and Laura J. Heyderman from the Laboratory for Mesoscopic System, ETH Zurich (Switzerland). The measurement process involved detailed analysis of small angle X-ray scattering of an ordered nanostructure array of varying size and density. This novel method of analysis could be used to evaluate inconsistencies in e-beam lithography processes, such as stitching errors, whilst giving a detailed image of large scale nano array structure, size and distribution.

The outcome of this project was a publication [24] in journal of applied physics (JAP), where I was responsible for finalising the analysis and interpretations of the data, drafting the manuscript and coordinating feedback from all contributors.

Thickness dependent magnetic measurements of high anisotropy Co/Pd multilayer coupled to NiFe thin films of various thickness

Polarised neutron reflectivity (PNR) measurements were carried out on Co/Pd multilayers coupled to NiFe layers, where the magnetic interaction of the perpendicularly aligned multilayer to in-plane aligned NiFe layer was investigated for a variety of spacer layer thicknesses. The fabrication and PNR characterisation together with X-ray characterisation was a joint project between Dr. William Griggs and myself. Samples were measured at Rutherford laboratory to quantify how a high anisotropy materials such as Co/Pd multilayers interact with a soft NiFe layer, under different temperature regimes. The two magnetic layers, where the stack of Co/Pd are treated as one layer, were separated by a non-magnetic palladium layer of varying thickness

to represent different exchange systems. The magnetic interactions between the layers was then investigated by modelling of the structure and magnetic state through PNR analysis, which was performed at multiple temperatures representing back-end fabrication conditions. This work was a combined effort of myself and Will Griggs with additional support given by the instrument scientists Christy Kinane and Andrew Caruana at STFC.

A manuscript is currently in preparation for this work.

Characterisation of buried interfaces using Ga K$_\alpha$ Hard X-ray Photoelectron Spectroscopy (HAXPES)

The commission of the Hard X-ray Photoelectron Spectroscopy (HAXPES) system began halfway through my PhD. As this was a new technique to the University it needed routine tests to validate its usability, where a series of samples with various capping layers were investigated to test probe depth. The technique is solely a characterisation of composition and the work involving MnAl was highly compositionally dependent, therefore a collaboration between myself and Ben Spencer was setup to investigate such samples whilst also testing the system. The measurements proved vital for the progression of this PhD whilst also refining the usability of the technique as our fabrication facilities helped further their understanding of its limitations.

The manuscript is currently in preparation, where the work highlights the new measurement technique and how it could be used within a wide range of the scientific community as sample preparations is not limited by X-ray penetration on the surface. The contribution to this work includes the fabrication of samples varying material thickness and testing capping layer effect on underlying materials. Further analysis of depth dependent composition was proposed but due to time restrictions it was not possible within the course of this PhD.

Uni-axial in-plane alignment of highly ordered L1$_0$ FePt

&

Investigation into exchange coupled in plane and out-of-plane FePt with NiFe as a function of thickness

The use of FePt within the spintronic community is highly topical, where it is nominally perpendicularly aligned. However, a new fabrication procedure for uniaxial in-plane FePt was designed for magnetron sputtering, where it is to be used in an exchange spring structure. This work is a collaboration between the University of Manchester and Exeter University, where sample fabrication and structural characterisation are carried out by myself at Manchester University, with additional SQUID magnetometry carried out by Adam Brookfield at Manchester University, and beam time X-ray FMR at Diamond light source is carried out by Rob Hicken's group from Exeter University.

The work can be broken into two parts; (i) is the new method for fabricating the desired uniaxial in-plane FePt using magnetron sputtering and (ii) is its interaction to a magnetically soft permalloy layer. The fabrication method was not available for the original beam time, where only perpendicular to in-plane exchange spring structure were investigated. Therefore, further investigation into in-plane to in-plane exchange spring interactions is needed for this work to be completed before a paper can be written. As this work was effected by closures simulations are being carried out by Exeter University, where further collaboration in the future is possible for both perpendicular and in-plane aligned FePt thin films.

Fabrication of thin film MnAl with L1$_0$ ordering under various fabrication conditions

One of the most exciting new L1$_0$ materials is MnAl, due to its cost effectiveness and surprisingly good magnetic properties. In recent years more publications are investigating its fabrication, but none have shown the problems faced with compositional variance. It has been found that a large amount of Mn is lost for the sputtering setup used in this work. The potential for this material to vary from system to system is worth investigating further as it could limit its potential uses going forward. The initial findings suggest that for a large sputtering chamber there is a correction factor between predicated and obtained Mn composition.

This work has made interesting findings but the parameter space investigated is still somewhat limited. Therefore before the writing process can begin further study into sputtering distance and temperature of deposition are needed. Following these results a complete story of compositional variance will be made and can be written up. The results of this work are vital for new research groups investigated this material as system variations make it difficult to diagnose complex phase growth problems found with this material.

1.6 Thesis Outline

The first chapters of this thesis cover the fundamentals of magnetism, magnetic materials 2 and $L1_0$ ordering 3. The basics of magnetism and interactions of magnetic materials are described in chapter 2 with an explanation of magnetic anisotropy and how it links to a magnetically ordered system. Magnetisation dynamics associated with a spin polarised current are discussed in the later sections of this chapter and enhanced upon in the discussion of application for $L1_0$ materials in spintronic devices. Long range ordering in binary alloys is covered in detail within chapter 3, where the intricate links between material fabrication and characteristics are explained in full. Chapter 3 includes a literature review of choice $L1_0$ materials, where the aim is to help the reader understand the complexities of forming such phases in thin film form.

Throughout the course of this PhD multiple systems have been used for fabrication and characterisation. Therefore, chapters 4 and 5 go into detail on the fabrication and characterisation of thin magnetic film respectively. A detailed description is built from the pre-fabrication cleaning to sample characterisation. These techniques are what make this work possible and therefore a complete understanding of constraints is detailed, where certain pieces of equipment have had to be intricately adapted for the course of this work. Details on the more specialised techniques have been covered where it falls outside normal use for the system such as in-situ heating.

Chapters 6 and 7 of this thesis detail the results obtained for FePt and MnAl thin films respectively. Chapter 6 describes new understanding of how uniaxial in-plane FePt can be fabricated by magnetron sputtering using an appropriate choice of substrate and seeding layers. Chapter 7 details MnAl thin films, where a comprehensive study was undertaken to understand the parameters and methodology needed to create magnetic

order. A comparison between two approaches, single target and co-deposition, is laid out with a decisive explanation on best fabrication procedure to follow.

The final chapter of this thesis concludes the study of both FePt and MnAl thin films and outlines the interesting findings and their uses going forward. As this work has a finite time limit there is always work that could be carried out and a list of ideas is laid out with their potential impact on the materials standing within the scientific community. It is the hope that this chapter can further the discussion on these materials uses going forward and spark an interest in their prospects.

Units within Magnetism

Historically, work on ordered magnetic materials has relied on the use of the c.g.s (centimetre gram second) system of units rather than the standard SI (International System of Units) units. Much of the literature published today retains this use of c.g.s. units as there is a natural separation of stimulus (field) and effect (moment). In keeping with this common practice, this thesis is present in c.g.c. units. The table below is the most commonly used quantities and the variations in the two units, as well as any conversion factors.

Quantity	Symbol	CGS	Conversion Factor	SI
Flux density (Induction)	B	Gauss	10^{-4}	Tesla
Magnetic Field Strength	H	Oersted (Oe)	$\frac{10^3}{4\pi}$	A/m
Magnetisation	M	emu/cm^3	10^3	A/m
Magnetic Moment	m	emu	10^{-3}	Am^2
Susceptibility	χ	dimensionless	4π	dimensionless
Permeability	μ	dimensionless	$4\pi \times 10^{-7}$	H/m
Demagnetisation factor	D	dimensionless	$\frac{1}{4\pi}$	dimensionless

Table 1.1: List of magnetic quantities used throughout this thesis and alternative units with conversions [25].

Chapter 2

Background on Magnetism and Magnetic materials

The identification of magnetism dates back to the ancient world where Greek philosophers were among the first to have scientific discussions on magnetic properties, around 600 BC [26]. In ancient China the earliest reference to magnetism dates to around 400 BC, where lodestones are depicted as having attractive properties with iron [27]. These early observations formulated the foundation for magnetic materials, which helped to inspire an interest in their uses for future technologies. Over two millennia later, around 1550 to 1620, William Gilbert began experimenting with magnetic compasses to determine unknown facts about the Earth's magnetic field, this was the first time a clear picture of Earth's magnetic field was formed. The work carried out by Gilbert confirmed definitively that the Earth itself was magnetic, details of which were published in his classic book *On the Magnet* in 1600 [28]. Two centuries later Oersted showed that an electrical current flowing in a conductor produced a magnetic field [29]. This consequently set in motion the investigation of electromagnetism, which over the years has driven technology to new heights with civilisation altering scientific discoveries. In the modern era the humble magnet has revolutionised technology with the digitalisation of mankind, therefore a deep understanding of magnetism and magnetic materials is essential to optimise devices and technologies for future applications.

A detailed understanding of the magnetic properties of materials relies on intimate knowledge of their structure, so this chapter first describes the basics of crystallography.

2.1   Basics of Crystallography

Most solids at the atomic scale can be described as a regular arrangement of atoms, this is known as the crystal structure [30]. The building block that describe a crystals structure can be thought of as three vectors from an origin point as shown in figure 2.1.
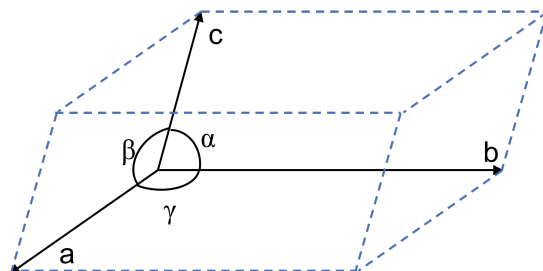
Figure 2.1: General image of unit cell with three basis vectors **a**, **b** and **c**.

The basis of using such blocks to define a crystal structure was described by Haüy's block model [30]. The blocks in the model were later removed and only the corner points considered, where the translation vector t, also known as the lattice vector, was defined from the origin to a point with coordinates (u,v,w):

$$t = u\mathbf{a} + v\mathbf{b} + w\mathbf{c} \tag{2.1}$$

All corners of the unit cell can be reached by one of the three basis vectors, where the sum of all corner points is the space lattice [30]. Each corner is a lattice point and there are seven fundamentally different combination of basis vectors in 3D space which are able to describe crystal structure, shown in table 2.1. In most general cases they are defined by the three vectors (a, b, c) and three angles (α, β, γ) as shown in figure 2.1.
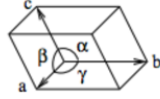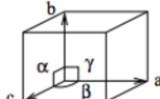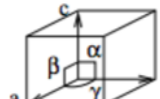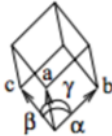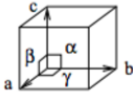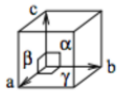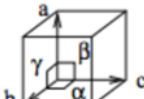
Conditions, symbol	Crystal System	Drawing
No conditions $a, b, c, \alpha, \beta, \gamma$	Triclinic	
$\alpha = \gamma = 90°$ $a, b, c, 90, \beta, 90$	Monoclinic	
$a = b, \alpha = \beta = 90, \gamma = 120$ $a, a, c, 90, 90, 120$	Hexagonal	
$a = b = c, \alpha = \beta = \gamma$ $a, a, a, \alpha, \alpha, \alpha$	Rhombohedral	
$\alpha = \beta = \gamma = 90$ $a, b, c, 90, 90, 90$	Orthorhombic	
$a = b, \alpha = \beta = \gamma = 90$ $a, b, c, 90, 90, 90$	Tetragonal	
$a = b = c, \alpha = \beta = \gamma = 90$ $a, a, a, 90, 90, 90$	Cubic	

Table 2.1: The conditions linked to each crystal system for lattice vectors a, b, c and angles α, β, γ, drawings taken from [30].

Within the seven crystal systems shown in table 2.1 the exact arrangement of atoms allows another tier of classification. As an example, the cubic system can be divided into Simple, Body Centered, Base Centered or Face Centered. This allows a total of 14 Bravais lattices to be identified and all crystals can be described as belonging to one or another of these types, as shown in figure 2.2 [31].
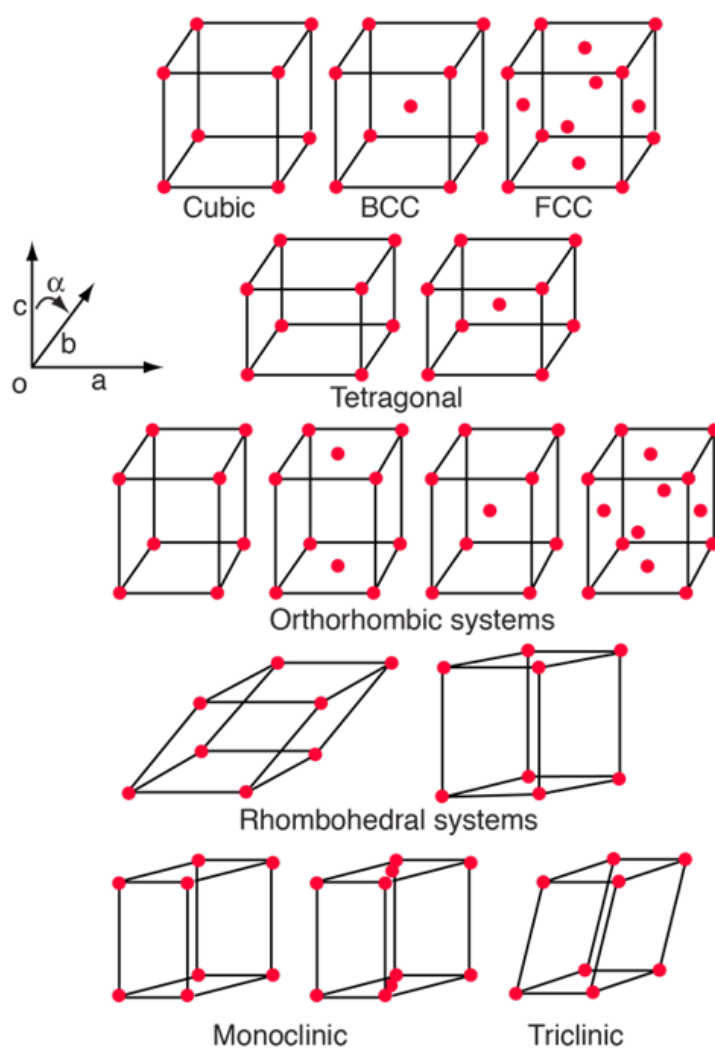
Figure 2.2: The 14 Bravais lattices associated with crystal systems [31].

2.1.1 Lattice Planes

The fundamentals of X-ray diffraction are covered in chapter 5, where the lattice spacing for a unit cell is represented by crystal planes. A crystal plane can be defined as a connection of points from an origin O, where separation is measured along the axes a, b and c. The example shown in figure 2.3 gives a vector **r**, where the direction is give by [uvw], such that OP is:

$$\mathbf{r}_{uvw} = u\mathbf{a} + v\mathbf{b} + w\mathbf{c} \tag{2.2}$$

Additional points Q and R follow the same principle as P but for different coordinates, where the plane with intercepts P, Q and R will have coordinates (P,0,0), (0,Q,0) and (0,0,R). The equation for the plane would simply be:

$$\frac{x}{P} + \frac{y}{Q} + \frac{z}{R} = 1 \tag{2.3}$$

$$QRx + PRy + PQz = PQR \tag{2.4}$$

$$h = QR \qquad k = PR \qquad l = PQ$$

$$hx + ky + lz = PQR \tag{2.5}$$
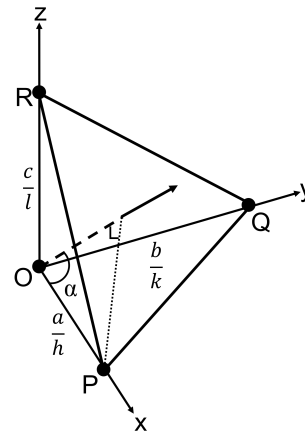
Figure 2.3: Representation of lattice spacing by using the space from Miller plane to origin [32]

The Miller plane is defined as (hkl), where a unit cell will intercept the x axis, y axis and z axis h, k and l times respectively. Miller planes are the surfaces that act as a mirror for constructive interferences to take place and therefore play an important role in relating the wavelength of X-rays to the angle for constructive interference for a defined lattice spacing of a unit cell. An example of common Miller planes is given in figure 2.4, with those important for this work highlighted.
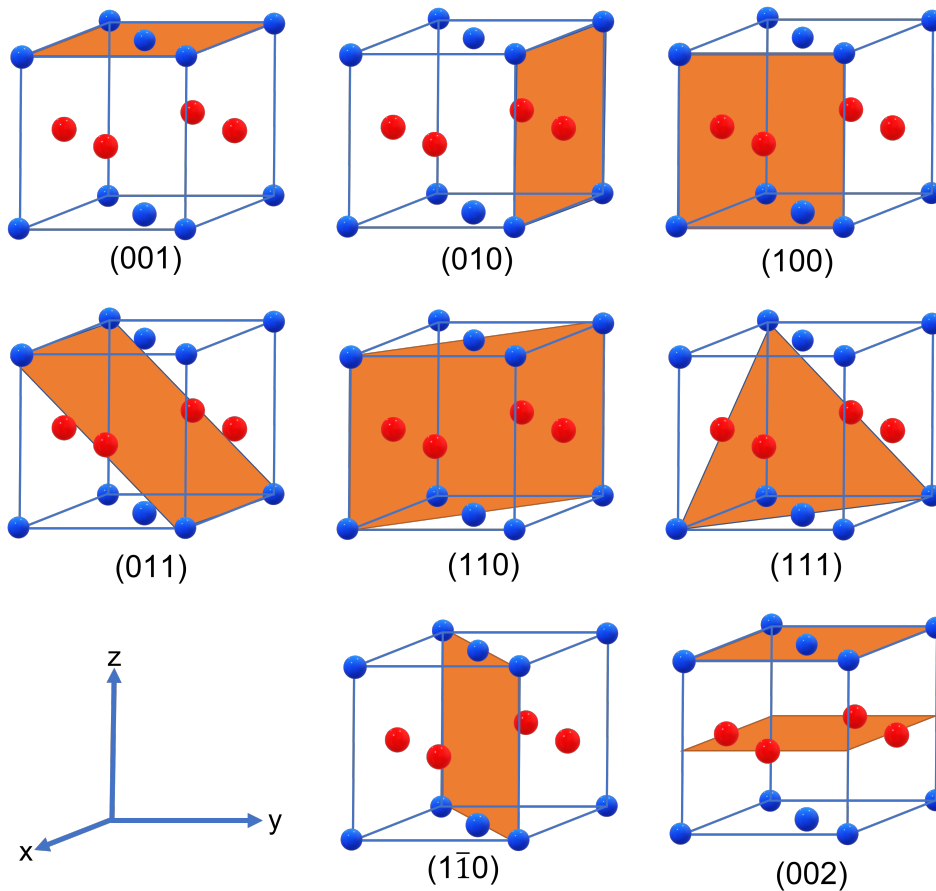
Figure 2.4: Miller planes for face centered tetragonal (FCT) unit cell.

2.2   Magnet Fundamentals

Any magnet, no matter the size, possesses two poles; in a simple picture the source of a magnetic field is the North pole and the corresponding sink point of the field is the South pole [26, 33]. A straightforward experiment to measure magnetic poles is to suspend a magnet from a string, where the magnet is free to rotate, it will manoeuvrer itself so that one of the poles points roughly towards the geographical north pole of Earth, this is the magnet's north seeking pole. To understand a magnet one must first have knowledge of how magnets interact with one another. Suspending a magnet from a torsion wire and exposing it to an additional magnet, as shown in figure 2.5, allows a concise understanding of how one magnet effects the other.
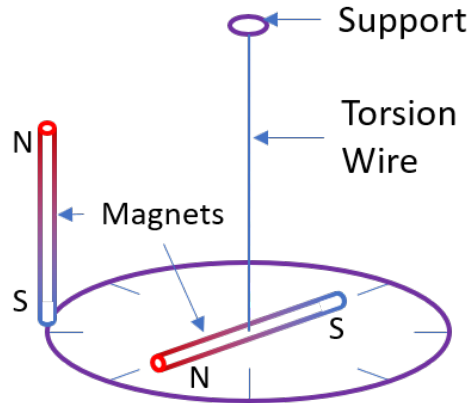
Figure 2.5: Early experiment used to show attractive and repulsive forces between magnetic north and south poles.

The law governing forces experienced by magnets was discovered by John Michell and Charles Coulomb independently in 1750 and 1785 respectively [34]. The law states that a force F experienced between two magnetic poles is proportional to the product of the pole strengths ,p_1 and p_2, and inversely proportional to the square of their distance apart d:

$$F = k\frac{p_1 p_2}{d^2} \tag{2.6}$$

Using a torsion wire of known stiffness (k) the magnetic force is calculable from the angle of rotation, the results of this experiment showed that like poles repel and un-like poles attract. The interaction can be conveniently visualised as a field, it is this field which produces the force on a secondary magnet. Therefore the force is proportional to magnetic field strength H:

$$F = kpH \qquad \text{where} \qquad H = \frac{p}{d^2} \tag{2.7}$$

If a magnet is placed in a magnetic field H, as shown in figure 2.6, there will be a torque that aligns the magnet parallel to this field, which is described by the equation:

$$\vec{m} = \frac{l(p\vec{H}sin\theta)}{2} + \frac{l(p\vec{H}sin\theta)}{2} = p\vec{H}lsin\theta \qquad (2.8)$$

where m is the torque experienced, also known as the magnetic moment, p is the pole strength of a magnet of length l that is at an angle θ to the applied field H. This relation between magnetic moment and the poles of the magnet becomes important as the poles themselves are simply a mathematical concept and not a physical reality. This comes down to poles inability to be separated for measurements as they are not a localised point, which means the distance l is indeterminate. However, the product of p and l is precisely measurable as the magnetic moment m. Therefore magnetic poles are useful in visualising problems with magnetic interactions.
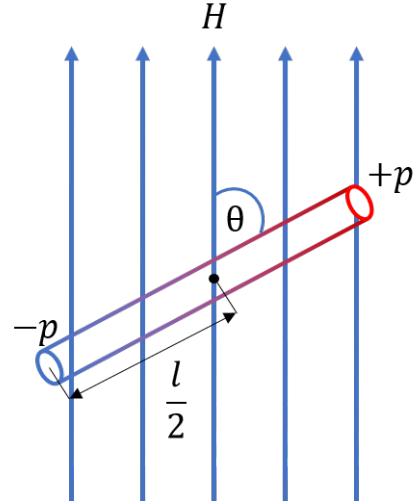
Figure 2.6: Bar magnet response to a uniform magnetic field H.

The energy needed to align the magnet parallel to the applied field is given by:

$$E_P = \int_\theta^{90} \vec{m}\vec{H}sin\theta d\theta = -\vec{m}\vec{H}cos\theta = -\vec{m}\cdot\vec{H} \qquad (2.9)$$

For convenience the zero energy point is taken as $\theta = 90°$, where $-mH$ is parallel and $+mH$ is antiparallel.

To understand a materials response to a magnetic field one must consider the magnetic moment of the material. Placing two identical bar magnets either side by side or in front of one another will have the same overall effect on the magnetic moment. If placed side by side the pole strength is summed $(2p)$, as shown in figure 2.7 (a), the magnetic moment is $m = (2p)l = 2pl$. In the case where the magnets are in front of another the pole separation doubles to $(2l)$, as shown in figure 2.7 (b), the moment is $m = p(2l) = 2pl$. Therefore, in both cases the magnetic moment of the system has doubled but the volume has also doubled meaning the magnetic moment per unit volume has not changed.
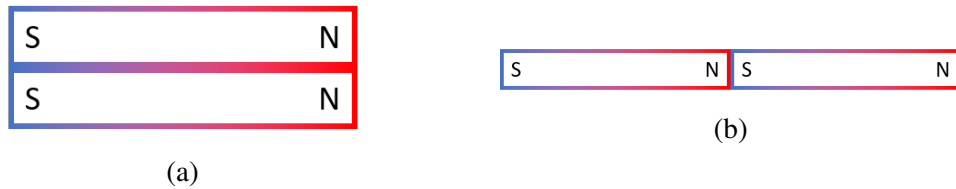
Figure 2.7: Two bar magnets place side by side so the;(a) pole strength is doubled and (b) the length between poles is doubled.

The measure of magnetic moment per unit volume is Magnetisation *M*, which is given as:

$$M = \frac{m}{V} = \frac{pl}{V} = \frac{p}{A} \tag{2.10}$$

where *V* is the volume and *A* is the cross-sectional area of the magnet. Therefore a measure of magnetisation is the pole strength per unit area of cross section, given the units *emu*/*cm*^{3}. Where *emu* is the electromagnetic unit of magnetic moment [34].

2.2.1 Fundamental Source of Magnetic Moment

The source of magnetism in materials is the angular momentum of elementary particles, where the prime contributor is the electron. Electron angular momentum is built upon spin and orbital motion as shown in figure 2.8. The nuclear magnetic moment is relatively low, $10^{-5}\mu_B$, and is therefore ignored in most circumstances. The orbital moment of an electron is equivalent to that of a current flowing in a wire, where:

$$Moment = Current \times Area = \frac{-e}{\tau}\pi r^2 \tag{2.11}$$
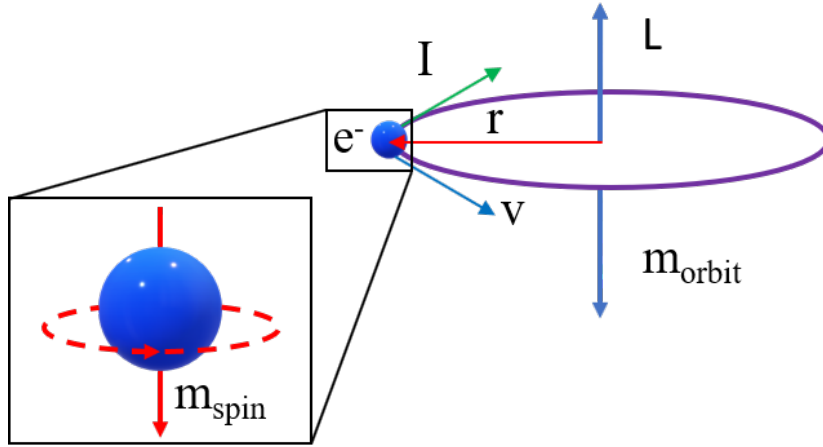
Figure 2.8: Electron in orbit of radius r and velocity
v producing a magnetic moment μ.

The velocity of the electron is given by v, its period of rotation is $\tau = \frac{2\pi r}{v}$ and area is
given by a circular orbit. Including the angular momentum of the electron, $\vec{L} = m_e \vec{r} \times \vec{v}$,
where m_e is the electrons mass and $\vec{r}$ is the radius of its orbit, the magnetic moment
becomes:

$$Moment = \frac{-e}{2}\vec{r} \times \vec{v} = \frac{-e}{2m_e}\vec{L} \tag{2.12}$$

The magnetic moment is therefore proportional to angular momentum, where the nega-
tive sign denotes that the magnetic moment and the angular momentum are in opposing
directions as shown in figure 2.8. However, the orbital angular momentum of an elec-
tron is bound by the laws of quantum mechanics which means its values are quantized
in units of $\hbar$ along a certain axis z, which is taken as parallel to the magnetic field
where $L_z = m_L \hbar$. Here m_L is the orbital magnetic quantum number which has integer
values between $-L \leqslant m_L \leqslant L$ [33]. The equation for magnetic moment therefore be-
comes:

$$Moment = -\frac{e\hbar}{2m_e}m_L \tag{2.13}$$

The smallest possible value and therefore the natural unit for electronic magnetism is
defined here as the Bohr magneton:

$$\mu_B = \frac{e\hbar}{2m_e} \tag{2.14}$$

As shown in figure 2.8 the electron possesses intrinsic spin angular momentum as well as orbital motion [35]. The associated magnetic moment can adopt two discreet orientations relative to a magnetic field, related to the spin quantum number $s = \frac{1}{2}$. To think of the electron as a spinning ball of charge is inherently wrong due to it being a point like particle, the mysterious built in angular momentum is a consequence of relativistic quantum mechanics. All particles possessing spin (fermions) have an associated magnetic moment, where the magnetic moment associated with spin is not a half but almost exactly one Bohr magneton [33]. The Pauli exclusion principle states that no two electrons can occupy the same state, as identified by the four quantum numbers n, l, m_l, s and m_s [36]. Where electrons confined within the same orbital will align antiparallel with a spin of $s = \pm\frac{1}{2}$, the magnetic moment in relation to the spin magnetic quantum number m_s is therefore given as:

$$Moment = -\frac{e\hbar}{m_e}m_s = -2\mu_B s \tag{2.15}$$

Spin angular momentum is twice as efficient as orbital angular momentum at creating a magnetic moment [33], as can be seen by comparing 2.13 and 2.15. However, with higher-order corrections for electrons intrinsic spin moment the gyromagnetic ratio γ gives spin moment as $1.00116\mu_B$, where for normal purposes this is ignored and the two factors are assumed to be equal.

The interaction between spin and orbital angular momentum is known as spin-orbit coupling, this creates a total angular momentum term J which has the following magnetic moment:

$$Moment_{tot} = -\frac{\mu_B}{\hbar}(L+2S) = -g_J\frac{\mu_B}{\hbar}J \tag{2.16}$$

where g_J is the Landé g-factor calculated from J, S and L [33, 36]. In an atom there are many electrons each nominally spinning about its own axis and moving in its own orbit. Therefore, each electron has a magnetic moment associated with itself. This magnetic moment of the atom is a vector sum of all electronic moments with two

possible outcomes:

1. Magnetic moments of all the electrons orientate themselves so they cancel out, therefore the atom as a whole does not posses a net magnetic moment.

2. There is partial cancellation of electronic moments and therefore some left over net magnetic moment. These atoms are denoted as magnetic atoms and they make up the classifications as shown in table 2.2.

2.2.2   Magnetic Exchange Interaction

The foundations of exchange is to consider two electrons interacting, following Pauli's principle which forbids double occupancy of identical quantum states [36, 37]. This causes electrons to be antiparallel to one another forbidding parallel spins within the exact same orbital. To realise a parallel spin orientation one electron must occupy an excited orbital, the necessary energy is given by Coulomb interaction between two electrons at r and r':

$$V_C = \frac{e^2}{4\pi\varepsilon_0 |r - r'|} \tag{2.17}$$

where V_C is electrostatic potential energy, e is the electron charge and ε is the permittivity of free space. The interaction is spin-independent but large for electrons in a common orbital compared to those in different orbitals, equating to a favourable situation for parallel spin alignment in different orbitals. However, this favoured situation is in competition with an increase in electron energy for one of the electrons. The exchange is therefore obtained by comparing the total energy associated with a ferromagnetic and antiferromagnetic two-electron wave function:

$$\Psi_{FM} \approx \phi_l(r)\phi_r(r') - \phi_r(r)\phi_l(r') \tag{2.18}$$

$$\Psi_{AFM} \approx \phi_l(r)\phi_r(r') + \phi_r(r)\phi_l(r') \tag{2.19}$$

where $\phi_l(r)$ and $\phi_r(r)$ are the atomic wave functions of left and right atoms, respectively. Comparing the two equations 2.18 and 2.19 it is clear that when the position r and r' are the same that equation 2.18 goes to zero, as this would contradict the Pauli exclusion principle where identical electrons cannot occupy the same space.

The symmetric and antisymmertric real-space wave functions $\Psi(r',r) = \Psi(r,r')$ and $\Psi(r',r) = -\Psi(r,r')$ correspond to $\uparrow\downarrow$ and $\uparrow\uparrow$ respectively, thus confirming the assignment of ferromagnetic and antiferromagnetism in equations 2.18 and 2.19 [37]. The energy of the system is evaluated, giving the exchange constants J:

$$J = \frac{E_{AFM} - E_{FM}}{2} \qquad \text{where} \qquad E = \int \Psi^*(r,r')H(r,r')\Psi(r,r')dV\,dV' \tag{2.20}$$

Therefore a positive exchange constant J is associated with ferromagnetic spin coupling, whereas a negative J leads to spins that are coupled antiferromagnetically [37]. The exchange constant J is therefore defined as the half energy difference between parallel and antiparallel states, as shown by equation 2.20, with dependence on interatomic distances and the number of electrons per atom.

2.3 Magnetisation and Magnetic Moment of Materials

An important measure of a magnetic material is the magnetic moment per unit volume, the magnetisation M as shown in equation 2.10. For a material with n number of elementary magnetic dipoles per unit volume the maximum value for magnetisation at a given temperature is $M_S(T)$, which is the saturation magnetisation, and is equal to the number of elementary magnetic dipoles times the magnetic moment of those dipoles m. The ability of an applied magnetic field H to magnetise a material is given by the magnetic susceptibility of the material χ and the resultant magnetic field inside the material compared to the applied field is given by permeability μ:

$$\chi = \frac{M}{H} \qquad \text{and} \qquad \mu = \frac{B}{H} \tag{2.21}$$

where the materials response to the applied magnetic field is the magnetic induction B given by:

$$B = H + 4\pi M \tag{2.22}$$

The induction came from an early understanding of magnetism where a piece of iron would be brought near a magnet and have induced magnetism [34]. The more common

term for *B* is now the flux density of the material.

2.3.1   Classification of magnetic materials

Magnetic materials fall into one of five categories described by the materials bulk susceptibility (χ), shown in the list below and summarised with magnetic structure in table 2.2.

1. Diamagnetism is a small negative response to an applied field, where $\chi \approx -10^{-5}$, with no net magnetisation without the applied field. A special form of diamagnetism are superconducting materials where $\chi \approx -1$.

2. Paramagnetism presents itself as no net magnetic moment in the absence of an applied field but a small magnetisation under an applied field, with $\chi \approx 10^{-3}$ to 10^{-5}. This arises from unpaired electrons that partially fill orbitals, when subjected an applied magnetic field they align to give a small magnetisation parallel to applied field.

3. Ferromagnetism, which is possibly the most useful, are materials with a net magnetic moment in the absence of an applied field. The value of susceptibility χ is normally much greater than 1 ranging from 50 to 10000. Under the application of an applied field they will align parallel to the field increasing in magnetisation until the saturation point at magnetic field H_{sat}, beyond this point no increase in moment is seen.

4. Antiferromagnetism similar to the ferromagnetic case each atom has a magnetic moment but here they align anti-parallel to one another typically on alternating atomic sites, so there is no net magnetisation for these material.

5. Ferrimagnetism is built upon a disproportionate magnetic moment from each contributing atomic site. This inequality causes the normal antiferromagnetic case to have some net magnetisation, where it is normally found in multi-element compounds as each element will have different magnetic moment to contribute.
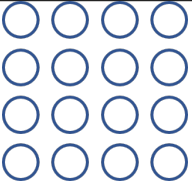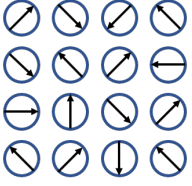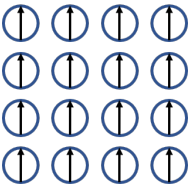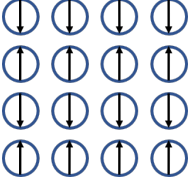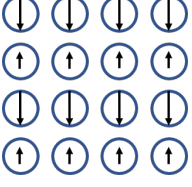
Class of Magnetic Material	Atomic Magnetisation (No Applied Field)	Example Materials
Diamagnetism		Inert gases, Copper, Silver, Gold and many non-metallic elements
Paramagnetism		Aluminium, Platinum, Manganese, diatomic gases O_2 and NO
Ferromagnetism		Cobalt, Iron, Nickel, Mn alloys such as MnBi and MnAl
AntiFerromagnetism		Cr, Cobalt oxide, Maganese oxide and Nickel oxide
Ferrimagnetism		Certain Iron oxides and alloys such as Fe_3O_4, Fe_2O_3 and FeGd

Table 2.2: Table summarising the various classification of magnetic materials with a list of example materials, magnetic moment is represented by the red arrows where the blue circles are atoms.

2.3.2   Susceptibility as a function of temperature

The classification of materials in 2.3.1 assumes a constant temperature for each magnetic effect. However, if a ferromagnet is heated it will reach a critical point known as the Curie temperature T_C, where the material becomes paramagnetic and the susceptibility falls towards zero. Not all ferromagnets are equal when it comes to Curie temperature, as shown in table 2.3.

Material	Curie Temperature (°C)
Iron	770
Nickel	358
Cobalt	1130
Gadolinium	20
Terfenol	380-430
Alnico	850
Hard ferrites	400-700
Barium ferrite	450

Table 2.3: Curie temperature of various ferromagnetic materials [26].

Similar to the ferromagnetic case, antiferromagnetic materials also have a point where the susceptibility changes significantly. However, antiferromagnetic materials do not react to temperature in the same manner, therefore the critical point in these materials is denoted as the Néel temperature T_N. The susceptibilities in both ferromagnetic and antiferromagnetic materials follows a modified Curie-Weiss law for susceptibility as a function of temperature, which gives:

$$\chi = \frac{C}{T - \Theta_P} \tag{2.23}$$

where Θ_P is the paramagnetic Curie temperature and C is the Curie constant that relates to the material under investigation. In the case of ferromagnetic materials $\Theta_P \approx T_C$ making $\Theta_P > 0$ whereas in antiferromagnetic materials $\Theta_P < 0$ [38].
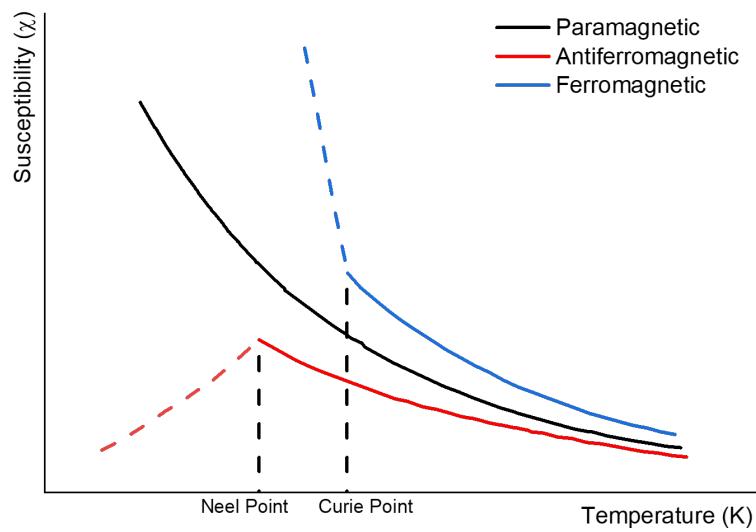
Figure 2.9: Susceptibility of ferro-, antiferro- and paramagnetic materials as a function of temperature [38].

2.3.3 Magnetic Hysteresis

An important property of ferromagnetic materials is their high relative permeability and susceptibility. Therefore to characterise such materials the magnetic induction *B* or magnetisation *M* is measured as a function of applied field *H*, this measurement results in a hysteresis loop. The hysteresis loop axis can therefore take two forms, either the magnetic induction *B* as a function of *H* or the magnetisation *M* as a function of *H*, both of these provide the same information since $B = H + 4\pi M$ but in magnetic material research the latter is always used.
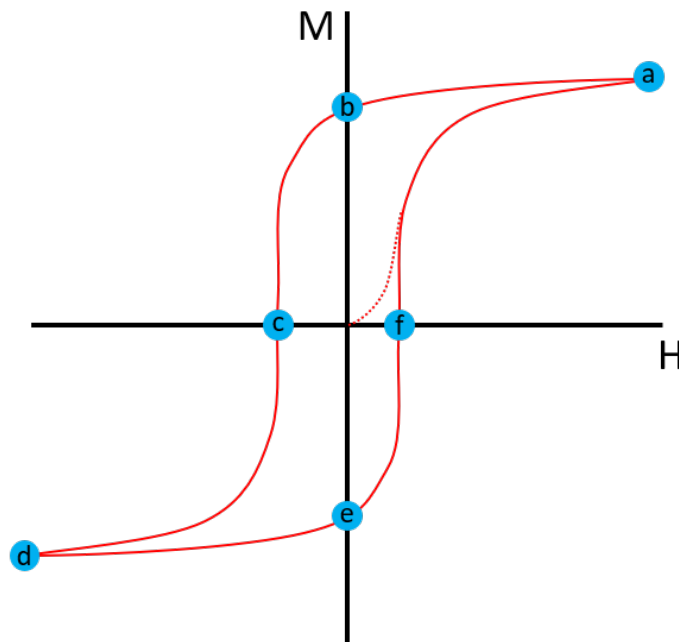
Figure 2.10: The M-H Hysteresis loop used to gain fundamental knowledge of ferromagnetic materials. Stages a to f correspond to points of interest along the hysteresis curve with the dashed line showing a virgin curve for a previously demagnetised sample.

A hysteresis loop has many points of interest linked to a materials properties [39], as shown by the stages in figure 2.10.

1. Points a and d correspond to a fully saturated sample, where all magnetic moments within the material are aligned parallel to the applied field.

2. Points b and e are the remanence, also known as retentivity, of the material and correspond to the magnetisation remaining within the material after the magnetic field being applied is removed.

3. Points c and f are the coercivity of the material, this value denotes the reverse applied field needed to bring a material from remanence to zero net magnetisation.

4. The dashed line is a virgin curve, this is a materials ground state response to a magnetic field, where the ground state has zero magnetisation either purposefully or because the material has never been exposed to an applied field.

An important feature of magnetic hysteresis loops are their shape, this allows classification of ferromagnetic materials based on their coercivity. The coercivity is structure sensitive and may be altered by changing the samples mechanical treatment and/or temperature, it should also be noted that there is a (normally) weak time relation due to thermal activation. A commonly used term is hard and soft magnetic materials, this comes from the fact that mechanically soft/hard Iron would have low/high coercivity respectively. Hard materials are those with coercivity values above 125 Oe whereas soft materials are those with coercivity below 12.5 Oe [26]. A hard material needs a larger applied field to switch the magnetisation, therefore it is most useful for stable field applications. A soft material is easily magnetised and is used in application where low coercive fields are a requirement, where systems normally require low power consumptions such as transformer cores.

2.3.4 Magnetic Anisotropy

Materials that have one or more axis of preferred magnetisation are known as being magnetically anisotropic. In these materials there is a magnetic anisotropy energy barrier that must be overcome to reorientate magnetisation from the preferred axis, known as the easy axis. An anisotropic system will have many contributing factors that cause a preferred direction(s) magnetisation including the shape, crystallinity and strain within the system. For rotations of magnetisation away from the easy axis direction their exists a anisotropy magnetic field H_K that acts to hold the magnetisation parallel to the axis. The anisotropy field H_K is a representation of the anisotropy energy as a field and is given by:

$$H_k = H_d + H_m + H_s \tag{2.24}$$

where H_d is the shape, H_m is the magnetocrystalline and H_s is the strain contributions. An in-depth understanding of a materials easy axis is used to formulate magnetic devices, where a strong anisotropy is a prerequisite for a hard magnetic material, whereas a low value corresponds to a soft magnet [33]. The energy associated with reorientation of uniaxial magnetisation is given by:

$$E = K_U sin^2 \theta \tag{2.25}$$

where K_U is the anisotropy constant of the material and θ is the angle between M and the easy axis. The anisotropy constant is often measured through a hysteresis loop by taking the applied field needed to saturate the hard axis of a material, given by:

$$K_U = \frac{M_S H_K}{2} \tag{2.26}$$

but as shown in equation 2.24 the value of H_k is made of multiple sources of anisotropy. So, to fully understand where a materials easy axis of orientation comes from and how to use this in device fabrication one must consider all sources of anisotropy.

2.3.4.1   Shape

A ferromagnetic material that is aligned will have a corresponding demagnetising field H_d, which acts in the opposing direction to the overall magnetisation M. The value of the demagnetising field is given by [39]:

$$\vec{H}_d = -N\vec{M} \tag{2.27}$$

where N is the demagnetisation factor, which aligns antiparallel to magnetisation. This alignment can be anywhere in three dimensional space, therefore three demagnetising factors are needed to fully represent the demagnetisation factor [39, 40]. The three demagnetising factors are orthogonal to one another and when summed give (in cgs units):

$$N_a + N_b + N_c = 4\pi \tag{2.28}$$

where each factor aligns to a certain coordinate system a, b, c. Stray fields arise from any "free" magnetic pole and have a related magnetostatic energy. The magnetostatic energy will be minimised by the formation of domains that orientate themselves to minimise free poles, as shown in figure 2.11. However, continuous division is not possible as each wall formed in the crystal has a wall energy per unit area which adds to the overall energy of the system [34]. The shape anisotropy is the energy associated with the geometry of the material and therefore acts in opposition to any field which alters the closure domain structure.
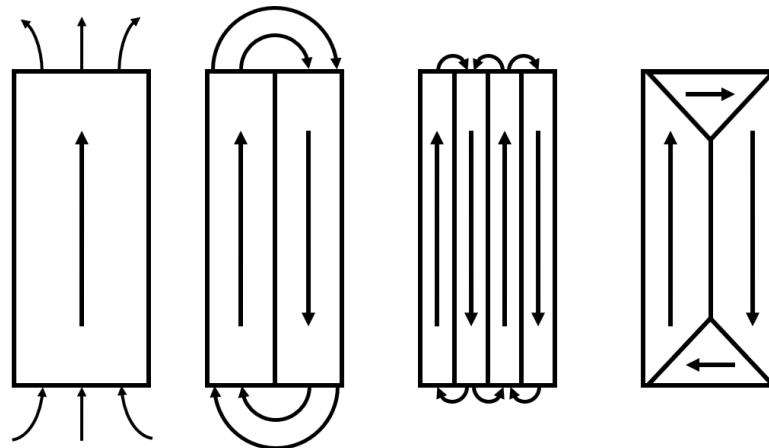
Figure 2.11: Domain structure formation to minimise the magnetostatic energy, transitioning from high (left) to low (right) energy.

The shape anisotropy energy for the simplest case of a symmetrical object such as a sphere where $a = b = c$, causing a uniform isotropic field where $N_a = N_b = N_c = \frac{4\pi}{3}$ [40]. Other examples include; (i) long cylinder with $a = b << c$ that induces a demagnetising factor of $N_c \to 0$ and $N_a = N_b \to 2\pi$ and (ii) a disc with $a = b >> c$, demagnetising factor $N_c \to 4\pi$ and $N_a = N_b \to 0$. Table 2.4 gives the relative geometries of the shape and their demagnetising factors:
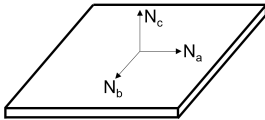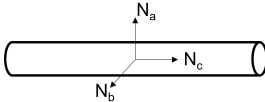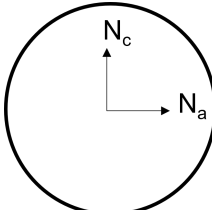
Shape		N_a	N_b	N_c
Flat Disk /plate		0	0	4π
Cylinder		2π	2π	0
Sphere		$\frac{4\pi}{3}$	$\frac{4\pi}{3}$	$\frac{4\pi}{3}$

Table 2.4: Table summarising demagnetisation factors for simple shapes.

The term shape anisotropy arises from this demagnetising factor and simply relates the relative geometry of the object to a preferred magnetisation state. The work carried out in this thesis relates to thin films that are approximated as a flat disc as shown in table 2.4, where there is no demagnetising factor along a or b but suffers a 4π factor out of the plane (c). Therefore, the shape anisotropy energy for thin films throughout this work can be represented as [40]:

$$K_s = 2\pi M_s^2 \qquad\qquad (2.29)$$

2.3.4.2   Magnetocrystalline

The shape of the material has been discussed but on a much smaller scale the crystallographic structure has an effect on the anisotropy. Magnetocrystalline anisotropy arises from spin-orbit coupling with links to the crystal lattice structure and therefore is not as easy to determine. This energy link between magnetisation and crystal lattice is known as the magnetocrystalline anisotropy energy [41]. For a simple cubic system such as iron or nickel, where M_S makes angles a, b, c with the crystal axes let $\alpha_1, \alpha_2, \alpha_3$ be the cosines of these angles, the energy of interaction is given by [34]:

$$E_{cubic} = K_0 + K_1(\alpha_1^2\alpha_2^2 + \alpha_2^2\alpha_3^2 + \alpha_3^2\alpha_1^2) + K_2(\alpha_1^2\alpha_2^2\alpha_3^2) + ... \qquad (2.30)$$

where K_0, K_1, K_2 are constants for the material of choice, expressed in erg/cm^3 (cgs) or J/m^3 (SI). The term K_0 is angle independent and usually ignored, because normally the interest lies in the change in the energy as the M_s vector rotates from one direction to another. Comparing a piece of iron and nickel by measuring their magnet responses along crystal axis it becomes obvious that not all materials respond in the same manner. The magnetisation vector will align where the energy to align is minimum, for iron this is the <001>crystallographic axes whereas for nickel it is <111>.
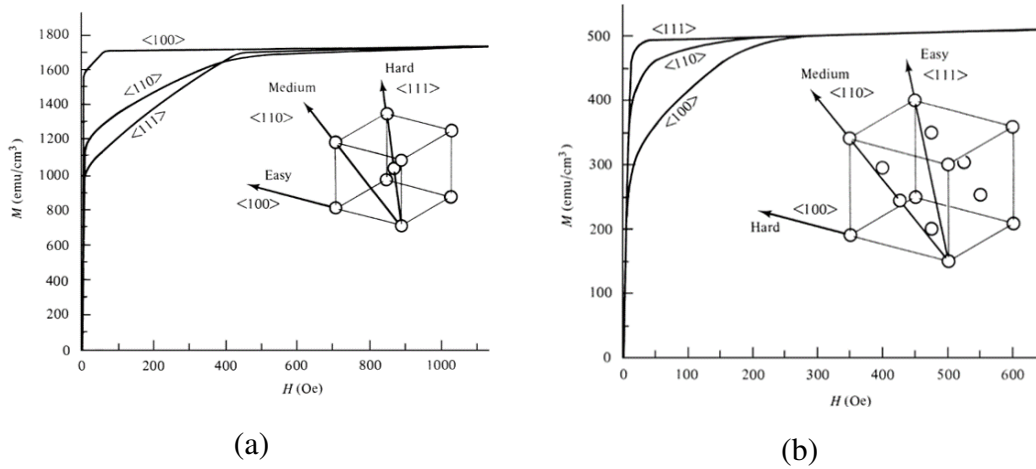
Figure 2.12: Magnetocrystalline anisotropy for iron (a) and nickel (b), where they have a body centered (BCC) and face centered structure (FCC) respectively [34].

The crystal anisotropy energy, as shown in equation 2.30, has the following solution for various crystal directions[uvw]:

[uvw]	a	b	c	α_1	α_2	α_3	E
[100]	0	90	90	1	0	0	K_0
[110]	45	45	90	$\frac{1}{\sqrt{2}}$	$\frac{1}{\sqrt{2}}$	0	$K_0 + \frac{K_1}{4}$
[111]	54.7	54.7	54.7	$\frac{1}{\sqrt{3}}$	$\frac{1}{\sqrt{3}}$	$\frac{1}{\sqrt{3}}$	$K_0 + \frac{K_1}{4} + \frac{K_2}{27}$

Table 2.5: Crystal anisotropy energy (E) for various direction in a cubic crystal [34].

Therefore, when K_2 is zero the direction of the easy axis of magnetisation is determined by the sign of K_1. In the case that K_1 is positive $E_{100} < E_{110} < E_{111}$ and where K_1 is negative $E_{111} < E_{110} < E_{100}$, for iron K_1 is positive and for nickel K_1 is negative the results of which are shown in figures 2.12(a) and 2.12(b).

In the case of cobalt, which forms a hexagonal close packed lattice, the easy axis is set as the hexagonal c axis with all basal planes found to be equally hard. These circumstances lead to anisotropy energy dependent on a single angle, θ between the M_s vector and the c axis. This anisotropy can be described as uniaxial as it wants to align in one direction, as shown in figure 2.13.
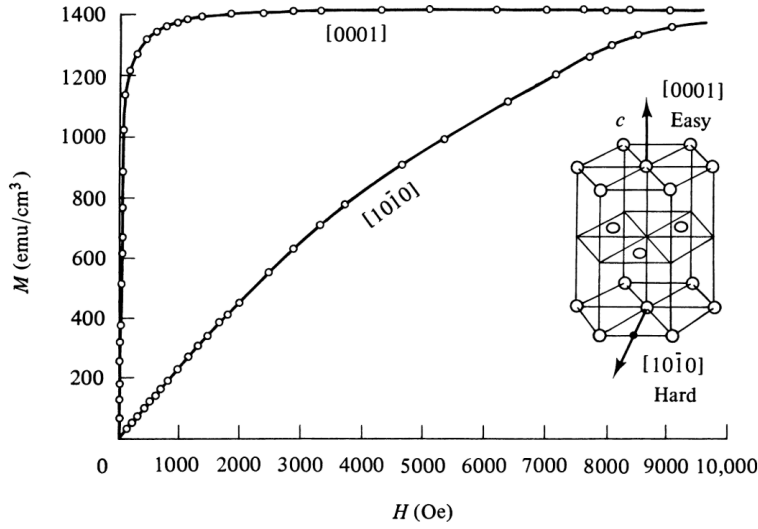
Fig. 7.5   Magnetization curves for a single crystal of cobalt.

Figure 2.13: Magnetisation curves for single crystal cobalt in hexagonal close packed structure [34].

The c axis for a hexagonal systems may either be an easy or hard axis denoted by the relative sign of K_1 and K_2, with the equation for anisotropy energy given as:

$$E_{Hexagonal} = K_0 + K_1 sin^2\theta + K_2 sin^4\theta + K_3 sin^6(\theta)cos(6\phi) + ... \qquad (2.31)$$

2.3.4.3   Strain

The factors controlling magnetocrystalline anisotropy also give rise to energy variation when magnetic ions in the lattice have modified positions. This feature comes down to the inability to produce a perfectly ordered structure, there will be areas of imperfection, which due to magnetoelastic coupling with the lattice, cause spontaneous deformation in order to minimise the free energy of the system [39]. This process may be reversed, where under an applied field the lattice will strain itself so that there is a fractional change in length given by:

$$\lambda = \frac{\delta l}{l} \qquad (2.32)$$

where l is the length of the material and λ is the magnetically induced strain on the

material, this process is known as magnetostriction. This effect in terms of specimen shape has a relatively small effect on the energy of the system for a diameter to thickness ratio of 10 or more, therefore corrections for this effect are negligible [34]. However, for thin film growth the lattice growth stage can be manipulated by growing films on single crystal substrates, such as MgO[100]. The strain anisotropy magnitude can be two orders larger than that of the magnetocrystalline anisotropy, therefore altering easy axis orientations. Lattice matching becomes vital to minimising strain present within the system as it can manipulate the preferred orientation of lattice and change the axis of magnetisation.

2.4 Magnetic Exchange Spring

The production of high energy product permanent magnets with large magnetisation and coercivity is difficult as typically heavy metal and rare-earth elements are required, which are expensive and often require oxygen free environment for manufacture [42]. It was proposed by Kneller and Hawig [42] that rather than use a single material to achieve high energy product magnetics a composite of materials consisting of two suitable ferromagnetic layers that are mutually exchange coupled could produce the desired properties. The two components consisting of a high coercivity fraction and a high saturation magnetisation fraction [42]. The high coercivity hard magnetic phase normally comes from a binary or ternary rare-earth transition-metal intermetallic compound, providing high magnetic anisotropy and coercive fields, while the soft rare-earth free phase enhances the magnetisation with the additional benefits of reducing the overall rare-earth content [43]. The use of magnetically hard and soft layers exchange coupled to one another is commonly called an 'Exchange Spring' or 'Exchange Hardened' magnets [43].

The magnetic hysteresis loop of magnetically coupled films is different from the single phase material shown in figure 2.10. In a magnetic exchange spring material the soft magnetic layer is switched by first and then the magnetically hard layer at higher fields. Figure 2.14 shows both simulation and experimental data for (a) micromagnetic simulations of magnetically hard FePt exchange coupled to magnetically soft Fe, with inset showing the movement of the magnetic alignment with changing applied field, and (b) experimental results for SmCo/Fe exchange spring [43].

(a)

(b)
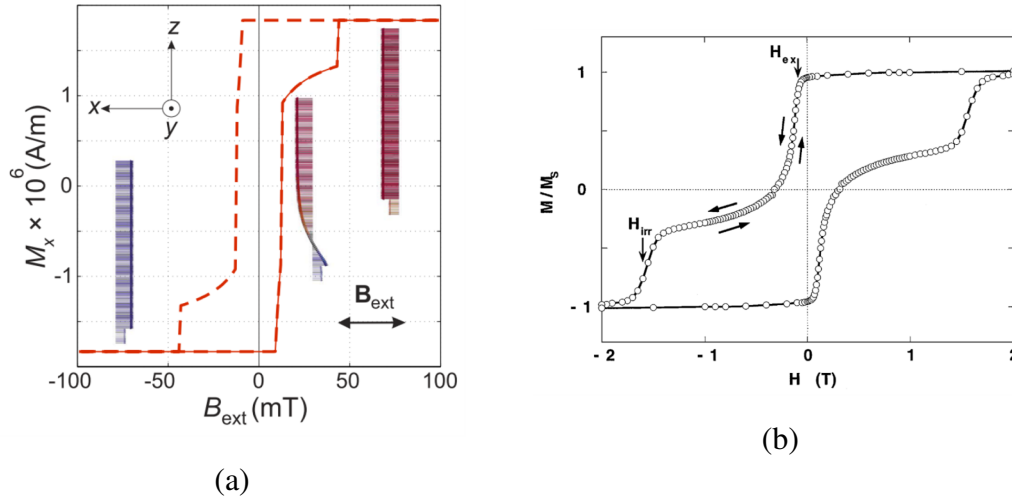
Figure 2.14: (a) Micromagnetic simulations of exchange-coupled magnetic layers [44] and (b) experimental results of SmCo/Fe exchange-spring [43], where H_{ex} and H_{irr} are the switching field of the Fe and SmCo layers respectively.

The experimental research of hard/soft magnetic films and multilayers has focused mainly on two fundamental topics: (i) the potential of enhancing $(BH)_{max}$ via the exchange hardening mechanism or (ii) to explore the physics of the exchange-spring reversal processes. This type of research requires nanometer scale permanent-magnet films [45, 46] and their incorporation into suitable magnetic heterostructures [43]. An alternative approach to exchange coupled films is exchange biasing, where a sample consisting of antiferromagnetic/ferromagnetic bilayer is cooled through the antiferromagnetic layers Néel temperature, resulting in a hysteresis loop shift for the ferromagnetic layers from $H = 0$ by an exchange field H_{ex} [43]. This arises from the unidirectional magnetic interaction of the ferromagnetic layer with the underlying antiferromagnet.

2.5 Magnetisation Dynamics

A non-equilibrium system in magnetically ordered materials causes the magnetisation to experience a time-dependent relaxation, where the torque described in equation 2.13 has additional factors [47]. In the absence of damping the rate of change of magnetisation is proportional to the torque applied, τ:

$$\frac{\delta \vec{M}}{\delta t} = -\gamma \vec{\tau} \qquad \text{where} \qquad \vec{\tau} = \vec{M} \times \vec{H_{eff}}$$

$$\frac{\delta \vec{M}}{\delta t} = -\gamma \vec{M} \times \vec{H_{eff}} \tag{2.33}$$

Where there is a torque on the magnetic moment the magnetisation will never align parallel to the applied field as it simply precesses around the applied field. Landau and Lifshitz [48] introduced a dissipation term that pushes the magnetisation in the direction of the effective field, giving the Landau-Lifshitz (LL) equation:

$$\frac{\delta \vec{M}}{\delta t} = \gamma(\vec{M} \times \vec{H_{eff}}) - \frac{\lambda}{M^2}\vec{M} \times \vec{M} \times \vec{H_{eff}} \tag{2.34}$$
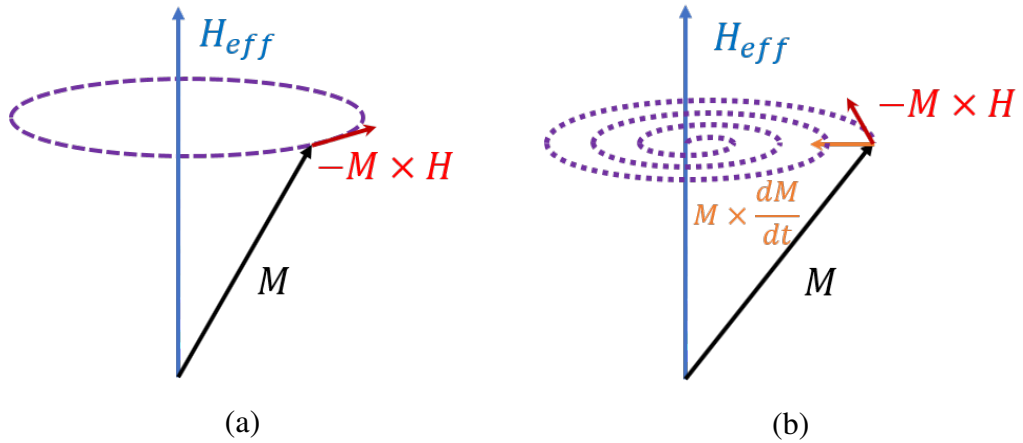
Figure 2.15: Precessional motion around an applied field, where (a) is undamped and will precess indefinitely and (b) has additional damping terms that cause the magnetisation to align with applied field.

The term $-\gamma(\vec{M} \times \vec{H})$ is precessional motion and the second is the damping term with λ being an adjustable damping parameter. Equation 2.34 was modified by Gilbert, who observed that since equation 2.34 can be derived from a Lagrangian formulation then the most natural way to introduce phenomenological dissipation was by introducing a kind of force, whose components are proportional to the time derivative of the generalized coordinates. Thus the Landau-Liftshitz equation was reformed in the

Landau-Liftshitz-Gilbert equation:

$$\frac{\delta \vec{M}}{\delta t} = \gamma(\vec{M} \times \vec{H_{eff}}) - \frac{\alpha}{M}\left(\vec{M} \times \frac{\delta \vec{M}}{\delta t}\right) + \gamma \alpha^2 \vec{M} \times \vec{H} \qquad (2.35)$$

$$\text{Where} \qquad \alpha = \frac{\lambda}{\gamma M}$$

for $\alpha << 1$ the third term $\gamma \alpha^2 (M \times H)$ is negligible and equation 2.35 becomes the Gilbert equation [33, 34]. Equation 2.35 is the most commonly used form for dynamic magnetisation studies, where numerical simulations assume the magnetisation M is uniform throughout the whole material. Neglecting the damping terms allows the LLG equation to be solved for thin films, giving precessional spin frequency:

$$\omega_0 = \gamma \sqrt{(H_{eff} + 4\pi M_s)H_{eff}} \qquad (2.36)$$

Equation 2.36 is known as the Kittel equation, where ω_0 is a fixed frequency for an applied field. The value of ω_0 for thin film magnetic materials is of the order 1 to 10 GHz, and is most commonly known as ferromagnetic resonance (FMR). For $L1_0$ materials with their high anisotropy the resonance has a line-width of ≈ 0.1 Oe [34].

2.5.1   Spin Transfer Torque

The LLG equation (2.35) gives a good description of the evolution of magnetic systems excited by an external magnetic field. However, with the presence of a spin polarised current in the system a phenomenon called spin-transfer torque (STT) adds a new factor. STT involves the transfer of spin angular momentum from conduction electrons, where the efficiency decreases within materials that have a strong spin-orbit coupling, where spin angular momentum is not conserved. The additional term is given by:

$$\vec{m_{STT}} \quad = \quad -\frac{\gamma}{St\mu_0 M_s}\vec{\tau} \quad = \quad -\frac{\hbar J \gamma P}{2e\mu_0 M_s t}\hat{P} \qquad (2.37)$$

The angular momentum transferred per unit time is $\tau \approx \hbar JSP/(2e)$, where J is the current density, e is electronic charge, P is spin polarisation with a value $0<P<1$, and S is the cross sectional area [49]. The spin direction is taken as $\hat{P}$ for the spin-polarised current incident on a FM. The magnetisation dynamics of STT apply only when m and

p form angles other than zero and π, therefore to isolate this factor the contribution to magnetisation dynamics are given as:

$$\vec{m}_{STT} = \gamma A_J \vec{m} \times \vec{m} \times \vec{p} + \gamma B_J \vec{m} \times \vec{p}, \qquad \text{where} \qquad A_J \approx \frac{\hbar P}{2e\mu_0 M_s t} J \qquad (2.38)$$

The factor A_J is known as the Slonczewski spin torque relating to the current density J, whereas B_J is the field-like spin torque [50, 51]. The factor m_{STT} acts like an anti-damping term when added to the LLG equation. Therefore when considering the STT contribution to precession it is evident that it is a driving force to magnetisation precession, which allows steady-state precession at zero field.

2.5.1.1   Switching Current

In the case where injectected spin polarisation $\hat{P}$ and effective field H are collinear, the effective damping can be made zero through spin torque. This is the case when $A_J > \alpha H$, since A_J is related to current, the switching current can be expressed as [50, 51]:

$$J_C \quad = \frac{\alpha H}{A_J} \quad = \quad \frac{2e M_s t \alpha}{\hbar P} H \qquad (2.39)$$

This is the theoretical threshold for current density to destabilise the magnetisation from a parallel configuration. The nominal values of J_c are on the order of 10^8 A/cm^2 [52]. Reducing the value of J_C is preferential as this allows lower energy switching, therefore small α materials are highly sought for power efficiency where switching currents are used. L1$_0$ materials are of particular interest for switching current purposes, where Mn-based alloys have attracted attention since they tend to have low Gilbert damping with high PMA, examples of such materials are MnAl ($\alpha = 0.006$ [53]).

2.5.2 Spintronic Devices

The cornerstone for understanding spin-
tronic applications is the "two cur-
rent" conduction that explains specific
behaviours in conductivity of ferro-
magnetic metals, such as Fe, Ni and
Co, as well as their alloys. The
two-current model by Mott [54] re-
lates to how both 4s and 3d elec-
tron bands contribute to the density of
states (DOS) at the Fermi level E_F.

Due to strong exchange interaction
favouring parallel orientation of elec-
tron spins, the spin-up and spin-down
3d bands are shifted in energy, creating
an imbalance between the number of up
(n_{up}) and down (n_{down}) electrons in the
3d band. The shape of energy bands is a

Figure 2.16: A simplified band struc-
ture showing the Fermi energies for
3d and 4s of ferromagnetic elements,
adapted from [34].

complicated problem, but the exact shape of the band does not affect the general argu-
ments [34]. There is overlapping of the 3d and 4s energy of elements Mn through Zn,
shown in figure 2.16, with first approximation assumption that the shape of these bands
does not change from one element to another known as the rigid-band model [34].

The 3d band can hold a total of 10 electron per atom in 5 orbitals and 2 spin states,
whereas the 4s band can only hold 2 electron per atom. The topmost filled level, as
shown on figure 2.16, is the Fermi level. Filled orbital energy levels cannot contribute
to magnetic moment, due to the electrons having opposing spins and thus cancel each
other out [34].

The resistivity of the two-current model can be represented as spin-up ($\rho^{\uparrow}$) and spin-
down ($\rho^{\downarrow}$) electrons, where their values are not necessarily equal due to the difference
of DOS between spin-up and spin-down sub-bands. Below the Curie temperature, T_c,
the overall resistivity can be expressed as:

$$\rho = \frac{\rho^\uparrow \cdot \rho^\downarrow}{\rho^\uparrow + \rho^\downarrow} \tag{2.40}$$

The d-bands have a narrower spread in energy compared to s-band, which results in very large effective masses for the d-band electrons. Therefore, electrical conduction is almost entirely due to s-electrons [55]. The resistivity of a magnetic multilayer used for GMR has spin-up or spin-down conduction channels, depending on the relative alignment of the magnetisation of neighbouring layers [56].
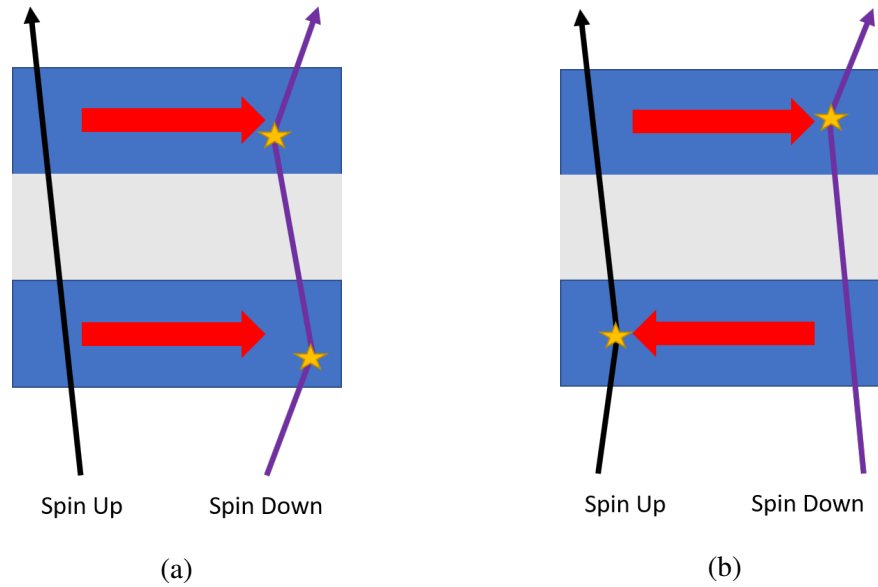
Figure 2.17: Scattering of spin-up and spin-down electron travelling through a magnetisation (a) parallel and (b) antiparallel.

The resistivity for electrons exposed to successive parallel (figure 2.17a) and antiparallel (figure 2.17b) magnetisation alignments is calculated as:

$$\rho_P = \left(\frac{1}{\rho^\uparrow + \rho^\uparrow} + \frac{1}{\rho^\downarrow + \rho^\downarrow} \right)^{-1} \approx 2\rho^\uparrow \tag{2.41}$$

$$\rho_{AP} = \left(\frac{1}{\rho^\uparrow + \rho^\downarrow} + \frac{1}{\rho^\downarrow + \rho^\uparrow} \right)^{-1} \approx \frac{\rho^\downarrow}{2} \tag{2.42}$$

This is the basis or GMR, whereby using a magnetic multilayer system initially magnetised in an antiparallel configuration that can later be aligned by an external magnetic field, which changes the resistivity dramatically. This phenomena can be used to produce spin-polarised electrons, where spin polarisation P is defined by:

$$P = \frac{N_\downarrow(E_F) - N_\uparrow(E_F)}{N_\downarrow(E_F) + N_\uparrow(E_F)} \tag{2.43}$$

where $N_\uparrow(E_F)$ and $N_\downarrow(E_F)$ are the number of electrons with spin-up and spin-down respectively at the Fermi energy. The polarised spin will remain until the electron encounters an event which perturbs the spin direction. The average distance travelled by the electron before such an event is the spin diffusion length. The spin diffusion length is related to the spin-orbit coupling of the material and is therefore shorter in ferromagnetic materials, typically on the order of 1-10 nm [57]. Alloys that contain heavy metal elements such as FePt are hindered due to their shorter spin diffusion length, whereas those without heavy metal elements such as MnAl possess low spin-orbit coupling thus producing efficient polarisation.

2.6   Summary

This chapter has covered the relevant fundamentals of magnetism and magnetic materials, which are vital in the later chapters of this thesis to interpret experimental results from magnetic thin films.

Chapter 3

L1$_0$ Crystal ordering in Binary Alloy Thin Films

Materials with a strong perpendicular magnetic anisotropy (PMA) are fundamentally appealing for various applications such as permanent magnets, energy efficient spintronic devices and data storage media. High PMA can arise from a number of sources including crystal structure, symmetry breaking at layer interfaces such as Co/Pd multilayers [58], and chemical segregation as found in Re-Tm alloys [59]. One promising class of materials that generate PMA through crystal structure are binary alloys with L1$_0$ ordering, sometimes referred to as natural multi-layers [60]. L1$_0$ alloys are promising material structures for improving the performance of current and future spintronic technologies. The L1$_0$ ordering gives rise to PMA due to the anisotropic nature of the spin orbit coupling resulting from unequal lattice constants [60], where control over the crystal phase and structure play a key role in optimisation of magnetic properties.

L1$_0$ materials are a specific crystal state of an alloy structure that is sometimes denoted as a natural multilayer, examples of such structures as well as common alternatives are shown in figure 3.1. In most cases the structure is made up of two elements A and B, but in some special cases such as $(Fe_{1-x}Mn_x)_{50}Pt_{50}$ a third element fills the central position of the top/bottom planes [61].

The notation L1$_0$ comes from the Strukturberich notation [30] where L represents an alloy material and 1 signifies that the structure is a derivative of the A1 elemental FCC structure type. The subscript depicts the various derivatives of the FCC structure, where there are three in total for L1 structures as shown in figure 3.1 [30]. The

L1$_0$ structure has a face centered tetragonal lattice, with atomic planes stacked in the c-axis direction, where in some cases composition designates the presence of strong PMA [60]. The other L1$_x$ structures have interesting magnetic properties but fall outside the scope of study within this thesis.
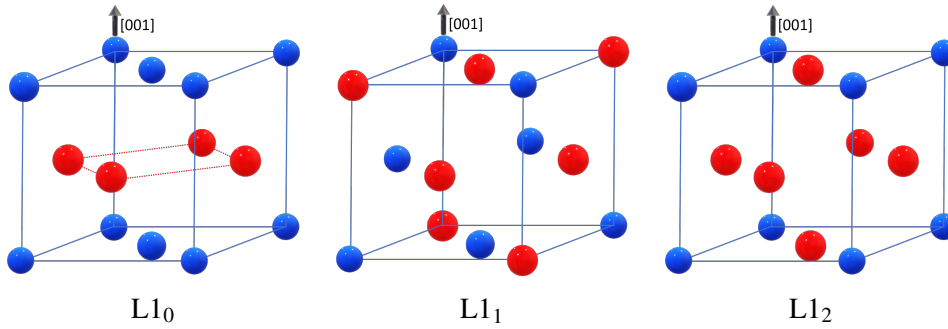
Figure 3.1: Unit cell for L1$_x$ ordered binary alloy where blue and red circles represents the two elements of the alloy, for example Fe/Pt or Mn/Al.

The magnetic properties of binary alloys is highly dependent on the degree of ordering within the structure, that being the percentage of unit cells that form the desired phase, where the ordering is heavily linked to the strain and energy of the material at the time of fabrication. In most of these materials the L1$_0$ phase is not the dominate phase and must be given energy to overcome energy barriers during the fabrication process. For example, in MnAl the L1$_0$ phase is metastable and does not form at room temperature but once formed can remain stable at room temperature. In the case of FePt elevated temperatures are needed to form the FCT structure compared to the FCC structure which is stable at room temperature. Therefore, to help achieve the best results in thin film growth it is advantageous to use a choice substrate and seeding layer to optimise strain present in the structure.

Elements	Ku (10^7erg/cm3)	Ms (emu/cm^3)	Tc (C)	a (Ang)	c (Ang)	Reference
FePt	7.0	1140	475	3.85	3.71	[19, 20]
FePd	1.8	1100	485	3.85	3.72	[12]
NiFe	1.3	1270	545	3.58	3.61	[62]
CoPt	4.9	800	566	3.80	3.70	[12]
MnAl	1.7	600	375	3.94	3.58	[15, 63, 64]

Table 3.1: Magnetic and structural properties of various L1$_0$ alloys.

It has been shown previously, [65], that the $L1_0$ phase growth can be encouraged by using seed layers and single crystal substrates. For this reason magnesium oxide, MgO single crystal (001) cut, substrates are used with a lattice parameter of 4.212Å. The larger lattice parameter helps to promote the growth of $L1_0$ phase in FePt, FePd and MnAl over the smaller cubic phases shown in table 3.1. Lattice matching to the a-axis helps to induce perpendicular uniaxial alignment as the easy axis lies along the c-axis of these structures. However, in parts of this study silicon oxide substrates are used as the study of disordered phase growth isn't possible with MgO due to diffraction peak intensities, where the substrate peak swamps any signal from the material.

3.1 Chemical order in Binary alloys

Many metallic alloys when brought to low temperature will adopt a chemically ordered structure, with specific atoms occupying sites within each unit cell [17]. This chemical ordering remains consistent throughout the material and is therefore denoted as long-range order (LRO) [17]. Temperature plays a key role in obtaining and maintaining LRO, as sufficiently high temperature give atoms enough energy to randomly occupy any lattice site. The point where LRO is lost is known as the critical temperature T_C, however there may still remain short range ordering at this temperature [17]. The fabrication and structural characterisation of binary ordered alloys in thin film form is vital for future applications, where understanding the long range ordering in these materials is key to developing fabrication procedures capable of obtaining the desired magnetic properties linked to specific phases.

The calculation of chemical ordering treats a binary alloy as having two kinds of atoms, A and B, where their atomic fraction is x_A and x_B. Chemically ordered structures will have defined A and B sites for each atom denoted as α and β, which have corresponding concentrations y_α and y_β. For a perfectly ordered structure with LRO, all sites for α and β will have A and B atoms, respectively. However, this is not always the case so parameters r_α and r_β represent the fraction of α or β sites occupied by the right atom. Similarly w_α and w_β are used to represent atoms in the wrong site. Combining these parameters allows the definition of long-range chemical order, denoted as the "Order Parameter" (S) [17]:

$$S = r_\alpha + r_\beta - 1 \qquad (3.1)$$

For complete ordering in the system $S = 1$ and for no chemical ordering $S = 0$, with S proportional to the number of atoms on the correct site. The materials covered in this work have magnetic properties linked to the atomic positions of atoms so it is therefore favourable to have a larger S value. However, from the definition of S it becomes apparent that maximum ordering is relative to stoichiometry, where an unbalanced number of atoms A or B will lower the maximum possible order within the system.

The definition given for equation 3.1 applies also to pockets of ordering in inhomogeneous materials, where an additional term is added to quantify chemical ordering in inhomogeneous materials, known as the fraction of the film that is chemically ordered f_0. This helps to distinguish between a structure with a high volume averaged ordering, as shown in figure 3.2, and those with highly ordered pockets but low volume averaged ordering shown in figure 3.3.

(a)   (b)
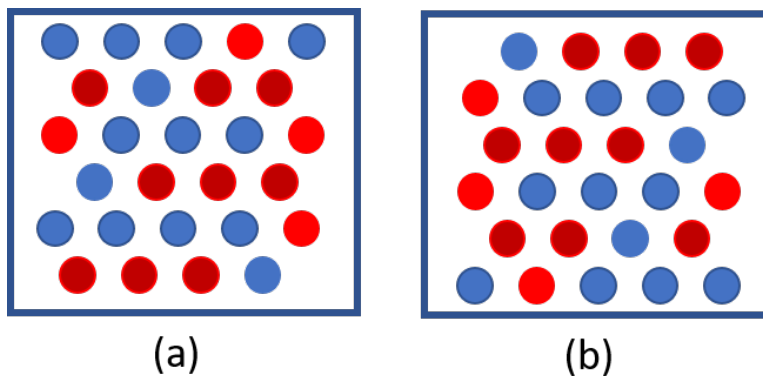
Figure 3.2: Homogeneous side-by-side grains (a) and (b) have an average ordering of $S_{avg} = 0.5$, but the overall film ordering is $f_0 = 1.0$.

Figure 3.2 represents a homogeneous material made up of two grains that have the same order parameter, $S = 0.5$, leading to $S_{avg} = S \times f_0 = 0.5 \times 1.0 = 0.5$. Alternatively, figure 3.3 is a inhomogeneous material that has one highly ordered grain with $S = 1$ and one disordered grain. In this case the volume averaged ordering is, $S_{avg} = S \times f_0 = 1.0 \times 0.5 = 0.5$. The ordering of the system can

(a)   (b)
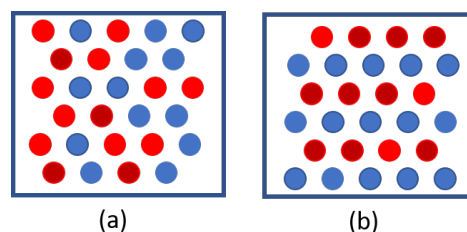
Figure 3.3: Inhomogeneous side-by-side grains (a) and (b) have an average ordering of $S_{avg} = 0.5$ and film ordering $f_0 = 0.5$.

only be S=1 for absolute zero temperature, above which thermal fluctuations reduce ordering below unity. The dependence of S on temperature is only modest, where a large extent (S≈0.9) can be found near transition temperature T$_C$ [17].

It is important to understand the mechanisms behind the different types of LRO and how they represent the material structure and properties. To achieve ordering within a system temperature annealing is often used, where a material is heated to a transition temperature T$_C$. A transformation occurs through nucleation and growth processes that often leads to coexistence of both ordered and disordered phase at T$_C$, where a two-phase model is used to describe most materials. The maximum value obtainable for ordering (S) is limited in experimental setups as factors such as temperature play a critical role in its calculation, where sometimes for ease in simulation a zero temperature regime is assumed. The experimental calculation is covered later in section 5.3.2.2.

3.2 L1$_0$ Material Applications

The enormous increase in areal density of magnetic media and the associated reduction in cost per gigabyte has been the catalyst for new recording applications, driven by consumer societies demand for data storage. The superparamagnetic limit imposed on conventional hard disk drives (HDD) ensures that there is a definitive scale limitation, due to trade-offs between signal-to-noise, thermal stability and write-ability as the density increases [2, 3]. The discovery of Giant Magneto-Resistance (GMR) [66] caused a breakthrough in read/write heads for HDD, where magnetic multilayers formed spin valves with improved sensitivity, allowing areal density of storage to increase. Spintronics began to cement themselves from 1988 onwards, where in-plane transitioned to perpendicular storage and further material advancements allowed the amount of data per inch to increase steadily over time.

3.2.1 Energy Assisted Magnetic Recording

It was mentioned in chapter 2 that the HDD is reaching its physical limitations due to the so called "trilemma". Overcoming this hurdle is the aim of energy assisted magnetic recording, where stronger write fields are capable of writing to higher anisotropy recording media that allow smaller bit sizes to be recorded. The first contender for

solving this issue is heat assisted magnetic recording (HAMR). The recording media with high anisotropy allows very small grain sizes whilst maintaining thermal stability. However, the high PMA means that in order to write a bit to this media localised heating is required, which temporarily reduces the anisotropy of the media allowing the reversal of magnetisation. This localised heating is only applied to switch the bit state and then the media is allowed to cool. Prime material examples for this type of media is L1$_0$ ordered FePt as the grain sizes can be very small, theoretically as little as 3 nm, and still maintain thermal stability.

Alternatively, a spin polarised current may be used to excite precession in a field generating layer of a spin torque oscillator (STO). This process allows a reduction in the anisotropy energy barrier of the storage media by exciting precession through ferromagnetic resonance. The energy absorbed from the oscillating field is at a higher rate than energy lost due to damping which helps to allow the available field from a write head to write the bit completing reversal process.

3.2.1.1   Heat Assisted Magnetic Recording

Heat assisted magnetic recording (HAMR) allows high anisotropy media to be utilised thus overcoming the supermagnetic limit for magnetic recording. The use of higher anisotropy media supports thermally stable grains that are smaller than those found in conventional CoCr based alloys. HAMR can also provide higher effective field gradients required for high density recording as both the field and thermal gradients contribute to transition profile [67]. HAMR works under applied heating to the media surface, as shown in figure 3.4, using an external laser coupled to an near-field transducer (NFT) slider or laser diode module integrated on the slide [67]. Heating the storage media close to its Curie temperature lowers its anisotropy field such that the magnetic grain may be switched by the write heads field, the media is then cooled to store the information in a frozen stable state. The proposed schematic of a HAMR device is shown in figure 3.4 along with the temperature cycle for storing information in the medium.
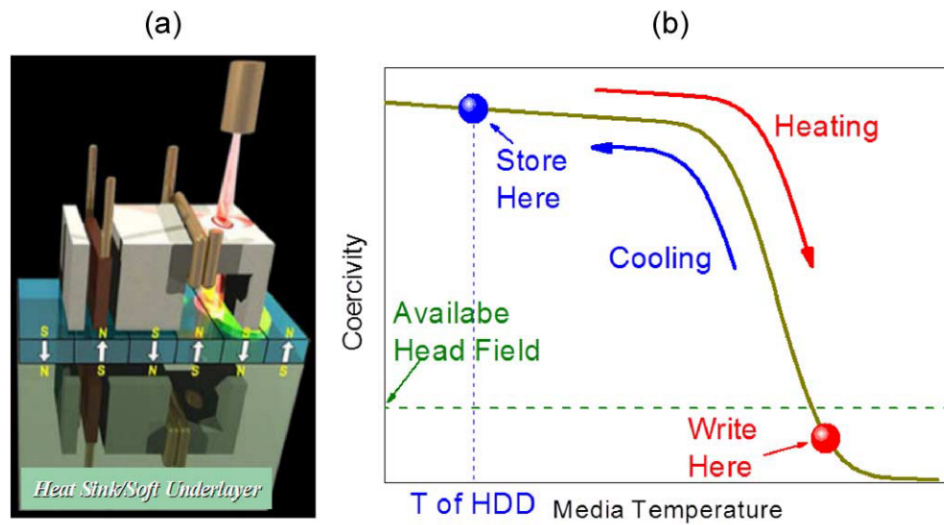
Figure 3.4: (a) Schematic of HAMR recording system, and (b) recording process showing the effect temperature has on the media coercivity, from Wu et al. [67].

Granular L1$_0$ ordered FePt is the frontrunner for HAMR media due to its high magnetocrystalline anisotropy [9, 18]. The crucial problem is the dispersion of the Curie temperature of each constituent grain, where fluctuations in composition and/or ordering has an effect [18]. Discrepancies in Curie temperature can cause the heating and cooling cycle to differ slightly between close pack grains, thus causing writing issues. Commonly used method for isolating grains are the use of oxides, however the addition of elements such as carbon have been proposed to obtain well-isolated FePt grains with small size due to their strong phase separation tendency [68, 69]. Further understanding of grain growth and uniformity are essential to utilising materials such as FePt for HAMR applications.

3.2.1.2   Microwave Assisted Magnetic Recording

Microwave assisted magnetic recording (MAMR) has been proposed as one of the prospective recording technologies for forthcoming tera-bit-class (Tbit/in^2) magnetic recording [70]. To achieve this goal microwave assisted switching (MAS) materials are excited by a spin torque oscillator (STO). The microwave field excites precession of the magnetisation in the medium which allows magnetisation reversal to occur at a lower head field. However, this is a very challenging in terms of creating a practical write head. MAMR was first proposed by Zhu et al. [71] who suggested that a STO

could be used as an RF (radio frequency) field generator. The structure of an STO is similar to the magnetoresistive read head present in HDD and therefore could be easily incorporated [72]. A schematic of an implementation is given in figure 3.5, where the STO is placed between the main pole and a trailing shield making up the write head.
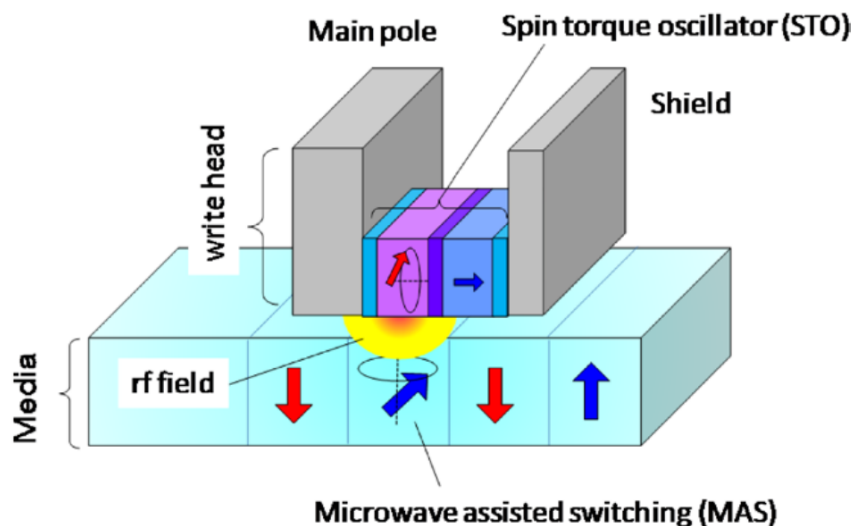
Figure 3.5: Schematic of microwave assisted magnetic recording consisting of a microwave assisted switching and spin torque oscillator from Okamoto et al. [70].

The STO is comprised of a perpendicularly magnetised reference layer acting as a spin polariser, a metallic interlayer, field generating layer (FGL), and a top perpendicularly magnetised layer. Flowing a spin polarised current through the FGL layer will cause magnetisation precession at a certain angle with respect to the perpendicular axis. According to simulations a material with large M_s will produce a field of a few kOe and a few tens of GHz [71, 73, 74], but requires a large K_U around 10^7erg cm^{-3} [70]. The large value of K_U required naturally suggest that L1$_0$ ordered binary alloys are prime choice for such applications.

3.3   Iron Platinum

Materials with high anisotropy are at the forefront of research for magnetic storage and a range of spintronic applications. High magnetic anisotropy ensures that small

(sub-10 nm) grains in a magnetic medium are thermally stable. FePt shows the highest PMA for $L1_0$ materials as given in table 3.1. This large anisotropy allows the grain size for storage to decrease substantially, to around 3 nm [75], whilst maintaining sufficiently high $k_U V$ to ensure thermal stability. The large anisotropy is caused by Fe and Pt interactions originating from spin-orbit coupling and the hybridization between Fe (3d) and Pt (5d) states [76]. The desirable $L1_0$ phase (γ_2) for FePt is achieved for a roughly equiatomic system, as shown in the phase diagram for FePt figure 3.6.
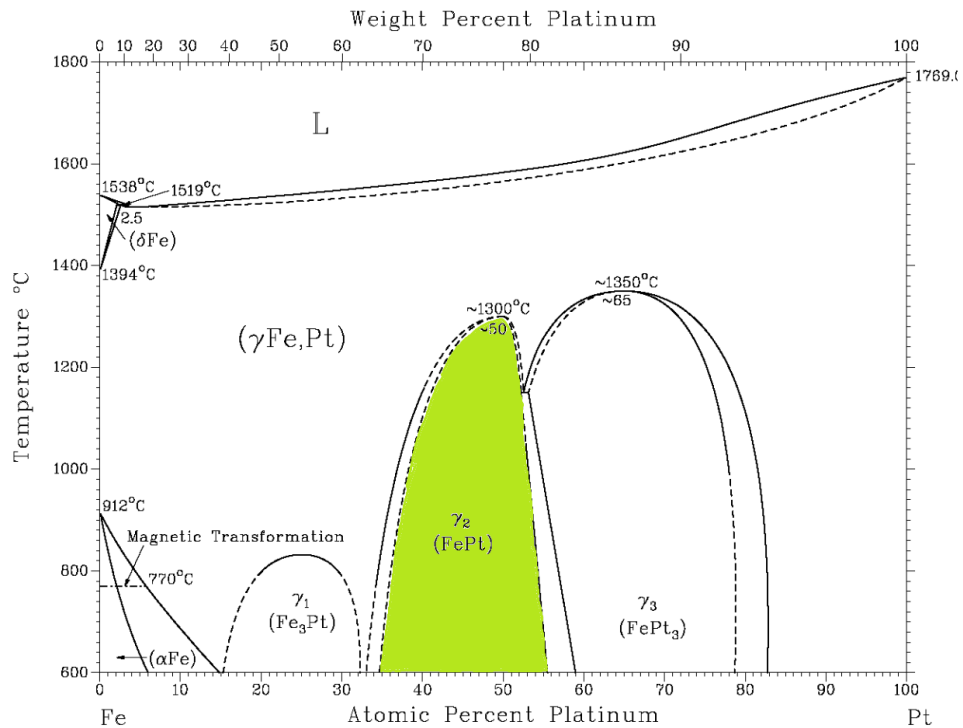
Figure 3.6: Phase diagram for bulk FePt where the $L1_0$ phase corresponds to γ_2 [77, 78].

The magnetically ordered anisotropic $L1_0$ FePt phase has a face-centred tetragonal (FCT) crystal structure, which is formed by a first order transition from the disordered A1-FePt, where neither Fe or Pt atoms have preferential sites [75]. The disordered A1-FePt phase in thin films forms after deposition onto substrates at temperatures below 400°C. Although this phase has a similar magnetisation to the γ_2 ($L1_0$) phase, its anisotropy is two orders of magnitude lower. The melting point of equiatomic FePt is approximately 1560 °C, therefore the rate of diffusion via bulk mechanisms at temperatures below 400°C is extremely slow [79]. There is an activation energy associated

with the phase transition from disordered A1-FePt to ordered L1$_0$ FePt, where higher
temperature treatment or deposition onto substrates heated beyond 400°C is needed to
overcome such energy barriers [75, 80].

Although the γ_2 phase spans a relatively
large composition, roughly 33at.% to
55at.% of Fe, it has been determined that
the magnetocrystalline anisotropy energy
increases monotonic with an increase in
Fe content from 46 at.% to 52 at.%
[81]. The activation energy for A1$\rightarrow$
L1$_0$ phase transformation has a minimal
value in the Pt concentration range of 47-
50 at.% [82]. However, the order pa-
rameter reaches a maximum value for
equiatomic FePt, as described in section
3.1 where the highest possible ordering
the system can achieve is related to the

Figure 3.7: Order parameter S
and anisotropy constant K$_U$ as a
function of iron atomic percentage
[81].

composition. To obtain L1$_0$ FePt films with the maximum value of magnetocrystalline
anisotropy it has been found experimentally that having slightly higher Fe at.% is
favourable. This is due to the imperfections that are always present in real material
systems, in particular the polycrystalline nature of the films.

Segregation of Pt occurs near-boundary regions of FePt grains, which causes some
deviations in concentrations between grains. These variations are problematic as
lower concentration decreases the L1$_0$ order parameter and anisotropy constant [81],
as shown in figure 3.7. Segregation is more pronounced for grain sizes below 15 nm
where doping elements are added to the FePt alloy, this is used to help improve order-
ing. The choice composition remains to have higher Fe content ($\approx$52at. %) down to
15nm grain size, and below this point to increase the Pt concentration to eliminate the
effect of segregation on the grain surface [75].

3.3.1   Uniaxial in-plane anisotropy FePt films

The study of FePt focuses mainly on its uniaxial magnetic alignment, where most stud-
ies focus on having perpendicular aligned films but few have shown in-plane magneti-
sation. This sections covers three of the main deposition techniques and key literature

results for in-plane aligned FePt films, where the deposition techniques are covered in chapter 4.

3.3.1.1 Magnetron Sputtering

Magnetron sputtering is a technique highly favourable for mass production of consumer devices. Therefore, fabrication methods created by magnetron sputtering are favoured for a materials further development into devices. A study carried out by Seki et al. [83, 84] investigated the growth of FePt on MgO(110) substrates with a Fe (1 nm)/ Au (40 nm) seed layer with (110) crystal alignment with the substrate. The temperature range for deposition under investigation was 240°C to 500°C, where a 18 nm FePt film was deposited using a working pressure of 5 mTorr. The hysteresis curves for the FePt films are shown in figure 3.8, where the temperatures are (a) 240°C, (b) 300°C, (c) 400°C and (d) 500°C.
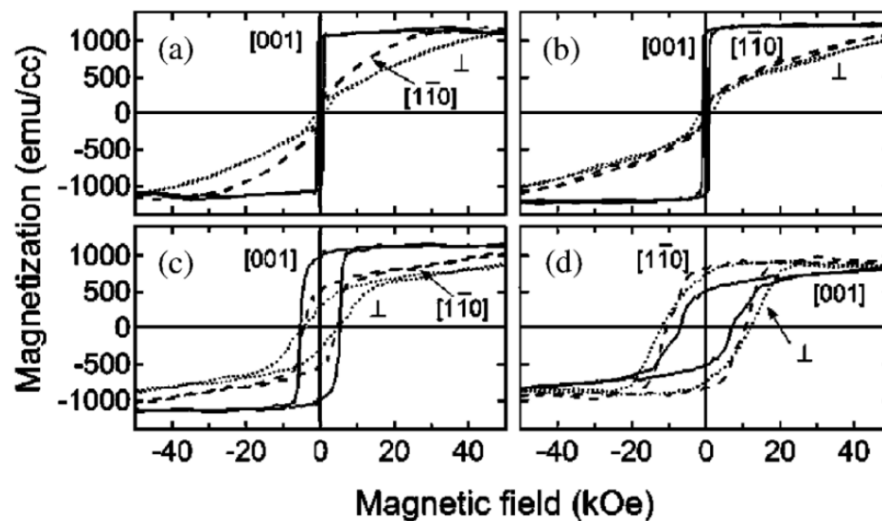
Figure 3.8: Hysteresis loops for 18 nm FePt films deposited at (a) 240°C, (b) 300°C, (c) 400°C and (d) 500°C on a Au (110) seed layer with alignment to MgO (110) substrate [83].

This study focused on the deposition temperature combined with a seed layer aligned to the substrate. FePt is commonly grown on various seed layers and it is known that deposition temperature is key to inducing $L1_0$ ordering in the film. The temperature ranges chosen gave a somewhat mixed uniaxial magnetic alignment shown by the hysteresis loops. The solid, broken and dotted lines for the hysteresis curves represent

field along the [001], [1$\bar{1}$0] planes and 90°rotation in plane respectively, see section
2.1.1 for unit representation of planes on unit cell. The uniaxial magnetic anisotropy
constant (K_U) in the film plane is measured as 2.4 erg/cm^3 for a deposition temperature
of 300°C. The success of the in-plane alignment is linked to the epitaxial relationship
between FePt[001]//Au[001], ensuring the easy axis lies in plane [83]. As the temper-
ature of deposition is increased beyond 300°C the coercivity increases, this is thought
to be due to a canted axis formed [83].

3.3.1.2   Evaporation

The use of a magnetically hard/soft
exchange coupled system is ideal for
on-dimensional models for studying
the influence of different magnetic
and physical properties [85].   For
such studies magnetically hard FePt
and CoPt with in-plane alignment are
sought, where evaporation technique
have been used to deposit such films
[85].   However, the main focus of
this work is FePt films and so CoPt
will not be covered.   A 1 nm Pt
seed layer was used to align the
FePt film to the MgO (110) sub-
strate.   The   substrate   temperature
for deposition was altered between
500 and 700°C. The hysteresis loops
for (a) 500°C, (b) 600 °C and (c)
700 °C are shown in figure 3.9.
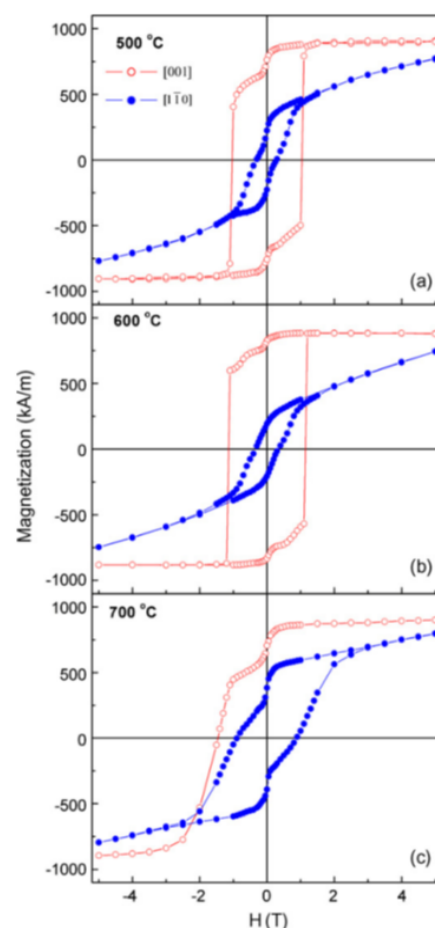
Figure 3.9: Hysteresis loops for FePt films
deposited at (a) 500°C, (b) 600°C and (c)
700°C using e-beam evaporation [85].

The FePt films have a saturation mag-
netisation between 850 and 900 emu/cm^3
in-plane, which is slightly lower than the
book value of 1140 emu/cm^3. The kinks

in the loops are indicators of poor magnetic coupling between the (0hh), (h0h) and

(hh0) planes [85]. As the temperature of deposition is increased from 500 to 600°C the kink is reduced, but as the temperature is further increased to 700°C the kink increases. The reasoning behind this is the coupling of magnetic phases is reduced and therefore multiple phases/orientations are present.

3.3.1.3 Molecular Beam Epitaxy

Initial studies into the formation of ordered FePt using MBE deposition found that elevated substrate temperatures during the deposition of more than 300°C for [110] (In-plane) and 500°C for [001] (Perpendicular) were needed, examples of well ordered FePt $L1_0$ phase was produced by Farrow et al. using these temperatures as shown in figure 3.10 [19, 20].

The hysteresis loop and XRD spectrum for both perpendicular and in-plane aligned FePt films are shown in figures 3.10 a,c and b,d respectively. It is clear that for figure 3.10 a,b, the [001] perpendicular case, there is some other phase present in the XRD spectrum. This is shown as the shouldering on the (001) peak, where it could be on the (002) as well but the substrate peak overlaps. The presence of a disordered phase is confirmed by the shape of the hysteresis loop, as the switching mechanism follows that of a slightly mixed system. In figure 3.10 c,d, the [110] in-plane case, there is well defined peaks with little to no shouldering, confirmed by the squareness of the [001] hysteresis. However, the alignment is not perfectly in-plane as a larger difference between the in-plane and 90°rotation in-plane should be more. Therefore there is potential for the (220) peak in the XRD to have a large (202) component but due to resolution this was not discernable.

(a)

(b)

(c)

(d)
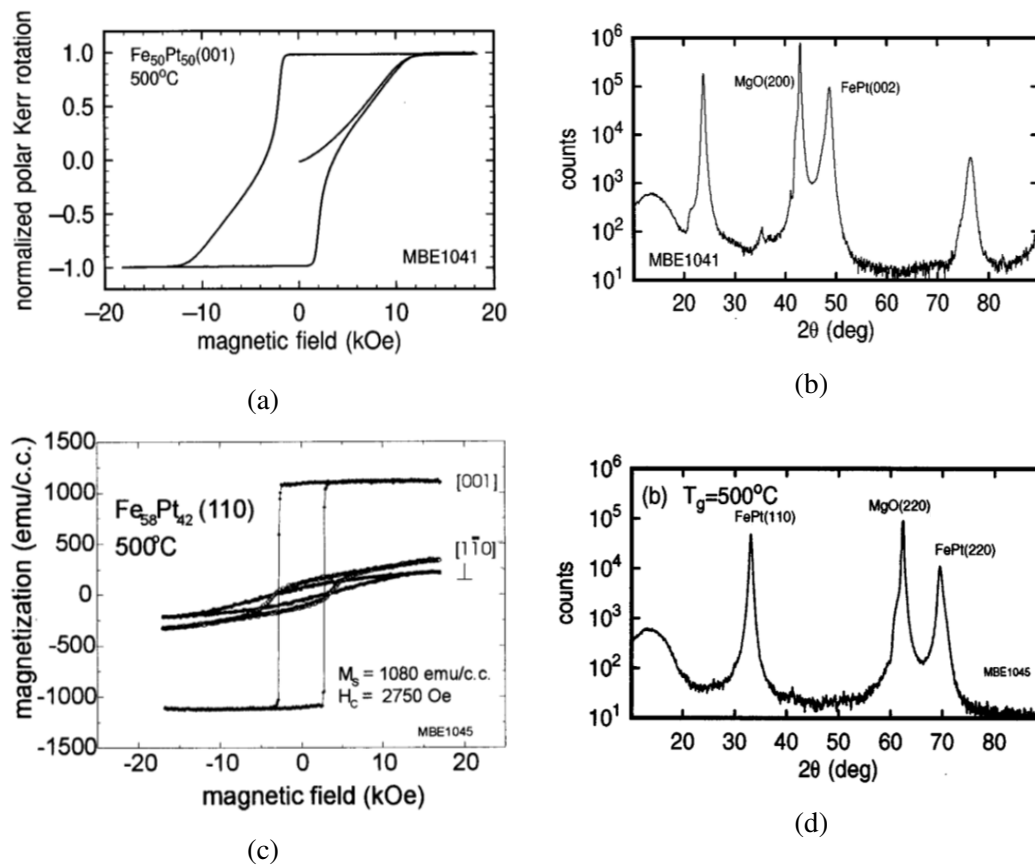
Figure 3.10: (a) and (b) early work by Farrow et al. into the ordering of FePt(001) on MgO(001) substrates [19]. (c) and (d) is their work on MgO(110) for in-plane FePt(110) [20].

Epitaxial layer growth by MBE was able to achieve ordering at a lower deposition temperature than was possible for sputter deposition. In the case of sputtering techniques it was found that temperatures between 550 and 700 °C are needed to induce ordering [86]. A combination of deposition and annealing is used to enhance atomic mobility at high temperatures, this however causes the grains to grow which is an unfavourable condition for storage device applications such as magnetic media. To combat the grain growth the temperature for ordering must be lowered, this is achieved by alloying FePt, where two main groups are considered: (i) elements forming ternary compound with FePt and (ii) elements acting as segregates along grain boundaries. Prime examples of elements and compounds used to alloy with FePt are Au [87], Ag [88], C [89], Cu [90], TiO$_2$ [91], and SiO$_2$ [92]. These examples segregate from the disordered A1-FePt and form crystal defects that promote the acceleration of the ordered L1$_0$-FePt phase formation [75].

3.4 Manganese Aluminium

Manganese Aluminium (MnAl) is a promising alloy for spintronic applications as the absence of a heavy metal element enables a low Gilbert damping constant, which can be directly related to the switching current mentioned in chapter 2. The magnetic properties are found in the $L1_0$ phase also known as the τ phase. The fact that neither Mn or Al are ferromagnetically ordered at room temperature make it fascinating that when combined in the correct composition and phase that they have a high moment (490 emu/cm^3 [93]) comparable to that of Ni (484emu/cm^3 [34]) and a large uniaxial anisotropy, whilst also having a small magnetic damping factor. First principle calculations for MnAl predict that in the ideal stoichiometry and perfectly ordered ferromagnetic phase produces large magnetic moment of 2.4 μ_B/Mn atom and a high magnetic anisotropy of $K_U = 1.5\text{x}10^7$erg/cm^3. High anisotropy materials normally need the strong spin-orbit coupling associated with 4f elements such as Pt but in the case of MnAl it is possible at room temperature without the need for Pt or other elements [63, 94]. These results combined with low spin orbit coupling, relatively low cost and abundance of materials promote MnAl usefulness in any application requiring high magnetic moment and high anisotropy [63, 64]. In spintronic applications such as spin torque oscillators the low damping constant provides new opportunities to optimise current storage techniques, where the lower the magnetic damping factor is linked to a more power efficient system.

The usefulness of magnetic materials can be directly linked to their cost, where the more abundant the material and the cheaper its sourcing the more likely it is to break into the market. Figure 3.11 gives the cost of each element provided by [95]. It is clear from the figure that materials such as Rh, Pt, Pd and Au will need to perform exceptionally well for them to be used in applications, whereas materials such as Mn and Al may be looked favourably due to their cost.

The area of interest shown by the bulk MnAl phase diagram, figure 3.12, is depicted by the cross-hatch region between 50 at.% and 60 at.% Mn. This highly sought after ferromagnetic metastable τ phase is surrounded by non-magnetic phases γ_2, β-Mn and ε MnAl.
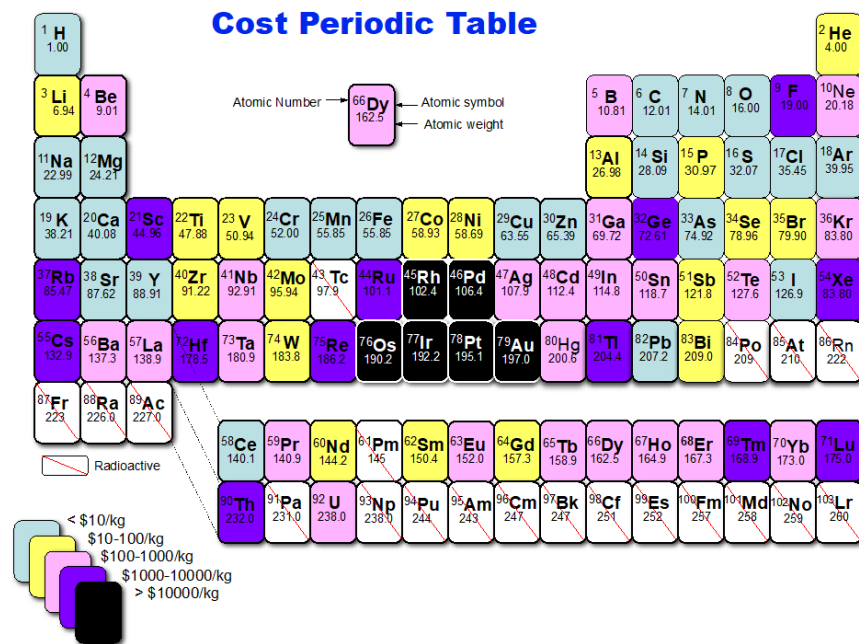
Figure 3.11: Cost periodic table showing the value of each element [95].
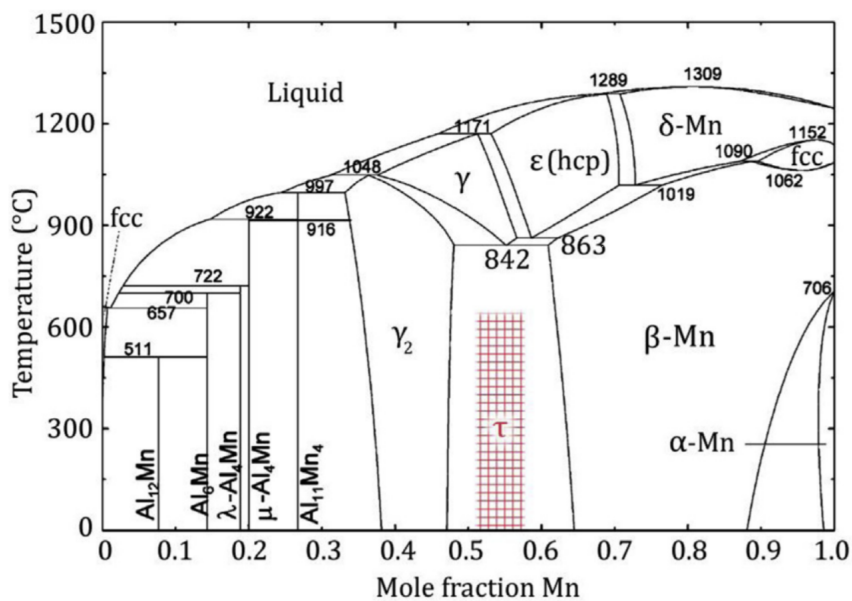
Figure 3.12: Phase diagram for bulk MnAl with metastable τ region shown between the equilibriums phases γ_2 and $\beta - Mn$ [96].

For bulk MnAl the τ phase can be formed at high temperature and then cooled to promote a stable state at room temperature. However in thin films there is a long timescale associated with atomic diffusion so the τ phase is difficult to form. Additionally there is a small range of composition, 50 - 60 atomic % Mn, making the fabrication process more challenging. Initial work to create τ-phase MnAl saw very few studies of thin films, as the metastable phase only formed under precise conditions. However, bulk MnAl research sparked interest, as the material possessed highly sought after permanent magnetic properties. When transitioning from bulk to thin film systems it is advantageous to use strain within the system to encourage the desired phase to grow at lower temperatures. This can be done by the careful selection of various seeding layers and substrates which help lower temperature of phase ordering [64]. Section 3.4.3 covers the use of multiple substrates and seed layers in more detail with a comparison between the magnetic results shown in table 3.4.

A linearised augmented plane wave (LAPW) method was used to calculate magnetic moment and mangetic anisotropy energy (MAE) of MnAl τ phase for $Mn_{50}Al_{50}$ [97]. This method is among the most accurate method for performing electronic structure calculations for crystals, where it is based on density functional theory (DFT) [97, 98]. The results of this study are shown in figure 3.13, where additional measurements of lattice constants from XRD analysis are given [97, 98].

In MnAl the lowest energy state occurs for c/a of 0.9 in FCT and 1.3 in reduced BCC unit cell, as shown in figure 3.13. This provides a magnetic moment of 2.37 μ_B/Mn atom (161 emu/g) and magnetic anisotropy energy of 1.525×10^7 erg/cm^3 [96]. The magnetisation is increased if the system is strained to the lower values of c/a, corresponding to the FCT structure is used throughout for MnAl systems.
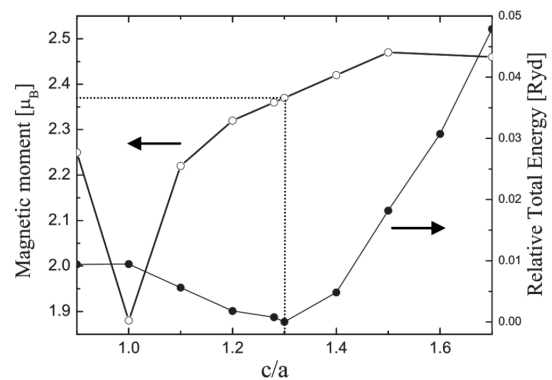
Figure 3.13: The c/a dependence of magnetic moment and relative total energy for $Mn_{50}Al_{50}$ [99].

It was confirmed in 1960, by the use of neutron diffraction, that the τ phase has a

Mn spin alignment parallel to the c-axis [100], this feature is beneficial for the materials application as market leading magnetic media currently aligns perpendicularly, and in the case of MnAl the magnetic properties are heavily linked to the crystallographic structure allowing a more refined optimisation process. The next 30 years of research saw investigations into stabilising the τ phase by the addition of elements making various alloys [101–103]. Around the 1990's Mn and Al alloys were being produced in thin film form, with some success (reaching saturation magnetisation of 490 emu/cm^3 and K4$_U$ of $9.8\mathrm{x}10^6$erg/cm^3) with MnAl deposited by MBE with at a thickness of 60 nm [104] and Mn-Al-Cu ternary alloys being sputtered at a thickness of 633 nm [105]. Limitations in sputtering methods meant that the formation of pure MnAl alloys in an ordered phase was only possible by epitaxial MBE growth, where sputtering was seen as a crude method of approach.

3.4.1   Phase Ordering

The challenge with MnAl systems is the phase formation during the fabrication process. The desired τ phase, as shown in figure 3.12, exists for a narrow band of composition between two equilibrium states and a further state at a higher temperature. These other phases are non-magnetic and surround the desired magnetic phase. When forming MnAl the possible phases present are; γ_2, τ, β Mn, ε and ε' as shown in figure 3.12. A summary of these phases and their associated lattice constants and structures is given in table 3.2.

		Lattice Constant			
Phase	Structure	a	b	c	Reference
γ_2	D8$_{10}$	12.67	12.67	7.94	[106, 107]
τ	L1$_0$ (FCT)	3.94	3.94	3.56	[100, 102]
β-Mn	A13	6.32	6.32	6.32	[108]
ε	A3	2.7	2.7	4.37	[109]
ε'	B19	2.7	2.7	4.37	[96, 110]

Table 3.2: Bulk MnAl phases with their corresponding lattice constants and structure.

As these phases have vastly differing structures and lattice parameters, as well as magnetic properties, it is straightforward to determine sample phase through methods such as X-ray diffraction and/or magnetometry. However, their production is a complex procedure and understanding why each phase is present and what conditions are necessary for their formation proves vital to the fabrication of MnAl in the desired phase.

The fabrication of bulk alloy samples show that the metastable τ phase forms at a high temperature through eutectoid transformation [96], where control over composition is vital to forming the ε phase as it rests between the two non-magnetic equilibrium phases of β-Mn and γ_2. The phase transitions shown in figure 3.14 begin with an initial formation of the non-magnetic ε phase at temperature in a hexagonal close packed structure. The ε phase then transitions to an intermediate ε' phase at elevated temperatures, where once cooled can be transitioned into the desired τ phase with face centered tetragonal structure. To achieve this a common approach found in literature is to form the ε phase at temperatures >1000°C for a long period of time, minimum hours but in some cases days [109], then allow the material to cool before further annealing it around 400 to 600 °C to induce τ phase ordering.
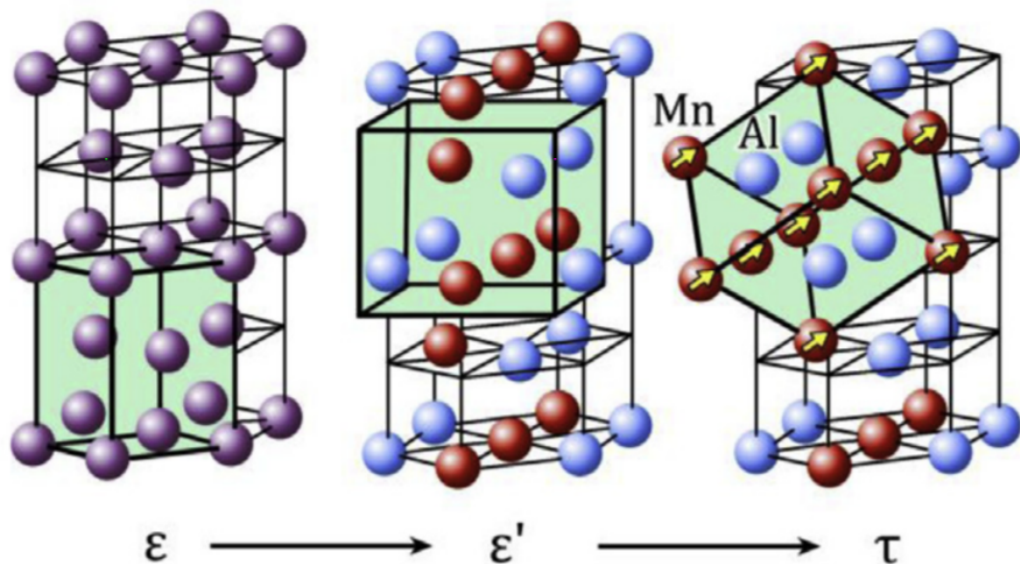
Figure 3.14: MnAl formation process as phase transitions from the HCP ε phase, where atoms can be in any position (given by the purple colour), to the FCT τ phase through the intermediate ε' phase, where Mn is represented by the red and Al blue [96].

For many years the conventional wisdom was that the τ phase is the product of a displacive or martensitic transformation following metastable B10 ordering (Strukturbericht notation for a two element compound [30]), as shown in figure 3.14. However, optical and electron microscopy, as well as kinetic analyses, have indicated that the formation of τ phase involves a compositionally invariant diffusional nucleation and growth process preferentially forming at the grain boundaries of the ε phase [110]. The study carried out by Yanar et al. [110] used ingots made by induction melting Mn and Al within an argon environment, producing samples of size 1.5 cm by 15 cm that were cut to thin slabs of 0.3 to 0.5 mm. These samples were then annealed in a Transmission Electron Microscopy (TEM) to observe directly the shearing and associated changes of the structure [110].

The τ phase originates from grain boundaries and the faceting of the interphase interfaces, as shown in 3.15. The grain boundary of the nuclei exhibit (111) and (002) facets but as the growth proceeds the apparent facets often have high index planes of growing τ phase [110]. Electron diffraction of these grain boundaries, carried out by [110], displayed a special crystallographic orientation relationship with one parent phase grain: $(0001)_\varepsilon//(111)_\tau$ and $(11\bar{2}0)_\varepsilon//(1\bar{1}0)_\tau$ [110].

(a)   (b)
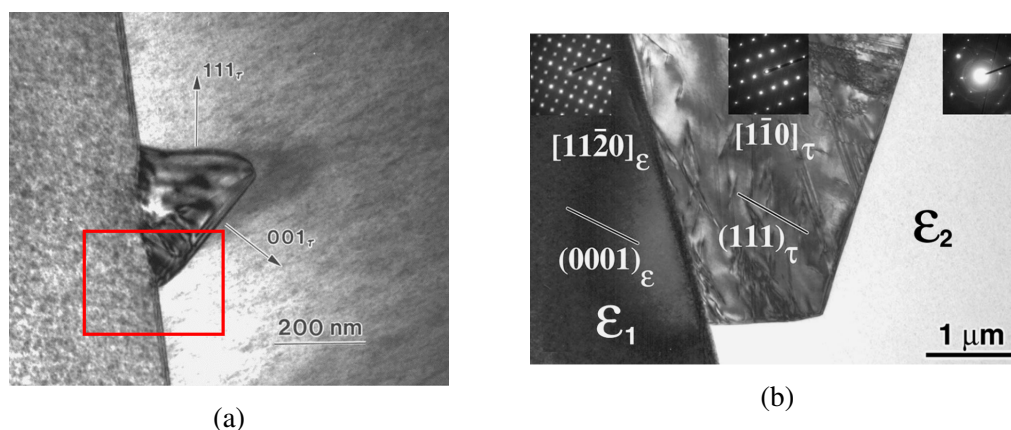
Figure 3.15: (a) Bright field transmission electron microscopy images of the τ phase nuclei appearing at the ε grain boundaries with zoomed in (b) electron diffraction patterns showing the orientation relationship between τ and ε phase across the nucleation interface [110].

This crystallographic orientation relationship can be seen under close inspection of

bright field transmission electron microscopy (BR-TEM), figure 3.15. Analytical electron microscopy and energy dispersive spectroscopy (AEM/EDS) across the interphase interfaces are shown in figure 3.15, where there are no composition difference between the product τ phase and the parent phases ε and $\varepsilon^{'}$ [110]. There is however a high density of defects in the resulting τ grain as the formation follows a quasi-continuous random atomic migration across the incoherent phase boundary from the parent phase [110]. The addition of stabilising elements such as carbon have been proposed to inhibit the diffusion of Mn and/or Al atoms. These elements would also slow the decomposition of the τ into the equilibrium states β Mn and γ_2.

It is now understood that both a displacive (or shear) mode and a massive mode of phase formation occur [110–112]. The displacive transformation occurs at lower temperature as it involves co-operative movement of atoms or groups of atoms which are not hindered by large energy barriers [111]. The massive transformation is that defined previously with a compositionally invariant nucleation and growth process involving change in crystal structure and/or degree of long-range order. The exact temperature range over which either mode dominates is yet to be determined due to lack of precise measurement methods [112].

3.4.2 Bulk MnAl

The realisation of the ferromagnetic phase from the non-ferromagnetic elements Mn and Al was a driving force behind a lot of the early research into MnAl. The first synthesis of bulk MnAl was in 1960's by Koch et al. [100] and Kono et al. [101], who rapidly cooled the non-magnetic ε phase to form the ferromagnetic τ phase. The first reports about the ferromagnetic τ phase of MnAl were based on its use as a permanent magnet material, with an Ms of 490 emu/cm^3, Ku of 10 Merg/cm^3, and (BH)$_{max}$ of 3.5 MGOe [103], soon improved to 7 MGOe by doping with C [113]. To achieve the τ phase in bulk samples a composition between 50 and 60 at.% Mn was needed with an annealing temperature between 500°C and 900°C.

A computational study by Kontos et al. [114] using COMSOL investigated the application of MnAl vs common rare earth and ferrite permanent magnets for electric machine applications. The simulations used a permanent-magnet synchronous generator (PMSG), with four cases under investigation of which two used MnAl, one NdFeB and the last Y40 Ferrite. The study concluded that although MnAl is not currently

implemented in a generator it has the potential to fill the gap show in figure 3.16 once the material properties are more fully known and in particular its limitations and phase formation [114].
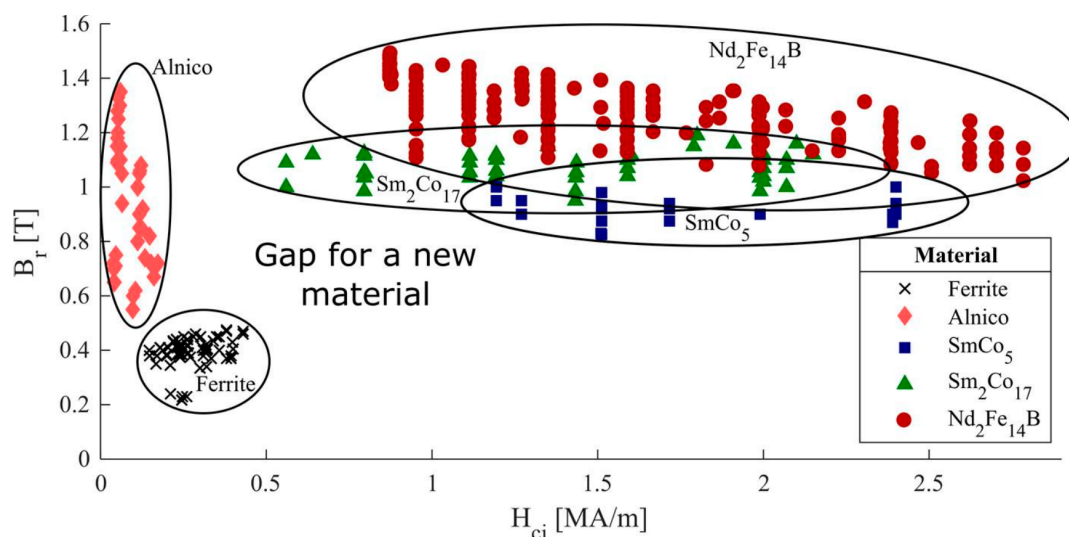
Figure 3.16: Examples of common Permanent Magnet (PM) materials and their magnetic properties, with a highlighted gap between ferrite and rare-earth PM [114].

The initial drive for MnAl was motivated by its lack of heavy metal elements, thus making it a cheaper alternative for applications such as permanent magnetic machines [114]. The drive for MnAl introduction to the permanent magnet industry was boosted by a cost analysis of common elements used to make permanent magnets: Dy $\approx$ \$600kg^{-1}, Nd $\approx$ \$90kg^{-1} and Sm $\approx$ \$40kg^{-1} [115].

In bulk materials it has been shown that the ferromagnetic τ phase has a high remanence, coercivity and saturation magnetisation [115]. Various bulk fabrication methods are shown in table 3.3 with their corresponding magnetic properties, other fabrication methods that produced good magnetic properties are solid state reaction with hot pressing [116] and cold rolling [112].

Method	Composition (atomic %)	Remanence (M_R Oe)	Coercivity (H_C Oe)	Reference
Hot-Extrusion	$Mn_{53}Al_{45}C_2$	6100	2700	[109, 117]
Hot-Deformation	$Mn_{53}Al_{45}C_2$	3300	2200	[118, 119]
	$Mn_{53.5}Al_{46.5}$	2900	1200	[119]
	$Mn_{54.5}Al_{45.5}$	3100	2200	[119]
Hot-compaction	$Mn_{53}Al_{45}C_2$	1720	3300	[118]
Microwave Sintering	$Mn_{53}Al_{45}C_2$	1550	1100	[118]
Sintering	$Mn_{54}Al_{46}$	2700	900	[120]

Table 3.3: Fabrication methods and their corresponding magnetic properties for various compositions.

A commonality between these fabrication methods is that β-Mn phase proved to play a vital role in producing the large coercive fields, where it acts as a pinning center to the magnetisation reversal process. However, the drawback was that the magnetic moment of such samples is reduced as the total amount of τ phase is reduced. Therefore alternative routes to increase magnetisation and coercivity is at the forefront of bulk MnAl research, whereas in thin films the phase segregation is not appropriate but grain boundary engineering may produce similar results.

The effect of carbon addition to MnAl alloys was investigated by Ping-Zhan Si et al. [112], who investigated $\varepsilon \rightarrow \tau$ phase transformation of $Mn_{54}Al_{46}C_X$ alloy. It was shown that the C content in the system increases the stability of the τ phase by inhibiting the diffusion of Mn and Al atoms. The addition of C however lowers the Curie temperature of the alloy, but with increased concentration they showed that this starts to rise again, as shown in figure 3.17.
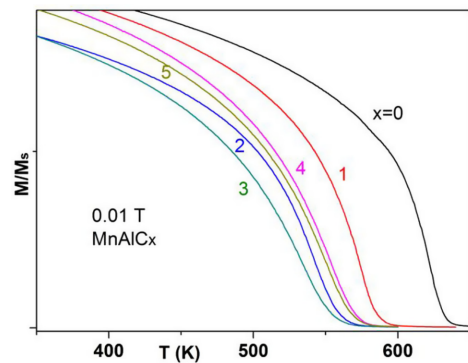
Figure 3.17: Magnetisation vs temperature for samples of MnAlC$_x$ measured using an applied field at 100Oe, T_c is 640, 590, 570, 565, 580 and 580 K for x= 0, 1, 2, 3, 4 and 5 respectively [112].
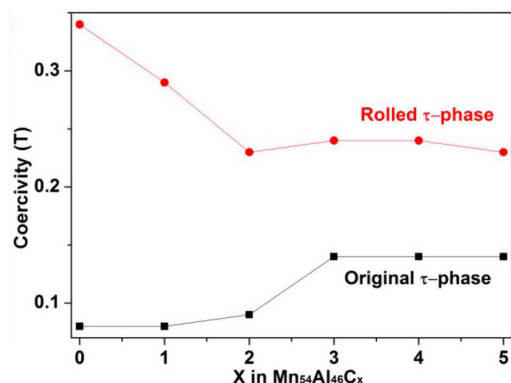
Figure 3.18: Comparison between coercivity measurement of as made $Mn_{54}Al_{46}C_X$ and cold-rolled [112].

Ping-Zhan Si et al. [112] showed that by passing the material through rollers applying compressive force at temperature below its recrystallisation temperature (cold-rolling) that their samples could increase the coercivity significantly, see figure 3.18.

The differences between MnAlC and MnAl are accredited to lattice constant variations, where the a-axis becomes shorter, see figure 3.13, with the addition of carbon to a point of saturation thereafter no changes are seen, corresponding to roughly 0.6 wt% C [112].

The addition of carbon to bulk MnAl alloys improves the formation of the τ ferromagnetic phase. However, as shown in figures 3.17 and 3.18 the magnetic properties can be diminished, especially the coercivity which is an important magnetic property for permanent magnets. The coercivity is affected by high density of defects in samples without additional carbon, where β-Mn would form thus creating domain-wall like pinning sites.

The fabrication method chosen can directly effect the magnetic properties of bulk MnAl, where methods such as hot-extrusion can produce larger remanence and coercivity. The different techniques commonly used are highlighted in table 3.3 along with their magnetic properties. Further research into the structure of MnAl alloys and its phase transitions is still needed in order to understand the optimum temperature and/or composition for bulk sample permanent magnet applications.

3.4.3   Thin Film

The fabrication of magnetic MnAl thin films was first attempted in the 1990's, but understanding of the growth mechanics for the $L1_0$ phase were slow due its complex compositional and temperature restrictions. The first investigations used a wide variety of substrates and/or seeding layers, which help to optimise film growth through strain control, notable examples include GaAs(001) [121, 122], MgO(001) [65], Cr-buffered MgO(001) [64], glass [123, 124], and TiN-buffered Si [125]. It was shown

in the early 2000's that structural and magnetic properties of MnAl thin films can be modified by varying the thickness, deposition temperature and post-annealing conditions [126]. Different techniques for deposition have been used, such as magnetron sputtering [124, 127–131], molecular beam epitaxy [122, 123, 132], and pulsed laser deposition [121]. However, magnetic properties have yet to achieve values similar to those obtained in bulk materials and this is attributed to the strong dependence between magnetic properties and the composition microstructure [126].

The ideal stoichiometric structure for thin film MnAl is an alternating A and B plane sublattice perpendicular to the c-axis. Mn atoms have been confirmed by neutron diffraction experiments to be ferromagnetically coupled within sub-lattices, where excess Mn and defects cause sub-lattices to align antiferromagnetically which increases coercivity [132, 133]. The control of defects is vital to the τ phase formation in thin films, where anti-phase boundaries act as both pinning and nucleation centers [132], similarly in bulk MnAl permanent magnets variation is seen in coercivity due to defects.

The use of various substrate and seed layers can be used to optimise the growth of MnAl thin films, where strain is used together with deposition/annealing temperatures to encourage τ phase growth. The following subsections focus on various literature sources for optimum substrate choices and where possible seeding layers. No preference has been given to deposition method, but as the main technique used in this thesis is magnetron sputtering comparisons will be made where possible.

3.4.3.1 GaAs Substrate

An early investigation of MnAl used MBE to deposit on to GaAs substrates with an AlAs(001) seed layer. The study focused on magnetic properties of MnAl thin films and how composition, Mn_xAl_{100-x} for x=50-70, and varying thickness, 10 to 100 nm shown in figure 3.19, effect the film properties [123, 132]. High quality MnAl films were made using an MBE system with in-situ rapid thermal annealing (30 s) to test various conditions for producing an ordered structure. The remnant magnetisation is found to increase with annealing (up to 500°C) whereas a corresponding decrease in the coercivity of the film is seen, figure 3.19. The reduced coercivity is due to the removal of pinning sites, seen by the shift in XRD peak from τ phase to ε phase. Increasing the temperature degrades the film into its equilibrium phases, ε, β and γ,

this is confirmed by the disappearance of the τ phase peak [132].
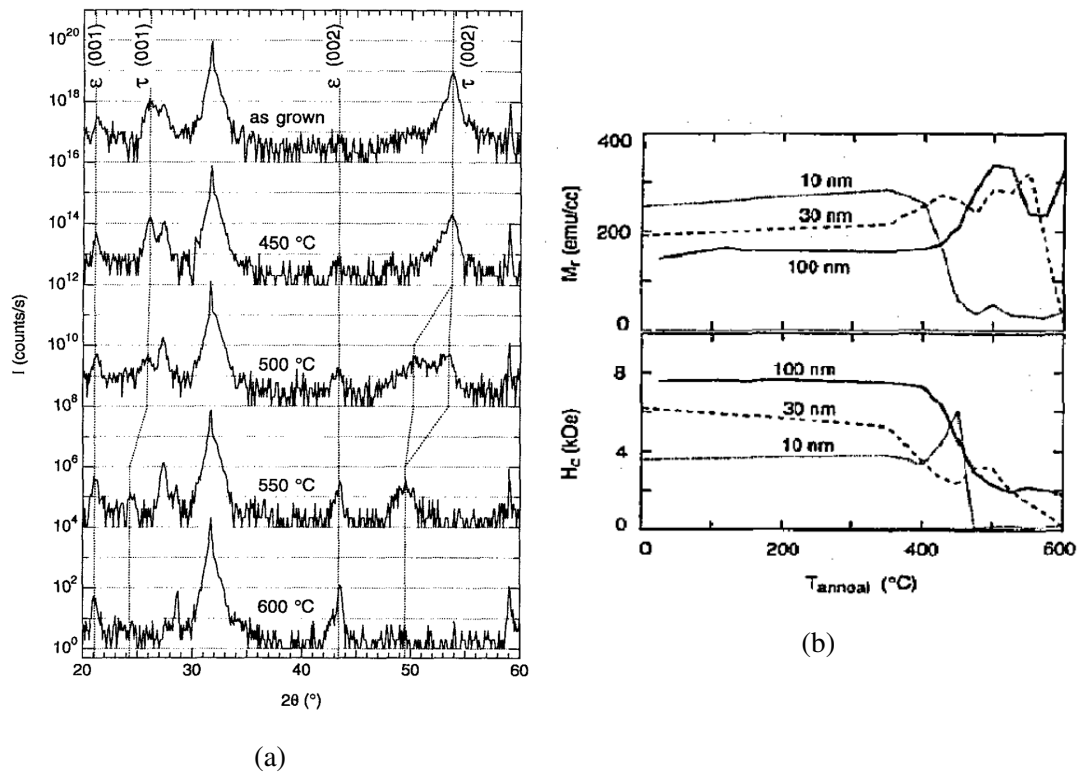
Figure 3.19: (a) X-ray diffraction of 30 nm $Mn_{60}Al_{40}$ film at various annealing temperatures [132], and (b) magnetic remanence and coercivity as a function of temperature for various thicknesses [123].

The choice of substrate and seed layer in this study matches closely to MnAl (110) plane, where AlAs on GaAs substrate has a lattice parameter of 5.66 Å whereas MnAl (110) is 5.57 Å, with a difference of 1.5% [132]. A large amount of Al is present at the boundary between the seed layer and MnAl film, thus allowing minimal reactivity between the film and seed layer giving a clean interface [132]. The use of GaAs as a substrate was to limit the strain in the system as much as possible. However for spintronic applications it is necessary to grow MnAl onto a tunnel barrier layer, which is typically MgO [15]. The use of MgO is standard within magnetic tunnel junctions (MTJ), which are of great importance for spintronic applications. Therefore being able to form an ordered structure with MgO is a requirement if it is to be used in STO devices. The lattice parameter difference between MgO (4.212 Å) and MnAl is 6.7%, this large difference will produce substantial strain in the film [134, 135]. The optimum choice for reducing strain is Cr or $Cr_{90}Ru_{10}$ seed layers with a BCC structure

and (001) orientation, they have a lattice constant of 2.884 and 2.900 Å respectively making a difference of 3.5% with MnAl (100) [64].

3.4.3.2 Glass Substrate

The use of glass substrates is common when producing thin films by sputtering, but in the case of MnAl it is problematic due to poor adhesion, therefore seed layers must be used. The use of Al as a seed layer helps to solve the adhesion issue, where changing the Al thickness can vary the crystalline ordering of the film [124], shown in figure 3.20.
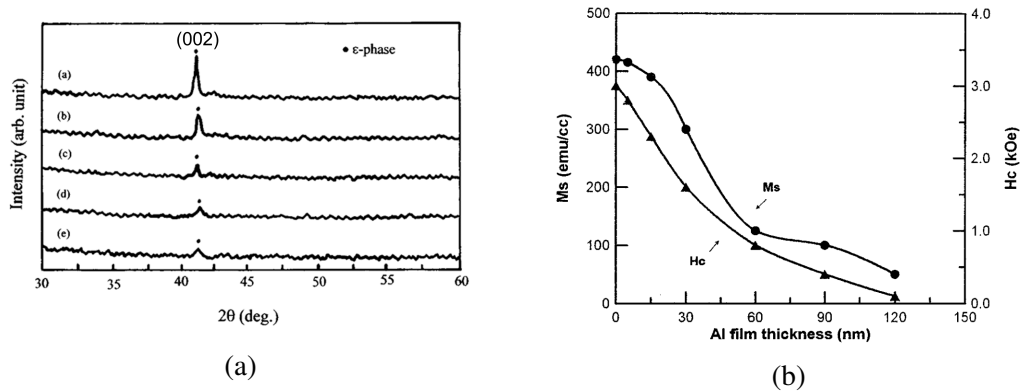
Figure 3.20: (a) MnAl/Al bilayer crystal ordering shown by XRD for a variety of Al thickness (a) 0 nm, (b) 30 nm, (c) 60 nm, (d) 90 nm and (e) 120 nm, with corresponding magnetic data shown in figure (b) [124].

The composition of the film was 50:50 (Mn:Al) atomic % but as the Al layer thickness is increased the growth of the γ increases, this is seen as both M_S and H_C decline for Al seed layer greater than 30 nm. The amount of τ phase present in the as deposited case is limited, but with the correct annealing conditions this can be increased dramatically as shown in figure 3.21.
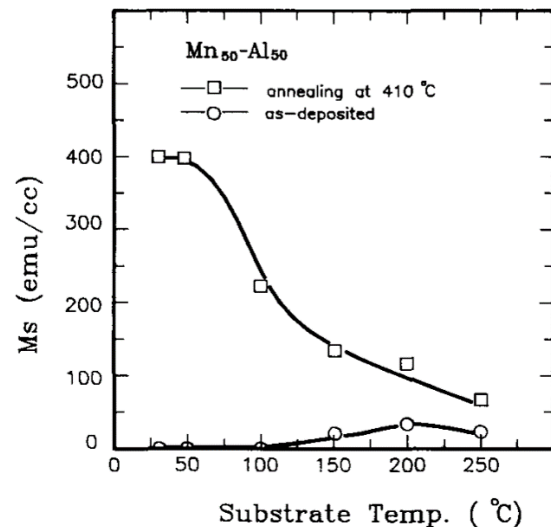
Figure 3.21: Saturation magnetisation as a function of annealing temperatures for MnAl film deposited at 410°C and RT [129].

The as deposited MnAl film is non-magnetic up to 100°C, after which some magnetic moment is detected which indicates that only a small amount of τ phase is present. Annealing samples at 410 °C increases the initial M$_s$, where the film has transition from the non-magnetic ε to τ phase during the annealing. The study found that at low deposition temperatures the energy of the sputtered atoms was not enough to form the metastable τ phase or the equilibrium β and γ phases. Therefore, the ε phase forms due to super quenching effects, this can then be further heated to form the τ phase [129]. These studies used a relatively thick MnAl layer (0.8μm), as it helped with adhesion issues. Below 700 Å the saturation magnetisation drops rapidly to 50 emu/cm^3. The ferromagnetic τ phase forms in a shear transformation with associated atom movements, therefore thinner films have difficulty forming the correct phase due to rigid substrate restrictions [129].

3.4.3.3   Silicon Substrate

Silicon based substrates improve the adhesion compared to glass substrates and are CMOS-compatible, which are a pre-requisite for MnAl-based structures in perpendicular magnetic tunnel junctions (p-MTJ) and STT-MRAM [125]. The formation of MnAl on various seed layers using silicon substrates was investigated, where MgO [136] and TiN [125] were the candidates which showed the most promise. The use of TiN as the seed layer improves the ordering of the film as its epitaxial growth on Si is much better than MgO. However, the substrate must have its native oxide removed by hydrofluoric acid buffering. The MgO seed layer has the advantage that no pre-treatment of the substrate is necessary, but produces slightly inferior magnetic properties.

The improved MnAl magnetic properties using TiN seed layers is believed to be due to strain present within the system, as TiN has a lattice constant of 4.3 Å and MgO is 4.2 Å [125]. The results of each seed layer for a variety of deposition temperatures is shown in figure 3.22.
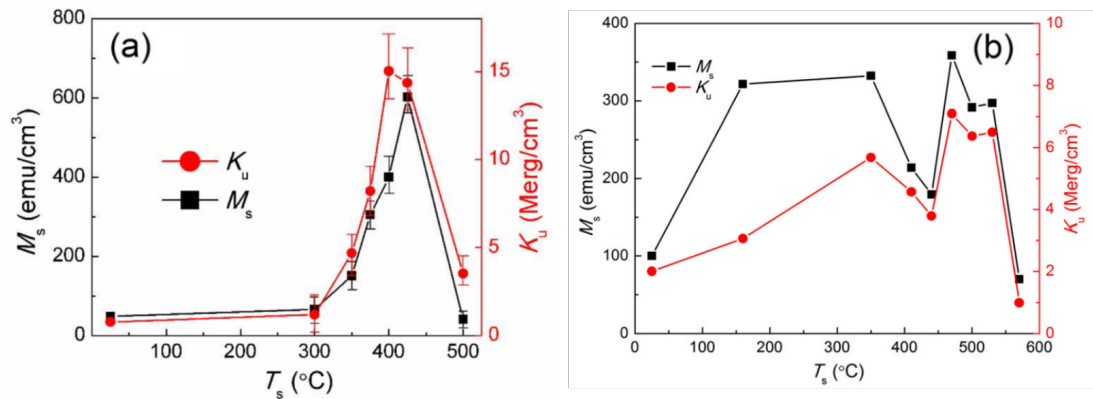
Figure 3.22: Comparing data for 30 nm of MnAl deposited onto (a) TiN [125]and (b) MgO seed layers as a function of substrate temperatures [136].

The sensitivity of the τ phase formation is emphasised by the small window of temperature conditions that lead to optimal magnetic properties, shown in figure 3.22. The TiN seed layers have better growth on the silicon substrates, whereas in the MgO case the seed layer formation cannot be compared to single crystal substrates.

3.4.3.4 MgO Substrate

Since the early 1990's the growth and magnetic properties of $L1_0$ MnAl has been studied on a variety of substrates. Despite the progress made there are only a few reports of MnAl epitaxial films having been grown on GaAs and MgO substrates. These substrates are significant in that they are able to support films with perpendicular magnetic anisotropy [65]. Many different ferromagnetic materials use MgO substrates, such as FePt, CoPt and FePd all of which have $L1_0$ ordering. Initial understanding of MnAl growth on MgO is shown in figure 3.23, where in-plane rotations of the XRD peaks show that there is a 45°offset in the (001) axis alignment between MgO and MnAl [137].
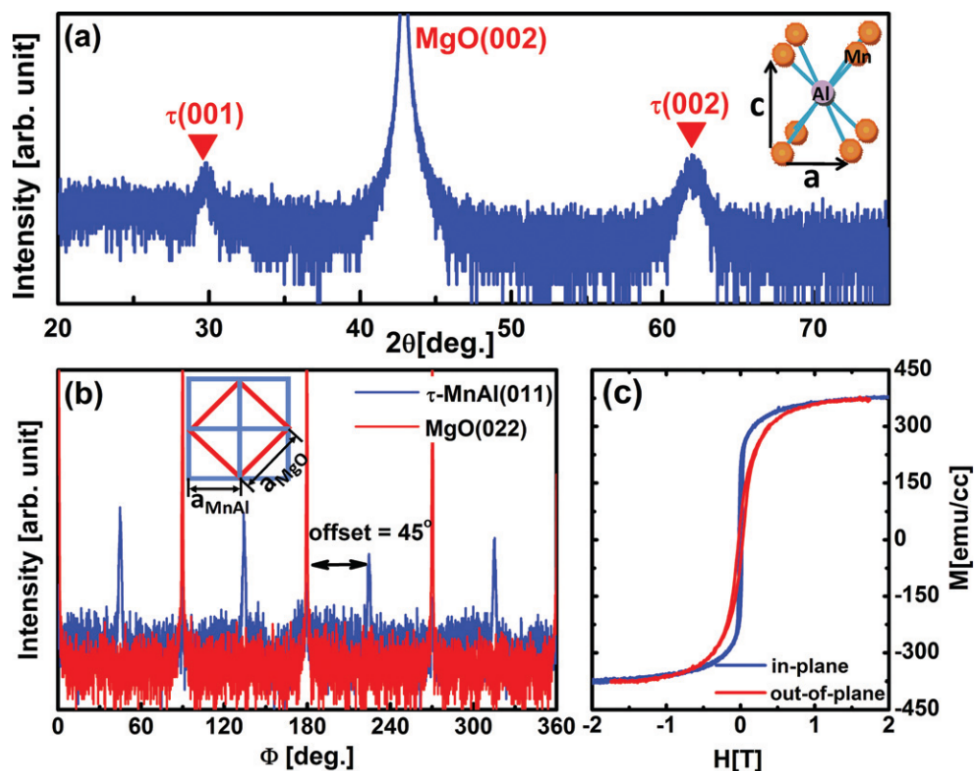
Figure 3.23: (a) XRD spectrum for MnAl film, (b) in-plane rotation showing proper alignment of crystal planes, and (c) magnetic response of MnAl film [137].

Strain plays a vital role in this system, where temperature of deposition and/or annealing can be reduced by induce/relieving strain within the system. A Cr (001) seed layer ontop of MgO (001) substrates can minimise the strain present, thus allowing a reduced temperature ordering for MnAl [138]. The substrate temperature controls initial ordering within the system where further annealing can induce a long range ordered system [139].

Experimental results show that by using a Cr (001) seed layer on MgO substrate reduces strain present in the system, allowing depositions as low as 200 °C to induce ordering as shown by the MnAl (002) and (001) peaks in figure 3.24 [139]. This ordering is further improved by annealing the sample, as shown in figure 3.24.
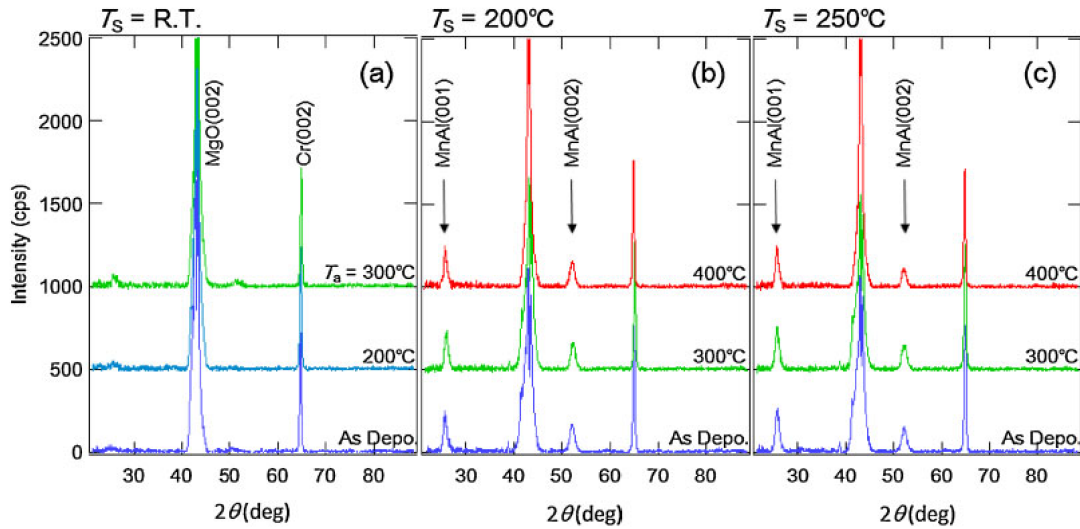
Figure 3.24: XRD spectrum showing the effects of annealing temperature (T_a) for Cr/Mn$_{56.9}$Al$_{43.1}$/Ta samples deposited at various temperatures (T_s) [139].

An investigation into varying the composition of MnAl target material showed comparable magnetic properties for Mn$_{46}$Al$_{54}$, Mn$_{48}$Al$_{52}$ and Mn$_{50}$Al$_{50}$ [138]. The smoothness of the surface was investigated by AFM, where an average surface roughness of 0.39 nm was achieved for deposition temperature of 200°C and annealing temperature of 450°C. The correlation between studies suggests that deposition temperatures around 200°C and annealing around 300-500 °C produced the optimum properties in MnAl on Cr seed layers [138, 139].

It is evident from the ε and β-Mn peaks around 32°and 22°in figure 3.25 that some disordering is present in the MnAl film up to 450 °C. As the temperature of the system is increased the disordered peaks make way for ordered τ phase, but after 500°C this phase decomposes to the high temperature ε phase.
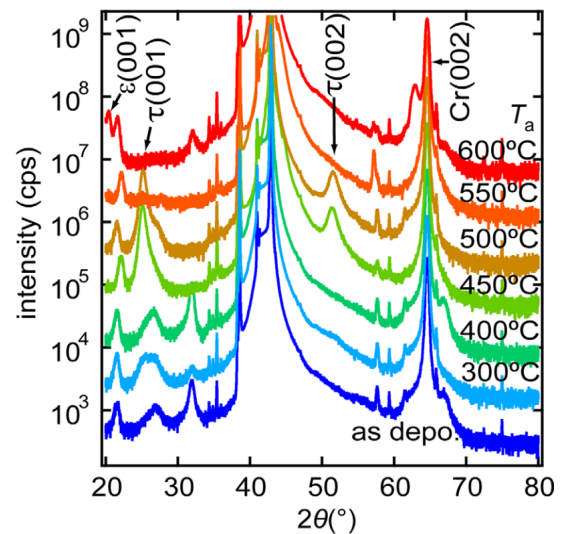
Figure 3.25: XRD spectrum for Mn$_{53}$Al$_{47}$ ordering as a function of annealing temperatures (T_a) [138].
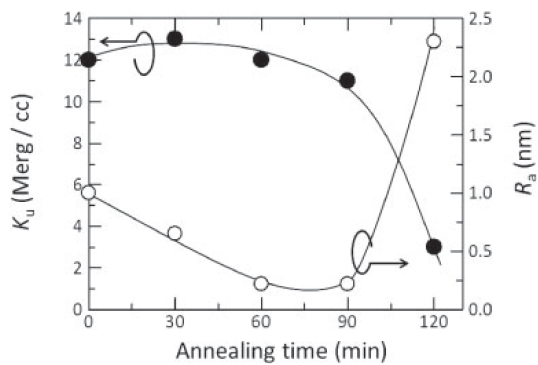
Figure 3.26: Annealing time effect on MnAl films roughness and corresponding magnetic properties [64].

It has clearly been shown that temperature and strain play vital roles in achieving ordering. However, with increased annealing times the ordering of the system can be lost due to surface roughness effects, shown in figure 3.26. It is understood that for annealing times < 90 min allow atomic diffusion in the film plane, which reduces the average surface roughness. The increased surface roughness and degregation of magnetic properties is due to the metastable τ phase transformation into more stable phases, such as γ MnAl and β Mn [64]. For a fully optimised system where MnAl plays a vital role in spintronic devices these problems must be solved.

Substrate with/without Seed Layer	Composition (at.%)	M_s (emu/cm^3)	H_c (kOe)	Deposition Temperature (°C)	Annealing Temperature (°C)	Thickness (nm)	Ref.
GaAs	Mn$_{50}$Al$_{50}$	370	8.2	100	400	2	[140]
GaAs	Mn$_{50}$Al$_{50}$	360	10.7	30	300	11	[141]
GaAs/AlAs (10 nm)	Mn$_{50}$Al$_{50}$	490	1.5	200	450	10	[141]
MgO(001)	Mn$_{50}$Al$_{50}$	394	0.3	RT	400	10	[137]
Glass/Al (30 nm)	Mn$_{50}$Al$_{50}$	390	2.2	RT	400	30	[124]
Glass	Mn$_{50}$Al$_{50}$	400	2.5	RT	410	30	[129]
Si/MgO (20 nm)	Mn$_{54}$Al$_{46}$	300	8	530	350	30	[136]
Si/TiN (10 nm)	Mn$_{54}$Al$_{46}$	250	12	400	350	50	[125]
MgO/Cr (40 nm)	Mn$_{54.1}$Al$_{45.9}$	600	3	200	450	50	[138]
MgO/Cr$_{90}$Ru$_{10}$ (40 nm)	Mn$_{54}$Al$_{46}$	560	3	250	450	50	[64]
MgO/Cr (40 nm)	Mn$_{56.9}$Al$_{43.1}$	530	2	250	N/A	50	[139]
Glass	Mn$_{60}$Al$_{40}$	78	1.6	RT	400	60	[142]

Table 3.4: Collection of magnetic properties and conditions of growth for MnAl films of varying thickness and composition, the order is by Mn at.%.

3.4.4   Summary

The use of L1$_0$ ordered materials is desirable for future spintronic devices thanks to their optimal magnetic properties. Prime candidates such as FePt and MnAl have been covered in this chapter where FePt posses very high anisotropy energy making it the leading candidate for HAMR media. Although the saturation magnetisation and anisotropy of MnAl is less than FePt its relative cheapness and its particularly low spin orbit coupling make it an outstanding for spin torque oscillators and future devices where control of dynamics is important.

FePt and MnAl are not without their challenges, where composition and growth conditions in both cases must be understood and carefully optimised. In the case of MnAl it has had mainly bulk studies, with few reports using magnetron sputtering to make thin films. Therefore, bridging this gap in knowledge by meticulous analysis of growth conditions provides the underpinning science necessary for its emergence in spintronic devices. A summary of various substrate/seed layer combinations is shown in table 3.4, with each films magnetic properties shown.

Chapter 4

Thin Film Fabrication

The investigation of ordered materials relies heavily on the fabrication technique capabilities, where highly pure material sources are vital in producing compositional certainty. There are many fabrication techniques that allow the growth of thin films within a vacuum chamber but the properties each technique produces in a film is not always consistent between techniques. This chapter aims to first highlight the relevant characteristics of each technique before validating the technique used for the work covered in this thesis. The main areas of consideration are the films surface roughness, growth regime, consistency between samples and the throughput time for fabrication.

Any source of contamination must be limited within the scope of this work as the properties of the films studied are highly reliant on composition. The materials chosen for fabrication are highly pure ($>99.99\%$), and therefore alternative sources of contamination must be considered to ensure target purity is utilised fully. A main area of concern for contamination is during the fabrication process, where contaminants can infiltrate the deposition chamber. To remove most forms of contamination from the deposition chamber ultra high vacuum conditions are implemented. Table 4.1 gives examples of how a monolayer (ML) of contamination, in this case nitrogen, may form under various vacuum conditions. The relative path length between collisions is also given to help the understanding of conditions within the vacuum chamber.

Vacuum Conditions	Pressure			Mean free path	Time for Monolayer growth
	Pa	mbar	Torr	L_{coll} (m)	t_m (sec)
Atmosphere	101300	1013	760	1×10^{-7}	1×10^{-9}
Coarse	133	1.33	1	1×10^{-4}	1×10^{-6}
Fine (medium)	0.133	1.33×10^{-3}	1×10^{-3}	0.1	1×10^{-3}
High (HV)	1.33×10^{-4}	1.33×10^{-6}	1×10^{-6}	100	1
Ultrahigh (UHV)	1.33×10^{-8}	1.33×10^{-10}	1×10^{-10}	1×10^6	1×10^4

Table 4.1: Vacuum conditions and their corresponding characteristics such as pressure, mean free path and formation of monolayer Nitrogen molecule contamination [143].

Table 4.1 is used later for comparing contamination growth between techniques under vacuum, both for fabrication and characterisation. The ideal scenario would be to always use ultra high vacuum conditions but the time and precautions necessary to pump each system does not allow this. Therefore where possible the vacuum conditions of each technique are highlighted and the potential source of contamination and its effect on the films properties are detailed.

4.1   Thin film growth - general considerations

The growth of thin films is possible using various techniques, where in this project only physical vapor deposition (PVD) techniques are considered. This section covers the pros and cons of different deposition methods, including molecular beam epitaxy (MBE), evaporation and magnetron sputtering.

Thin films and layered structures require a high degree of control over the growth process, where film uniformity and smooth interfaces play a key role in determining magnetic properties [144]. For example atomically smooth interfaces are typically needed to form the desired magnetic properties in Co/Pd multilayers [58, 144]. Molecular beam epitaxy (MBE) is a relatively expensive technique that is capable of creating accurate atomic layer by layer growth of films, where it operates under ultra high vacuum as shown in figure 4.1. However maintenance and time per sample is low as the ultra-high vacuum conditions are difficult to maintain. The use of MBE for thin film

growth has been around for a number of decades [145], and is principally used where layer by layer growth is required. Although it can produce high quality films its ability to quickly produce samples for parameter space analysis is quite limited.

An alternative technique that operates at high vacuum conditions is evaporation, which uses a crucible sometimes denoted as a 'boat'. Evaporation techniques uses two methods for heating, either crucible heating, which heats the whole crucible, or focused electron beam (e-beam), which evaporates a point on the source material. For the crucible heating method there is contamination issues due to out-gassing or evaporation of the crucible, which occurs during the evaporation process [146]. The e-beam method overcomes contamination issues, but the point source can have detrimental effects on film uniformity [146]. The last technique considered is magnetron sputtering, which operates at a few mTorr pressure. This technique is capable of sputtering a large list of materials simultaneously with

Figure 4.1: Classification of deposition methods for magnetic thin film growth based on the range of working pressures [146]. The mode of transport refers to the manner in which atoms travel from the source to the substrate.

good uniformity, grain size and at a high throughput for batch processing [146]. Magnetron sputtering also allows the substrate to be preconditioned/cleaned by reversing the polarity of the sputter guns. A summary of all methods along with their working pressure and mode of transport is shown in figure 4.1.

The technique used for fabrication in the work reported in this thesis is magnetron sputtering as it allows large compositional range from multiple target sources, whilst also minimising contamination by using ultra pure (99.9999%) argon gas for plasma

generation. The following sections highlight the methodology behind magnetron sputtering, giving details of how the system works and its limitations. This is followed by a descriptions of how films grow on substrate surface and how certain growth regimes are controlled before an introduction to the technique itself along with some precautions taken for contamination minimisation.

4.2   Sputtering

The term "sputtering" describes the method by which material is eroded from a source (target) and deposited onto a substrate. The process takes place in a vacuum chamber to minimise contamination, where prior to deposition it is pumped to a base pressure below $3x10^{-8}$ Torr, the potential contamination at these pressures is very low where a monolayer (ML) will take 100's of seconds to grow, as shown in table 4.1. Once a substrate is loaded into the deposition chamber an inert gas, such as argon, is injected into the ultra-high vacuum chamber. The pressure within the chamber is automatically set by controlling the vacuum pump rate for a steady flow of gas in. The gas injection is normally set so that the pump is in a 50:50 (open:closed) position to allow room for alterations.

To spark the ignition of a plasma an electric potential is applied to the gas within the chamber, where a sea of electrons collide with the neutral gas and produce a mixture of ions and electrons. The positive ions are accelerated towards the target material, which is held at a negative potential, where they collide with the surface and eject atoms into the chamber. The ejected atoms are free to move in the low pressure conditions within the chamber, where a number of atoms move towards the substrate. To ensure a collision free path for the ejected atoms it is important that the pressure of the plasma is sufficiently low so the mean free path is larger than target to substrate distance. Upon arrival at the substrate these atoms reach a thermal equilibrium with the substrate forming the structure of the films.

4.2.1   Sputter Yield

The ion bombardment process removes numerous surface atoms, where the total number of atoms removed per incident ion is known as the sputtering yield (S) given in

equation 4.1, and is related to plasma conditions and material source [147].

$$S = \frac{\text{Atoms Removed}}{\text{Incident Ions}} \qquad (4.1)$$

However, equation 4.1 is a very simplistic view of sputtering, a more accurate representation is to consider the maximum possible energy transfer from the collision of an incident ion and target material [147]:

$$T_m = \frac{4M_1 M_2}{(M_1 + M_2)^2} E \qquad (4.2)$$

where the energy of the incident ions is E with mass M_1, which collides with the target atoms of mass M_2 [147, 148]. Under a first approximation the sputter yield S related to the first collision energy T_m is given by:

$$S = k \frac{1}{\lambda(E)cos(\theta)} \frac{M_1 M_2}{(M_1 + M_2)^2} E \qquad (4.3)$$

where k is a constant that relates to the different possible target materials, λ is the mean free path for elastic collisions near the target surface and θ is the angle between the target surface and direction of incidence ions [149]. Equation 4.3 relates the relative power used for sputtering to the yield of sputtered material. The rate of growth is further affected by the mean free path of sputtered atoms, which is partly determined by the distance between target material and substrate.

The mean free path of a sputtered atom is determined by the operating pressure and its initial momentum, where a heavier atom will lose less momentum when interacting with Ar atoms within the chamber thus arriving at the substrate with a higher energy when compared to lower mass atoms. For this reason co-sputtering from multiple targets is particularly difficult as each material source will interact with the gases present in the chamber differently and therefore have a different sputtering rate that must be controlled by gun power individually.

4.2.2   Alloy Target Sputter Yield

It has been mentioned that the working gas used to create the plasma for sputtering can collide with atoms as they travel to the substrate. In the case of alloy target materials the relative mass of each element can have an effect on film composition. The relative mass of the element being sputtered to the mass of the working gas, in most cases argon, determines how the collision will effect the trajectory. For relatively light atoms the scattering angles can be up to 180°, whereas a heavy atom does not deflect significantly from its path. It is therefore more likely that single collisions of light atoms have a larger effect on the composition than heavy atoms. A study carried out by Sarhammar et al. [148] investigated multiple points within a sputtering chamber, as shown in figure 4.2. The study compared rates and composition of different target materials and how distance from target had an effect, as well as the relative angle between target and substrate.

The effect of sputtering gas conditions were investigated for different alloy materials. There are four main sampling points considered within the deposition chamber are; I normal deposition to substrate, II chamber wall deposition, III slightly backscattered on chamber wall and IV complete backscattering. A combination of all four points allows further understanding of the collisions occurring during the deposition process and how the sputtering gas pressure effects the results.
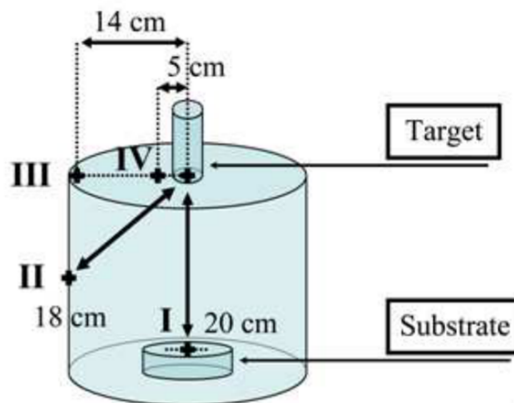
Figure 4.2: Schematic of vacuum chamber for four positions of interest when sputtering [148].

Figure 4.3: Measured composition at various points within a vacuum chamber for low pressure (2 mTorr Left) and high pressure (20 mTorr right) [148].

The example of TaAl from Sarhammar et al. [148] in figure 4.3 shows how compositional variance can occur for an alloy target, where the heavier atom Ta (atomic number 73) is compared to Al (atomic number 13). The dotted white line in figure 4.3 indicates the nominal composition of the target material where the Ta and Al are labelled. For high pressure conditions (20 mTorr) RHS of figure 4.3 the mean free path is small and collisions occur often. The difference between the two elements is the largest for the high pressure conditions. Under low pressure (2 mTorr) LHS of figure 4.3 there are less collisions and the Ta is not backscattered at all, as is shown the data from point IV in figure 4.3. The study by Sarhammar et al. [148] is relevant to the work on MnAl reported in this thesis as will be shown in chapter 7.

4.2.3 Magnetron Sputtering

The method of sputtering described at the beginning of section 4.2 is the building block for magnetron sputtering, where a magnetic field is applied to confine the plasma above the targets surface. Confining the plasma helps overcome certain disadvantages of conventional sputtering, where it is known to be slow and have a high level of electron bombardment on the substrate. The constant bombardment of electrons causes the substrate to heat during the sputtering process, making control over temperature a more difficult task. Magnetron sputtering is not without its drawbacks as it causes an erosion pattern to form on the target surface, the pattern is given the name 'race track' as it forms a circular pattern similar to the race track for Nascar racing. The racetrack forms due to the consistent magnetic field lines that confine the plasma above the target, thus creating high density plasma with maximum ion bombardment on the target material surface [150], an example of a magnetron sputtering target is shown schematically in figure 4.4.
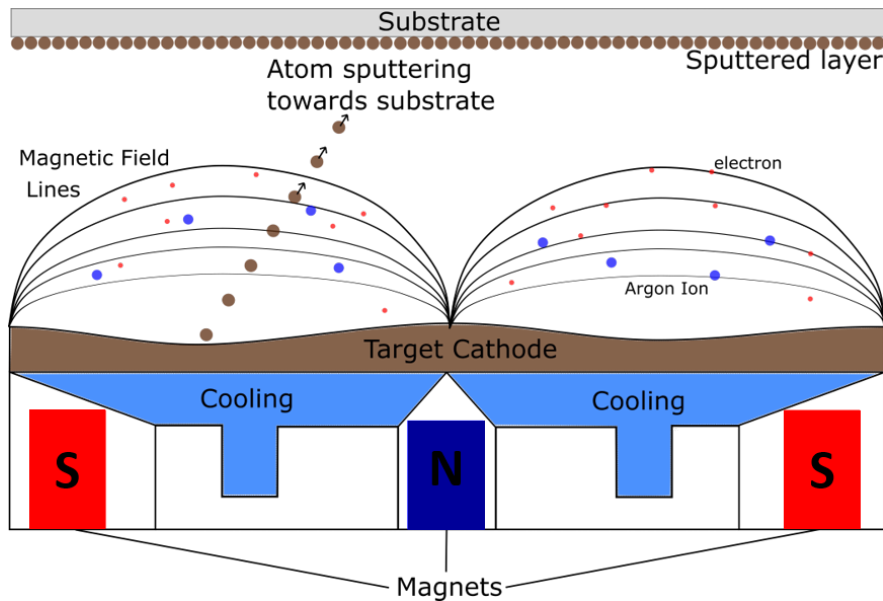
Figure 4.4: A simplified view of magnetron sputtering, consisting of one target material. Where the plasma forms above the targets surface and subsequent ions are directed by magnetic field lines towards the target.

The pressure of the gas used to create the plasma affects the mean free path of the atoms leaving the target material, thus changing their energy upon arrival at the substrate. Tuning the pressure of the gas allows control of film properties due to the change in atom mobility upon arrival, this process utilises control over vacuum pump rate and gas flow rate to ensure a stable plasma. The arriving atoms will have a set energy, but this is not always optimal and additional heating of the substrate up to 900°C is used to increase their surface mobility. The additional heating enables energy barriers to be overcome, where material can form complex phase not possible under normal conditions.

4.2.3.1   Confocal magnetron sputtering

The use of multiple sources opens new scientific possibilities as complex alloys can be sputtered. To enable multiple sources to be used simultaneously a confocal arrangement of targets is used, as shown in figure 4.5. The risk of depositing one material to another target by backscattering, a process denoted as 'poisoning' of the target, is reduced further by having targets at opposing ends of the chamber during co-deposition. This arrangement reduces the interactions between plasma/atoms of different targets,

thus ensuring plasma stability and reducing possibility of contamination.
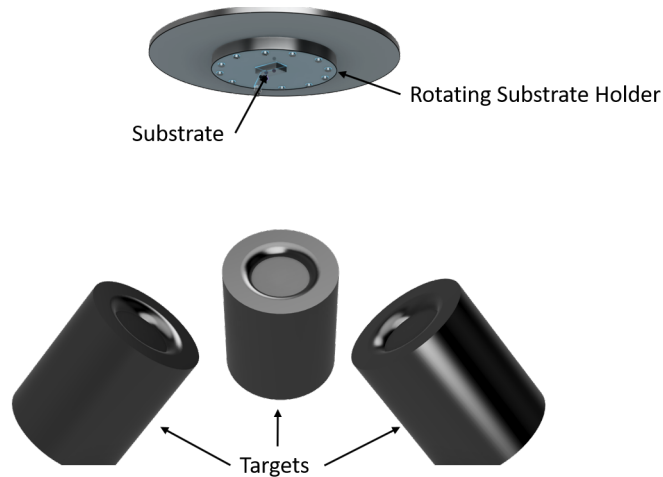
Figure 4.5: Example of confocal sputtering arrangement for three sources pointed towards a central sample plate holding a rotating substrate for uniform films.

4.2.3.2 Radio Frequency Sputtering

The nominal method of sputtering as described previously uses a supply of power known as direct current (DC), which is applicable for most material sources. However, as the need for non-metallic material increases alternative power sources emerged such as RF. DC power supplies are low cost and deposit material quickly, but suffer from a build-up of charged ions on the surface of insulating target materials, this build-up causes the plasma above the target surface to destabilise and thus halts the sputtering process. RF sputtering allows deposition of non-conducting insulating materials as it alternates the electric potential, thus allowing a cleansing of charge build-up on the target surface. During the positive cycle electrons are attracted to the surface of the target material thus creating a negative bias, negating any charge build-up from the negative cycle. The radio frequency typically used is 13.56 MHz, as it is an internationally allowed frequency for experiments and does not interfere with other RF devices. The high frequency also ensures that the heavier ions cannot follow the same process as the electrons due to their mechanical inertia [151].

RF sputtering has some advantage over DC, where lower pressure conditions are easier to maintain allowing fewer collision between sputtered material and the working gas.

However, as this process cycles to cleanse the target surface there is a portion where no bombardment takes place, therefore this method is much slower in comparison to DC sputtering. For this reason DC is the obvious choice when sputtering conducting materials and RF for insulating targets.

4.2.4   Film Growth

The energy of atoms on the surface of a substrate (Surface energy) is a key consideration in film growth, where it was mentioned in section 4.2 that plasma conditions can change the energy of the arriving atoms. Additional energy is given to deposited atoms by heating the substrate, this increases the surface energy allowing formation of complex phases.
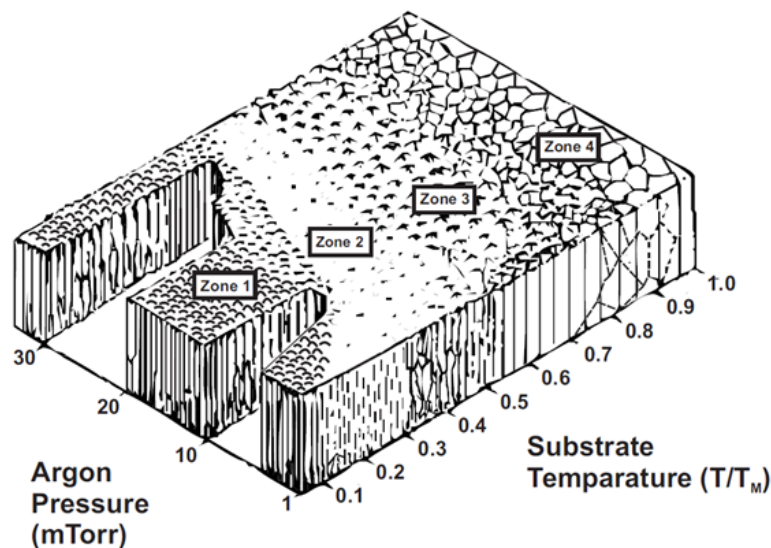
Figure 4.6: Structure-zone diagram for magnetron sputtering of a metal film, with various substrate temperatures (T_M is materials melting temperature) and argon working gas pressure [152]. Four growth regimes are identified; zone 1 columnar growth, zone 2 transition zone with fibrous grains, zone 3 columnar grains with boundaries, and zone 4 equiaxed grains.

With the addition of temperature the atoms on the substrate surface have more energy to move, where the formation of islands is decreased and the atoms nucleate into a continuous film. The complex relationship between working gas pressure and substrate temperature is shown by the zone model of Thornton [152, 153] in figure 4.6.

There are four main zones of concern in the Thornton zone model. Those models have brief description below:

Zone 1 - High argon pressure reduces the mean free path and subsequently collisions are common, leading to a porous columnar structure with high surface roughness where low substrate temperature doesn't allow the atoms freedom to move and reduce roughness. There is also the possibility of voids in the film as atomic shadowing effects occur, thus creating points of contamination within the film.

Zone 2 - Commonly referred to as the transition zone between zones 1 and 3 there is minimal roughness as the material grows as small crystallites.

Zone 3 - Boundaries are commonly found in this zone as columnar growth dominates, where increased temperature allows diffusion of surface adatoms which plays an important role during the formation of this zone.

Zone 4 - As the temperature reaches melting point it plays an important role in the bulk diffusion process, therefore dense structures of equiaxed grains forms and recrystallisation occurs.

Controlling the pressure of working gas allows for changes in sputtering rate and the energy of atoms upon arrival at the substrate, where voltage and current used to form the plasma become a tool of energy manipulation of deposited atoms. The relationship between sputter gas and material was shown in equation 4.3, where sputter yield relates to ion energy and target material choice. However, in alloy targets the different elements will have varying energy as the transfer of momentum is linked to the relative mass of the material. There are also the bonds formed in the alloy that must be overcome, where gaining a full understanding of alloy target deposition becomes quite complex. A lower sputtering gas pressure increases the mean free path and therefore more material can make its way to the substrate surface without interference. However, the plasma stability at lower pressures means there is a finite limit to pressure/power conditions. Combining the three sources of film quality then makes a trilogy of pressure, power and temperature for control over film growth and structure where it may only be possible to grow certain phases at a given temperature and thus limitation are set on other parameters.

With the guidance of the zone model, films are produced at low sputtering pressures, with additional temperature to form low surface roughness films with a preferred crystalline structure. This work aims to reamin within zone 2, as this produces the lowest roughness films with small crystallites associated with the $L1_0$ phase [12].

4.2.4.1   Growth Mechanisms

The formation of thin films is a combination of growth and nucleation processes. There are three main mechanisms describing the formation of thin films [147, 149], and these are highlighted in figure 4.7 and summarised below;

1. **Volmer-Weber** - Atoms have a strong tendency to couple together rather than forming bonds to the substrate surface, this leads to 3D island growth on the surface of the substrate.

2. **Frank-van der Merwe** - Free to move atoms form 2D layer by layer growth, where crystal layers tend to be completed before a new layer is started.

3. **Stranski-Krastanove** - A combination of 1 and 2, where there is an initial 2D growth that transitions into 3D island growth.
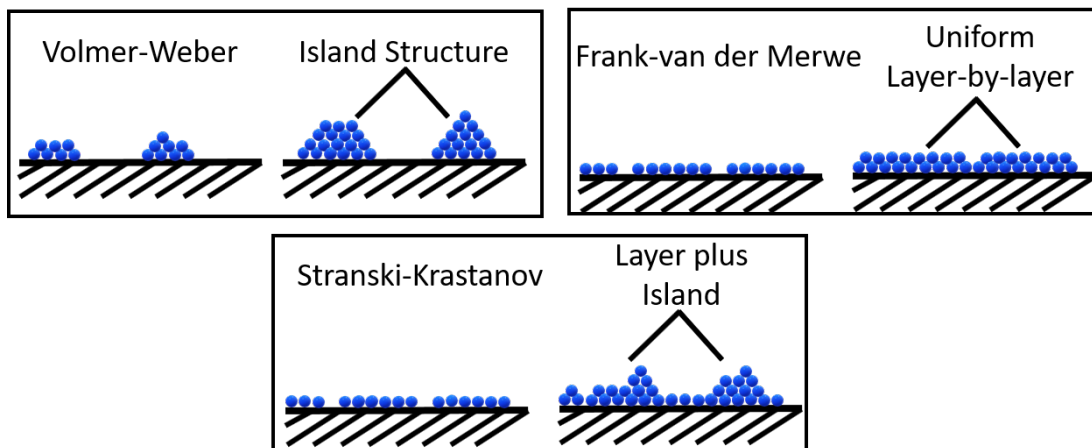
Figure 4.7: Three example modes of film growth [147].

Frank-van der Merwe growth is very temperature dependent, and normally only possible in MBE systems [149]. For magnetron sputtering the Volmer-Weber growth is common, where islands grow to form clusters and coalesce to minimise surface energy. Grain boundaries are formed where islands meet, which creates a polycrystalline

film for grain orientations at random and an epitaxial film for parallel grain orientations.

4.3 Implementation of thin film growth

The basic mechanics of how sputtering works and the film growth types have been discussed in section 4.1. This section looks to highlight the many unique characteristics of the specific sputtering system used for the work described in this thesis and highlight the novel approaches taken. The system of use was an AJA magnetron sputtering system capable of using either a heated or cooling rotating substrate holder. The targets within the system can be arranged in two configurations, (i) 11 targets with the 3 inner targets set to $\frac{1}{4}$ chimney size or (ii) 9 targets with 8 in the outer ring and one in the centre. The more commonly used 11 target configuration is shown later in figure 4.9, where the shutters are in a closed position on all targets and the reduced chimney size can be seen by the reduces size shutter on inner ring targets.

4.3.1 Cleaning of substrates

To ensure a pristine substrate surface prior to deposition a set process for cleaning is carried out. This process has a number of steps, each proving vital to minimising any form of surface contamination as shown in figure 4.8. The cleaning process for cleaning both MgO and Si/SiO$_2$ substrates is shown in table 4.2.

The cleaning of substrates follows a modified version of commonly used cleaning procedure, which follows steps 3 to 6 in table 4.2. Updating this process to include a detergent (Decon 90) for MgO substrates allows the removal of residue left behind by the manufacturers polishing that standard cleaning procedure of acetone and isopropyl alcohol does not remove. A detergent helps the mixing of water with contamination such as oil or grease, where it then allows easier removal of dirt and other particulates. Figure 4.8 shows the results of following steps 3 to 6 (figure 4.8a) and the new cleaning procedure 1 to 6 (figure 4.8b) for MgO substrates.

Process Number	Si/ SiO$_2$	MgO
1 **Detergent**	Not Applicable	Place sample in a detergent solution of Decon 90 and sonicate for 3 minutes.
2 **Remove Detergent**	Not Applicable	Remove residual detergent by sonicating in de-ionised water, twice for 5 minutes.
3 **Acetone**	Sonicate sample in acetone for 5 minutes.	
4 **Isopropyl Alochol**	Sonicate sample in isopropyl alcohol for 5 minutes.	
5 **Dry Surface**	Blow dry sample with nitrogen gun to remove any liquids.	
6 **Remove any Liquid**	Place sample on hot plate, 200 degree C , for 10 minutes.	

Table 4.2: Process for cleaning both MgO and Si/SiO$_2$ substrates, where steps 1 and 2 are not applicable for silicon substrates.

(a)
(b)
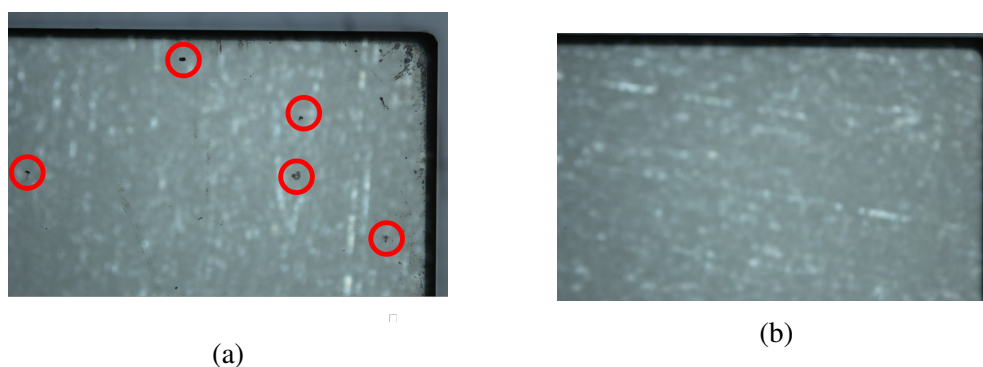
Figure 4.8: Optical image of a corner of (a) MgO substrate cleaned by standard cleaning procedure and (b) post detergent cleaning procedure. Remnants of the polishing are highlighted in (a) with their successfully removal in (b).

It has been made clear that contamination is a high concern, therefore cleaning procedures were optimised where possible. It has been found that not every manufacturer of

MgO substrates is consistent with one another [154], it is therefore beneficial to have a rigorous cleaning procedure that removes any unwanted contamination.

4.3.2 AJA Magnetron Sputtering system

This research project uses an AJA magnetron sputtering system equipped with 11 material sources, 3 of which are in a central position and 8 in a confocal arrangement as shown in figure 4.9. The system is equipped with a load lock for sample transfer that minimises the need to break vacuum in the main chamber, where pumping the smaller volume load lock takes less time thus optimising the loading of samples. The load lock is equipped with a manual lifting mechanism that can load a total of 6 sample plates (measuring 6 inches in diameter), each capable of holding up to 9 substrates. The sample plates are transferred under vacuum from the load lock to the main chamber, where the vertically moving stage lowers to lift the plate into position for deposition. The substrate holder can be equipped with either heating or cooling capabilities, but for this work only the heated stage was used. The system is capable of providing temperatures up to 900°C ($\pm$1°C), where the sample plate rotates to ensure consistent heat distribution across the plate. The rotation mechanism of the plate can be manually controlled or tuned between 0 RPM and 100 RPM.
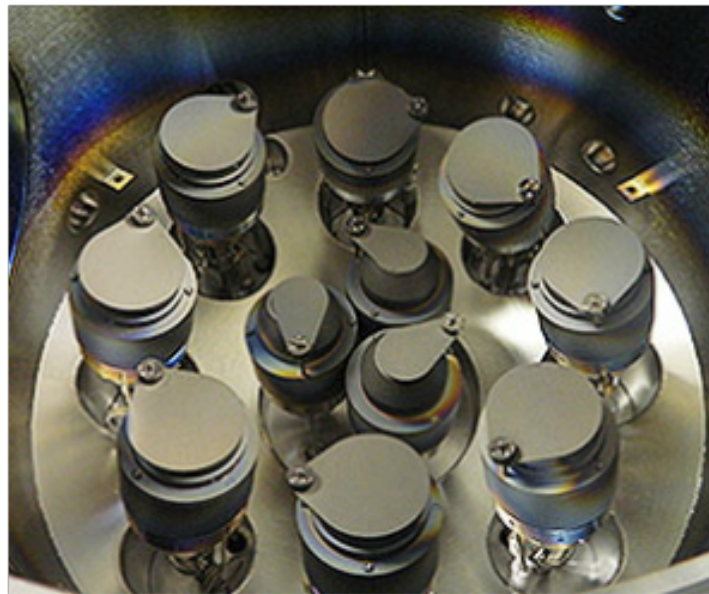
Figure 4.9: Main chamber of AJA magnetron sputtering system in its 11 target figuration.

The main chamber is pumped to ultra-high vacuum conditions, typically 10^{-9} Torr, prior to the insertion of the working gas in this case high purity Argon (99.9999%). The chamber remains under vacuum when not in use to minimise contamination. The system is equipped with two power source options, direct current (DC) and radio frequency (RF), the properties of which were covered in section 4.1. There are a total of 6 DC power supplies and 3 RF power supplies allowing the system to sputter from 9 targets at once. Although multiple targets can be used at the same time the main purpose is not to use all targets simultaneously but rather to enable seamless transition between multi layer structures, where there is no need for cable changes between layers. Independent control over the power supplied to each target also allows the manipulation of composition when co-depositing, which proves vital in the work covered in this thesis as there is an intimate link between composition, film growth conditions and the magnetic properties gained.

The control of temperature within a vacuum chamber has certain limitations, where heat dissipations can only be achieved through radiative means. The time taken for cooling cycles after a heating cycles is problematic as it can allow the formation of contamination layers, where cooling times can be up to 6 hours. However, the system is pumped to ultra-high vacuum conditions for heating procedures, where the system can cool for roughly 12.5 hours before a monolayer of contamination grows as is shown by the times in table 4.1 for monolayer growth of nitrogen at various vacuum conditions. This highlights the importance of maintaining ultra-high vacuum conditions prior to and after the deposition process, including any heating/cooling cycles. With the maintained vacuum conditions the 6 hours needed for cooling is insufficient to allow a single layer of contamination to grow and therefore the film properties would be maintained.

4.4   Post deposition Annealing

The formation of desired characteristics in thin films is often associated with a transition from one phase to another. The formation of alternative phases for an already made film is possible through post deposition annealing. In order to understand the process of phase transition a thin film can be deposited then characterised fully, heat

treated by post deposition annealing and characterised again. This process is then re-peated for multiple temperatures to fully determine the phase transition characteristics of the sample. This method allows a single sample to be made but a full understanding of potential fabrication conditions to be determined.

The annealing process takes place in a controlled environment quartz tube, with an induction wire coils around the outer tube to heat the inside. The quartz tube allows heating up to 1100°C, with temperature control of $\pm$ 1°C. The atmosphere in the tube is controlled by the pump rate and gas in flow rate, where a forming gas constantly flows to ensure no oxidation occurs. The forming gas used in this work consists of hydrogen-argon (90:10 % Ar:H_2) mix that reacts with any oxygen present in the tube before being flushed out the system, as shown in figure 4.10.
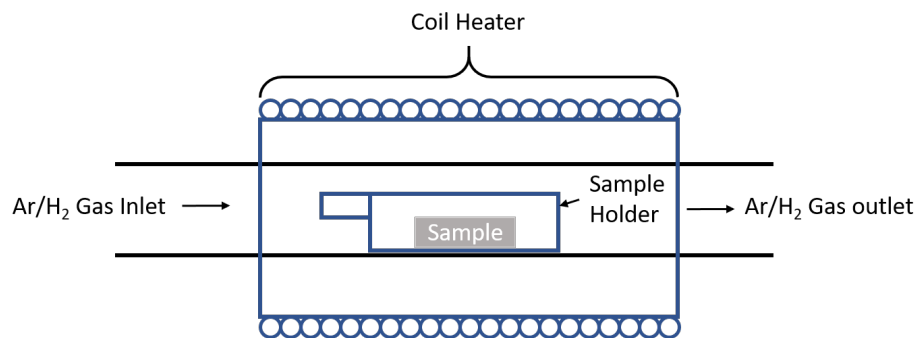
Figure 4.10: Schematic showing a sample loaded in the central position of an induction coil tube furnace.

The complete process for annealing a sample using the tube furnace is:

1. **Insert Tube** - Swap quartz tube to magnetic material tube, ensuring no cross contamination with samples.

2. **Pump Tube** - Pump quartz tube to remove any residual air.

3. **Removal of surface contamination** - Heat quartz tube to 600 °C for 1 hour to remove surface contamination, such as water.

4. **Cooling Cycle** - Allow tube to cool before breaking vacuum and inserting sample.

5. **Gas Removal** - Vent quartz tube with forming gas to ensure no oxygen is present.

6. **Tube Pumping** - Pump tube to lowest achievable vacuum.

7. **Vacuum Improvements** - Repeat steps 5 and 6 until vacuum reaches low 10^{-3} mbar.

8. **Sample Heating** - Heat sample to desired temperature with controlled steps of 5°C per minute.

9. **Annealing Step** - Sample sits at temperature to ensure thermal equilibrium, normally 1-2 hours.

10. **Sample Cooling** - Allow sample to cool to RT before removing it from the tube.

This process ensures a clean tube prior to sample transfer, which helps minimise any forms of contamination during the annealing process. The forming gas flow is set at 0.2 litres/second during the heating/cooling process, which ensures oxidation only happens with the gas and is quickly removed from the tube. Following this procedure allows for controlled heating/cooling of the sample, therefore expanding the possible characterisation conditions per sample and increasing the speed of diagnosis of phase growth for a give material.

4.5 Summary

In order to understand the formation of $L1_0$ ordered thin films the basic principles of the fabrication techniques used in this work were outlined. The characterisation of samples is introduced in the following chapter, where the results form a feedback loop with fabrication techniques described in this chapter to optimise the growth of preferential phases within binary alloy materials MnAl and FePt.

Chapter 5

Characterisation of Thin Films

Several experimental techniques are used throughout this research project for the fabrication and characterisation of magnetic thin films. There is an intimate link between the structural and magnetic properties of thin films, especially alloy materials with a complex phase diagram where composition restricts magnetic properties. Various metastable states may be achieved in thin films under certain conditions, where ordering and disordering are two mechanism under investigations. To form a stable state, one must control the fabrication parameters precisely. However, without a deep understanding of composition and other crystal phase formation it is quite possible to lose desirable properties through phase transitions.

To ensure a consistent composition from the fabrication process a strict verification process is carried out using hard X-ray photoelectron spectroscopy (HAXPES). The parameter space covered for thin film materials is quite large, therefore an investigation of structural properties is performed by X-ray diffraction/reflection (XRD/XRR) with corresponding magnetic properties probed by vibrating sample magnetometry (VSM). In particular cases superconducting quantum interference device (SQUID) magnetometry is used for greater scope in parameter space with higher applied fields and low temperature capabilities. However, as access to this system is more restrictive and the cost running is increase compared to the VSM it is only used for samples that cannot be measured on the VSM due to lower maximum applied field. Table 5.1 gives each characterisation technique used together with insight gained.

Technique	Parameter Insight
X-ray Reflectivity (XRR)	Thickness, roughness, density
X-ray Diffraction (XRD)	Long range crystal ordering
Hard X-ray Photoelectron Spectroscopy (HAXPES)	Composition
Vibrating Sample Magnetometry (VSM)	Magnetic Properties $(H_{max} = 2T, T_{range} = 270 - 900K)$
Super Conducting Quantum Interference Device (SQUID)	Magnetic Properties $(H_{max} = 7T, T_{range} = 2 - 400K)$
Atomic Force Microscopy (AFM)	Surface Roughness

Table 5.1: Characterisation technique and the property of a sample probed, note all measurements are non-destructive.

This research project is primarily based on a detailed understanding of growth dynamics of binary alloys forming crystallographic ordered thin films. The fabrication procedures must be characterised fully to understand the conditions necessary for routinely producing such complex phases in thin film binary alloys. There are a number of key parameters that inform the growth of these alloys, each aiding the improvement of the structure for future work; (i) Film structure relating the thickness, density and roughness, (ii) overall composition of the film and (iii) the magnetic and electrical properties of the ordered films. These parameters and the experimental technique utilised are highlighted in table 5.1, where each technique proves vital to furthering the knowledge base of such films.

The techniques used within this thesis for characterising films are covered in detail in this chapter. Alternative techniques where possible have their pros and cons considered, where the reasoning for final technique choice is explained.

5.1 Composition

Binary alloys have unique magnetic properties that are present only in particular phases, where the phase is determined by the composition and temperature treatment for metastable phase formation. Gaining insight into alloy phase transitions is vital to the work covered in this thesis. A prime example of how composition can change a materials properties is in the steel industry where vast differences in properties are seen for minimal

changes in composition. Although steel (a Fe C alloy) is a complex structure made of multiple elements an understanding of how phase growth plays an important role can be learnt from this industry. Composition manipulation of binary alloys can produce vastly different properties using a single system, where co-sputtering first described in section 4.2 allows accurate manipulation by varying sputtering power.

Selecting the correct analysis technique requires a thorough understanding of the relative merits of the various techniques. An extremely accurate measure of composition is inductively coupled plasma (ICP), with the alternative being analysis of elemental X-ray's. Table 5.2 highlights properties related to ICP and X-ray analysis:

Property	Inductively Coupled Plasma (ICP)	X-ray Analysis
Sample treatment	Sample destroyed	Non-destructive
Limit of detection	parts per billion	parts per million
Calibration	Daily	Monthly
Measurement times	$<10s$	300-1000s
Multi-element Analysis	Yes	Yes

Table 5.2: Comparison of measurement techniques ICP and X-ray for thin film composition analysis [155].

Although ICP has outstanding limits of detection it is not efficiently setup for thin film analysis. In order to achieve sufficient mass for accurate detection of composition using ICP, a sample thickness of several 100's of nm is required. The fabrication procedure for 100's of nm increases the chances of contamination as the deposition times must be increased. The films deposited in this work typically have a growth rate of 0.02 nm/s, so realising a sufficiently thick film takes many hours and is a highly inefficient use of the sputter target. This also raises other issues, where long deposition times heat the target material and the rate of deposition begins to change and inconsistencies arise. As the material under investigation is an alloy it is not guaranteed that both elements will vary in the same manner with temperature, so as the target materials heat and their deposition rate changes it is not guaranteed that the composition analysis will still be valid. This is consistent both for alloy target deposition and co-deposition as in both cases three is no guarantee that both elements will remain consistent. However, co-deposition adds varying temperatures of each target which complicates the problem further. Alternatively, measuring the energy of X-rays produced by inner shell

electrons can give an accurate measure of composition through energy dispersive X-ray (EDX) analysis. However, this technique has a large penetration depth and does not produce accurate results, as covered in the following section. Alternatively X-ray photoelectron spectroscopy (XPS) uses X-rays to remove electrons from atoms and measures composition from their energy, covered in more detail in section 5.1.2. However, this technique is very surface sensitive due to the lack of penetration of the X-rays into the film. The use of capping layers only exasperates the problem. To overcome the issue of penetration the energy can be increased, where hard X-ray photoelectron spectroscopy (HAXPES) uses a much higher energy described further in section 5.1.2 to penetrate deep into a sample and give an accurate measure of composition.

5.1.1　Energy Dispersive X-ray

Scanning electron microscopes (SEM) are commonly found in laboratories around the world, where they're routinely used for surface imaging, but these systems can be equipped with X-ray detectors that capture element spectra given off during imaging process. The source electron beam interacts with core electrons of atoms, where the high energy electrons pass energy to core electrons causing them to be ejected from the atom [156], as shown in figure 5.1. The electron gap left behind is then filled by a higher energy electron, where the energy difference between the high and low state is emitted as an X-ray [156]. The emitted X-ray is used to analyse the elements present in the system as there is a specific link between electron orbitals of every element, where the energy of the X-ray is analysed to determine the element that produced it.
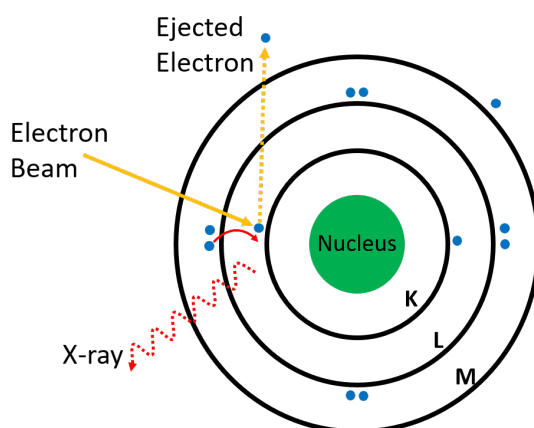
Figure 5.1: Generation of X-rays by the bombardment of high energy electron beam with shell electrons of an atom, giving rise to a high energy electron and allowing a high level electron to fall to a lower energy level.

The penetration depth of the incident electron beam, typically $>\mu$m, exceeds standard thicknesses normally used for thin films, <100 nm [157]. This penetration depth makes it a relatively inaccurate measure for thinner samples as the signal from the deposited film is swamped by the background from the substrate. To improve this measurement the energy of the incident electrons can be reduced along with the use of calibration samples of similar thickness. This will improve the overall accuracy of the measurement but will not significantly improve the signal received compared to the background, therefore if peaks of interest are close to background peaks then they become unresolvable. For this reason SEM analysis of composition has been used as a quick confirmation throughout the research project but the finer detail was not taken into account as an accuracy of approximately 5-10 at.% falls outside a useful range.

5.1.2 Hard X-ray Photoelectron Spectroscopy

Hard X-ray photoelectron spectroscopy (HAXPES) is a non-destructive measurement of composition that works in the reverse order to EDX described in section 5.1.1. Rather than measuring the X-ray produced by inner shell electrons, a high energy monochromatic X-ray source is used to remove electrons from their atomic shells. The kinetic energy of the electron is measured to give a spectrum indicative of the elements present within the sample made possible by the following relation [158]:

$$hv = E_K + E_B + \phi \tag{5.1}$$

where hv is the energy of the incident X-ray, E_K and E_B are the kinetic and binding energy of the electron respectively and ϕ is the work function of the specimen. A normal XPS system has an X-ray source energy of roughly 1.5 keV by using sources such as Mn [159]. However the system used for this research is a state of the art liquid gallium source which produces 9.25 keV X-rays. This increased energy not only increases the range of elements that the instrument can measure, as it can eject higher binding energies, but also increases the penetration depth of the electrons, as shown in figure 5.2.
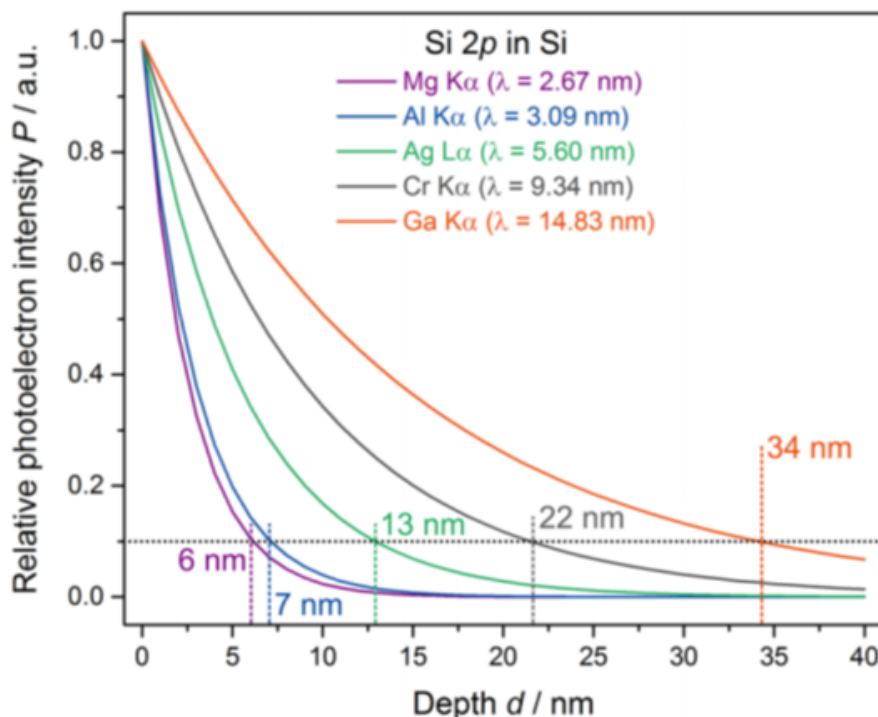
Figure 5.2: Various penetration depths for XPS sources on the 2p orbital of Silicon [159].

The capping layer for most samples made in this project is roughly 5 to 10 nm, this ensures that no oxidation of films under investigation occurs. Figure 5.2 demonstrates that only the Cr and Ga sources could penetrate those capping layers effectively. Therefore, when considering the source material to use one must consider the sample under investigation, as the example given is for Si but the penetration depth for other elements will be different [159]. Therefore, this work must utilise the high energy Ga source as it can penetrate the desired layer and capping layer sufficiently. The increased energy of the liquid Ga source means that thicker samples can be measured routinely, with the ability to resolve stacked structures as well [159]. The HAXPES system works under ultra-high vacuum conditions, roughly 10^{-10} Torr, see table 4.1, which allows accurate measure of electrons in this system. The resolution of the monochromator is $<0.5eV$ with the energy analyser resolution at peak energy being $\delta E < 100 meV$ making this system highly efficient at detecting differences in chemical states [159].

This system is vital in the work on MnAl, where composition plays a key role in obtaining the desired magnetic properties. Example spectra from HAXPES measurements are given in chapter 7, where the composition of MnAl layers is measured.

5.2 Magnetic Properties

The materials under investigation in this work are proposed for future magnetic storage devices. Therefore, the characterisation of magnetic properties is essential to their success. There are two main systems used in this work to measure a materials magnetic properties; (1) a vibrating sample magnetometer (VSM) and (2) a superconducting quantum interference device (SQUID). The functionality of these two systems is covered in the following sections, where the reasoning for using one over the other is explained.

5.2.1 Vibrating Sample Magnetometry

The vibrating sample magnetometer measures the magnetic moment of materials by using flux changes in a coil of wire when exposed to the magnetic field of the sample vibrating in close proximity. The sample used is commonly a small disc attached to a non-magnetic rod (made of quartz), where the opposing end is fixed to a 'loudspeaker' that vibrates at a known frequency, typically 75 Hz. As the sample vibrates it induces an alternating emf in the detection coils (U_{ind}), where the magnitude of the signal is proportional to the magnetic moment of the sample, given by equation 5.2 [34].

$$emf = \frac{d\Phi}{dt} = U_{ind}(t) \propto -\frac{m\omega n_w n_c G cos(\omega t)}{y_0} \tag{5.2}$$

where the flux change U_{ind} is proportional to the number of detection coils n_c that have n_w turns. The samples magnetic moment m is measured by the detection coils at a frequency ω, where G is a geometric factor of the sample that is y_0 distance from the pickup coils.

The measured signal is typically small, on the scale of μV, and so lock-in amplifiers are used to improve the signal to noise ratio. A VSM has the capability of measuring μemu, which corresponds to approximately 10^{-9} g of iron making this a particularly good technique for measuring thin film samples. A schematic of the system is shown in figure 5.3, where the sample is situated between the two pole pieces and vibrates vertically.
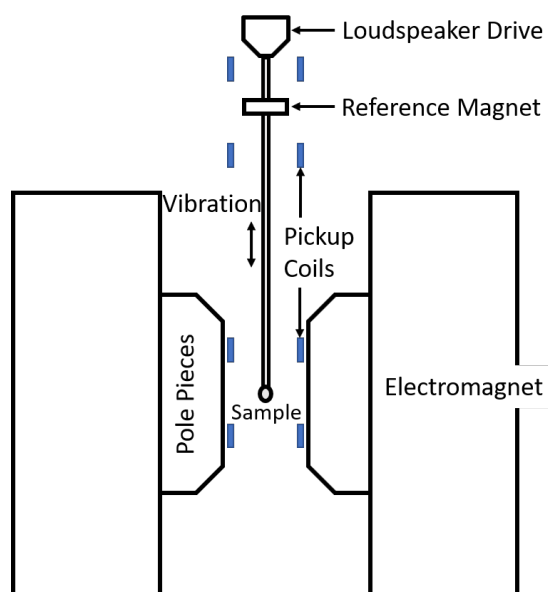
Figure 5.3: Schematic of a VSM where a sample is placed between two pole pieces and centred in pickup coils to measure the induced emf.

The instrument used in this work is a Microsense Model 10 Mark II vector VSM, which is placed upon a rotational stage with movement of -540 to 540 degrees with resolution better than 0.1 degrees. This system is equipped with heating and cooling capabilities, allowing a temperature range from -195 °C to 600 °C. The field range this system can generate using electromagnets is between 20 kOe and 22 kOe, dependent on the pole pieces fitted.

The normal measurement procedure is to measure two applied field angles; (i) field applied parallel to the samples surface and (ii) field applied perpendicular to the samples surface. The samples for measuring are cut to an 8 mm disc to match the calibration sample size for optimum accuracy. The calibration sample is a nickel disc, with moment of 6.39 emu. Prior to measurements the calibration sample is used to align the coil angles and to set the detection coil sensitivity, where calibration can correct slightly for off-centre alignment of the quartz rod. Calibration is complete when the measured emf is set for the known magnetic properties of the nickel disc, giving a measure of emu/V. The sample is then loaded and a recipe file started which loads field range, step size, time per measurement and number of repeat measurements per field step.

The principal measurements employed in this work is the hysteresis loop, see section 2.3.3 for its introduction, where moment as a function of applied field at a fixed temperature is determined. Measurements of d.c. demagnetising remanence curves (DCD curves) have also been done for particular samples and are explained when the data are introduced in section 6.2.2.

5.2.2 Superconducting Quantum Interference Device

The superconducting quantum interference device (SQUID) consists of two superconductors separated by a thin insulating layer, called a Josephson junction. A current flows between the two superconducting materials so that it is equal on both sides of the insulator, this is known as the measuring current. A changing magnetic flux through the ring, as shown in figure 5.4, generates a voltage and current that is measurable according to Faraday's law. The induced current adds to the measuring current in one junction and subtracts from the other [34].
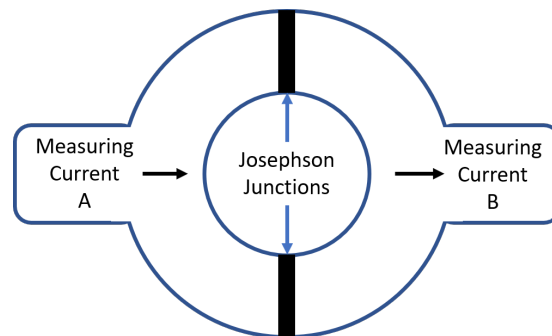
Figure 5.4: SQUID flux sensor made up of a Josephson junctions with a measuring current A and B in the two superconducting materials.

The wave nature of superconducting currents and the variation between point A and B due to the magnetic signal induces a voltage. The voltage step corresponds to the passage of a single flux quantum across the boundary of the ring. Incorporating a SQUID sensor into a magnetometer allows higher sensitivity measurements to be made, where moments as low as 10^{-8} emu can be detected. In this project SQUID magnetometry measurements were undertaken using a Quantum Design MPMS 3 [160] instrument where the maximum applied field is 7 T (70 kOe) and a temperature range of 2 - 400 K (-271.15 to 126.85°C) is available. However, the measurement times are longer than the VSM and thus the technique is only used where VSM measurements do not cover the full parameter range needed.

5.3 Structural Characterisation

Determining the structure of the films is a key step in understanding their magnetic be-
haviour. The various techniques used for characterisation were outline in table 5.1. A
physical representation of the surface of a film is gained from atomic force microscopy
(AFM), which is then used in collaboration with X-ray reflectivity (XRR) to fully char-
acterise the structure of the film. The structure is defined as the films thickness, density
and roughness, where additional measurements are carried out using X-ray diffraction
(XRD) to give the crystal phases present. The combination of these three measure-
ments gives an in-depth understanding of the sample structure, which can then be fed
back to the fabrication procedure for optimisation.

5.3.1 Atomic Force Microscopy

Scanning probe microscopy (SPM), or atomic force microscopy (AFM), physically
measures the surface of a film with nanometre accuracy. This technique uses a probe
in close proximity to the surface, as shown in figure 5.5, where a force dependent on
the sample surface deflects the cantilever [161]. A laser beam is reflected from the back
surface of the cantilever, where deflections from the origin are measured using a pho-
todetector. These small deviations from the centre point allow an accurate measure of
surface interactions [146, 161]. This information is used by a feedback loop to map the
topological features on the surface of the samples, where an image is formed by either
maintaining constant force or constant oscillation amplitude during scanning [146].
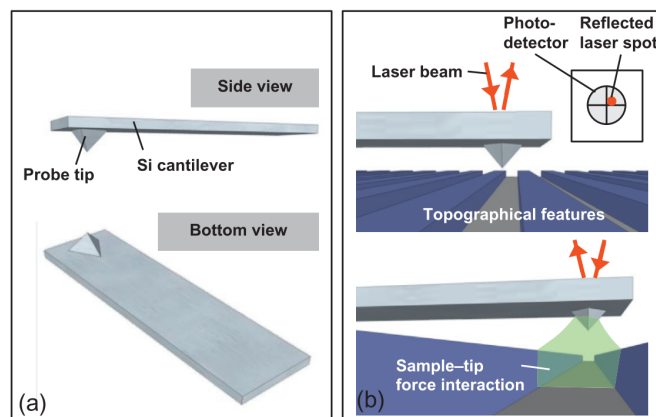
Figure 5.5: (a) SPM probe tip carried by Si cantilever, (b)
sample-to-tip force interactions and the photodetector detec-
tion process [146].

There are two main modes of imaging used in AFM, contact mode and tapping mode. The contact mode keeps the tip in close contact with the surface and was the first mode developed [162]. However, the force can damage the fragile tip and/or the sample. Tapping mode allows high resolution topographic imaging of sample surfaces that are easily damaged. The tapping mode overcomes problems associated with friction, adhesion, electrostatic forces and other difficulties by tapping the surface to obtain surface information [146, 161].

The use of AFM for sample analysis is limited in this work to physical representation of sample surfaces, where X-ray reflectivity analysis covered in section 5.3.3 can use this technique to solve problematic sample surface roughness fits by substituting their physical values.

5.3.2 X-ray Scattering

X-rays are electromagnetic waves with wavelengths in the region of 0.01 to 10 nm and can therefore be used to probe atomic layer spacings. Additionally the high penetrative ability of X-rays, resulting from weak electromagnetic coupling to orbital electrons, makes them a natural choice for crystallography. Two main X-ray scattering techniques are used in this work, XRD and XRR, which investigate the crystallographic structure of films as well as their roughness, density and thickness.

5.3.2.1 X-ray Diffraction

The basics of diffraction can be briefly explained by considering a single plane of atoms, represented in figure 5.6 by a line with dots at regular spacing a. If a beam of X-rays is directed at this surface under an angle θ then part of the radiation will be reflected by the top plane, with other parts penetrating this layer to be reflected by all underlying planes. Considering the simple case of two wave reflected as shown in figure 5.6, wave 1 is incident on the first plane at point O with an incidence angle θ and wave 2 undergoes the sample process at point O', where part of the intensity is reflected at an angle θ. The waves 1' and 2' leave the crystal and travel in the same direction towards an observer. Since the wavelength of the two waves is the same they will interfere with each other, where the interference will depend on the phase difference between the two waves.
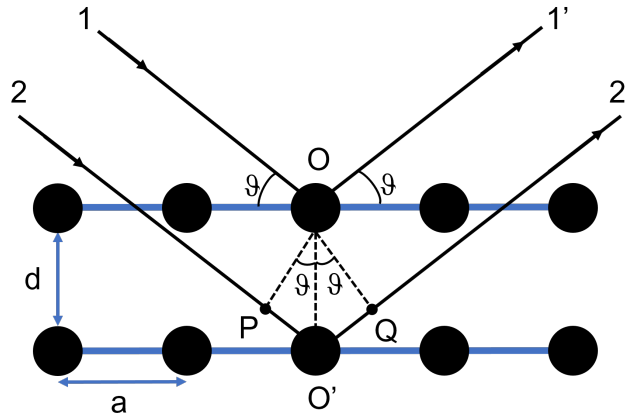
Figure 5.6: Schematic diagram of an X-ray interactions at the boundaries of a layered structure.

The phase difference is derived from the path difference of the two waves, where wave 2 has clearly travelled further through the crystal than wave 1. The path difference is equal to the sum of the distances PO' and O'Q, where constructive interference will only occur if the path difference equals a multiple of the wavelength λ. The following equation therefore described constructive interference for the waves:

$$PO' + O'Q = n\lambda \qquad (5.3)$$

$$OO'(sin\theta + sin\theta) = n\lambda \qquad (5.4)$$

The fundamental equation for diffraction is known as the Bragg equation, after W. L. Bragg who first derived it in 1912 [30, 163]. To obtain the equation the inter-planar spacing d is substituted into equation 5.4 to form:

$$2dsin\theta = n\lambda \qquad (5.5)$$

The integer n defines the order of the diffraction process, where in general only first order (n=1) reflections are considered in XRD [30]. The spacing between parallel planes of a crystal is represented by d, where these crystal planes are known as Miller planes and are characterised by Miller indices (hkl). These indices describe a reciprocal lattice of points which is a spatial Fourier transform of the crystal lattice [30]. Points in this reciprocal lattice are given by:

$$g = ha^* + kb^* + lc^* \tag{5.6}$$

where the length of a reciprocal lattice vector is equal to the inverse of the interplanar spacing of lattice planes (hkl), given by:

$$|g_{hkl}| = \frac{2\pi}{d_{hkl}} \tag{5.7}$$

The basic structure of a unit cell is shown in figure 5.7, where the lattice constants are a,b and c with corresponding angles α, β and γ. The Miller planes are the surfaces that act as a mirror for constructive interference to take place and therefore play an important role in relating the wavelength of X-rays and the angle for constructive inference to the lattice spacing of a unit cell.

Figure 5.7: Schematic of a unit cell showing the lattice constants a,b and c along with their angles α, β and γ.

To find the lattice spacing for different unit cells the relationship of equation 5.7 is used, where for a face centred cubic (FCC) $\alpha = \beta = \gamma = 90°$, with other examples are shown in table 5.3, in the FCC case the equation becomes:

$$\frac{1}{d_{hkl}^2} = \frac{h^2 + k^2 + l^2}{a^2} \tag{5.8}$$

Incorporating equation 5.8 into Bragg's equations 5.5 allows the lattice spacing of a unit cell to be measured, shown in equation 5.9, by taking the diffraction peak angle θ and relating this to the corresponding plane (hkl) of diffraction, where the X-ray source has a known wavelength.

$$a = \sqrt{\frac{\lambda^2}{4sin^2\theta}(h^2 + k^2 + l^2)} \tag{5.9}$$

The alternative expressions for $\frac{1}{d}$ are given for other unit cell configuration in table 5.3.

System	$\frac{1}{d}$ Expression
Cubic	$\sqrt{\frac{h^2+k^2+l^2}{a^2}}$
Tetragonal	$\sqrt{\frac{h^2+k^2}{a^2} + \frac{l^2}{c^2}}$
Orthorhombic	$\sqrt{\frac{h^2}{a^2} + \frac{k^2}{b^2} + \frac{l^2}{c^2}}$
Hexagonal	$\frac{4}{3a^2}(h^2+k^2+hk) + \frac{l^2}{c^2}$

Table 5.3: Example crystal systems and the lattice spacing length relation to unit cell parameters [30].

A Rigaku Smartlab X-ray diffractometer is utilised for X-ray diffraction (XRD) and reflectivity (XRR) measurements. This system is equipped with a sealed Cu X-ray tube source operating at a nominal 3 kW, and typical parameters used for measurements are 45 kV and 40-50 mA [164]. This source produces X-rays at the $K_{\alpha1}$, $K_{\alpha2}$ and K_{β} wavelength of Cu, corresponding to wavelengths 1.544, 1.541 and 1.392 Å respectively [164]. A monochromatic source is needed for measurements as there is an angular separation between $K_{\alpha1}$ and $K_{\alpha2}$, which gives twin peaks for highly ordered structures. To achieve a monochromatic source of X-rays a narrow band monochromator is used, which distinguishes between the different wavelengths to improve the resolution of measurements [164]. The monochromator operates under Bragg's law by constructively interfering the desired X-ray source and destructively interfering any other sources. In this system Germanium crystal is used as the monochromator, which allows only $K_{\alpha1}$ X-rays to pass, thus producing a monochromatic source of X-rays. There are two crystals present in the systems monochromator, which act as a periscope to preserve the original direction of the beam [164].

A sample is placed on a low noise plate to reduce the background signal for room temperature measurements, the plate is a slab of silicon cut along the (531) plane where the cut ensures minimal signal from the Si plate during measurements. In order

to undertake XRD measurement as a function of temperature an Anton Paar heating stage equipped with either a graphite or PEEK dome allows in-situ heating, within the temperatures ranges of RT to 1100°C and 350°C respectively [164]. As temperature dependent XRD is an important measurement for the work of this project, the finer details of the heated stage are covered in more detail later in this section. A 1D detector capable of operating in both 1D and 0D modes is used to collect the data with 256 strip lines allowing a broad range of measurements without the need to change system components [164].

The axes of movement for the Rigaku system are shown in figure 5.8, where standard measurements only move ω and 2θ but the capability to rotate and probe in-plane are also available.
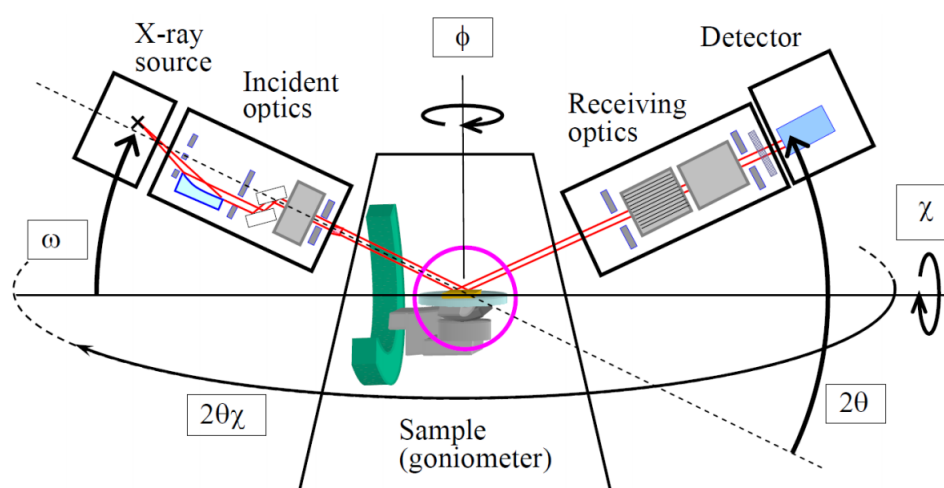
Figure 5.8: Schematic of the five degrees of movement for Rigaku Smartlab diffractometer [165].

The multiple axis of rotation in the Rigaku system allow in-depth analysis of any sample, as the user can investigate both in/out-of-plane thanks to the movements of the goniometer. The various measurements possible give details of a sample crystallographic structure, grain sizes, strain and thicknesses. As X-rays have a wavelength similar to the lattice spacing (0.01 to 1 nm) they will scatter off the atoms causing interference patterns to form. The scattered wave will either have the same or less energy than the

incident wave, known as either elastic or inelastic respectively. Inelastic scattering produces an incoherent background signal whereas elastic scattering from a crystal will coherently scatter under certain conditions giving constructive interference, which is detected as a peak in intensity compared to the background signals.

5.3.2.2   Long Range crystal ordering

Long range ordering in $L1_0$ materials was introduced in section 3.1, but its determination is related to the ratio of the integrated intensity of superlattice and fundamental peaks (001) and (002), respectively [11]. These two planes are shown in figure 5.9 for an example $L1_0$ ordered material. The equation used for calculating the long range ordering, also known as order parameter (S) is:
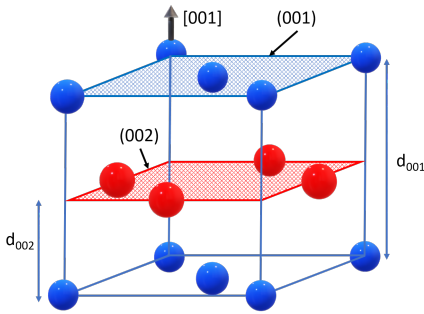
Figure 5.9: Face centered tetragonal lattice corresponding to the $L1_0$ phase with (002) and (001) superlattice planes shown.

$$S = \left(\frac{I^*_{002}}{I^*_{001}} \frac{I_{001}}{I_{002}} \right)^{\frac{1}{2}} = constant \times \left(\frac{I_{001}}{I_{002}} \right)^{\frac{1}{2}}$$

(5.10)

where I^* is a theoretical value for the integrated intensity of peaks and I is the measured integrated intensity from XRD. The theoretical value incorporates the samples thickness as well as composition in order to give an accurate measure of ordering [11, 166], where a fully ordered structure has an order parameter $S = 1$.

The equation given above is a simplified version, where the calculation of the constant is given by the factors F, L, P, D and A defined in equations 5.12 to 5.16. The example given is for $L1_0$ FePt at 50:50 at.% but the same methodology applies to other $L1_0$ alloys:

$$\frac{I^*_{002}}{I^*_{001}} = \frac{(|F|^2 \times LPDA)_{002}}{(|F|^2 \times LPDA)_{001}}$$

(5.11)

In order to calculate the order parameter for $L1_0$ ordered films each contributing factor from equation 5.11 must be calculated. These values are sample dependent and must

be calculated each time, where sample thickness and composition play a role. The equations used for calculating these values is given below:

F is the quantity describing scattering from a complete unit cell, known as the structure or Debye Waller factor and given by [30]:

$$F_{hkl} = \sum_{N}^{j=1} f_j(\vec{K}) e^{2\pi i (hx_j + ky_j + lz_j)} \tag{5.12}$$

where $\vec{K}$ is the atomic form factor [30]. Equation 5.12 for the materials considered in this work (FePt) becomes [86]:

$$F_{hkl} = f_{Fe}(1 + e^{\pi i(h+k)}) + f_{Pt}(e^{\pi i(k+l)} + e^{\pi i(h+l)}) \tag{5.13}$$

where f_{Fe} and f_{Pt} are the atomic scattering factors of Fe and Pt.

L and P combine to form the Lorentz polarisation factor, representing different scattering by unpolarised X-ray beam [30]:

$$LP = \frac{1 + cos^2(2\theta)}{sin^2(\theta)cos(\theta)} \tag{5.14}$$

D is the temperature factor and represents the fact that atoms in a crystal are not rigidly attached to their lattice sites, where the amplitude in their motion is determined by the available energy. The attenuation factor due to this effect is written as [30, 86]:

$$e^{-2M} \text{ where } M = sin((\theta)/\lambda)^2 \tag{5.15}$$

A is the absorption factor and corrects for the intensity partially absorbed by the material the X-rays are travelling through [30, 86]. The absorption factor is an angular dependent function given by:

$$A = 1 - exp\left(\frac{-2\mu t}{sin\theta}\right) \tag{5.16}$$

where t is the thickness of the film, θ is the Bragg diffraction angle and μ is the average

mass absorption coefficient, calculated as:

$$\mu = [\mu_{Fe} \times wt\%Fe + \mu_{Pt} \times wt\%Pt] \times [\chi_{Fe}\rho_{Fe} + \chi_{Pt}\rho_{Pt}] \tag{5.17}$$

where χ_{Fe} and χ_{Pt} are the atomic fractions of Fe and Pt in the sample, ρ is the density and the values of μ_{Fe} and μ_{Pt} are tabulated [86].

The combinations of equations 5.13 to 5.17 give the order parameter equation [86, 167, 168], which for 10nm FePt film with 50:50 composition is:

$$S \cong 0.493 \left(\frac{I_{001}}{I_{002}}\right)^{1/2} \tag{5.18}$$

The equation is vital in analysing crystallographic order of an $L1_0$ ordered structure, where it can be used to determine the degree of ordering within the structure of the desired crystal phase. This is often used as a measure of film quality in literature, where anything below S=0.5 is defined as a poorly formed structure, and anything about S=0.7 is a well defined crystal structure. However, other aspects such as the roughness and magnetic properties of films also play a role in defining the quality of the thin films.

5.3.2.3 In-Situ Heating and XRD

The Rigaku smartlab system allows the stage to be changed from a standard low noise plate holder to a heated or cooling stage. These stages encapsulate the sample in a dome made of PEEK or Graphite, where the pressure within the dome is pumped to low $\times 10^{-3}$ mbar in order to limit contamination and oxidation. Samples are held in place by Inconel arms in order to achieve the best possible thermal contact from a silicon carbide plate. An image of the stage is shown with and without the dome in figure 5.10a. The cooling of the dome is performed by a airflow from above, as shown in figure 5.10b, where the tube holes allow use of the PEEK dome above its melting point to a maximum temperature of 900 °C.
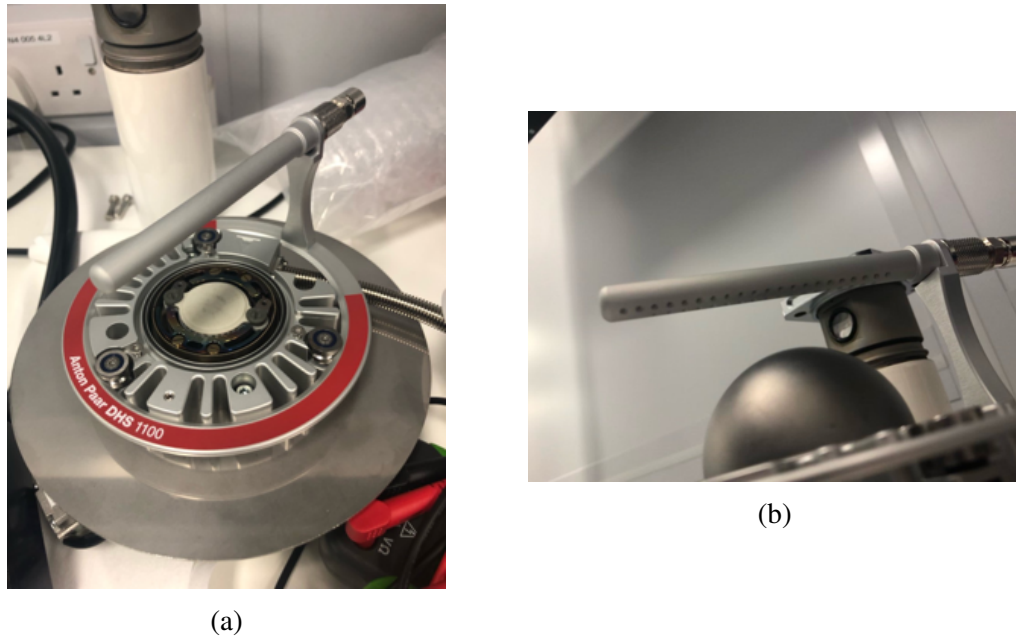
Figure 5.10: (a) XRD heating stage capable of temperatures up to 1100°C and (b) cooling nozzle over the dome ensuring any heating of the dome is kept to a minimum.

The heated stage plays a vital role in analysing phase formation with temperature, where due to the vacuum within the dome thermal contact between the stage and substrate can be difficult. The temperature of the stage is given by the Rigaku system, which can be compared to the substrate temperature. In order to measure the temperature of the substrate its XRD peaks are used, where peak position is measured at room temperature and then each corresponding temperature set-point. The XRD peak angle for the substrate is converted to its lattice constant using equation 5.9 defined in section 5.3.2.1. The change in lattice constant is used to estimate the temperature of the substrate, where the substrates thermal expansion coefficient converts lattice constant change to temperature.

The example of temperature set-point and substrate temperature for an MgO substrate is given in figure 5.11, where the thermal expansion coefficient for MgO substrates varies between 9 and 11 x10^{-6}/K [134, 135]. This variation makes precise measurement of the temperature difficult, where in this work an approximation for thermal expansion coefficient for the lattice constant of 9.9 x10^{-6}/K is used. The corresponding temperature calculation shown in figure 5.11 indicate good thermal contact between the substrate and stage as the temperatures increase consistently together.
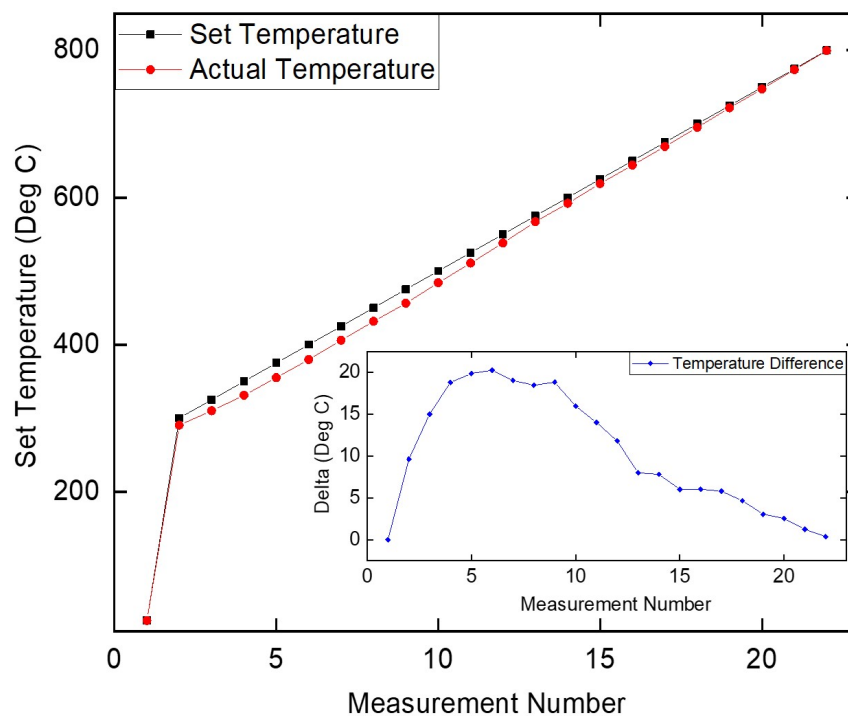
Figure 5.11: Temperature set point compared to the substrate calibrated temperature, each measurement took $\approx$ 4hours.

The standard arrangement of the Anton Paar DHS 1100 limits the use of the PEEK dome to 350°C and Graphite to 1100°C. However an upgraded cooling nozzle allows the PEEK dome to be used to 900°C. Therefore the choice of dome is based on parasitic interference due to diffraction from the dome, where the background signal from both the PEEK and Graphite dome for a Si/SiO$_2$ (290 nm) substrate is shown in figure 5.12.
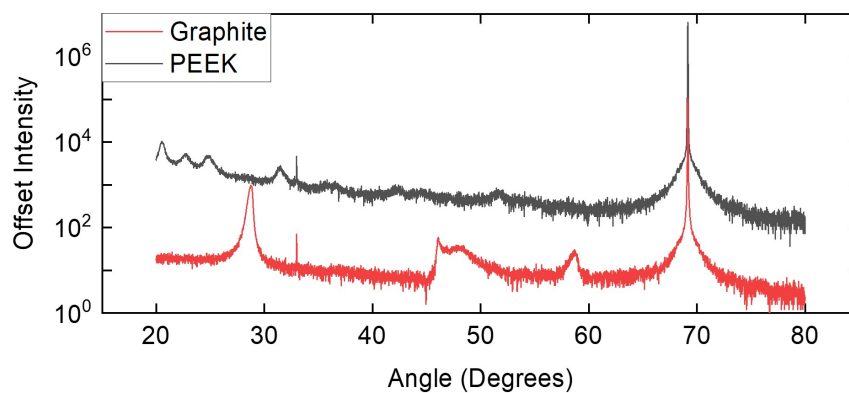
Figure 5.12: Heating stage background signal for both the Graphite and PEEK dome.

The choice between the two domes depends on where the sample peaks are expected, where the regions 20°- 26°, 30°- 32°, 34.6°- 37°, 41°- 46°, 50.5°- 53° are affected by the PEEK dome and the regions 26.5°- 30°, 45°- 50°, 57°- 60° are affected by the graphite dome. The background signal in these regions is higher, and therefore smaller peaks falling within them could be missed. Therefore, when comparing the two dome choices one must consider where the peaks of interest will reside and choose accordingly.

5.3.3 X-Ray Reflectivity

The crystal phases of a film are investigated by X-ray diffraction, but further analysis of the structure is achieved through X-ray reflectivity (XRR). Layered structures such as semiconductor heterostructures, metallic multilayers and thin films systems in general are probed by low angle X-ray reflection, where knowledge on structural parameters such as interface roughness, density and thickness are gained. The interactions of X-rays with the material is given by a classical model for an electron interactions with a material, where the complex index of refraction is written as [169]:

$$\eta = 1 - \delta - i\beta \tag{5.19}$$

where δ and β represent the scattering and absorption of the material respectively. The refractive index of X-rays in air is very close to 1 and the material an X-ray propagates into is <1 [170]. If the angle of incidence of the X-ray is sufficiently small then the beam will totally reflect from the materials surface, this is known as total external reflection and occurs for incident angles smaller than some critical angle θ_c. In the absence of attenuation where X-rays are moving from air/vacuum ($\eta = 1$) to a medium with ($\eta = 1 - \delta - \iota\beta$) the critical angle is given as:

$$\theta_c^2 = 2\delta \tag{5.20}$$

The critical angle is able to provide useful information, as it is linked to the density of the film, normally given by number density but can be changed to g/cm^3 by knowing the composition of the film. The dispersion factor δ is given by:

$$\delta = \frac{r_0\lambda^2}{2\pi} \cdot (n_e) \tag{5.21}$$

where r_0 is the classical radius of an electron, λ is the wavelength of the X-rays, and n_e is the electron density given by $n_e = Z \cdot \frac{N_A}{A} \cdot \rho$ where N_A is Avagadros number, A is the atomic weight, Z is the number of electrons per atom and ρ is the density [169]. Therefore, a direct link can be made between the critical angle and the density of the film, this relationship can then be used when analysing new/unknown materials. The density of a single film can approximately be related to the critical angle through $\theta_c = \sqrt{\rho}$, the results of which are shown in figure 5.13 as the high density FePt (15.2 g/cm^3) film has a much larger critical angle than the much lower density Al(2.7g/cm^3).

Simulations of idealised thin film samples has been carried out to help the understanding of an XRR dataset. The main characteristics investigated with this technique are thickness, density and roughness. Therefore these parameters have been simulated in isolation to help understand their effect on the overall shape of the measurement technique.
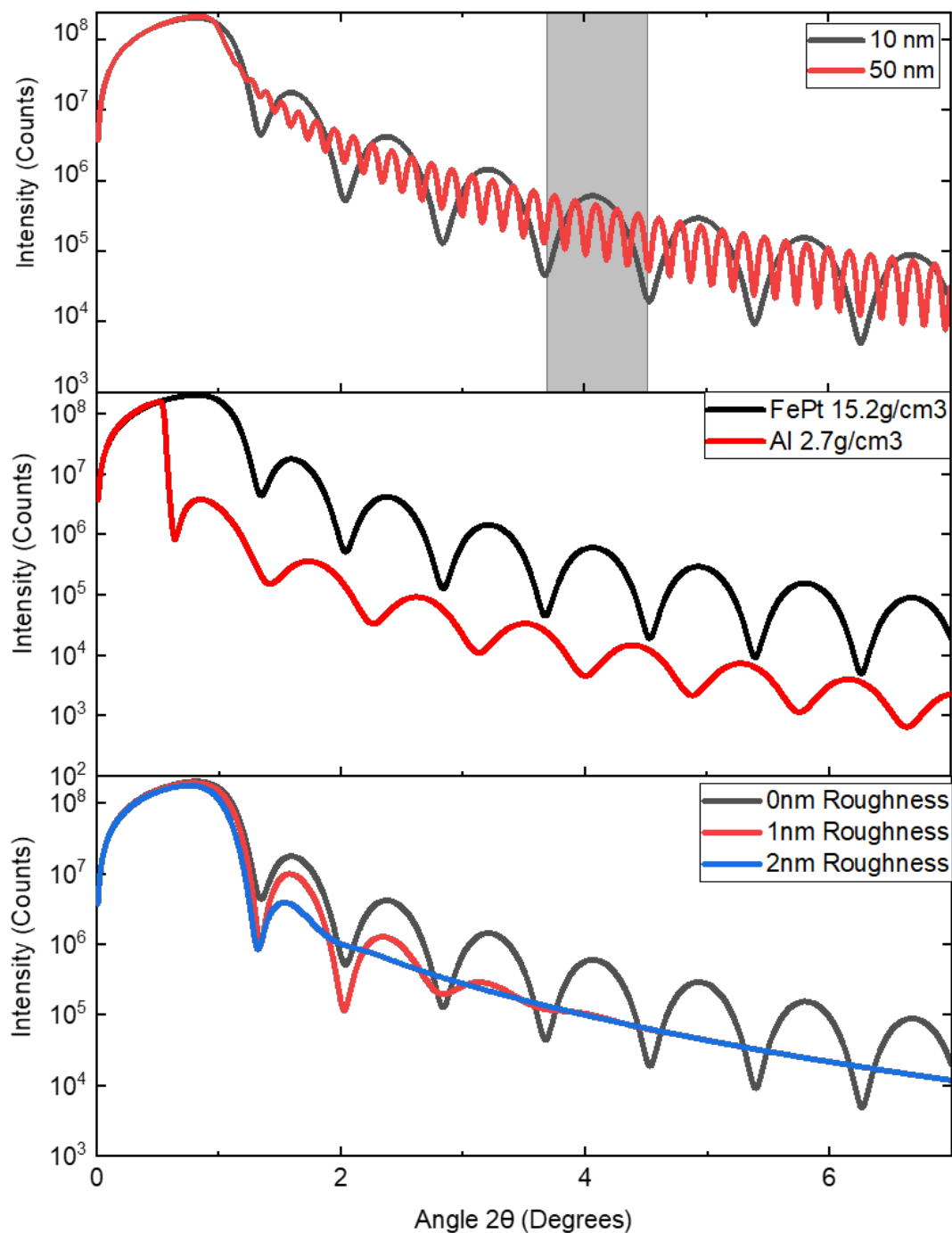
Figure 5.13: Simulations of (a) Thickness fringe for FePt on MgO(001) where shaded region shows 1 to 5 ratio in fringes for 5 times the thickness, (b) critical angle variation with density of film (both on MgO(001)), and (c) surface roughness of a 10 nm FePt film on MgO(001). Simulated using GenX.

The thickness of a film can play a critical role in magnetic multilayer systems, such

as Co/Pd [58], as the ratio between layers is highly linked to magnetic properties. As shown in figure 5.13 (a) the thickness fringes increase with film thickness, where the shaded region shows 1 oscillation for 10 nm FePt and 5 oscillations for 50 nm FePt.

Surface roughness and interfacial roughness play an important role in thin film applications as rough surfaces are not compatible with the growth of a thin continuous film. Roughness at interfaces compromises the desired magnetic properties in multi-layer systems and therefore significant resources are spent optimising film growth to minimise roughness [58]. Figure 5.13 (c) shows the effect that surface roughness has on the XRR measurement, where only 2 nm roughness will completely quench any fringes.

X-ray reflectivity is fundamentally a measure of the reflection from each individual interface through a sample and the refraction caused by variations in density between layers. It has been shown that there is a reflection due to the total reflection at the surface but there is also a contributing factor from the interfaces, where the penetration depth of the X-rays mean the substrate must be treated as an infinite layer [171]. There are many contributing factors that influence the signal received from a sample, but key parameters are the sample size and the smoothness of its surface. The size is important because the X-ray source will provide a consistent flux of X-rays, but when a small sample is measured the beam must be truncated to minimise the signal from surrounding surfaces. Measurement times must then be increased to obtain sufficient signal to noise ratio for higher angle measurements as the intensity begins to drop.

The simulations shown in figure 5.13 are a very simple demonstration of XRR as they only consider one change within an ideal system. An XRR measurement is shown in figure 5.14 for the structure MgO/Pt/FePt/Ta/Ta$_2$O$_5$. Rather than the very periodic structure seen in the previous simulations there is now much a more complicated superposition of fringes due to each individual layers contribution. In order to be able to simulate such a structure, with reasonable confidence, it is important to have an initial set of conditions that are of the same order as the actual structure. It is therefore key to have an idea of the system structure prior to simulations as over complicating the fit can give a 'false' fit to the data, but these false fits normally have non-physical values for one or more parameters.
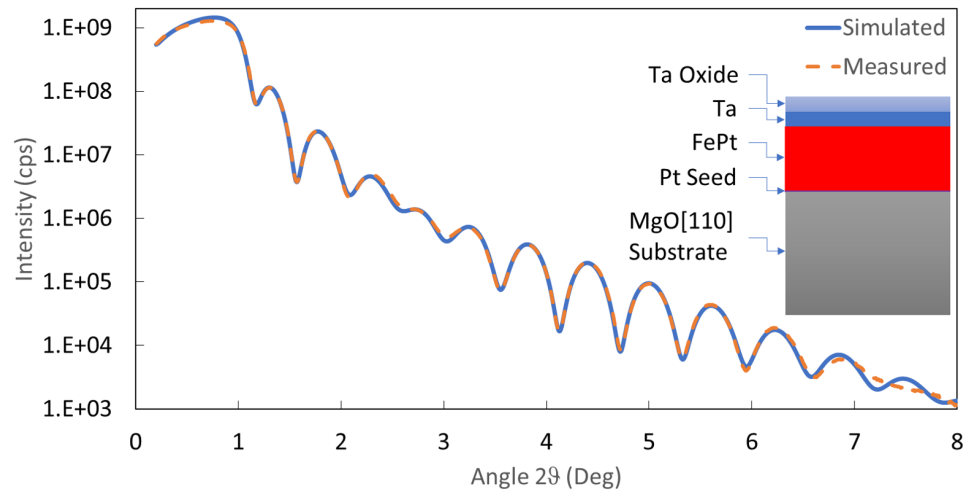
Figure 5.14: X-ray reflectivity for sample structure MgO[110]/Pt(0.3 nm)/FePt(13 nm)/Ta(3 nm)/TaO$_2$(3 nm), figure of merit for fit 0.031.

5.3.3.1 Fitting of X-ray Reflectivity data

Simulations of all XRR data presented in this thesis uses GenX reflectivity software, which fits measured data using a Fresnel model and recursive Parratt algorithm [172, 173]. Data simulation is carried out simultaneously using a differential evolution (DE) algorithm [172]. The type of genetic algorithm gains its name from the comparisons made to biological evolution, where the values converge towards an optimal solution through random mutations and recombinations.

The software optimises its fitting parameters (thickness, roughness and density of layers) by using a log figure of merit (FOM), defined as the average of the absolute difference between the logarithms of the data and simulation [172, 173]. This FOM makes the fitting algorithm sensitive to minima in the reflected intensity, where the beam is probing deeper into the sample stack [172, 173]. GenX provides an estimate of uncertainty by taking a fit that is 5% greater than the optimal FOM value found, however in practice this does not provide a good representation of uncertainty for individual parameters and so it was not used as part of this project. Therefore the value for the FOM is used as a measure of the goodness of the fit, where values of FOM below 0.1 are deemed acceptable [172]. An example of a fitted dataset for the structure MgO[110]/Pt(0.3)/FePt(13)/Ta(3)/Ta2O5(3), where all values are given in nm, is shown in figure 5.14 with the lateral size of the sample 10 x 10 mm. The software fits each individual layers thickness, density, and roughness simultaneously to give the

overall structure values. However, a limit on each fitting parameter must be set as a false minimum may be achieved with overcomplicated structures. This process is refined within limits for each fitting parameter, where the fit is then run again to test for false minima in the FOM.

5.3.3.2   X-ray Diffraction Thickness Fringes

The use of X-ray reflectivity for thickness analysis is well known but additional analysis can be performed on epitaxial films with thickness fringes around an XRD peak. These peaks form because of the variation in path lengths of the X-rays, thus creating constructive and destructive peaks around the well pronounced XRD signal. The thickness of the film can be calculated by taking two neighbouring peaks n_1 and n_2 and using equation 5.22 [174]:

$$t = \frac{(n_1 - n_2)\lambda}{2(sin(\theta_1) - sin(\theta_2))} \tag{5.22}$$

The thickness t is therefore related to peak positions θ and the wavelength of the X-ray λ. For multiple thickness fringes an average can be taken, this gives a detailed measure of thickness for epitaxial films and enhances the X-ray analysis of thin films. An example is given below for FePt on MgO[110], where the XRR fitting produced a layer thickness of 10.2 nm and thickness fringe analysis gave 9.74 nm. The lattice size for FePt is roughly 0.35 nm, therefore around 1 unit cell discrepancy is seen between the two measurement techniques.
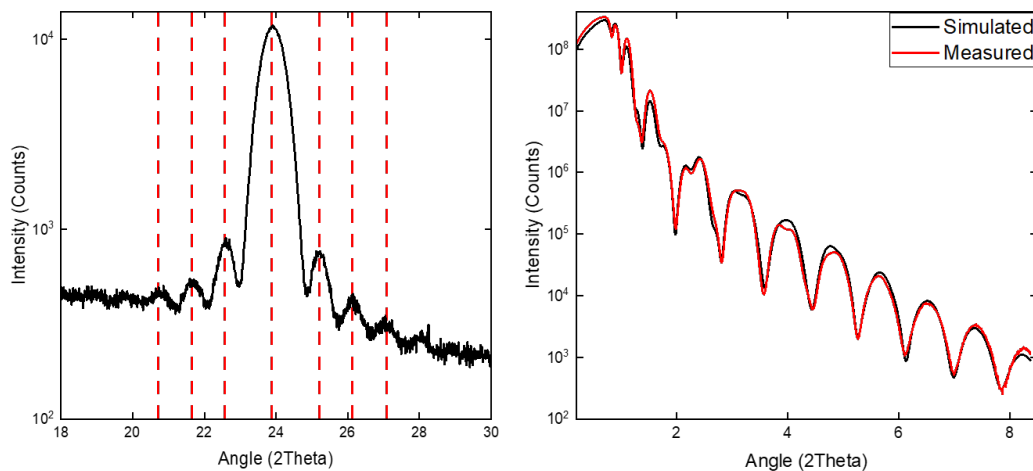
Figure 5.15: (Left) Thickness fringes of FePt (001) XRD peak along with (Right) XRR fitted dataset with figure of merit of 0.06.

It is believed that the differences in values is linked to the initial and final growth of thin films, where there is often strain. Therefore thicknesses measurements by XRD fringes are one to two unit cell length below the measured value by XRR. However, the relatively low variation makes this a valuable method for quick analysis of film thickness and a good sign of epitaxial growth.

5.4 Summary

The techniques used in this work for characterising a magnetic thin film have been discussed in this chapter, with details on specialist approaches given where necessary. The following chapters utilise the results gained from these techniques in order to make interpretations about the properties of the films produced.

Chapter 6

$L1_0$ ordered FePt thin films with uniaxial in-plane anisotropy

Equiatomic Iron Platinum (FePt) in the $L1_0$ phase is a leading contender as the medium for heat assisted magnetic recording (HAMR) [9, 18] and potentially for spintronic applications [17]. The utility of FePt in the $L1_0$ phase is due to its magnetic properties as it has one of highest magnetic anisotropies so far discovered ($7 \text{x} 10^7$ erg/cm^3) together with a significant saturation magnetisation (1140 emu/cm^3) [18]. In addition to HAMR, the very high magnetic anisotropy of FePt could find application in magnetic exchange springs. There are two potential areas of interest in FePt based magnetic exchange springs. Firstly, FePt could act as a pinning layer so that placing a soft magnetic layer such as $Ni_{80}Fe_{20}$ (Permalloy) in intimate contact with FePt would allow a twisted magnetic structure to be created in the permalloy under application of a magnetic field. A second related application is that a similar soft magnetic layer could act a conventional exchange spring system allowing the FePt to switch magnetization direction at a lower field than would be the case for a single FePt layer. In either case the creation and thorough characterization of both single layer and bilayers of FePt and permalloy is essential in order to make progress. This chapter details the deposition together with the structural and magnetic characterisation of FePt and FePt/permalloy bilayer thin films. The work is, in part, motivated by a collaboration with the Hicken group at the University of Exeter where X-ray FMR was proposed as a technique to explore the dynamic properties of strongly pinned magnetic exchange springs with the aim of characterising the spin wave interactions and understand the underlying mechanism of magnetisation switching [175].

A novel aspect of this work is the development of FePt with both the conventional perpendicular magnetic anisotropy (PMA) and an in-plane, uniaxial magnetic anisotropy. The fabrication of perpendicular FePt films has many reports in literature [11, 18–20] to date, using a range of deposition techniques including MBE, evaporation and sputtering [11, 18–20]. FePt with uniaxial, in-plane magnetic anisotropy is a much less mature area of research despite both orientations being reported in the initial literature of ordered FePt thin films [20]. These initial works reported FePt thin films grown by careful MBE deposition. The versatility of sputter deposition is essential if FePt with in-plane uniaxial anisotropy is to be incorporated into magnetic exchange springs for device applications.

The work reported here is ultimately aimed at creating two regimes of magnetic exchange springs, in-plane to in-plane and out-of-plane to in-plane. Firstly, the well established fabrication of single layer $L1_0$ FePt with PMA is briefly summarized. The deposition and characterisation of single layer $L1_0$ FePt with in-plane anisotropy is then described in detail. Finally the fabrication and characterization of a perpendicular FePt/Permalloy magnetic exchange springs are described which could be easily extended to the in-plane system.

6.1 Fabrication of FePt Thin Films with Perpendicular Uniaxial Anisotropy

The fabrication of FePt with strong PMA has been widely reported [11, 18–20], including studies by the University of Manchester (UoM) where the highly ordered $L1_0$ structure is formed for FePt thin films grown on either a MgO (001) substrate or MgO seed layer with the same orientation [4, 21]. These fundamental studies focused on the transition of FePt from a disordered FCC phase into the desired $L1_0$ phase.

The phase transition is controlled by the energy present within the system, with temperature typically the dominant parameter. Temperature can be controlled in two ways, one by setting the substrate temperature during deposition and secondly by post deposition annealing. Figure 6.1 shows a series of XRD spectra for 20 nm thick $Fe_{50}Pt_{50}$ produced by remote plasma sputtering as a function of annealing temperature. These data demonstrate the emergence of $L1_0$ ordering shown by the appearance of FePt (001) and (002) peaks.
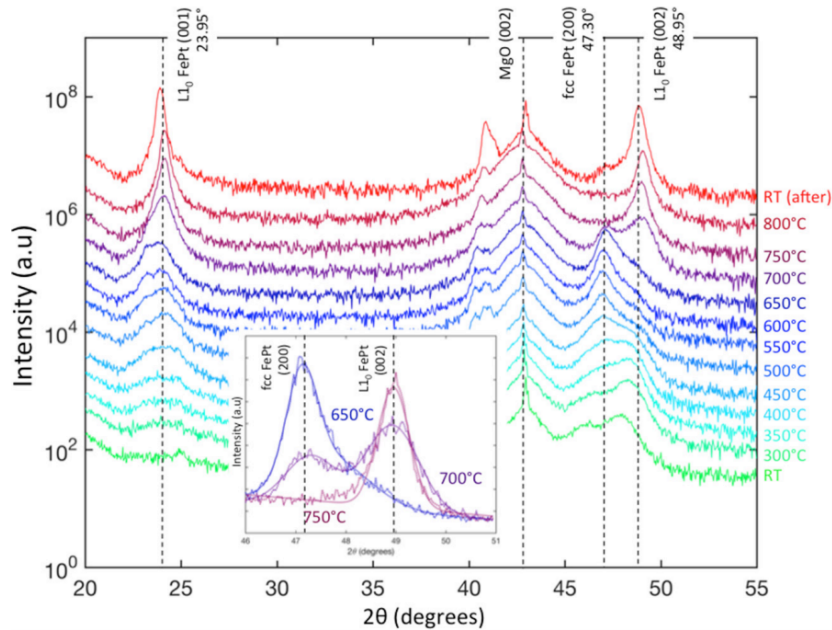
Figure 6.1: Waterfall plot of XRD data obtained by Zygridou et al. [4], showing L1$_0$ ordering of FePt as a function of temperature. The desired L1$_0$ phase emerges at an annealing temperature of 700°C.

The previous work carried out by David Huskisson [21] used both an alternative remote plasma deposition system and the same system used for the work described in chapter 4. Their work determined that working pressures of 3 mTorr produced the lowest roughness for the films, where the power ratio of Fe:FePt targets was investigated and determined to need the co-deposition of Fe and FePt at 60 W and 100 W respectively to produce a 50:50 at.% FePt film needed for L1$_0$ ordered phase formation [21]. However, the deposition and annealing temperatures had to be optimised further to achieve larger percentage of L1$_0$ ordering as much of David's research had limitation of in-situ heating to 300°C.

The work carried out in this thesis focuses on the use of DC magnetron sputtering as it has greater flexibility, where alternatives such as RF sputtering reduce the rate of deposition thus increasing the chance of contamination within the film. The use of DC sputtering is also a preferred method for device manufacturers, thus ensuring the materials usefulness in future devices. In order to achieve uniaxial anisotropy in the system MgO (001) substrates are used, where the lattice matching between the L1$_0$ phase of FePt and the MgO substrate ensures that the desired phase and orientation grows [19]. Lattice matching the substrate can also allow the formation of the L1$_0$ phase at lower

temperatures, which reduces the roughness of the film [17].

The fabrication method for $L1_0$ ordered perpendicular FePt films was achieved by David and Zygridou [4, 21]. The final product is as follows:

1. **MgO Surface Clean** - The surface of the MgO is cleaned of any chemically bonded surface contamination by heating to 800°C for 1 hour.

2. **Cooling** - The sample is allowed to cool to RT over 6 hours under ultra high vacuum conditions ($< 5x10^{-8}$ Torr).

3. **FePt Flash Layer** - A layer of FePt, using 3 mTorr pressure and co deposition of Fe:FePt at 60:100 W, is deposited at room temperature for 20 s to ensure good adhesion to the surface.

4. **Pre-deposition Heating** - Sample is heated to deposition temperature (650°C) and allowed to thermalise for 2 hour.

5. **Deposition FePt** - The Fe & FePt sputtering targets are co-deposited using 3 mTorr Ar pressured at powers 60 W Fe and 100 W FePt for a 50:50 at.% Fe:Pt composition onto the heated substrate, at a deposition rate of 0.14 nm/second.

6. **Cooling** - The sample is allowed to cool to RT for a maximum of 6 hours under ultra high vacuum conditions ($< 5x10^{-8}$ Torr).

7. **Capping** - A capping material (5 nm of Pt or Ta) is applied to ensure no oxidation occurs, this is done at RT to ensure no layer mixing.

6.1.1 Magnetic and structural properties with film thickness

A series of single layer FePt thin films of varying thicknesses from 5 to 30 nm were deposited and characterized both structurally and magnetically. The purpose of this study was to develop a reliable process for creating $L1_0$ FePt thin films with perpendicular anisotropy which can then be incorporated into exchange spring structures.

XRD and SQUID measurements are shown in figure 6.2 and 6.3 respectively for 5, 10, 20 and 30 nm FePt films, where the order parameters are shown in the top right of the XRD measurements using equations given in chapter 3. All parameters of the deposition, with the exception of deposition time for the FePt layer, remained constant; this includes the heating/cooling times and capping layer of 5 nm Pt. A consistent capping layer thickness ensures that oxidation of the FePt film does not occur and heating/cooling consistencies ensure thickness is the only variable.
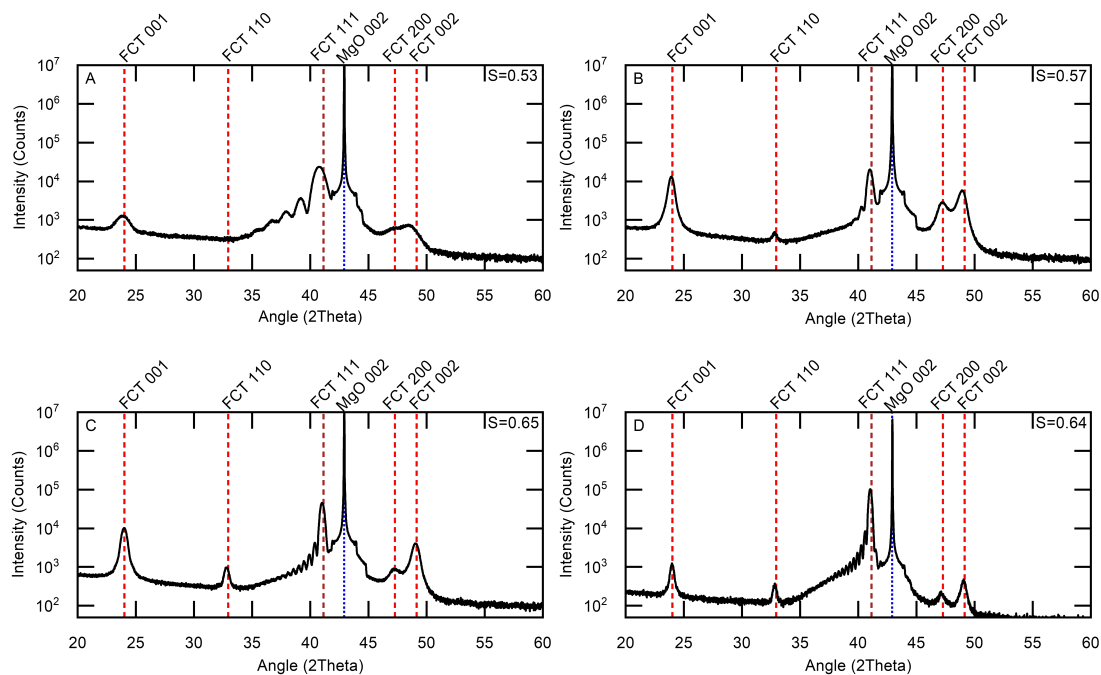
Figure 6.2: XRD for a thickness series of FePt films on MgO [001] single crystal substrates; (A) 5 nm, (B) 10 nm, (C) 20 nm, and (D) 30 nm.

Ordering of the samples is measured by comparing the intensities of the 002 and 001 peaks, as mentioned in chapters 3 and 5. The initial island growth regime for FePt films causes the thinnest (5 nm) sample to produce a low order parameter, where FePt films less than 10 nm tend to not form a uniform film but islands [17]. The samples produce a mixed L1$_0$ growth structure shown by the presence of the 110 and 111 peaks, where the order parameter is comparable to literature values of S = 0.7. However in the 30 nm case the 001 and 002 peak intensities are a lot lower than other thickness, due to the substantial (111) orientation formed within the bulk of the material. The 20 nm sample has the best order parameter from the thicknesses measured and so could play a pivotal role in exchange spring structures. The 10 nm sample is hindered by the

growth of alternative phases (FCC FePt), which can be seen as the bridging between the FCT 200 and 002 peaks. However, the growth of the FCT (111) peak is smaller than all other thicknesses, which indicates that this thicknesses magnetic properties are aligned better than others.
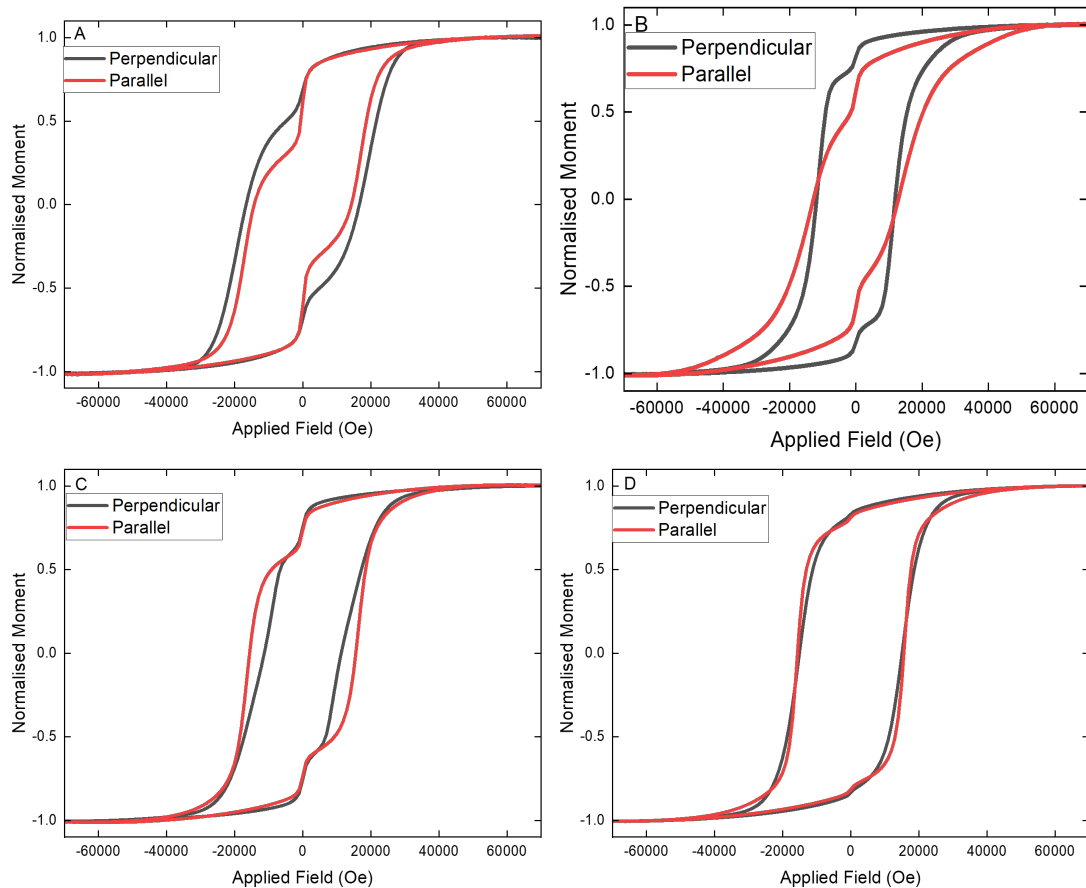
Figure 6.3: Normalised room temperature SQUID measurements for a thickness series of FePt films on MgO [001] single crystal substrates; (A) 5 nm, (B) 10 nm, (C) 20 nm, and (D) 30 nm.

Figure 6.3 shows the normalised hysteresis loops for thicknesses 5 to 30 nm using SQUID. The shapes of the loops are able to give a good indicator of the degree of anisotropy present in each thickness. The M_s values for each thickness are given in table 6.1:

Thickness nm	Parallel Magnetisation (emu/cm^3)	Perpendicular Magnetisation (emu/cm^3)
30	640	835
20	685	1010
10	610	1075
5	975	1040

Table 6.1: Magnetisation saturation with error of $\pm$ 20 emu/cm^3 for series of FePt films of varying thickness, for the normalised hysteresis loops shown in figure 6.3.

The M$_s$ values for perpendicular measurements are close to the expected values (1140 emu/cm^3 [20]), but the parallel applied field values show a large degree of variation, it is unclear why this variation is observed. Given the variability in the data it is assumed that the sample mounting is less precise for parallel measurements. The data in figure 6.3 (B) for the 10 nm FePt film clearly demonstrate that it has the greatest anisotropic behaviour of the thicknesses shown. This material is proposed for use in exchange spring structures where uniaxial alignment is needed, therefore 10 nm is chosen for its magnetic properties.

6.2   Uniaxial In-Plane FePt

In order to create magnetic exchange springs with an in-plane hard layer, it is first necessary to develop a material with a strong uniaxial, in-plane magnetic anisotropy. Such thin films are uncommon as most materials with in-plane anisotropy have cubic anisotropy [34] or the uniaxial anisotropy is relatively weak [176] and unsuitable as a component in an exchange spring. As early work on L1$_0$ ordered FePt [20] demonstrated that it could be grown with both a perpendicular and in-plane uniaxial anisotropy, this material is a natural choice with which to create an in-plane exchange spring system, see section 2.4 for more detail on exchange springs. This is due to the materials large anisotropy energy for in-plane aligned films, thus making them a prime candidate for the strong uniaxial base layer. This is reinforced by the extensive literature which has accumulated on creating FePt thin films with perpendicular anisotropy that provides an understanding of some of the processes involved [4, 11, 17–20].

The production of in-plane uniaxial FePt thin films with $L1_0$ ordering has much less attention and therefore not the same level of development. The fabrication techniques that have produced the best quality films in literature are MBE and evaporation [20, 177–180], where the details of these publications are covered in chapter 3. The fabrication technique most widely used in the manufacturing of devices is magnetron sputtering, where few publications show successful fabrication of FePt with in-plane anisotropy and of those the best case is a canted axis somewhere between perpendicular and in-plane alignment [175], covered in detail in chapter 3.

6.2.1 Deposition of in-plane uniaxial FePt thin films with $L1_0$ ordering

$L1_0$ FePt with perpendicular anisotropy set a requirement of two criteria of the magnetic properties that must be fulfilled for fabrication procedure to be deemed successful. Firstly, the system must exhibit the required ordering and secondly the required orientation. As shown in figure 6.1, ordering is essentially a thermodynamic process where a suitable choice of deposition temperature or post deposition annealing can induce the required $L1_0$ phase providing the film has the correct stoichiometry. The orientation is set by the substrate and/or seed layers on to which the thin film is deposited. Perpendicular anisotropy is induced by depositing FePt directly onto MgO (001) where the lattice matching of the MgO (001) unit cell maps to the FePt. The in-plane aligned FePt thin films follows the trend set by the perpendicular case, where an MgO (110) substrate is used for alignment. However, in the case of in-plane FePt to optimise the ordering achievable a Pt (110) seed layer is used. The Pt seed layer is sufficiently thin that it mimics the orientation of the MgO substrate, the fabrication method for this followed closely that used by Farrow et al. [20] where in-plane $L1_0$ ordered FePt was deposited by MBE.

The fabrication of the Pt (110) seed layer was achieved by reproducing the growth procedure by Farrow et al. [20, 179] but rather than growing a 0.5 - 0.7 nm film it was deposited slightly thicker at 1 nm. The choice to grow the layer slightly thicker is to ensure a uniform film as magnetron sputtering and MBE growth differ, where magnetron sputtering often forms an island growth regime and so care must be taken to ensure the film is complete before depositing the next layer. The final deposition of the seed layer was a 50 W power for 20 s and at 700°C, producing the desired (110) crystal

structure as can be seen later in figure 6.4. This layer not only helps the adhesion of the overall structure but also acts to imprint the (110) structure on the FePt film as shown by the work by Farrow et al. [20, 179].

A series of samples were made using magnetron sputtering to test the growth of L1$_0$ ordered FePt films with in-plane uniaxial anisotropy using magnetron sputtering, where the purpose of the films is for future exchange spring investigation. A Pt (110) seed layer is deposited onto MgO (110) substrates to align the FePt film in-plane. It has been shown before by Farrow et al. [20, 179] that there is a temperature dependence for the formation of in-plane L1$_0$ FePt. Following the findings using MBE an investigation was carried out on two samples using magnetron sputtering at the same temperatures investigated in [20]; (i) deposited at 300 °C and (ii) at 500 °C. As deposited these samples showed indications of ordering but no in-plane uniaxial anisotropy was detected, the post annealing of these samples is further investigated in the following sections. The fabrication procedure using DC magnetron sputtering for all layers with a base pressure prior to deposition of $< 2 \times 10^{-8}$ Torr produces a 10 nm FePt film with strong hard axis in-plane is:

1. **MgO Surface Clean** - The surface of the MgO is cleaned of any chemically bonded surface contamination by heating to 800°C for 1 hour.

2. **Cooling** - The sample is allowed to cool to RT over 6 hours under ultra high vacuum conditions ($< 5 \times 10^{-8}$ Torr).

3. **Pt Seed layer** - A thin (≈ 1 nm) layer of Pt is deposited using 3 mTorr working pressure and a power of 50 W for 20s to help adhesion to substrate.

4. **Annealing of Pt Seed** - The Pt seed layer is annealed at 700°C for 2 hours to form the desired [110] structure.

5. **Pre-deposition Heating** - Sample is heated to deposition temperature (300 or 500°C) and allowed to thermalise for 2 hour.

6. **Deposition FePt** - The Fe & FePt sputtering targets are first cleaned at 30 mTorr with the shutter closed and then deposited using 3 mTorr and 60 W Fe with 100 W FePt for a 50:50 at.% Fe:Pt composition onto the heated substrate at a deposition rate of 0.14 nm per second.

7. **Cooling** - The sample is allowed to cool to RT for a maximum of 6 hours under ultra high vacuum conditions ($< 5 \times 10^{-8}$ Torr).

8. **Capping** - A capping layer of Pt is deposited at 100 W for 50 seconds to achieve a 5 nm film ensuring no oxidation of lower layers occurs. This is deposited at RT to ensure no layer mixing.

6.2.1.1 Structural characterisation of in-plane uniaxial anisotropy of FePt thin films

The structure of the FePt thin films grown on MgO(110) substrates was characterized using X-ray diffraction (XRD) and X-ray reflectivity (XRR) as described in chapter 5. The evolution of ordering in these films was monitored by XRD as a function of temperature using a heated sample stage (Anton Paar DHS 1100). An example of XRD data from the initial heating at 300°C and the final temperature of 700°C is shown in figure 6.4. The samples were heated to the desired temperature at a ramping rate of 10°C per minute, having reached the set temperature the sample was thermalised for one hour. The full temperature range of 300 to 700°C was measured with no breaking of vacuum, therefore each temperature is held for 1 hour of thermalisation and then a further 4 hours for the measurement and as the step size was kept small the temperature of the sample is ensured to be accurate. In order to check the temperature calibration, the position of the MgO (220) peak was monitored. A thermal expansion coefficient for the lattice constant of 10.5 $\times 10^{-6}$ per °C was used for calibration following equation 6.1 [181–183]:

$$\Delta T = \frac{\Delta L}{L\alpha} \tag{6.1}$$

where L is the lattice constant value, ΔL is the change in the lattice constant, α is the thermal expansion coefficient and ΔT is the change in temperature. The temperature calibration for the stage can be seen in chapter 5.

The desired orientation of the $L1_0$ phase for in-plane FePt corresponds to a well defined (220) peak, with a super lattice (110) peak [20]. The (220) peak produces a larger intensity when compared to (110), this is due to it being the fundamental peak. Therefore any XRD presence is expected to begin with (220) peak formation with a well ordered structure forming the (110) peak. Additionally, as the XRD measurement angle is increased the separation between the ordered $L1_0$ phase and disordered phases such as the FCC increases, thus allowing differentiating between the two states easily.

The XRD temperature measurements for the sample deposited at 500°C are shown for the beginning measurement at 300 °C and the final temperature measurement at 700°C, shown in figure 6.4, where a definitive shift can be seen for the FePt (220) peak.
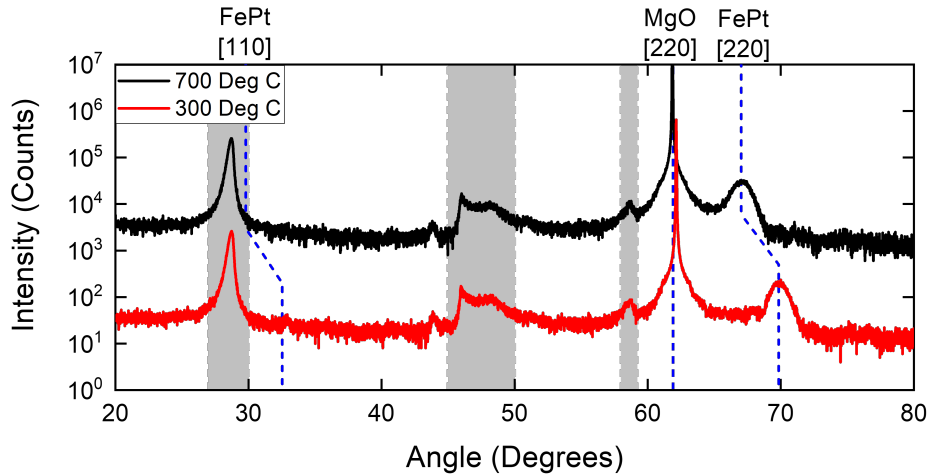
Figure 6.4: In-situ heated XRD spectrum, taken at the start temp of 300°C and end temperature of 700°C, for FePt deposited at 500°C on MgO [110] substrate. Shaded regions represent that background signal from the graphite dome.

The overall shape of the peak remains similar, where peaks related to the graphite dome background signal are shaded. The FePt (110) peak at temperature is extremely close to the dome background, but as a large portion of this work is on optimising the formation of the $L1_0$ phase the (220) peak can be used on its own as it is the fundamental peak, as described in chapter 5. For any order parameter calculations the sample is measured on the low noise plate with no dome background signal.

The peak position of FePt (220) is measured from the temperature series XRD and compared to both the disordered (FCC) and the ordered ($L1_0$) phases in figure 6.5. This is to further understand how the FePt thin film evolves with post-deposition annealing temperature. The peak position is calculated using Bragg's law, stated in chapter 5, where a thermal expansion coefficient for the lattice constant of 10.5×10^{-6} per °C is used to measure it as a function of temperature. The room temperature lattice constants for FCC of $a = b = c = 3.71$ nm and $L1_0$ of $a = b = 3.85$ nm and $c = 3.71$ nm [11].
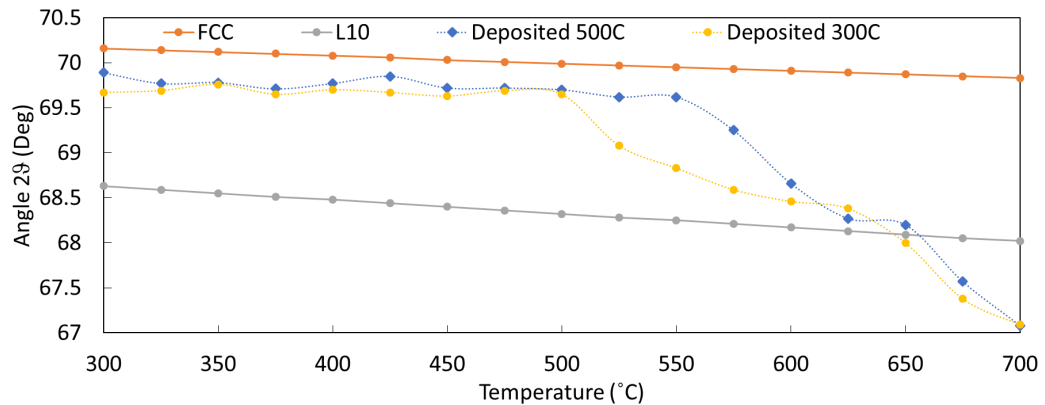
Figure 6.5: Peak position as a function of temperature for FePt deposited at 300 and 500°C, compared to predicted values for disordered FCC and ordered L1$_0$ phases for each temperature measurement.

The XRD measurements show the (220) peak shifting to lower 2θ angles with temperature, which is expected as the dominant phase shifts from FCC to L1$_0$. However, the remanent disordered phase within the system cause the (220) peak to broaden, shown in figure 6.6. Comparing the samples deposited at 300 °C and 500 °C, shown in figure 6.5, it is clear that while the sample deposited at 300 °C starts to transition at lower temperature the transition is not complete until 625-650°C is reached. Alternatively, the 500 °C sample transition occurs at a steady rate, starting at a much higher temperature of 550 °C. The consistency shown for phase transition allows accurate control over its restructure with a 50 °C window for L1$_0$ ordering.

The FePt (220) peak for the sample deposited at 500°C shows no movement in figure 6.5 until a temperature of 550°C. The slow transition from the disordered FCC state to the ordered L1$_0$ phase then occurs over 3 measurements, with optimal agreement between L1$_0$ and measured peaks at 625°C. A summarised plot of all temperatures measured (300 to 700 °C) is shown in the form of a 2D-plot in figure 6.4, where the XRD measurements were taken every 25 °C. Figure 6.6 shows the shape of the peak can be seen to remain relatively constants through the heated XRD measurements, showing the structure of the film is not undergoing changes that could effect film roughness. The peak width is also a good indicator that no oxidation is occurring in the film, as the peak shape would be expected to broaden. It can be seen that for the final measurement at 700°C there is broadening of the peak, this is due to the film structure changing substantially.
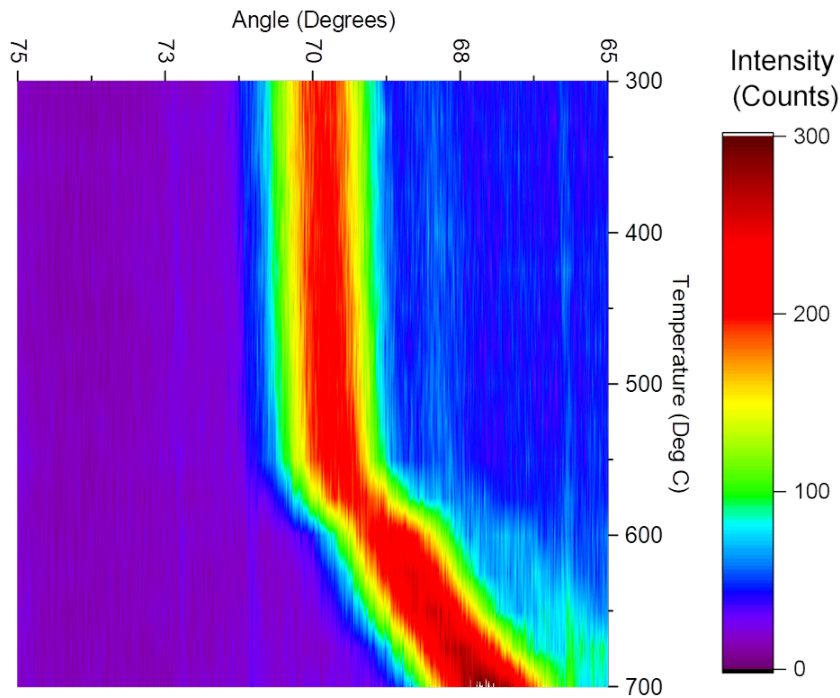
Figure 6.6: XRD with in-situ post deposition annealing for FePt deposited at 500°C, focussing on the FePt (220) peak evolution with temperature.

To achieve the maximum ordering in the system a deposition temperature of 500°C and annealing at 625°C is chosen as this corresponds to the closest match between theoretical peak position and achieved peak position, as was shown in figure 6.5.

The foundation for film growth with fabrication conditions for deposition and annealing temperatures for uniaxial in-plan FePt has been determined. Following the results shown in figure 6.5 a sample was deposited at 500 °C and annealed in-situ at 625 °C. The sample structure from fabrication was MgO[110]/Pt[110] (1 nm)/FePt(10 nm)/Ta(5 nm), where the sample is given two hours at 500 °C to thermalise before the FePt layer is deposited and a further two hours to anneal at 625 °C. The sample is cooled for 6 hours in vacuum before the Ta capping layer is added, which acts to inhibit any oxidation of the FePt film. The XRD spectrum, shown in figure 6.7, for these fabrication conditions show FePt (220) crystallographic structure with a corresponding FePt (110) peak indicating long range ordering within the film. However, there is also FePt (202) peak indicating some canting/disorder to the film.
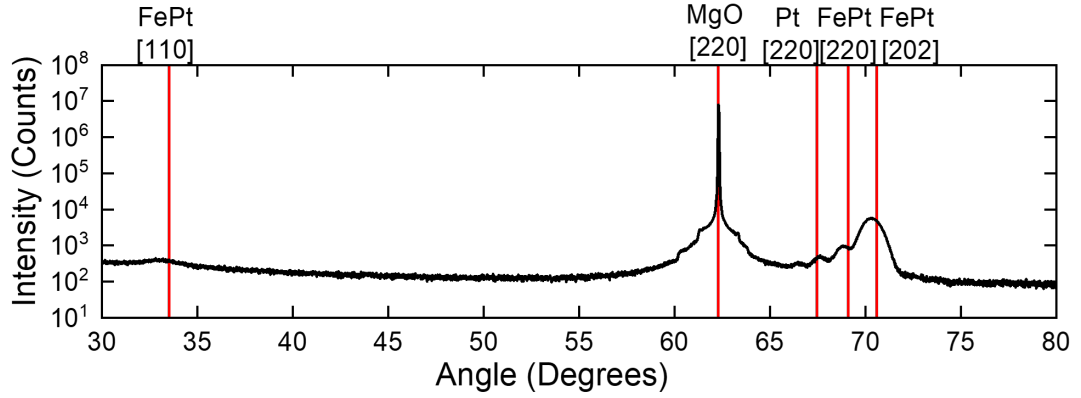
Figure 6.7: X-ray Diffraction profile for MgO[110]/Pt(1 nm)/FePt(10 nm)/Ta(4 nm)/Ta$_2$O$_5$(4 nm) deposited at 500 °C and annealed at 625 °C, with peaks of interest labelled.

The structure of the film was investigated by XRR measurements, as shown in figure 6.8. Through various iterations of the XRR simulation it was determined that the Pt seed layer was absorbed into the FePt structure to form a Pt rich FePt base layer, where simulations using a separate Pt seed layer failed to capture the critical edge and oscillations of the XRR measurement. It was therefore determined that the sufficiently thin Pt layer was combined with the FePt layer as it was deposited at temperature, where the Pt passes its alignment with the substrate to the newly forming FePt structure. The combination of the Pt and FePt layers proves vital in forcing the FePt structure to lattice match the substrate for (110) growth, which is needed for in-plane uniaxial anisotropy to form. The results from the fitting for the full stacked structure are shown in table 6.2.

Layer	Thickness nm	Roughness nm	Density g/cm^3
Ta$_2$O$_5$	4.28	1.70	7.0
Ta	4.05	0.60	18.0
FePt	9.59	0.60	15.5
FePt with Pt Seed	1.51	0.37	16.9
Substrate	N/A	0.48	3.6

Table 6.2: X-ray Reflectivity fitting parameters as obtained from fitting software GenX [172], FOM for fit was 0.047.
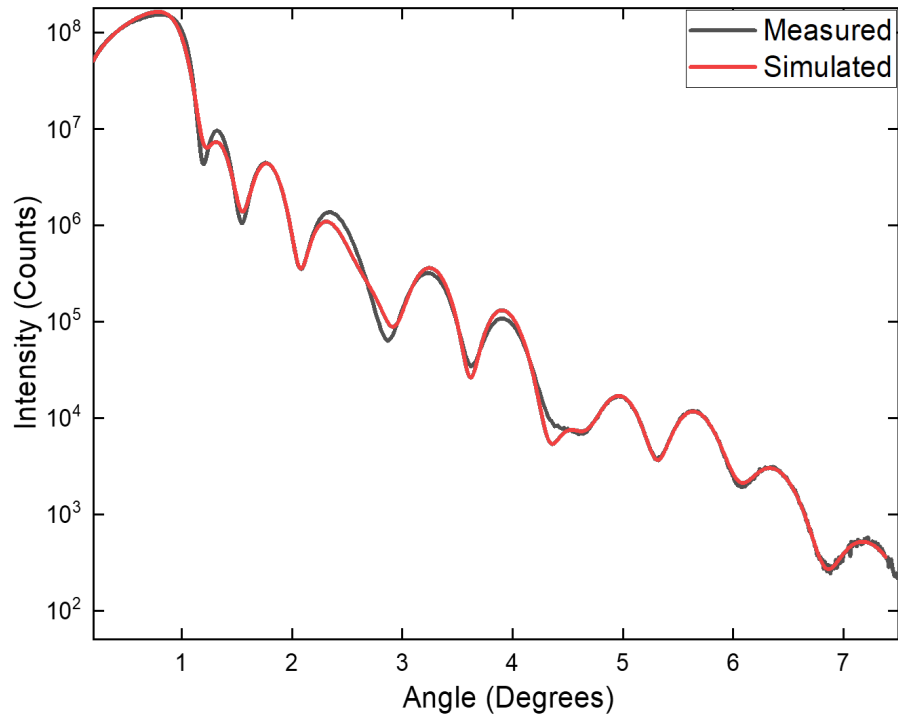
Figure 6.8: Fitted XRR profile for MgO[110]/Pt/FePt/Ta/Ta$_2$O$_5$, with FOM value of 0.047.

The XRR fit confirms that the layer structure was close to the intended 10 nm of FePt was deposited onto MgO [110], where the measured thickness from XRR simulations is used for calculations of saturation magnetisation. The structure itself has a roughness similar to that of the MgO substrate for all layers, apart from the top most Ta$_2$O$_5$ layer which is a native oxide to the capping film and is expected to be rougher.

The fitting procedure for the sample shown in figure 6.8 followed an initial approximation from rate tests. The rate tests use single layer deposition on MgO substrates, which allows the determination of accurate deposition rates without other layers complicating the fit. These values are assumed to remain consistent within a $\pm$ 20% window, this ensures any alterations from growth on different material are factored in. During this fitting procedure it was found that encompassing the Pt layer into a Pt rich FePt layer gave a better fit, measured by its figure of merit which increased by an order of magnitude from 2×10^{-2} to 2×10^{-3}.

6.2.2 Magnetic characterisation of in-plane uniaxial anisotropy FePt thin films

As FePt is a material with intricate links between the structural and magnetic properties it was assumed from the XRD results that the magnetic properties would produce in-plane alignment, which is of great interest for its implementation in exchange spring structures. The magnetic properties were determined from measurements of hysteresis loops and DC demagnetising remanent curves. The crystal growth of FePt on MgO (110) is shown in figure 6.9, where at 0 degrees there is alignment with the (001) plane of FePt, with a 90 degree rotation in the plane giving a measure of the ($1\bar{1}0$) plane, see section 2.1.1 for more detail on crystal planes.
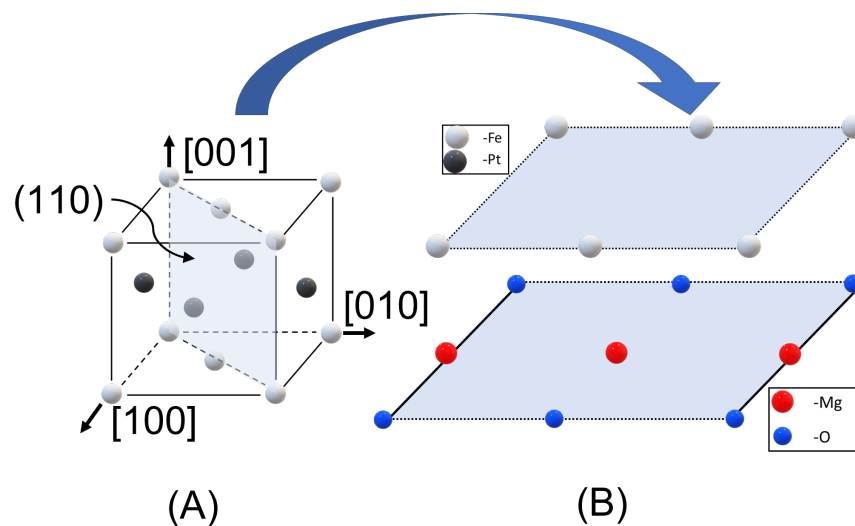
Figure 6.9: (A) shows the unit cell for FePt with the (110) plane shaded, (B) is the growth of FePt (110) plane atop the MgO (110) substrate.

The hysteresis loops measured using the VSM for field applied in-plane show that as the field is rotated the material reacts differently, thus confirming a uniaxial alignment. At 0 degrees ((001) aligned) it can be seen that the FePt layer easy axis is fully saturated, but as the field is rotated through 90 degrees the hard axis (($1\bar{1}0$) aligned) cannot reach saturation.
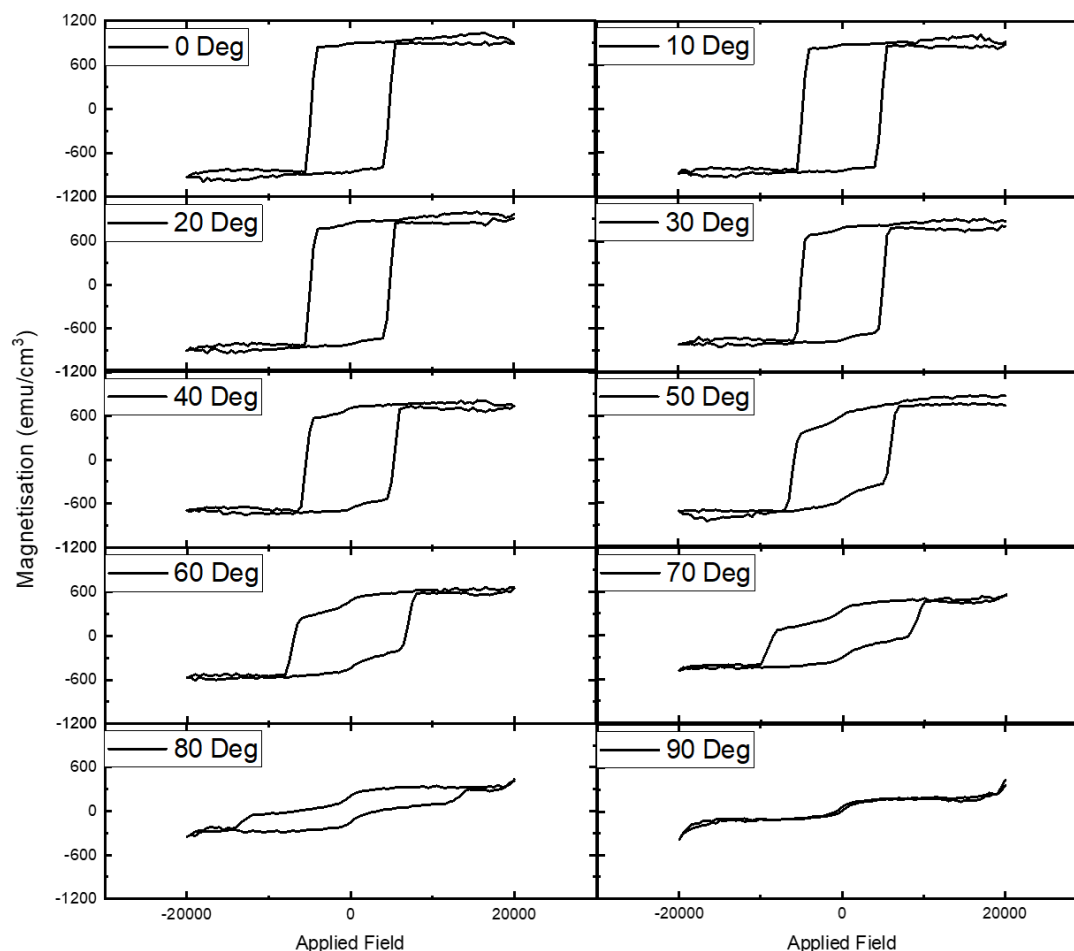
Figure 6.10: In-plane rotation measurements from the (110) plane of FePt correspond-ing to the easy axis at 0 Deg to the (1$\bar{1}$0) FePt plane hard axis at 90 Deg.

The irreversible component of the film was investigated, to better understand any hard and easy axis alignments in the plane of the film. Direct current demagnetisation (DCD) curves were measured to see the magnetisation switching as a function of field angle. This measurement starts at an assumed saturated state for the film, with max applied field of 2 T. The applied field is then removed and applied in the opposite di-rection in incremental steps (500 Oe), at each increment a measurement is taken as shown in figure 6.11. These measurements show the ability for the newly applied field to reverse the remanent magnetisation of the film, where the results in figure 6.11 show a hard (90 Deg) and easy (0 Deg) axis DCD curve.
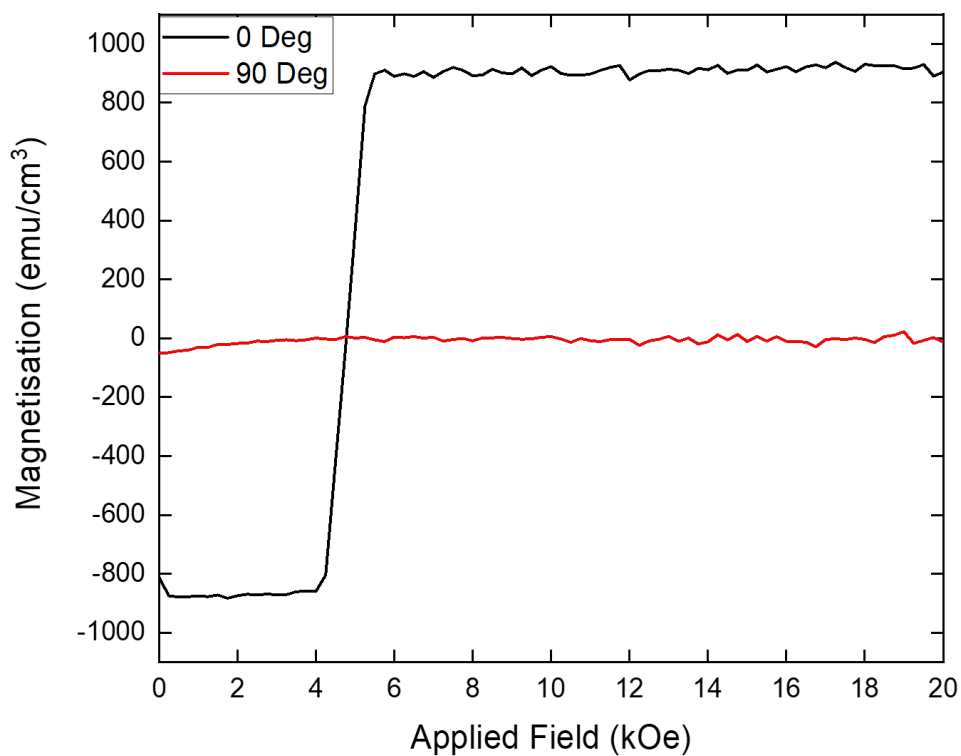
Figure 6.11: DCD curves for hard (90°) and easy (0°) axis of FePt (110) on MgO(110) substrates.

The evolution of the switching can be seen in figure 6.12, where the 2D plot summarizes the DCD curves showing a well defined easy and hard axis within the film. The easy axis aligns to 0 degrees, as the formation of FePt (001) plane coincides with the substrates (001) plane.
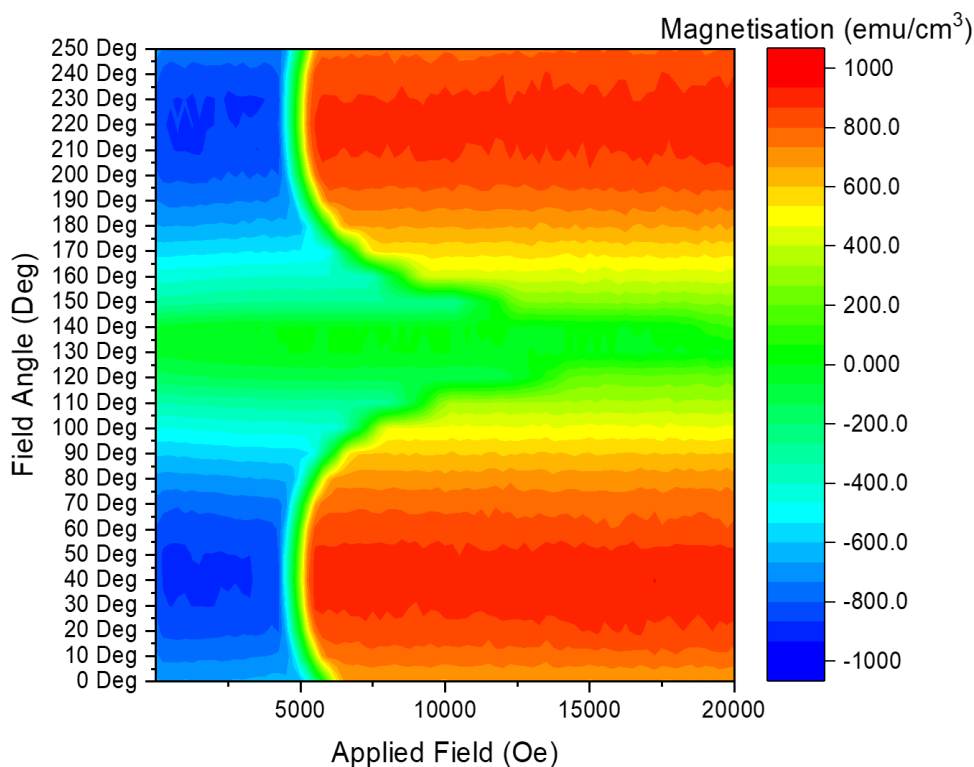
Figure 6.12: 2D plot of DCD curves showing remanent magnetisation coercivity H$_{CR}$ magnetisation as a function of applied field angle of 10 nm FePt on MgO [110] substrates.

The results from the VSM measurements showed that as a 90 °in-plane rotation is approached the sample is not fully saturated, as shown by the tail effects in the hysteresis at max field in figure 6.10. As the VSM was not able to fully saturate the sample for all angles measured further measurements were carried out using a SQUID magnetometer with a maximum applied field of 7 T. However, whilst the VSM is equipped with a rotation stage capable of controlling rotation with an accuracy of 0.01 degrees the SQUID relies on manual sample mounting where the accuracy is approximately 5 degrees. Therefore, the VSM measurements from 0 to 360 degrees in-plane were used to scribe a line on the back surface of the substrate to allow affirmation of axis alignment. Two levels of certainty were achieved by using the VSM measurements as the line marker and VSM vs SQUID measurements combined confirmed that any misalignment were corrected. The rotation measurements from the VSM played a vital role in accurately finding the hard axis, as it was found only a 15°window shows the hard axis of the FePt film in plane. The data from the SQUID are shown in figure 6.13 where easy and hard axis in-plane are shown as well as comparative out-of-plane axis.
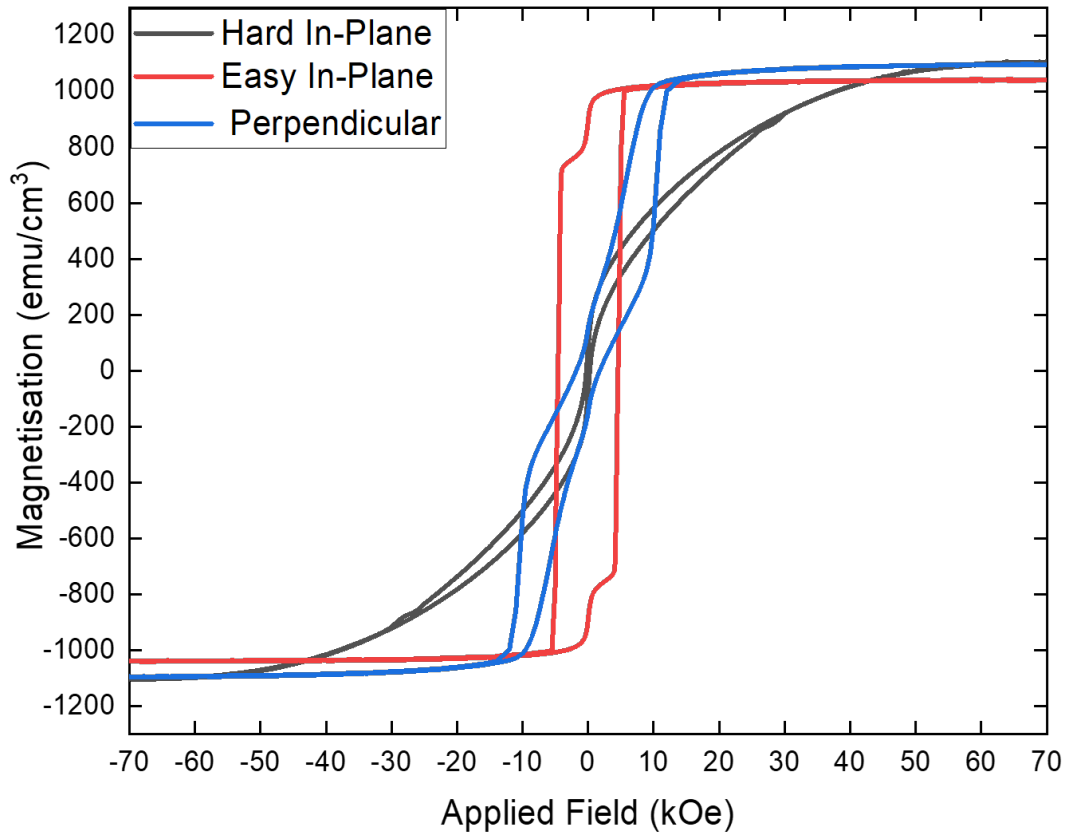
Figure 6.13: SQUID measurement for uniaxial in-plane aligned FePt on MgO [110], where the hard axis in plane is $(1\bar{1}0)$, easy axis in plane (001) and perpendicular is out of the plane.

The SQUID measurements performed showed an easy axis alignment corresponding to the (001) FePt axis with a 90 degree in-plane rotation showing a very hard axis corresponding to $(1\bar{1}0)$ FePt plane. The perpendicular axis normally investigated for FePt thin films was also measured, this magnetic axis showed properties of both the easy and hard axis for an FePt film. As uniaxial in-plane FePt thin films are very difficult to form perfectly in the plane it is assumed that the shape of the perpendicular measurement is due to the canted magnetic axis.
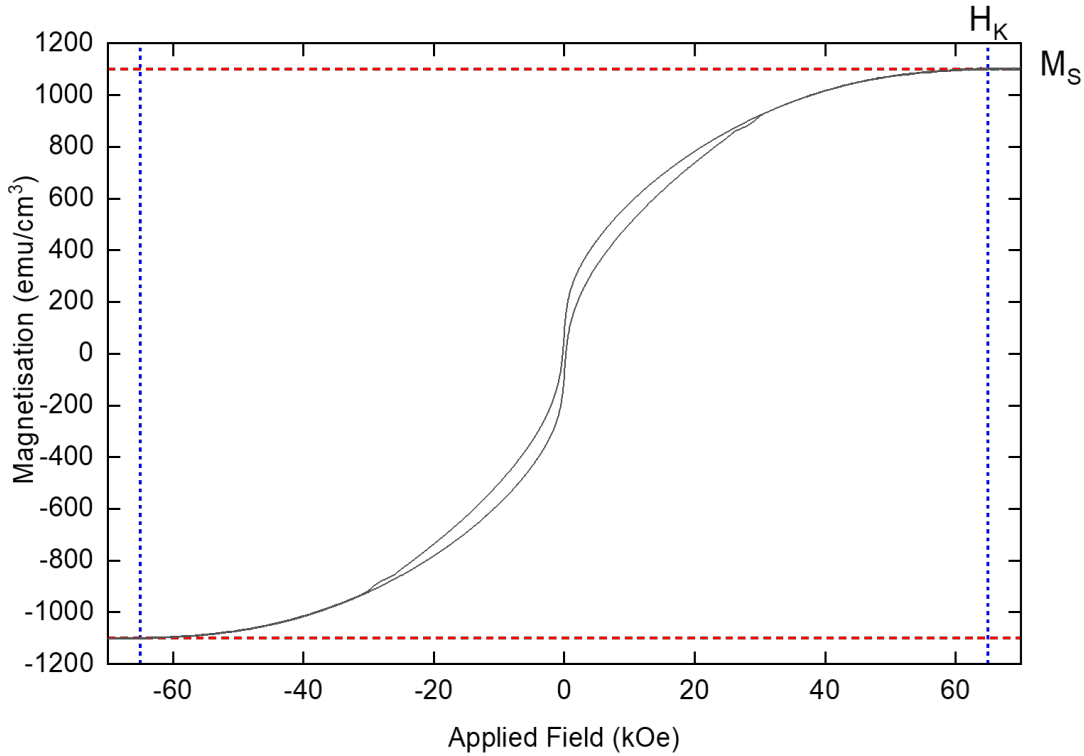
Figure 6.14: SQUID measurement of FePt hard axis with corresponding reference lines for saturation magnetisation M$_S$ and anisotropy field H$_K$.

The magnetic properties of the FePt film including H$_K$ are taken from the SQUID hysteresis curves, as shown by figure 6.14. The saturation magnetisation M$_S$, anisotropy field H$_K$ are used to calculate the anisotropy energy following equation 6.2, first described in chapter 2:

$$K_U = \frac{M_S H_K}{2} = \frac{1100 \times 3.6x10^7}{2} = 3.6x10^7 \tag{6.2}$$

The properties of the film produced in this thesis and those found in literature are compared in table 6.3. The future use of these films in devices relies on their magnetic properties, most importantly is the uniaxial alignment which can be compared by taking their anisotropy energy for the hard axis. Therefore when comparing the samples produced in this thesis with others in literature it is found that it outperforms the competition whilst also being the thinnest. There is also the added benefit that these films were produced using magnetron sputtering, meaning their implementation in device manufacture is a lot easier.

Substrate	Seed Layer	FePt Thickness (nm)	Deposition Technique	Deposition Temperature (°C)	Saturation Magnetisation (Ms emu/cm^3)	Anisotropy Field (Hk Oe)	Anisotropy Energy (Ku erg/cm^3)	Reference
MgO (110)	Fe(1 nm)/Au(40 nm)	18	DC Magnetron Sputtering	300	1000	48000	2.4×10^7	[175]
MgO (110)	Pt (0.7 nm)	100	MBE	500	1080	28000	1.5×10^7	[20]
MgO (110)	Pt (1 nm)	30	E-beam Evaporation	500	900	≤ 75000 (Estimated)	$\leq 3.4 \times 10^7$ (Estimated)	[85]
MgO (110)	Pt (1 nm)	10	DC Magnetron Sputtering	500 (625 Annealed)	1100	65000	3.6×10^7	This Work

Table 6.3: Comparison between FePt (110) magnetic properties from literature results to those obtain in this thesis. The values obtained show the progress made for fabricating FePt with in-plane anisotropy using magnetron sputtering.

The values obtained for anisotropy energy in this work are larger than those found in literature for similar structures, where alternative deposition systems have been considered. The main difference between these pieces of work is the deposition and annealing temperatures, where literature results only deposited at temperature and did not further anneal their samples. This additional heating step allows further ordering of the material, as was found and shown in figure 6.5.

6.3   Fabrication of L1$_0$ FePt Exchange Springs

Having developed the fabrication processes necessary to create L1$_0$ ordered FePt thin films with either perpendicular or in-plane uniaxial anisotropy, these films can now be incorporated into exchange spring structures. Within the limits of the time available, the remaining part of the work focused on creating exchange spring structures where the hard layer has perpendicular anisotropy. However, the translation of this work to a uniaxial in-plane hard layer structure can be expected to follow directly as the key step of creating the hard layer film was demonstrated in the previous section.

6.3.1   Deposition of FePt/Permalloy exchange springs with perpendicular anisotropy

The fabrication process developed by Huskisson and Zygridou [4, 21] was adapted to include in-situ heating within the deposition chamber, this fabrication procedure allowed highly ordered FePt thin films on MgO (001) substrates to be exchanged coupled to a NiFe film. Fabrication of the structure is carried out using the AJA magnetron sputtering system described in section 4.2, where the complete process for the exchange spring with an ordered FePt film is as follows:

1. **MgO Surface Clean** - The surface of the MgO is cleaned of any chemically bonded surface contamination by heating to 800°C for 1 hour.

2. **Cooling** - The sample is allowed to cool to RT over 6 hours under ultra high vacuum conditions ($< 5\mathrm{x}10^{-8}$ Torr).

3. **FePt Flash Layer** - A layer of FePt, using 3 mTorr pressure and co deposition of Fe:FePt at 60:100 W, is deposited at room temperature for 20 s to ensure good adhesion to the surface.

4. **Pre-deposition Heating** - Sample is heated to deposition temperature (650°C) and allowed to thermalise for 2 hour.

5. **Deposition FePt** - The Fe & FePt sputtering targets are co-deposited using 3 mTorr Ar pressured at powers 60 W Fe and 100 W FePt for a 50:50 at.% Fe:Pt composition onto the heated substrate, at a deposition rate of 0.14 nm/second.

6. **Cooling** - The sample is allowed to cool to RT for a maximum of 6 hours under ultra high vacuum conditions ($< 5 \times 10^{-8}$ Torr).

7. **Spacer Layer** - A 2 or 5 nm layer of Pd separates the two magnetic exchange layers, the thickness is varied to test varying degrees of interaction between the magnetic layers.

8. **Exchange Layer** - A layer of soft magnetic material, in this case 50 nm of NiFe, is deposited at room temperature to create the exchange spring structure.

9. **Capping** - A capping material (5 nm of Pt or Ta) is applied to ensure no oxidation occurs, this is done at RT to ensure no layer mixing.

The process of cleaning the substrate, described in section 4.3.1, helps to minimise any contamination before the film is deposited, as the heating process may allow surface contamination to migrate into the film causing defects to the $L1_0$ ordered structure. The 'flash' layer helps to reduce surface roughness by encouraging initial growth of the film, where deposition at room temperature allows the atoms to stick more readily. The heating times allow adequate time for the temperature to reach equilibrium on the entire substrate, ensuring the required temperature for ordering is achieved. Step 8 is the addition of a soft magnetic layer to create the exchange spring structure, where it is possible to substitute the NiFe for another soft magnetic layer. The final step ensures that oxidation of the magnetic films does not occurs, where it acts as a sacrificial coating protecting all those under.

6.3.1.1   Structural characterisation of perpendicular to in-plane exchange spring

Similar to the in-plane FePt study, the films are structurally characterised using XRD and XRR. However, in this case there is no temperature measurements performed on the XRD system to avoid the possibility of thermally induced interlayer mixing. The structures are characterised using XRD spectrum to show the long range ordering

achieved and evaluate the quality of the films. A 10 nm FePt film with 50 nm of NiFe separated by a 2 nm Pd spacer is shown in figure 6.15. The Pd spacer thickness can be varied to test various regimes of coupling between the FePt and Py layers for future beam time experiments, where it is expected that as the spacer layer increases the effects on the FePt from the Py layer are reduced.
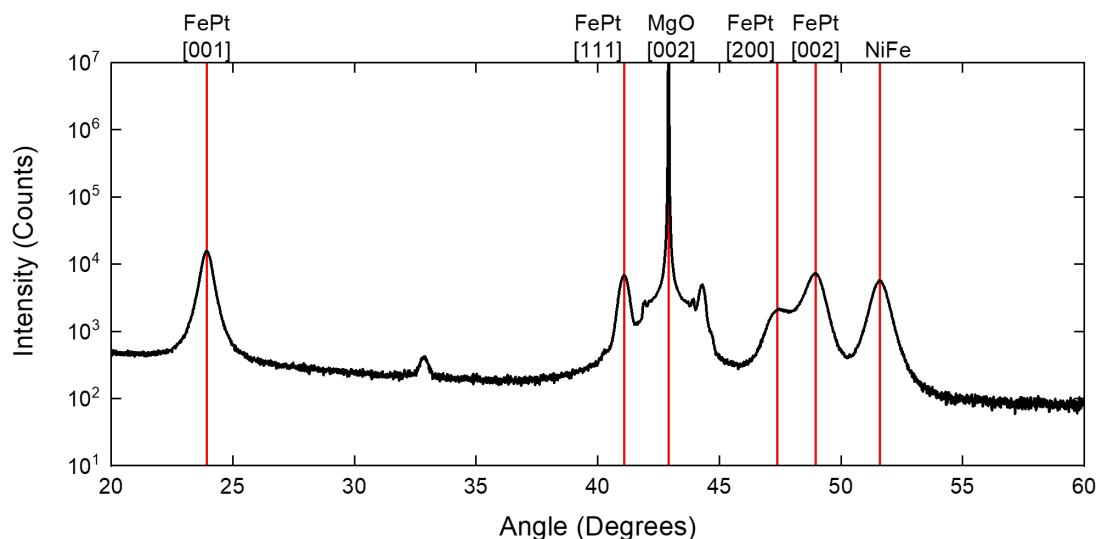
Figure 6.15: A measure of MgO(001)/FePt(10 nm)/Pd(2 nm)/NiFe(50 nm)/Ta(5 nm) structure, confirming presence of L1$_0$ ordering in FePt.

To calculate the order parameter for FePt films the XRD peaks must be fitted for the integrated intensity to be measured. The XRD peak fitting procedure is broken into two parts, as shown in figure 6.16, representing one for each peak of interest. The fundamental FePt peaks are (001) and (002), where care must be taken with the two closely matched FCC and L1$_0$ (FCT) phases.

The (001) peak can be fitted as a single voigt profile, where the FCC and L1$_0$ phases are too close together to differentiate. The (002) peak is separated into three different peaks, two from the L1$_0$ phase forming alternative orientations and one from the FCC phase. The fitted peaks are shown in figure 6.16, where care has been taken to ensure all phases/planes have been fitted to obtain the most accurate area of the peak for order parameter calculation. The values obtained from fitting each peak is summarised in table 6.4.
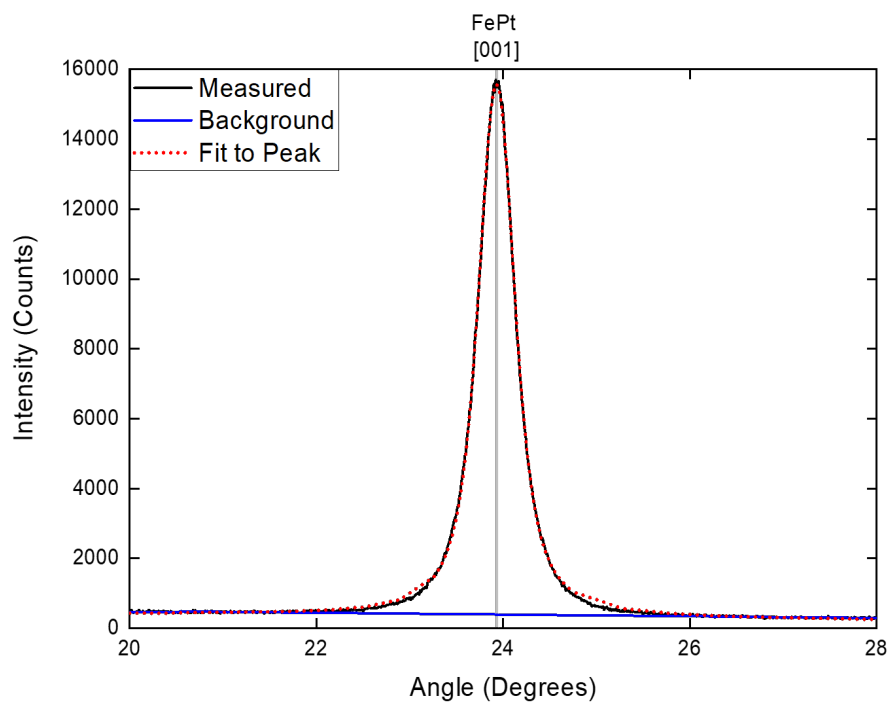
(a)
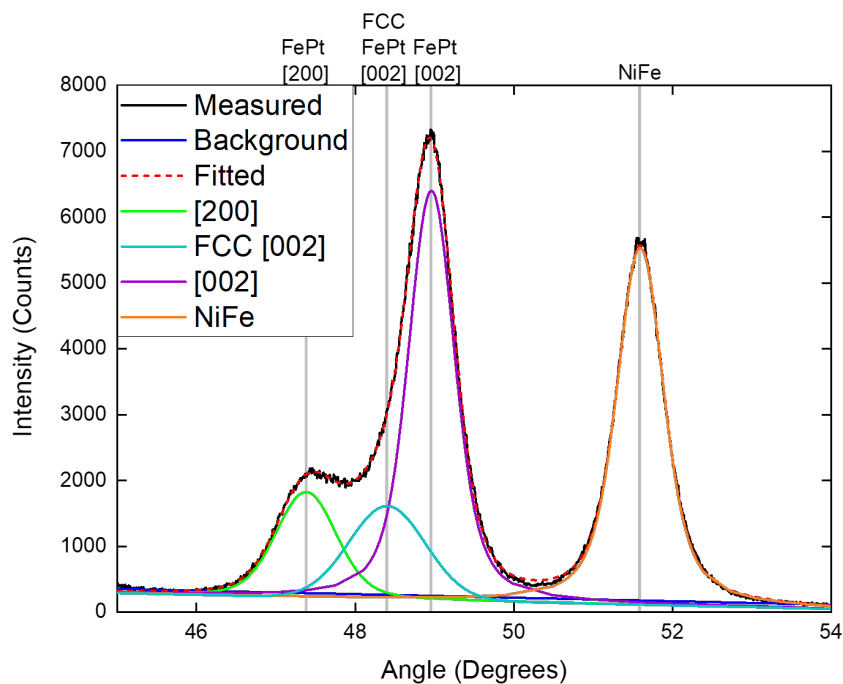
(b)

Figure 6.16: (a) [001] FePt peak fitting, and (b) [002] FePt peak fitting with alternative peaks labelled.

Peak	Peak Center	FWHM	Max Height	Area Integrated
FePt 001 (L10)	23.92	0.47	15231	9738
FePt 200 (L10)	47.38	0.90	1596	1646
FePt 002 (FCC)	48.40	1.13	1411	1701
FePt 002 (L10)	48.96	0.69	6214	5236
NiFe	51.59	0.70	5417	4827

Table 6.4: Full list of peaks fitted for order parameter calculations, where the peaks were fitted as a voigt profile. The

The order parameter equation derived in section 5.10 is used to calculate the long range order of FePt films. The integrated intensity of (001) and (002) peaks are input as shown below to give the order parameter of the film:

$$S \cong 0.493 \left(\frac{I_{001}}{I_{002}} \right)^{1/2} = 0.493 \left(\frac{9738}{5236} \right)^{1/2} = 0.67 \tag{6.3}$$

The order parameter calculations give a value of S = 0.67, where the (001) peak is fitted as a single L1$_0$ phase but the (002) is split into contributing factors from separate peaks of FCC and L1$_0$ phases. Comparison values obtained from literature for FePt range from 0.7 to 0.9 depending on temperature and deposition technique used, where higher ordering is normally achieved by molecular beam epitaxy (MBE) [11].

While some disordered phase is present in the system, shown by the FCC peak shouldering the (002) L1$_0$ peak, the strong signal from both (002) and (001) FePt L1$_0$ (FCT) peaks demonstrates that good overall ordering within the structure has been achieved. Attempting to fit the (002) solely with L1$_0$ phase peaks creates a larger dip between the two peaks, meaning that the FCC peak must be incorporated for the fitting to work.

The values obtained for order parameter of the exchange spring structure are in agreement with those found for single layer films in section 6.1. The values obtained for the exchange structure are lower than those quoted in literature for single layer deposition, where differences are suspected to be due to the coupling of FePt to the magnetically soft NiFe layer.

6.3.1.2 Perpendicular to in-plane exchange spring magnetic characterisation

The confirmation of long range ordering in the FePt layer within an exchange spring structure allows further investigation into the magnetic interaction between the Py layer and L1$_0$ ordered FePt. A Pd spacer layer is used to alter the coupling between the NiFe and FePt layers, where a thinner spacer layer will have a more heavily effected magnetic structure. An example magnetometry measurement is shown for a thin (2 nm) Pd spacer, showing a heavily influence FePt/Pd/NiFe exchange spring in figure 6.17, where definitive two phase switching is seen.
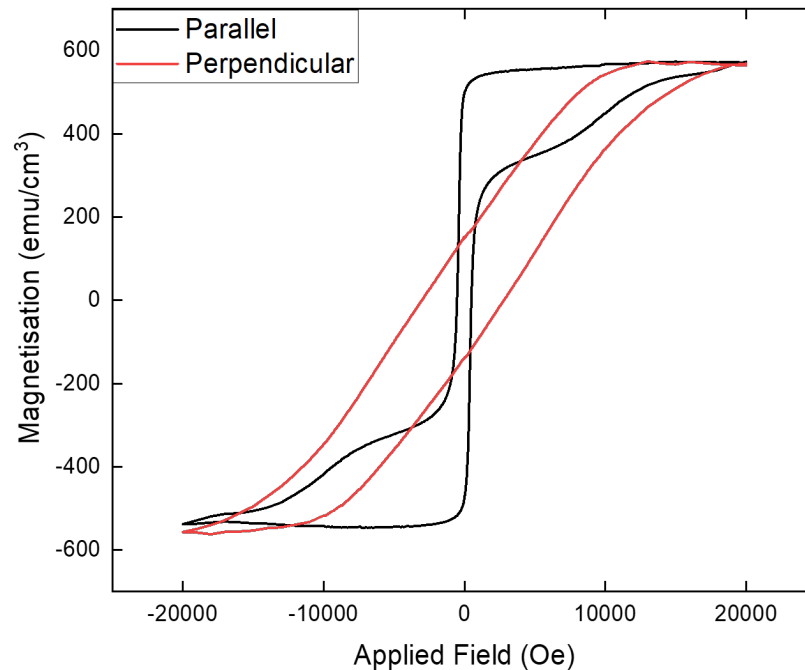
Figure 6.17: Hysteresis loop for both perpendicular and parallel applied field angles for an exchange spring structure FePt(20 nm)/Pd(5 nm)/NiFe(50 nm).

The phased switching present in the hysteresis loop is due to the magnetically soft permalloy layer switching at a lower applied field, while the high anisotropy FePt layer requires significantly higher applied field to flip. Therefore, the switching feature at very low field (500 Oe) is due to the exchange between NiFe and FePt. The perpendicular applied field does not show the same switching mechanism as only the FePt film is aligned to this plane, where a reduced saturation magnetisation is seen when compared to a single FePt film expected to be due to the effects of the NiFe on the FePt layer as the order parameter does not show any reduction.

6.4   Summary

A thorough understanding of the structure and crystallographic state was developed for a uniaxial in-plane L1$_0$ ordered FePt fabrication method using magnetron sputtering. The use of a very thin Pt seed layer, [110] which aligned to the substrate, proved vital in achieving order within the structure as the initial growth of the FePt film combined with the Pt seed through heating. The initial study on phase formation used XRD measurements with in-situ heating (300 to 700 °C). These results allowed the temperature at which the disordered FCC to L1$_0$ (FCT) phase transition occurred to be identified efficiently.

Magnetometry data measured using a VSM with a maximum applied field of 2 T allowed the in-plane magnetic properties to be determined. The presence of a very high anisotropy in-plane hard axis was confirmed by SQUID magnetometry with a maximum applied field of 7 T. The magnetic properties of the films outperformed other found in literature as was shown in table 6.3, where the properties of interest are anisotropy energy (3.6 x10^7 erg/cm^3) and saturation magnetisation (1100 emu/cm^3). The magnetic properties gained are consistent with the best anisotropy values obtained for sputtered films of 7 x10^7 erg/cm^3 [17]. Some additional fine tuning may also be possible to optimise the alignment of the FePt film in the plane.

Based on previous work, a fabrication procedure for ordered L1$_0$ FePt with PMA is implemented in an exchange spring structure of a perpendicularly hard layer and an in-plane soft layer. The magnetometry results for the exchange spring are shown in figure 6.17, where the shape changes drastically when compared to the single FePt layer shown in figure 6.3. The exchange structure proposed uses a Pd spacer layer to investigate the interaction between the hard/soft layers. However, due to time limitations it was not possible to further the understanding of exchange interactions. It was also not possible to create the in-plane to in-plane exchange spring using the fabrication procedure described in section 6.2.1. However, all the components needed to create these exchange springs are now in place and the initial demonstration of a perpendicular exchange spring using the same materials gives good confidence that this next step is possible. A concern that has been nullified is the possibility of a reduction in the order parameter for the FePt layer in an exchange spring structure, where a reduction in its magnetic properties would be expected to follow. However, it has been shown that for the perpendicular anisotropy FePt there is no reduction to its properties

with the addition of a magnetically soft layer and therefore the fabrication procedures determined in this thesis are able to be directly applied to future studies.

Chapter 7

MnAl Thin Film Fabrication

The formation of the metastable $L1_0$ phase in binary alloy MnAl would provide an alternative material for high frequency spintronic devices. Neither Mn or Al show ferromagnetic ordering, making it fascinating that when combined under the correct conditions particularly composition and temperature, that they would posses such high moments (490emu/cm^3 [93]), large uniaxial anisotropy ($K_U = 1$x10^7erg/cm^3) and small damping factors ($\alpha = 0.06$) [63]. Such properties are normally only found in materials where the 4f orbitals play a significant role in the spin orbit coupling, such as Pt, which are needed in order to produce high magnetic anisotropy. In recent years there have been very few reports on the fabrication of thin film MnAl with a review of the literature given in chapter 3. To date the most noteworthy work is by the Oogane group in Japan [64], where they showed the best $L1_0$ ordering for a film with order parameter of >0.9, surface roughness of 0.3 nm, and saturation magnetisation of 560emu/cm^3 [64].

Given the natural advantages of $L1_0$ ordered MnAl this lack of literature strongly indicates that the creation of thin films of $L1_0$ MnAl presents signifiant difficulties. The work presented here focusses on understanding the challenges that need to be overcome to create $L1_0$ ordered MnAl and details progress made towards this goal.

7.1   Element trajectory within the sputtering chamber

Fabricating consistent composition alloys for thin film characterisation is a main hurdle when investigating complex phase structures for alloys. In the case of MnAl there is a 10 at.% composition window (50-60 at.% Mn) for the desired phase, where within this range ferromagnetic properties can form due to the metastable τ phase. There are a

number of contributing factors that can often be ignored for simplistic single target depositions, but when attempting to keep compositional certainty extra procedures must be put in place, such factors include the travel distance of depositing atoms.

This work focuses on compositional consistency, where the elemental ballistics within the sputtering chamber are dictated by the relative mass of sputtered material compared to the sputtering gas Argon, where Al is $0.675 \times$Ar and Mn is $1.375 \times$Ar. Therefore, Al may need only 1 scattering process to completely alter its trajectory whereas Mn would need multiple. The mean free path (λ) of these elements is plotted in figure 7.1, calculated using equation 7.1 [184]:

$$\lambda = \frac{k_B T}{\sqrt{2}\pi d^2 p} \tag{7.1}$$

where λ is the mean free path, k_B is Boltzmann constant (1.380649×10^{-23} JK^{-1}), T is temperature set at 300 K, d is the diameter of the atom and p is the pressure.
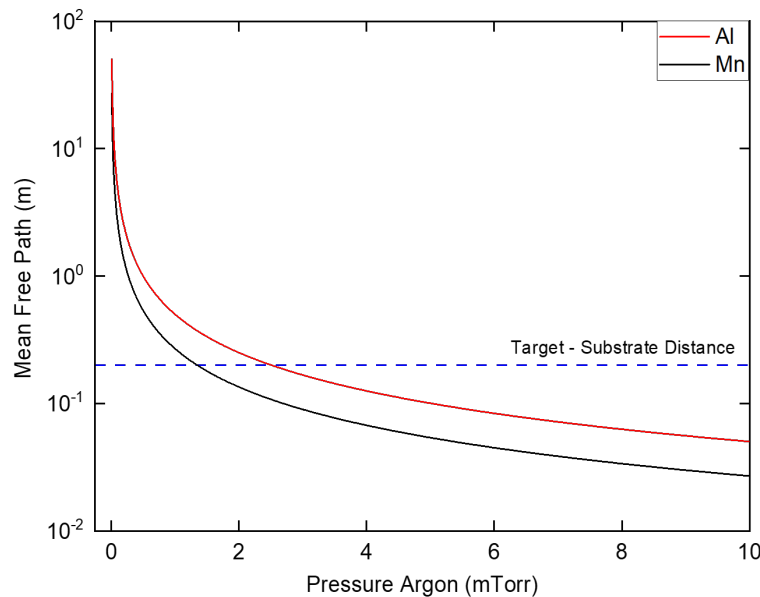
Figure 7.1: Mean free path for both Mn and Al within the sputtering chamber for a range of working pressures.

This work is carried out in a large sputtering chamber with a distance of approximately 20 cm between target and substrate, which can cause sufficient scattering to alter composition. The chance of these scattering events occurring are small but not zero, however lowering the working pressure for sputtering can reduce the probability

to negligible levels. Further details on compositional variance within a sputter chamber for high and low pressure conditions is covered in chapter 4.

7.2   Fabrication of $L1_0$ MnAl thin films using a sintered alloy target

To achieve ferromagnetism in MnAl thin films it must be in the correct crystallographic phase, the growth of which is dictated by composition, adatom energy, substrate temperature and crystallographic template. Achieving the desired composition was initially thought to be a straightforward task, where a sintered alloy target measuring 2 inches in diameter of Mn:Al 48:52 at.% was obtained. The composition of the target was based on literature results [64] that showed $L1_0$ growth of MnAl for a range of target compositions, for which Mn:Al 48:52 at.% produced the largest $L1_0$ phase ordering [64]. In the process of obtaining the alloy target a well renowned target manufacturer made multiple attempts at forming a target using a high purity induction melting process. However, the target brittleness caused it to crack at the final stages, revealing the copper backplate and rendering the target unusable for sputtering. Following rigorous testing the manufacturer was able to make a sintered target of the desired composition, but this too was not without difficulties where only at the third attempt did they achieve a smooth surface with no cracking. Following the manufacturers guidance, the sputtering process for such a brittle target was adapted to ensure that it does not undergo thermal shock and crack during a deposition. In order to achieve this a slow ramping rate was used and the upper limit of plasma power is kept below 60 W on the manufacturers recommendation.

An important piece of learning from this experience was that for MnAl, the production of high purity targets is a significant challenge, which would need to be addressed to allow wide scale use of this material. The alternative approach of co-sputtering is described in section7.4.

7.2.1   Deposition of MnAl from an alloy target

Initial testing of the alloy target used low wattage deposition (20 and 40W) to test deposition rates and crystal phase formation. These wattages represent the lowest stable plasma (20 W) for deposition and the middle ground (40 W) between lowest power

and maximum power (70 W). MnAl was deposited onto Si/SiO$_2$ (290 nm) substrates as they are readily used for thin film fabrications due to their smooth surface (<0.5 nm), and in the case for MnAl the XRD peaks for the substrate are sufficiently far away that they do not interfere with analysis for ordered/disordered peaks. The deposition rate of MnAl for 20 and 40 W matches those used in literature of 0.02 nm/s [64]. As a starting point for this work a reproduction of literature values is desirable, therefore matching the deposition conditions is favourable.

The XRD spectrum for a $\approx$ 50 nm film of MnAl is shown in figure 7.2, where no discernable peaks are seen indicating an amorphous film structure. Interestingly not only are there no ordered peaks, later found to be due to composition falling outside the L1$_0$ range, but there is also no disordered phases present such as γ-MnAl or β-Mn. This made it impossible to solve the initial problem of phase growth by solely using XRD analysis.
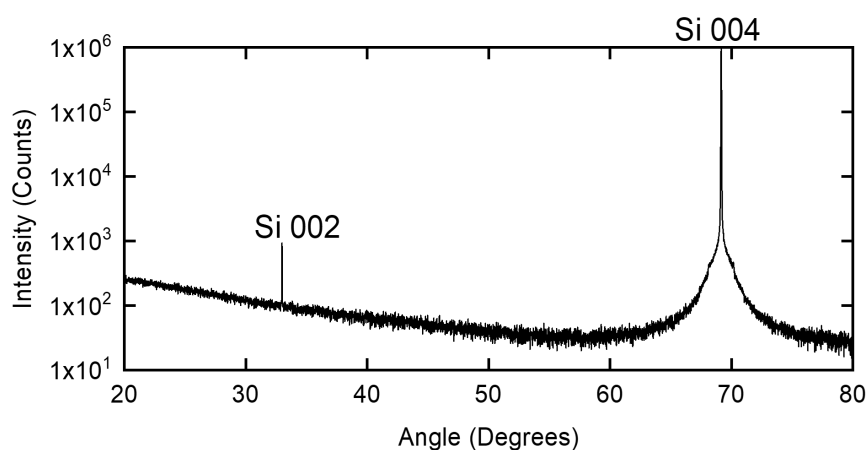
Figure 7.2: XRD profile for 40 W MnAl on a SiO2 Substrate with a Ta capping layer. Only the Si substrates fundamental peaks are present.

The formation of L1$_0$ ordered MnAl films was thought to be a search in temperature space of various phases with feedback from XRD spectra, but the lack of peaks for the first samples indicated additional difficulties where a lack of understanding was apparent. Therefore a new approach had to be taken, where it is understood that the L1$_0$ phase only occurs within the composition window 50-60 at.% Mn. The composition was probed by hard X-ray photoelectron spectroscopy (HAXPES), covered in more detail in chapter 5. This is an advanced version of X-ray photoelectron spectroscopy (XPS), which is normally only a surface sensitive measurement due to the energy of the

X-ray source. The increase in X-ray penetration depth with HAXPES allows capping layers to be used, thus allowing samples to be measured using other techniques such as VSM or XRD and remeasured on the HAXPES system as there are no oxidation effects.

The HAXPES measurements were carried out by Ben Spencer, a collaborator within the University of Manchester. As the system itself was only being commissioned during the course of this work it was not possible to gain access to the system directly. An example of the HAXPES measurement is shown in figure 7.3, where the peaks of interest are highlighted. The fitting procedure for these peaks was performed by Ben using CasaXPS software [185], where the Mn 1s and Al 1s peaks are used to identify their quantity within the material thus giving the composition of the film. At this stage it is also possible to probe any impurities in the film, such as carbon, by looking for its signal in the full spectrum.
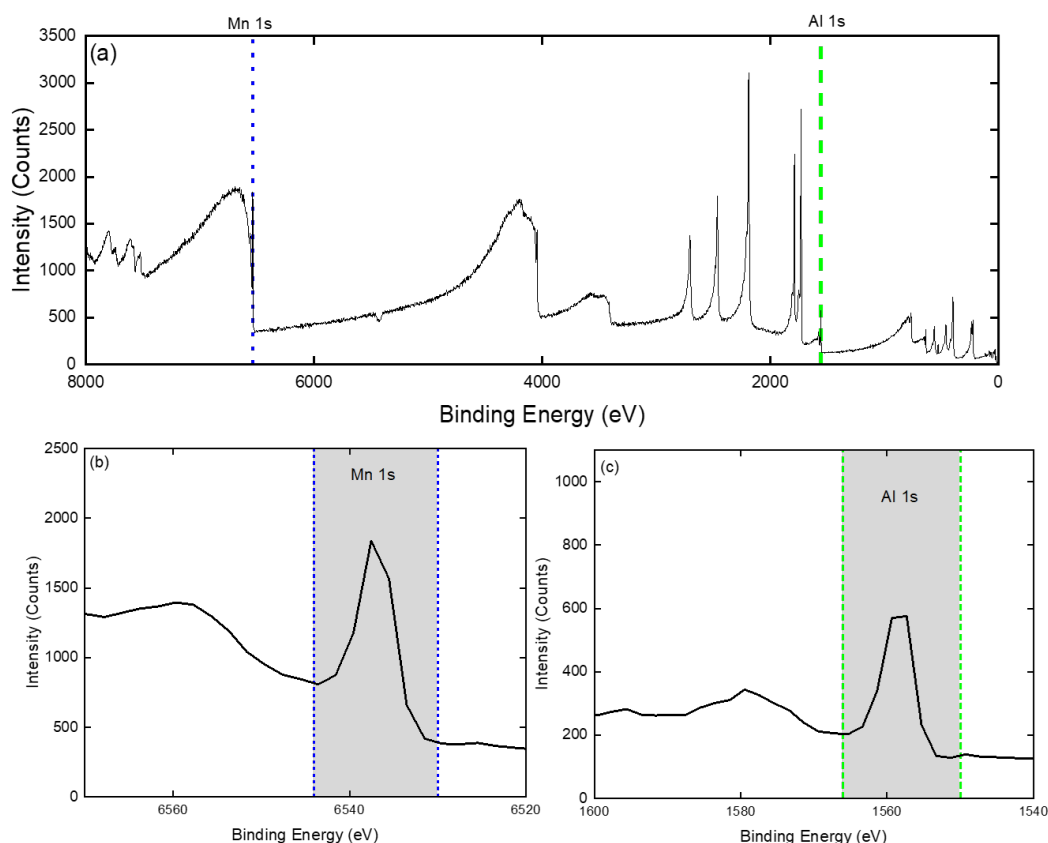
Figure 7.3: Full HAXPES spectrum (a) for 50 nm MnAl film on SiO_2 substrate using 40 W power for fabrication, zoomed in sections showing (b) Mn 1s and (c) Al 1s peaks used for analysis.

HAXPES compositional analysis was carried out by Ben Spencer on preliminary samples and showed that Mn is lost in the sputtering process, where for target powers of 20 and 40 W MnAl a composition of 32 at.% and 39 at.% Mn respectively was found, as shown in figure 7.4. The measured composition values are significantly and unintentionally outside of the expected 47 at.% and 54 at.%, obtained by using same composition target and deposition rate to literature [64].

In order to overcome the Mn deficiency and ensure the composition is within the $L1_0$ phase window a Mn target, purity 99.99 at.%, is co-sputtered during the deposition. The study using additional Mn covers the composition window for the $L1_0$ phase, as shown in figure 7.4. Multiple samples were fabricated with varying powers on the co-deposited Mn target, where the maximum wattage through the Mn and MnAl targets is limited due to the sensitivity of these materials, where large powers can cause cracking thus allowing deposition of the copper backplate.
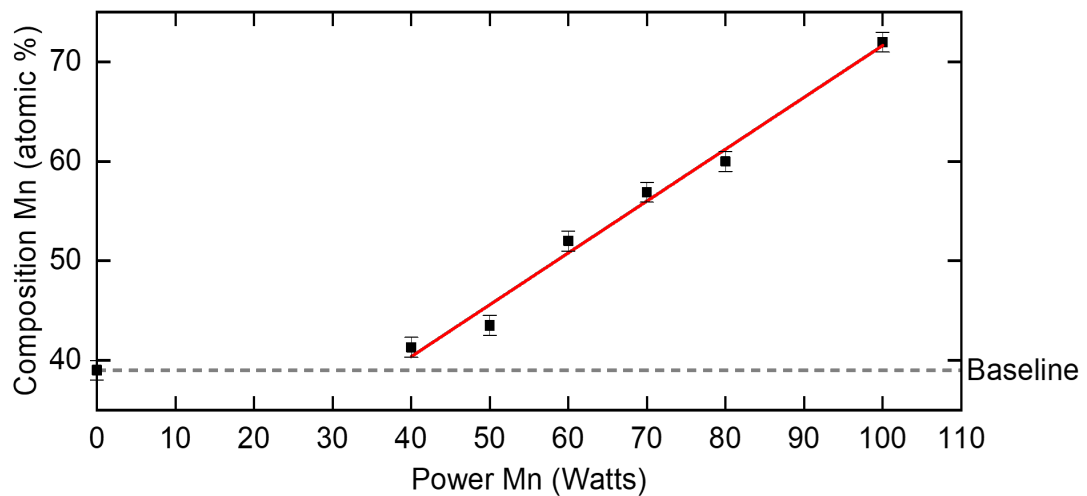
Figure 7.4: Composition of MnAl films as a function of Mn gun power in watts (MnAl kept constant at 40 W) with a line of best fit for co-deposition of Mn, measured using HAXPES.

There is a baseline for the composition given by solo deposition of the MnAl target, in this case 39 at.% at 40 W. The linear increase in the Mn composition corresponds to an increase in the co-deposited Mn power, which corresponds to an increase in the deposition rate of the material. The linear response of the composition allows manipulation of Mn power to remain within the desired window of 10 at.%. It should be noted that the baseline composition measured contradicts similar studies for MnAl shown

by [64], where they report that the composition of the target material closely matched that of the sputtered film.

As the measured composition of the films falls substantially below the predicted values a correction factor is used to compare values. The correction factor is represented by the composition as deposited and that predicted from literature, in this case a 1.4 reduction to Mn (71% of expected value obtained), where the equation of conversion is:

$$\text{Composition Predicted} = \text{Correction Factor} \times \text{Composition Measured} \qquad (7.2)$$

Possible causes for the discrepancy are the large vacuum chamber and corresponding distance between target and substrate increasing chance of collisions between particles. However, during testing, the Mn target was moved to a series of different positions on the outer ring of targets, see figure 4.9, while the MnAl target remained in a consistent position within the sputter chamber and no discernable difference was seen in composition. Therefore, the most likely case for composition variance is adhesion to the substrate surface, where energy of arrival of atoms play a key role. This hypothesis would account for the threshold value for the Mn target power shown in figure 7.4. However, further investigation would be required to confirm this explanation.

The sputtering system is as described in chapter 4, where for this study all targets have remained on the outer ring. Prior to deposition the cleaning procedure detailed in section 4.3.1 is carried out to ensure smooth growth of the initial layers. The deposition procedure determined after compositional correction with the additional Mn target is as follows:

1. **Target Cleaning** - A high working pressure (30 mTorr) is use to ignite the plasma at a low power, then held for 2 minutes with the shutter closed to remove any surface contamination from the target.

2. **Co-Deposition** - The working pressure is lowered to the desired value (1-3 mTorr) and the plasma allowed to stabilise on both Mn and MnAl targets before the shutter is opened for the deposition.

3. **Ramp Down** - The shutter is closed and the power reduced slowly to kill the plasma.

4. **Capping layer** - The same cleaning, deposition and ramp down procedures are followed for a capping material (Ta or Pt) used to stop oxidation of the MnAl film.

The target cleaning procedure ensures the removal of surface contamination from the targets surface prior to deposition, where the plasma power is increased slowly to prevent thermal shock of the target. The deposition step reduces the working pressure slowly to ensure the plasma remains ignited, where once a stable plasma is obtained the shutter opens and the sputtering process occurs for a defined period of time for the desired film thickness. Multiple target power combination on the Mn and MnAl targets are used throughout this work, therefore their values are detailed with relevant experimental results. To ensure the target material is protected once sputtering has finished and the shutter is closed the plasma power is slowly reduced to ensure no current/voltage spikes as the plasma decays. The final step is to apply a capping layer to the structure, thus protecting the film from oxidation and damage once removed from the chamber.

7.2.2 Structural characterisation of MnAl films

The desired compositions between 50 and 60 at.% Mn, corresponding to an additional Mn wattage between 60 and 75 W. Following the compositional analysis the phase formation of the film was investigated by XRD with in-situ annealing. The sample of choice was a 50 nm thick 40:60 W MnAl:Mn co-sputtered film, deposited at room temperature and annealed between 200 and 600°C at varying steps as shown in figure 7.5. The thickness of the film was chosen to allow more phase formation within the full structure that may then be optimised for $L1_0$ phase growth. The room temperature deposition shows no defined XRD peaks for the MnAl film but rather a broad feature corresponding to a section of closely packed $\varepsilon, \beta, \gamma$ and τ phases. However, after undergoing heating within the XRD systems heated stage covered in chapter 5, shown in figure 7.5, peaks began to emerge and remained after annealing, as shown by the before and after spectrum in figure 7.6.
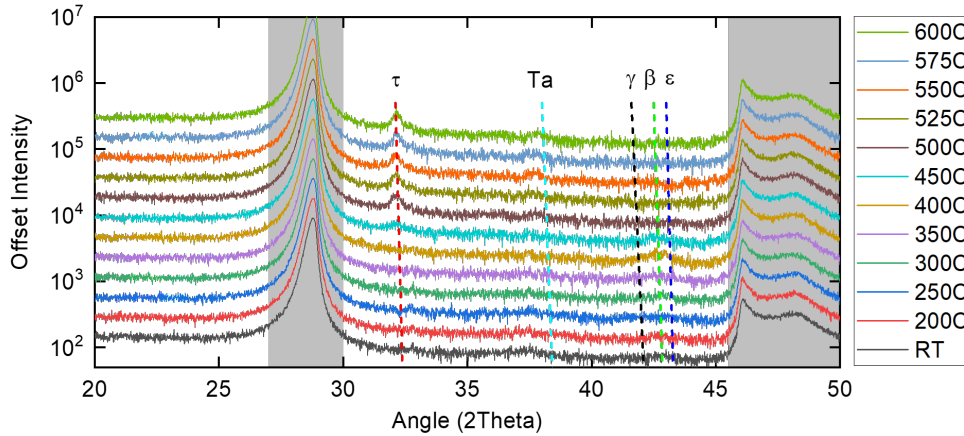
Figure 7.5: Heated XRD measurements for 40:60 W MnAl:Mn with reference lines showing the relative position for various MnAl phases, the shaded regions represent the graphite dome background signal.

Figure 7.5 shows that up to 400°C there is no discernable phase changes, but after 450°C there begins the formation of the τ phase. As the temperaure rises from 450 to 600°C the τ phase remains and the β, γ and ε phases do not increase. It can therefore be assumed that for depositions at room temperature, substantial annealing temperatures are needed to begin the phase change. The before and after XRD spectra shown in figure 7.6 confirm that the τ phase remains after the temperature is removed, therefore confirming the formation of the τ phase.
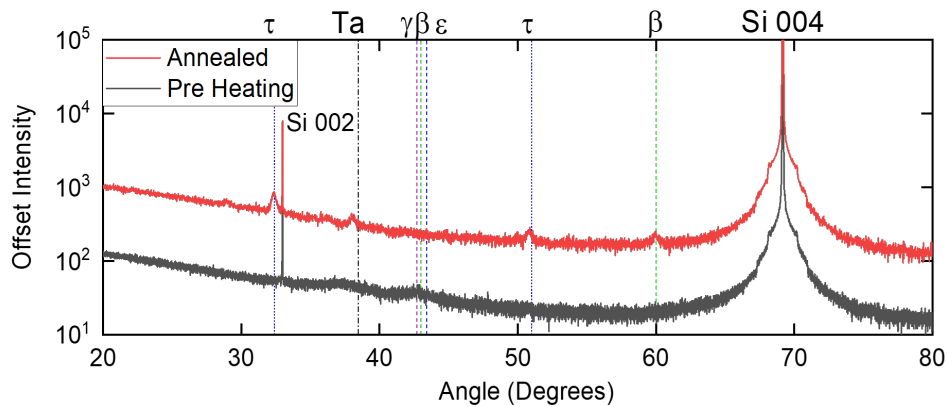
Figure 7.6: XRD spectrum for the sample before and after heating to 600 °C, with all peak phases for MnAl labelled.

The XRD spectrum of the annealed sample was measured using the low noise sample mounting plate that allows smaller peaks to be differentiated from the background signal. This allows the remains of some fraction of the β phase to be seen in the

system, as shown by the small peak at 60 degrees. However, the overall structure of the film shows good τ formation with a small tantalum peak due to the capping layer forming a crystal structure with annealing.

7.2.2.1 X-ray Diffraction Over Phase Boundary

The formation of the τ phase, for 40 W MnAl co-deposited with 60 W Mn, is confirmation of the compositional analysis, as only within the 50 to 60 at.% Mn window will this phase form. A study was carried out investigating lowering the Mn content of films to see these effects on the XRD spectra with temperature. Testing whether some small regions of the film might still form the τ phase for film of composition < 50at.%. A sample of same thickness (50 nm) by co-sputtering MnAl at 40 W with 40 W additional Mn, which corresponds to around 42 at.% Mn as shown in figure 7.4. The XRD spectrum for this sample was measured from 300°C to 600°C as shown in figure 7.7. The results show the formation of the γ MnAl phase associated with the composition moving away from the desired 50:50 region of the phase diagram, where some segregation of Mn within the film, as shown by figure 7.7, this is shown by the formation of β-Mn for a less Mn rich film.
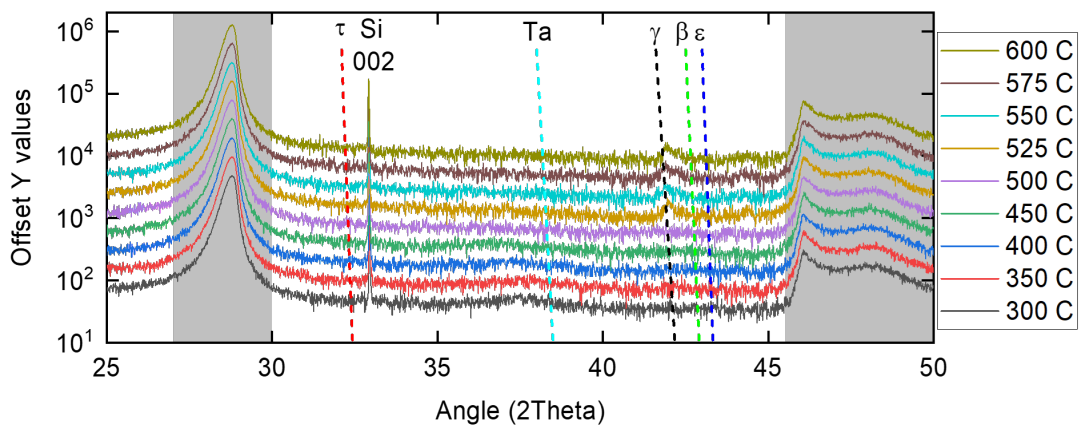
Figure 7.7: Heated XRD for a less Mn rich sample, using 40:40 W MnAl:Mn. Where the dominate phase growth is γ-MnAl

The two annealed XRD spectra for both the 40 W and 60 W Mn co-deposited samples, corresponding to 42 and 52 at.% Mn respectively, give confidence in the HAXPES compositional analysis as the lower Mn sample gives the expected phase changes when consider the phase diagram as previously shown in figure 3.12. Plotting the two composition annealed XRD's shows how much they differ, where there is no indication of

any phases from either side of the composition window in the 60 W sample.
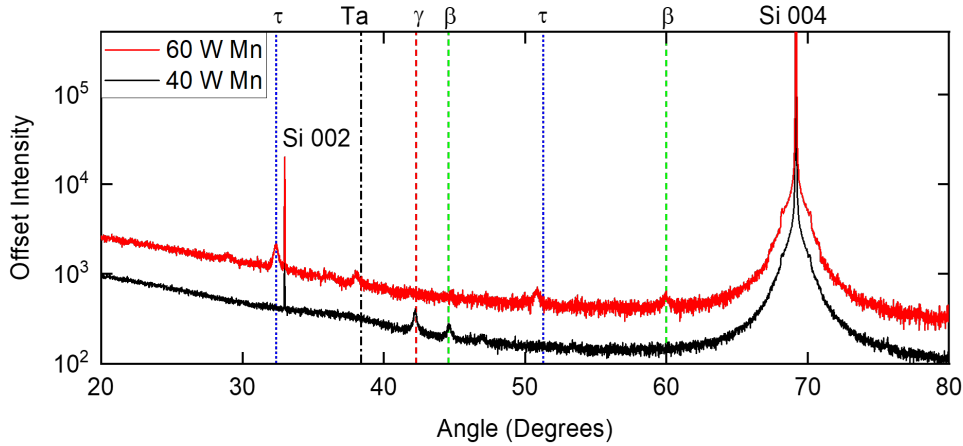
Figure 7.8: Post annealed (600°C) XRD spectrum showing phase formation as a function of additional Mn sputter power.

The unexpected composition variance produced by the target meant that multiple steps had to be taken to ensure full confidence in the measurement, where both the HAXPES analysis and XRD crystal phases agree. The origins of this inconsistency between results gained and those found in literature are still unknown, where it would take a more in depth analysis using computer simulations on the physics behind film formation on the surface of the substrate to fully grasp the problem.

7.3   Surface Roughness Optimisation using Low Pressure Deposition

The confirmation of compositional certainty for 60 W Mn and 40 W MnAl co-deposition allows further optimisation of the fabrication process, where focus is moved from composition to the formation of the τ phase. To achieve further ordering in the system it must be both deposited at temperature and annealed, where a study was carried out in section 7.2.2 investigating the effects of annealing on the formation of the τ phase with annealing temperature. A new series of samples were investigated for the annealing temperatures effect on surface roughness, where the working pressure of the deposition was kept constant at 3 mTorr to ensures plasma stability, with a deposition power of

40 W MnAl and 60 W Mn. As the deposition temperature is increased, a temperature normally used to achieve ordering in MnAl (350°C) [15] the roughness of the films increased, this is shown in figure 7.9 with values given in table 7.1.
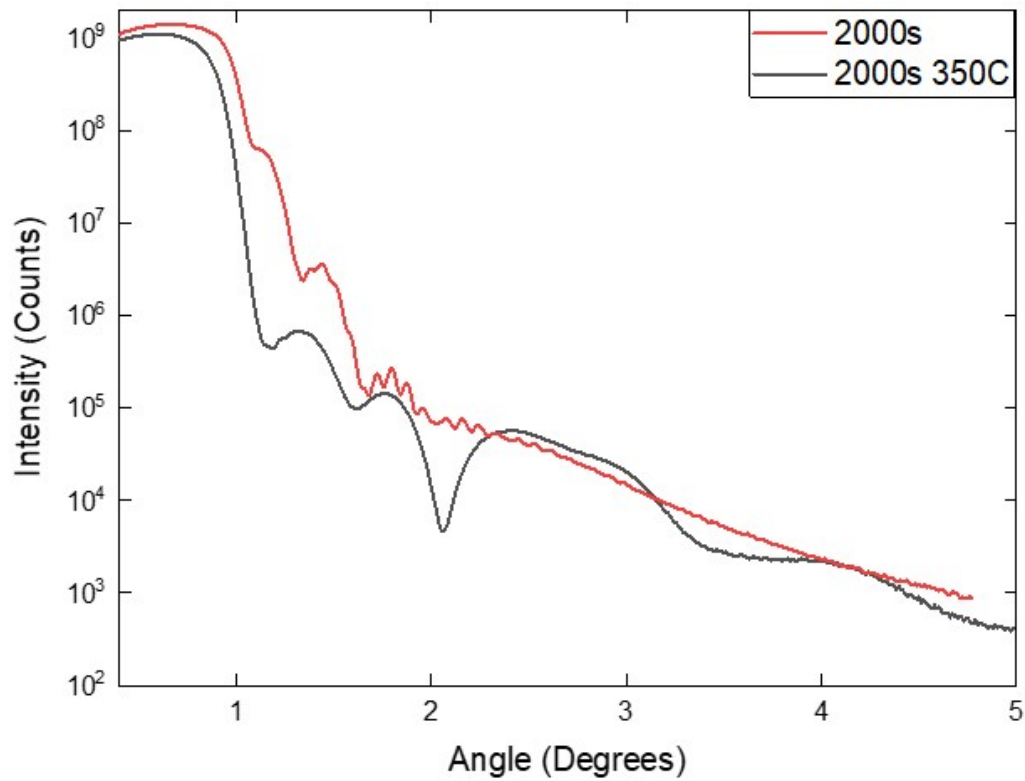
Figure 7.9: X-ray reflectivity for a 2000 s room temperature (FOM 0.028) and 350°C (FOM 0.072) deposition using 40 W MnAl and 60 W Mn.

Temperature °C	MnAl Thickness (nm)	MnAl Density (g/cm^3)	MnAl Roughness (nm)	Figure of Merit
RT	86.46	6.74	2.14	0.028
350	83.26	6.84	6.71	0.072

Table 7.1: Results from fitting XRR measurements for RT and 350°C deposited MnAl layers in figure 7.9.

The XRR profiles shown in figure 7.9 indicate both roughness and density changes, associated with a smoothing of the profile and change in critical edge angle respectively. The values obtained for roughness of the MnAl/Ta interface from fitting the XRR spectra is ≈ 2 nm for room temperature deposition and as high as 6 nm for those at temperature. However, the fitting becomes difficult as the roughness increases to values greater than 2 nm as the fringes associated with the MnAl layer are smoothed, this effect of roughness on XRR profile was first shown in the background on XRR in section 5.3.3. It has been determined that as the deposition of the MnAl layer is increased the surface roughness increases to an extent that the capping layer (Ta of thickness >5 nm) was not continuous and would therefore not stop oxidation without an increase in Ta layer thickness. However, increasing the capping layer thickness has an adverse effect on both compositional analysis, as the X-rays wouldn't penetrate as far into the sample, and XRD spectra as it produces Ta peaks close to MnAl phases. Therefore in order to move forward with temperature deposition the surface roughness must be minimised.

To further optimise the fabrication process of MnAl an investigation to reduce the surface roughness for room temperature deposition was carried out. Multiple samples are made with varied working pressure of the argon gas used for deposition between 1 and 9 mTorr for a consistent co-deposition power of 40 W MnAl and 60 W Mn. As the argon pressure in the sputter chamber is reduced, the energy distribution of the Ar ions is narrowed, therefore the rate of deposition for the Mn and Al atoms increases as more Ar ions are in the higher energy regimes [186]. The benefits of faster deposition include; reduced contamination, faster throughput of samples, and reduced heating of the target material. The mean free path of the depositing elements is also increased as the pressure is lowered, as was shown previously in figure 7.1 for the deposition chamber. The larger mean free path ensures that both the Mn and Al atoms have undisturbed paths to the substrate. The results from fitting multiple XRR datasets is summarised in figure 7.10, where the key elements of roughness and thickness are shown.
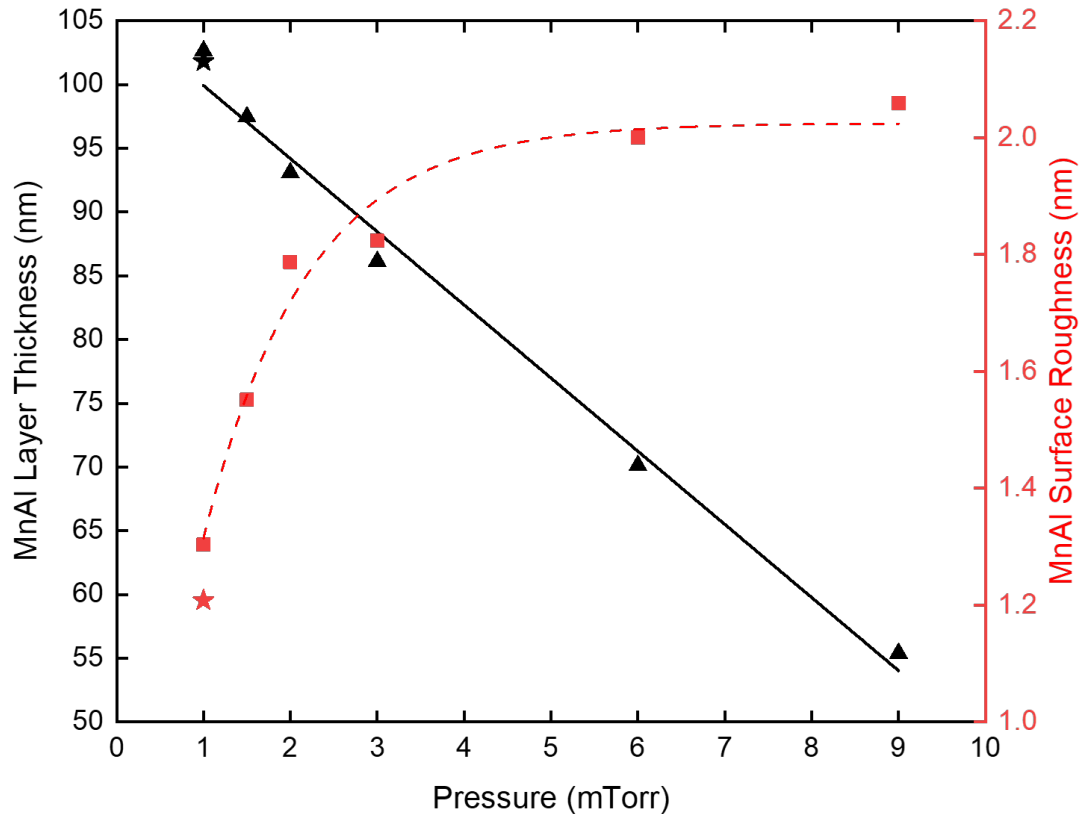
Figure 7.10: Fitting results for a series of deposition pressures, where the 1 mTorr condition has a second sample indicated by the star measured to ensure repeatability.

As the pressure of the argon gas used for deposition is reduced the roughness of the films decreases, as shown in figure 7.10,where all deposition and measurements were carried out at room temperature. The reduction in roughness of the film is linked to the reduction in the energy distribution of the argon ions [186].

The reduced pressure deposition investigation is built upon by also considering its effects on deposition temperature, where a comparison is made between RT and 200°C depositions for a standard sputtering power of 3 mTorr and the smallest roughness producing pressure 1 mTorr. The thickness and roughness of the films are measured by XRR, where the measurements are shown in figure 7.11 and the values obtained from fitting given in table 7.2.
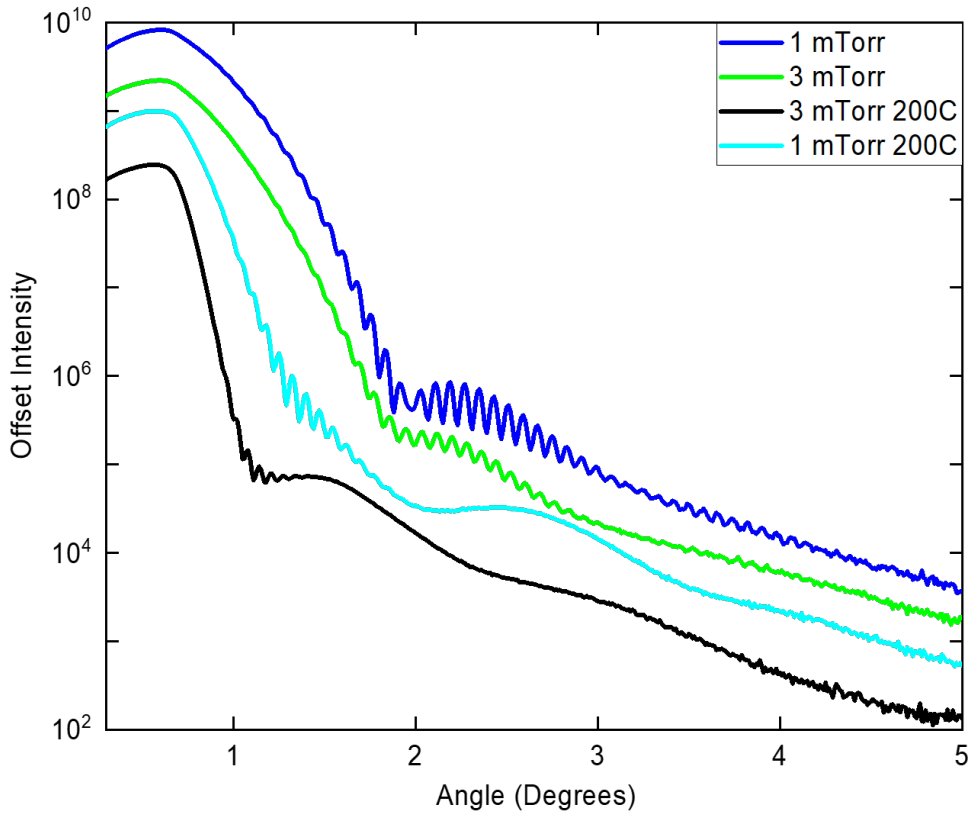
Figure 7.11: X-ray reflectivity measurements for 1 (FOM 0.027) and 3 mTorr (FOM 0.072) deposition powers at both room temperature and 200 °C.

Pressure mTorr	Temperature °C	MnAl Thickness (nm)	MnAl Density (g/cm^3)	MnAl Roughness (nm)	Figure of Merit
1	RT	102.65	6.14	1.66	0.027
1	200	102.66	6.96	2.42	0.051
3	RT	86.13	6.10	2.80	0.061
3	200	86.34	6.36	4.34	0.072

Table 7.2: Results from fitting XRR measurements for 1 and 3 mTorr pressure with RT and 200°C temperature depositions of MnAl layers in figure 7.11.

Comparing the 3 and 1 mTorr XRR profiles show the effects of a smoother film; where the fringes are more pronounced, with increased amplitude and remain at a higher angle, all of which are associated with smoother films. The films deposited at 200°C

show the same trend as the room temperature deposited samples, where the fringes amplitude is greater, and there are more of them. The 200°C 1 mTorr sample is comparable to the 3 mTorr room temperature sample in terms of roughness and structure. Depositing at temperature still increases the roughness as shown by the increase in gradient after the critical edge. Although this increase in roughness is undesirable it is something that should be expected as the mechanism for growth of the film changes with temperature, where energy barriers for phase formation change and therefore how the film grows changes modes as was shown in the Thornton model on background of sputtering in section 4.2.4. An investigation into the additional effects of annealing temperature have not been carried out, but it has been shown in literature [15] that the effects on roughness are smaller when compared to deposition temperature. Priority for investigation has been given to first forming the $L1_0$ τ phase in the MnAl films with as little variables as possible.

Alloy Target Deposition Summary

There is a lack of ferromagnetic properties for the films produced by co-depositing MnAl and Mn, as shown in figure 7.12. The diamagnetic response of the film comes from the substrate and non-magnetic film, where the XRD spectra was shown previously in figure 7.6. The XRD showed a small presence of the τ phase, but no magnetic properties were found for the film.
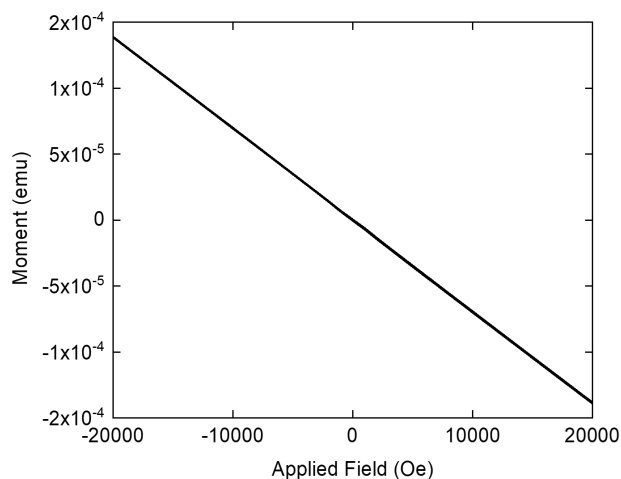
Figure 7.12: VSM measurement for 40 W MnAl and 60 W Mn deposited film annealed at 600°C.

The lack of any ferromagnetic properties in the film are linked to both a small fraction of the film being in the $L1_0$ τ phase and also problems in the preparation process for the VSM measurements. To measure samples using the VSM it must first be cut to size, during this process the sample is stuck to a aluminium plate face down using

wax, this is to protect the surface of the film during the grinding process where it cuts from back to front surface. The sample has a small portion cut to fit within the VSM and match the calibration sample size, where the wax is removed by soaking in acetone followed by IPA. However, it is believed that the removal of the wax also removes a some portion of the MnAl film. In order to overcome this issue for the following sections the samples are scribed to remove the waxing process.

Progress has been made in the optimisation of the fabrication procedure using an alloy MnAl target. However limitation in power for deposition make remaining within the desired composition difficult, where higher power can cause the target material to crack. The upper limit of both Mn and MnAl target is 60-80 W, any higher deposition power cause sufficient heating to crack to the surface thus showing the copper backing plate. To remain within the desired composition window of 50 to 60 at.% Mn the Mn target has had to be within the upper limit of sputtering power, therefore a new procedure was needed if the films properties were to be optimised further.

7.4   Co-Deposition of Mn and Al

To overcome fabrication limitation when using the alloy target an alternative co-deposition from 99.99 at.% pure Al and Mn targets was investigated. The deposition rates of both the Mn and Al targets was measured separately using XRR, where the power used for deposition was varied from 20 to 60 W for 1000 s to characterise the limits of powers used. The rates of each material is then altered so that the desired 52:48 at.% Mn:Al is achieved when co-depositing. This is possible due to the linear response of the sputtering rate, as shown in figure 7.13.
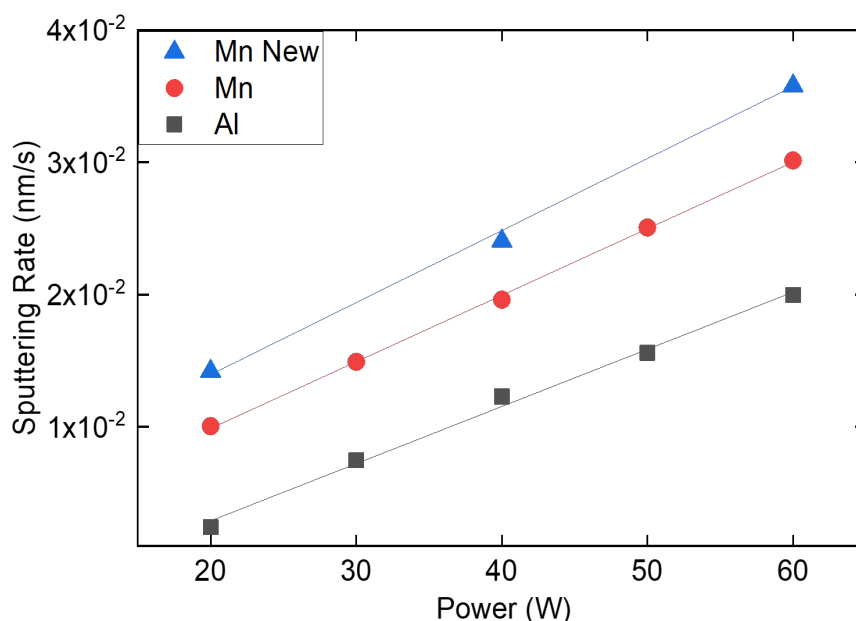
Figure 7.13: Sputtering rate for Mn (old/new) and Al target at various powers, with constant depositing pressure of 1 mTorr.

Throughout this experiment the Mn target became quite worn and so to stop any contamination from the copper backplate a new target was acquired. The rate of deposition for the new target was also measured over the range 20 to 60 W. Due to the effects of the magnetron race track, the new sputtering target deposits slightly faster than the old target. This is a prime example for why periodic measurement of composition/deposition rate is needed to ensure consistency.

7.4.1 Compositional Analysis

Co-deposition of Mn and Al was performed, where the Mn wattage remained constant and the Al was varied to alter the composition of the films. The samples were deposited at room temperature and characterised by XRD, XRR and HAXPES to gain information on the crystal structure, thickness, density, roughness and composition. As the samples were deposited at room temperature there was no discernable XRD peaks, whereas the XRR measurements allowed the thickness, density and roughness of the films to be compared. The MnAl films followed the same deposition procedure as the alloy target where MnAl was deposited onto a Si/SiO$_2$ (290 nm) substrate and capped with Ta to form the structure Si/SiO$_2$ (290 nm)/MnAl/Ta/Ta$_2$O$_5$.

The deposition rates shown in figure 7.13 are used to calculated predicted composition for the MnAl films. The predicted composition values are obtained by using constant Mn wattage of 20, 30 and 40 W and varying the Al wattage so that the relative deposition rate between the two targets will vary, where a 1:1 deposition rate will give a 50:50 at.% film. The relative composition gained for each constant Mn power with varying Al power on the y-axis is shown in figure 7.14. As the Mn content in the film starts to saturate the alloy its gradient decreases, where it tends to 100 at.% Mn when the Al gun is at zero. The sputter power of Mn chosen for investigation represents (i) the lowest stable power (20 W), (ii) an intermediate step with room for optimisation (30 W) and (iii) a high energy fast deposition (40 W).
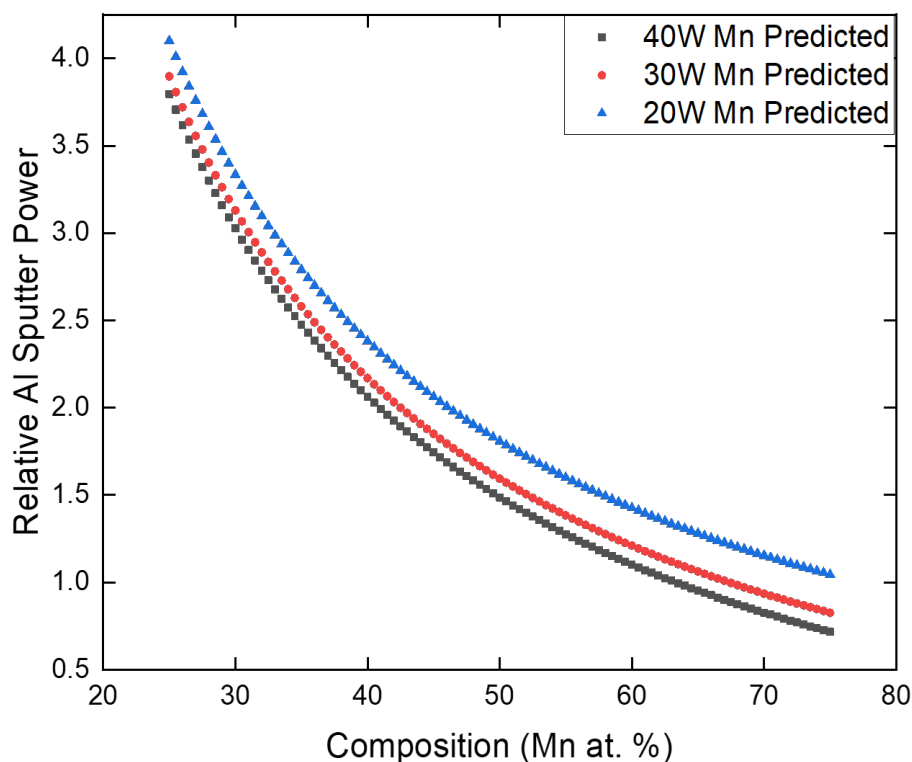
Figure 7.14: Predicted values for composition from Mn and Al rate tests.

Following the results from the predicted compositions a series of 4 samples were made for each Mn power. The combination of Mn and Al powers represent low, high and two intermediary compositions around the 50:50 at.% Mn:Al. These samples were characterised by XRR to ensure the thickness of the film was sufficient for compositional

analysis. The XRR measurements gave some insight into the change in the structure as the density of films varied from 2.2 to 2.7 g/cm^3. The quantity 'density' in this scenario is a representation of both materials density and composition, where the composition was set to a fixed value for all films and the density allowed to vary. However, the problem with this approach is that the density of each film produced would need to be identical for a true representation of compositional change between samples.

The fitted XRR measurements for the co-deposition of 30 W Mn with varying wattage Al are shown in figure 7.15, where the conversion multiplier from Mn power to Al power for each sample is given. The results of fitting all XRR datasets is summarised for all wattages in table 7.3.
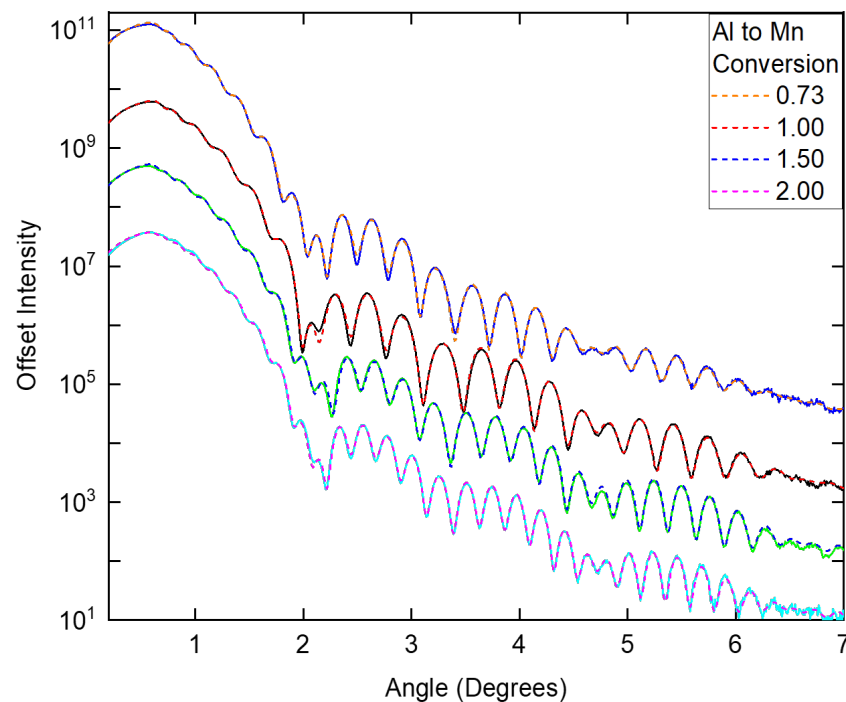
Figure 7.15: Fitted XRR spectrum for 30W Mn samples made for HAXPES compositional analysis.

Mn Wattage	Al to Mn Conversion	MnAl Thickness (nm)	MnAl Density (g/cm^3)	MnAl Roughness (nm)	Figure of Merit
40	0.75	32.86	2.71	0.8	0.014
40	1.00	33.15	2.67	0.7	0.025
40	1.38	39.10	2.52	0.6	0.034
40	2.00	48.37	2.24	0.8	0.018
30	0.73	24.71	2.66	0.6	0.022
30	1.00	27.78	2.71	0.8	0.024
30	1.50	30.80	2.48	0.6	0.030
30	2.00	35.88	2.51	0.6	0.029
20	1.25	18.73	2.43	0.5	0.022
20	1.75	22.12	2.44	0.5	0.015
20	2.25	25.77	2.33	0.5	0.014

Table 7.3: Results from XRR fitting of 40, 30 and 20 W Mn samples made for compositional analysis.

The XRR results shown in table 7.3 ensure that the thickness of each sample is in a measurable range for the HAXPES system. The roughness of the films mimics the substrate itself showing optimal growth of the film, where the previous study in section 7.3 on deposition pressure for the alloy target enabled low roughness growth. The samples listed in table 7.3 had their composition measured using HAXPES, where the measured compositions is given in figure 7.16 along with a new fit following the same trend as the predicted composition. The four samples for 30 and 40 W Mn span the desired composition window of 50-60 at.% Mn, but the 20 W Mn was not able to hold a stable plasma for the Al target below 20 W.
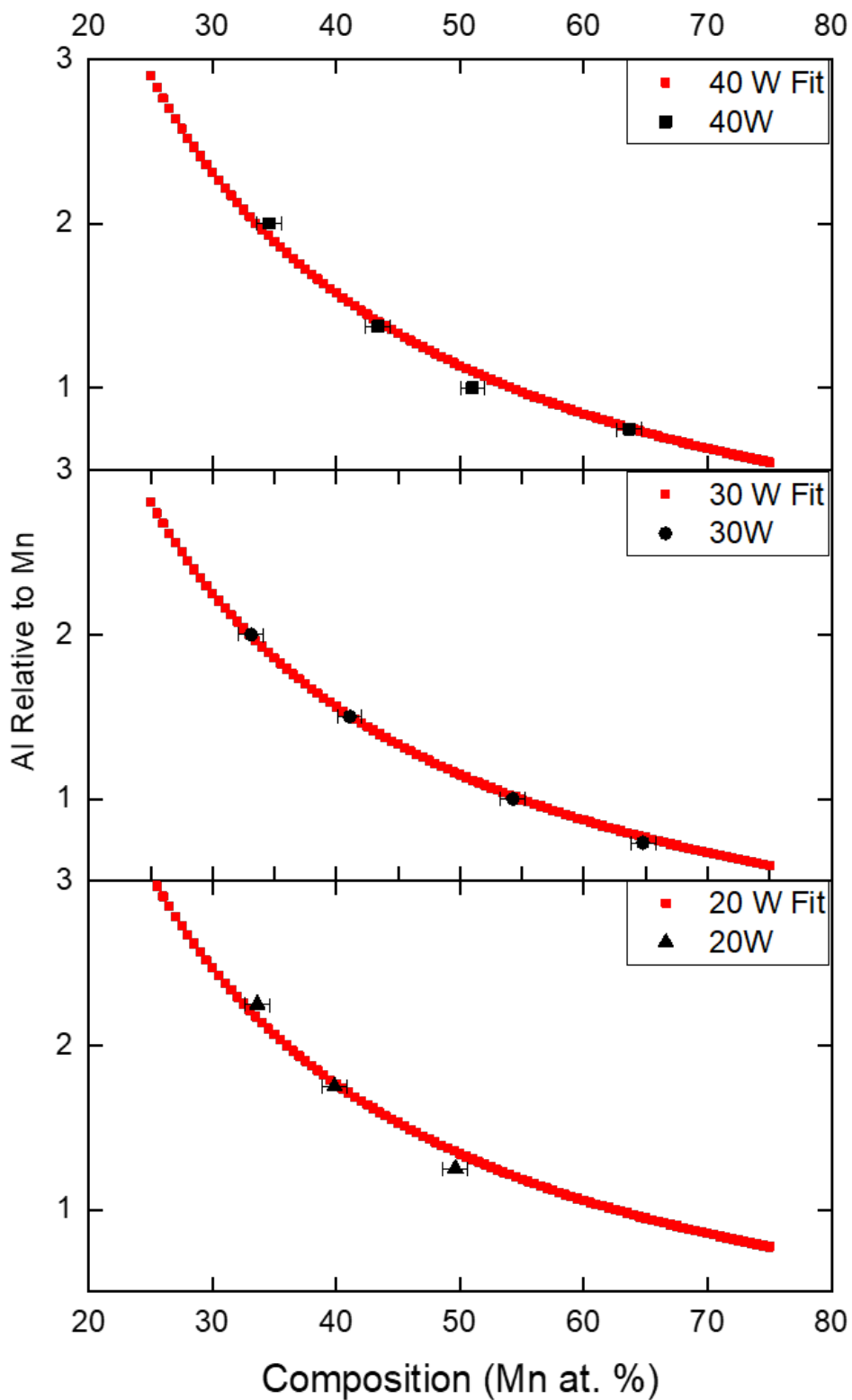
Figure 7.16: Co-Deposition composition results from HAXPES measurement of sample series, 40, 30 and 20 W Mn with varying Al wattage.

The composition measurement for the Mn power series has a reduced Mn content when compared to the predicted values obtained from XRR fitting. However, a correction factor can be applied to the predicted trend to obtain the fit shown in figure 7.16. The drop in Mn content is between a factor 1.3 and 1.4 lower than prediction shown in figure 7.17, where the MnAl alloy target gave a value of correction value of 1.4 in section 7.2.2. The difference in composition obtained has a substantial impact on the materials usability, as it shows different system setups may produce substantially different compositions of the final film. The reasoning behind the loss of Mn is still unknown, but it is believed to be due to adhesion of Mn on the substrate surface, where Al will stick readily to the surface making it Al rich.

The correction factor, first described in section 7.2.1, obtained for each power of Mn is shown in figure 7.17, where all measured powers are within error-bars. The reduced value obtained for the 20 W samples is thought to be due to the lower energy Mn sticking more readily and therefore the correction is smaller. There is also the contribution from Al to consider, where lower energy Al deposition will mean any collision that occurs between removal from the target and arrival at the substrate surface will likely cause the depositing atoms to never reach the desired destination.
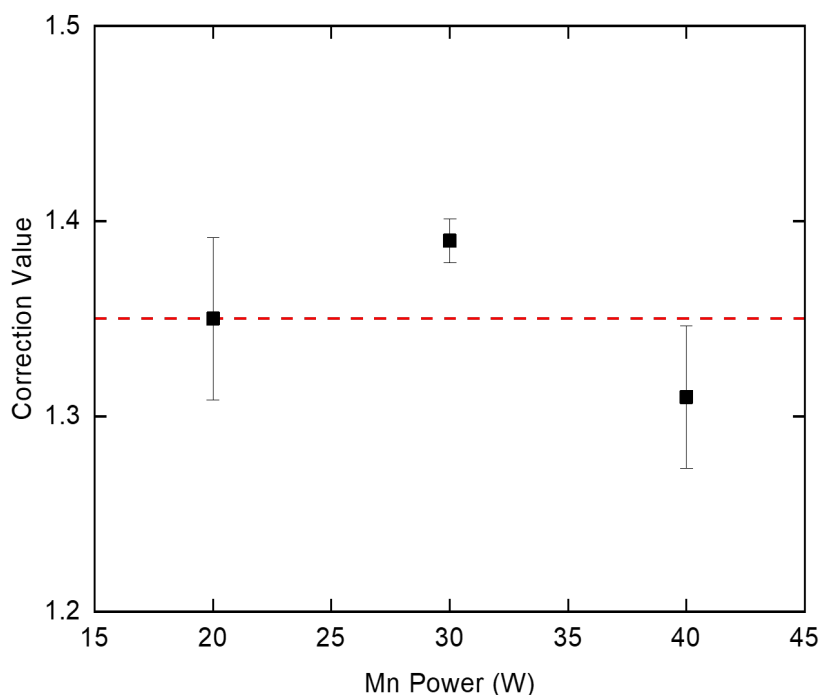
Figure 7.17: Correction values between predicted Mn content and those obtained through HAXPES for 20, 30 and 40 W Mn gun sputter power.

The best agreement between the corrected predictions from the XRR results and the HAXPES measured composition are for the 30 W Mn samples. The use of 20 W Mn is not possible for further study as the lower limitations in Al power with a stable plasma restricts the composition to below 50 at.% Mn. Additionally, as the samples for this study were deposited at room temperature the plasma is most stable, where deposition and/or annealing temperature can cause further plasma instability, therefore 20 W cannot be used for further study.

The optimisation of the fabrication procedure for MnAl looks to encourage the growth of $L1_0$ phase, but as this material is to be used in devices, where it will be placed in intimate contact with other layers, it is also vital that the surface roughness is minimised. The roughness of the 30 and 40 W Mn samples are within 0.2 nm of one another, but the 30 W samples are more consistently on the lower end of 0.6 nm roughness range, as was shown in table 7.3. Therefore moving forward 30 W Mn is used, as this falls within an optimal position for fabrication optimisation whilst also having the best composition agreement between predicted and obtained values.

7.4.2 Structural characterisation as a function of deposition temperature

The measurement of composition for MnAl films was described in the previous section, where a correction factor is applied to the fabrication procedure to reach the desired composition between 50 and 55 at.% Mn. Although the $L1_0$ ordered state spans 50 to 60 at.% Mn the best magnetic properties have been produced for those below 55 at.% Mn, and so the composition is kept under this value. To optimise the formation of $L1_0$ phase the deposition temperature was investigated, where a room temperature deposited MnAl film produced no order as shown in figure 7.18, which is the same as the previous study using alloy target deposition. The lack of order in the system is believed to be due to energy barriers halting phase propagation of the metastable τ phase. To induce order in the system samples were deposited at 150, 300, 450 and 600 °C. The working pressure for all samples was kept constant at 1 mTorr with powers of 30 W on Mn and 32 W on the Al target, corresponding to a composition of 52 at.% Mn.
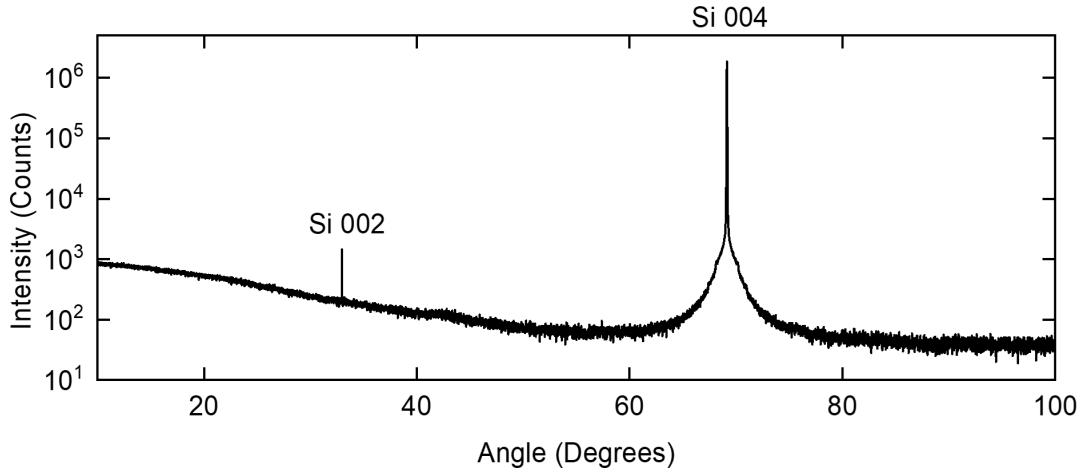
Figure 7.18: XRD for room temperature deposition at $\approx$ 53 at.% Mn, the smaller peak at 32°is a forbidden satellite peak from the substrate.

The temperature range for deposition under investigation is 150 to 600 °C, where the lower range should ensure the film is as smooth as possible whilst also helping promote alternative phase growth. The higher temperature deposition helps to overcome energy barriers but also run the risk of forming the high temperature ε phase. The resulting XRD data for all temperature measurements is shown in figure 7.19, where steps of 150 °C are used to ensure no intermediate phase growth is missed.
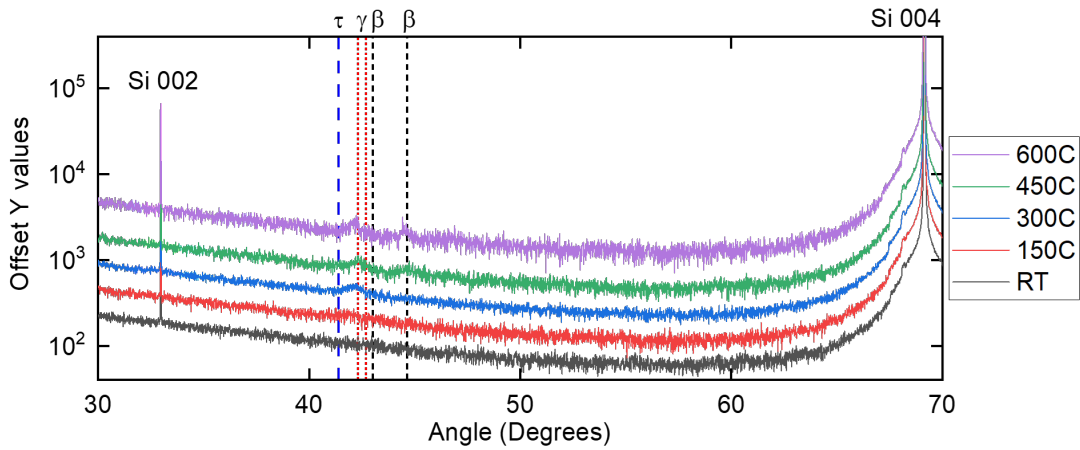
Figure 7.19: XRD as a function of deposition temperature for 53 at.% Mn on SiO2 substrates. Th data are offset on the y-axis to aid readability.

As energy is added to the system and the temperature increases there is a shift in the preferred phase growth, this is seen by the MnAl peak shifting from predominately γ growth to a competition between the γ and β phases. The thickness of these films was

characterised by XRR, as shown in figure 7.20 with results summarised in table 7.4. As temperature is added into the system not only is the phase growth changing but the roughness is increasing.
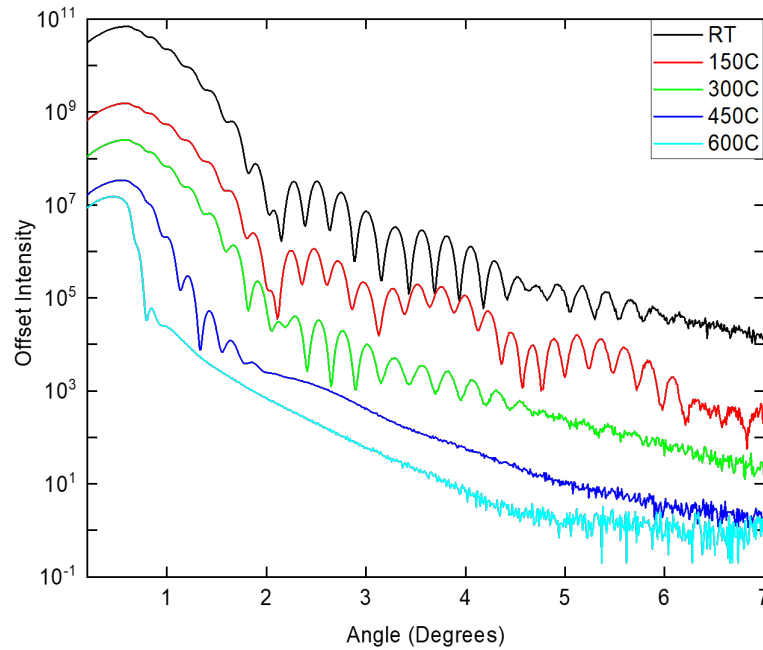
Figure 7.20: XRR as a function of deposition temperature for 53 at.% Mn on SiO2 substrates.

Deposition Temperature °C	MnAl Thickness (nm)	MnAl Density (g/cm^3)	MnAl Roughness (nm)	Figure of Merit
RT	32.90	2.53	0.70	0.046
150	33.29	2.56	0.48	0.051
300	33.02	2.65	1.04	0.051
450	34.16	2.56	2.61	0.054
600	36.03	2.55	4.07	0.078

Table 7.4: Summary of MnAl layer parameters determined by modelling the XRR data using GenX for heated deposition.

The XRR profiles give the structure of the film, where beyond 300°C the roughness exceeds a useable range ($<$2 nm). This increase in roughness is likely due to the β Mn phase growth, where islands of Mn will form preferentially within the film causing

the large increase in roughness. For the room temperature to 300°C measurements it is clear that some changes are occurring, as the periodicity of peaks changes and the higher angle is damped more, which is an indication of increased roughness.

The thickness measurements show that as temperature is added to the system the thickness increases slowly, likely due to Mn and Al forming β and γ phases readily. This coincides with the increase in roughness, where island formation of various phases cause increased roughness. The fitting of the 450 and 600°C XRR measurements is only possible due to their similarities (density and capping layer) with the lower temperature deposited samples, as the roughness has reached a point where the fringes are suppressed significantly increasing the uncertainty in the fit. Therefore the results of these fits are reasonable estimates but should be treated with caution.

7.4.3   X-ray Diffraction with additional In-Situ Heating

The formation of the desired metastable τ phase is normally achieved by a two stage process; (i) deposit MnAl at an elevated temperature and (ii) further anneal the material to form the desired phase structure. The smoothness and composition of MnAl films has been optimised so far, where deposition at temperature is yet to yield the desired phase. To further the understanding of phase formation for fabrication the room temperature, 150, 300 and 450 °C deposited samples are further annealed from 150 to 600 °C whilst measuring their crystal structure using XRD. These measurements are vital in the understanding of phase growth within the material, where having multiple deposition temperatures allows a large parameter space to be investigated.

XRD measurements with in-situ heating is covered in detail in chapter 5. The measurements carried out use a ramping rate of 10°per minute and allow the sample to thermalise for at least one hour before measuring. During the heating and measurement process the sample is encapsulated in a protective graphite dome, which holds a vacuum down to $1x10^{-3}$ mbar. Once the heating and measurement procedure is complete the sample is allowed to cool under vacuum, ensuring no oxidation/damage to the sample occurs.

The various phase growth of each material will now be described in ascending temperature, starting with the room temperature deposited sample. The sample deposited at room temperature gives a good indication of how deposition and annealing temperatures vary the properties of the film. The deposition temperature began to show some

phase formation as soon as 300 °C but annealing of a room temperature deposited sample does not show peak formation until 500°C, as shown in figure 7.21.

Figure 7.21: In-situ heated XRD measurements for room temperature deposited MnAl film with 30 W Mn and 32 W Al. Shaded regions represent the graphite dome background signal.

The formation of the γ phase does not occur until 500°C in the room deposited sample. The temperature at which this phase change occurs is associated with difficult to overcome energy barriers formed during the deposition stage. The XRD spectrum of the sample before and after annealing is shown in figure 7.22, where it is discovered that phases formed at temperature remain after cooling.
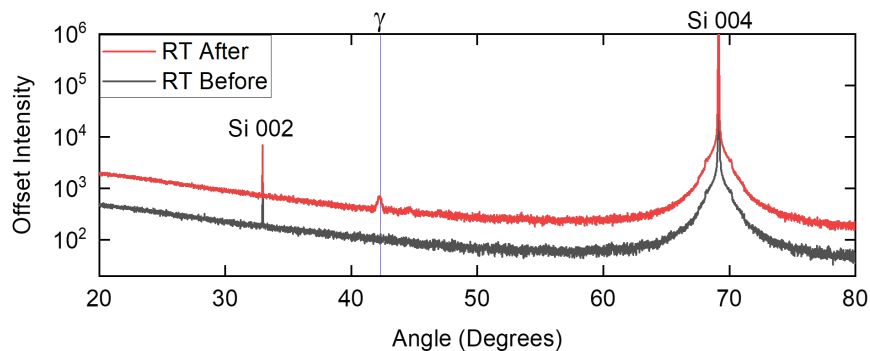
Figure 7.22: XRD spectrum for room temperature deposited MnAl film before and after annealing to 600°C. Measurements at RT using the low noise sample Si (531) stage.

The desired τ phase is not observed for any anneal temperature, but interestingly phase changes appear after 450°C which was also found for the study using alloy target deposition, where the same temperature range for alterations is seen where only after

450°C. However, alloy target deposition showed the τ phase as shown by figure 7.5. Co-depositing shows the formation of the γ phase and not an equilibrium of γ and β, which potentially indicates the films inability to change structure, where the γ phase growth is preferential below 50 nm [64].

The samples deposited at temperature were investigated following the same procedure as the room temperature deposited sample. This investigation is used to characterise potential annealing temperature for the fabrication process. The XRD spectra for the 150°C deposited sample are shown in figure 7.23, where again no change is seen until 500°C.
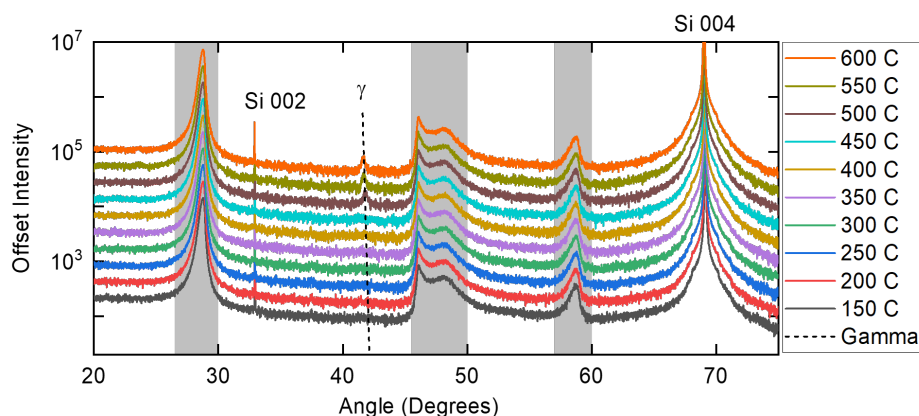
Figure 7.23: In-situ heated XRD measurements for 150°C deposited MnAl film with 30 W Mn. Shaded regions represent the graphite dome background signal.

The thickness and density measurements for the room temperature and 150°C deposited samples was almost identical, where the roughness of the 150°C sample was reduced. The XRD profiles for both these samples showed lack of phase growth and so it is not surprising that their annealing shows peak formation at the same temperature.

The as deposited and annealed XRD spectra for the 150°C sample are shown in figure 7.24, where it can be clearly seen that only the γ phase is produced.
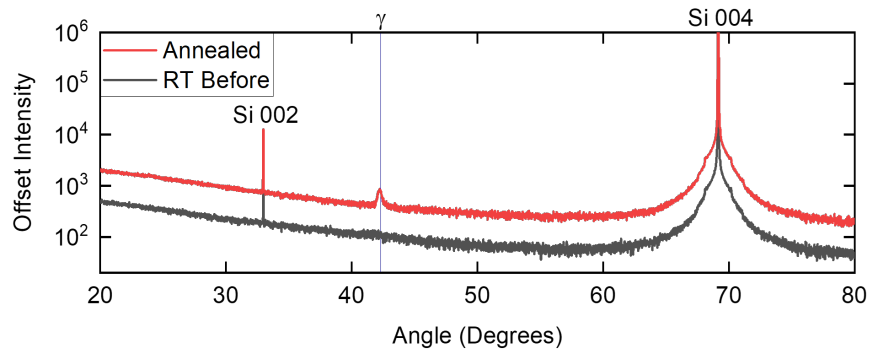
Figure 7.24: XRD spectrum for 150°C deposited MnAl film before and after annealing to 600°C. Measurements at RT using the low noise sample Si (531) stage.

Depositing MnAl at 300 °C has a similar film roughness when compared to the room temperature. However the crystal structure starts in a slightly ordered state with a very broad γ peak. As temperature is added there is no increase to the γ phase or formation of new phases, as shown by the heated XRD measurements in figure 7.25.
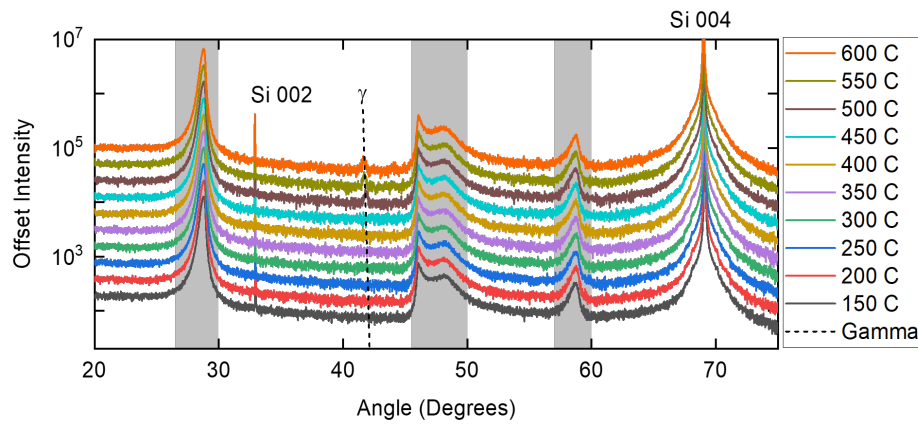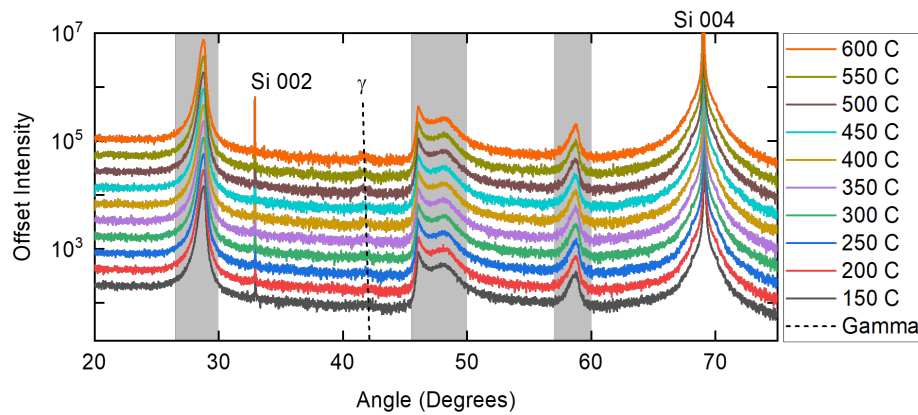

Figure 7.25: In-situ heated XRD measurements for 300°C deposited MnAl film with 30 W Mn. Shaded regions represent the graphite dome background signal.

The before and after heating XRD shown in figure 7.26 show that no changes have occurred to the film even though it was heated to 600°C, indicating that as the γ phase had already somewhat formed during the deposition stage it could not form another phase with heating. The wideness of the before and after peaks may also indicate that

there are alternative phases present as there is close proximity between the γ, β and ε phases, as was shown in figure 7.6.
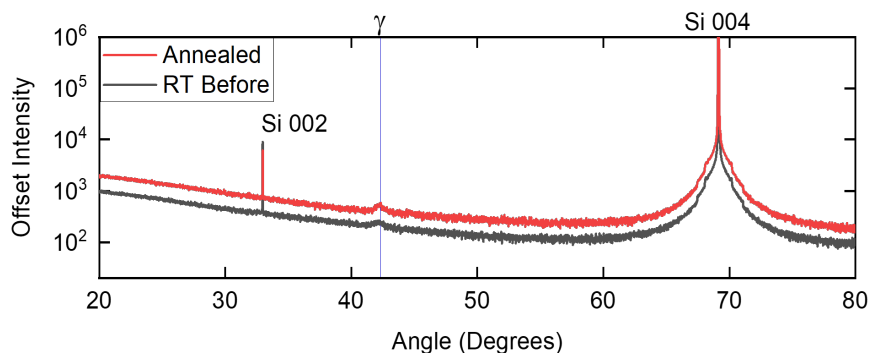
Figure 7.26: XRD spectrum for 300°C deposited MnAl film before and after annealing to 600°C. Measurements at RT using the low noise sample Si (531) stage.

The deposition temperature is seen to have a larger effect on the phase formation than annealing, where annealing temperature does not show effects until after 450°C on phase formation. This could be due to large energy barriers between the random phase formation and those formed through increased temperature deposition. The movement of Mn within the system could also be limited, as it is seen that γ phase grows preferentially at both low temperature and after annealing. The final sample measured through heated XRD shown in figure 7.27 was deposited at 450°C, where its starting position was already a somewhat mixed γ and β phase.
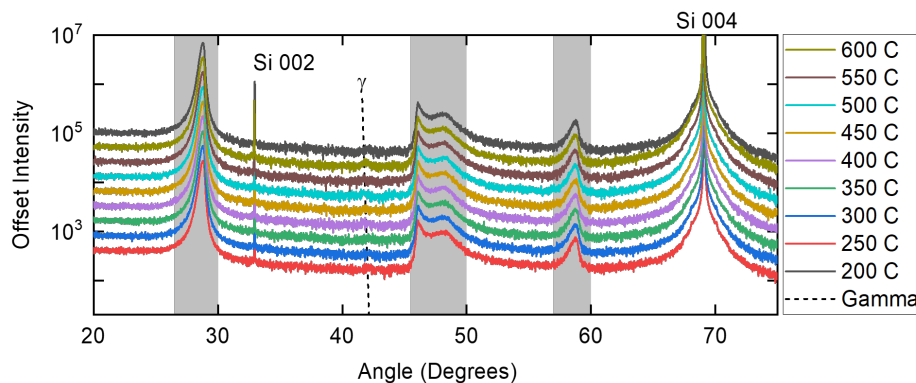
Figure 7.27: In-situ heated XRD measurements for 450°C deposited MnAl film with 30 W Mn.

The results obtained for the 450°C deposited sample show that as the equilibrium of γ and β phases is formed it becomes extremely difficult to change the properties of the film. The overall structure of the film does not seem to change over the full heating procedure, where before and after XRD shown in figure 7.28 show the same peaks.
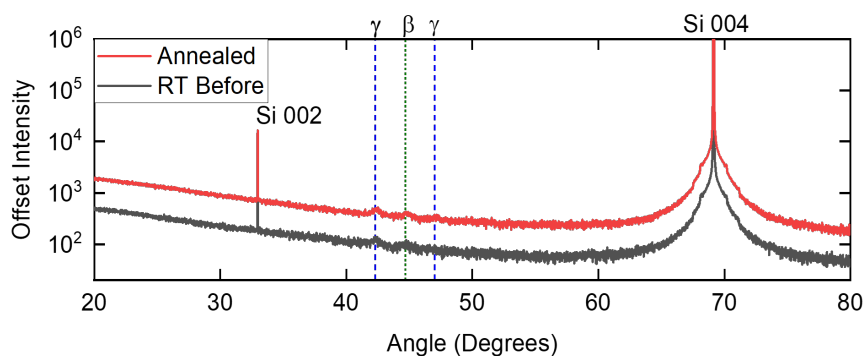
Figure 7.28: XRD spectrum for 450°C deposited MnAl film before and after annealing to 600°C. Measurements at RT using the low noise sample Si (531) stage.

The original film roughness was high (2.61 nm) and therefore the surface of the sample oxidised during the heating process. The surface is shown in figure 7.29, where oxidation of the MnAl layer occurs due to its roughness not allowing a continuous capping layer film to form.
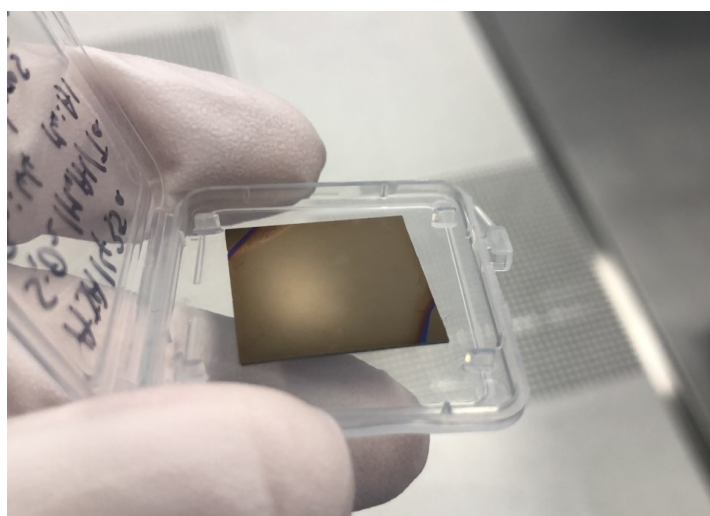
Figure 7.29: Tarnished surface of MnAl film post heating to 600°C under 1×10^{-3} mbar.

The capping layer thickness is minimised (<5 nm) to ensure XRD peaks from the Ta layer do not interfere with analysis, where peaks can be found at 32.7°and 38.5°. It was discovered that MnAl layers with roughness >2 nm oxidise during the heating procedure causing potential damage to the films properties. Therefore, any samples that posses substantial roughness must be capped with a thicker layer to ensure the films underneath are protected.

7.4.4   Magnetic characterisation of MnAl films as a function of deposition temperature

The magnetic properties of the MnAl films deposited at temperature were measured using VSM hysteresis curves. The XRD spectra for the films showed mainly a β and γ phase growth, which are non-magnetic phases. Therefore any signal gained from magnetometry measurements are indications that τ phase is present in the system as it is the only magnetically ordered phase for MnAl. The perpendicular and parallel applied field measurements for the 150°C deposited film show identical hysteresis curves in figure 7.30. This indicates that the sample formed randomly orientated ferromagnetic phase within the 3D film structure.
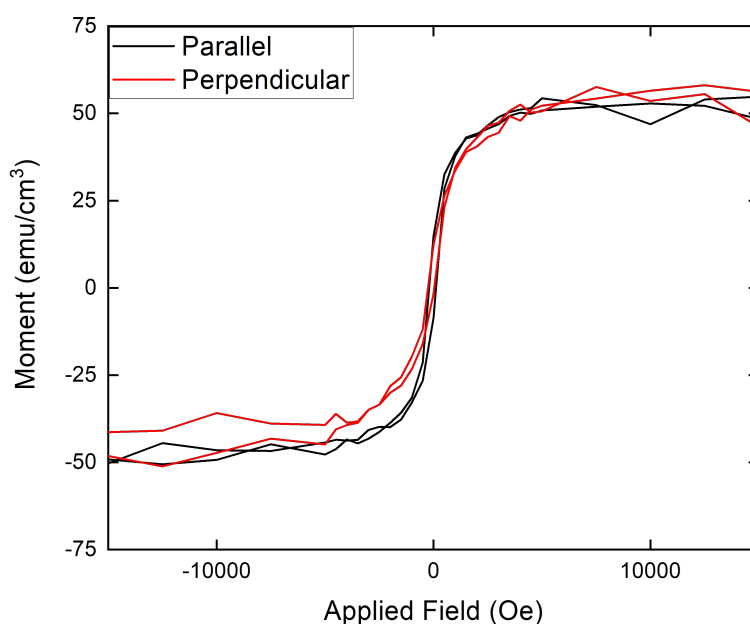
Figure 7.30: Hysteresis curves for in-plane and perpendicular applied field for 150°C deposited MnAl film (not annealed).

The noise present in the hysteresis curve is due to the small fraction of the total film volume that is in the τ phase, which explains the absence of τ phase in the XRD data. This noise is potentially increased by the sample preparation, where normal procedure is to cut a disc of the material matching a calibration sample of known magnetic properties. However, during the compositional analysis it was discovered that large quantities of Mn is lost if the sample is ground into a disc. This is thought to be due to poor adhesion of Mn, where any friction to the surface will readily remove Mn from the sample. To overcome this issue the samples are scribed and broken into small squares of similar size to the calibration sample. The various deposition temperature for MnAl films is measured by the VSM, where the parallel applied fields are compared in figure 7.31.
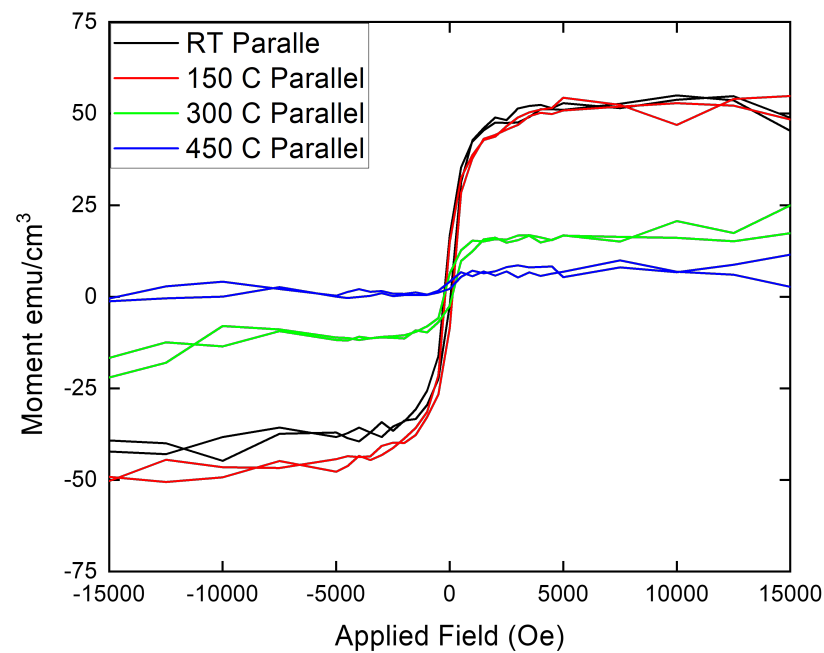
Figure 7.31: Hysteresis curves for in-plane applied field on room temperature, 150°C, 300°C and 450°C MnAl samples (all samples not annealed).

The hysteresis curves for the full series of deposition temperatures show an interesting effect, where the room temperature and 150°C samples have the largest magnetic moment but also have the smallest XRD signals. This indicates that as other phases form in the material the magnetic signal is lost, which is expected as only the τ phase

is ferromagnetic but this shows that it is being removed to form these other phases. The signal obtained from the 450°C sample is negligible, as it has almost completely removed any τ phase and formed the equilibrium state of γ and β phases.

7.5 Summary

The complex phase formation of $L1_0$ MnAl has been thoroughly investigated using both alloy and Mn/Al co-deposition sputtering methods. It has been found that a substantial loss of Mn occurs at the substrate surface due to, what is assumed to be, adhesion issues of the Mn. Comparison between the two sputtering approaches show that around 70% of the expected Mn content remains on the substrate surface after deposition. The fabricated films with capping layer for protection also show poor adhesion, where the application and removal of wax from the surface during sample preparations removes substantial amounts of Mn from the sample.

The use of HAXPES compositional analysis was vital to the work covered in this chapter. Although the values of composition fell below predictions it was possible to find a linear fit for alloy target doped with Mn and a correction factor for predicting co-deposition composition. Therefore moving forward with these materials it is possible to correct for compositional calibration after some initial study is carried out. The XRD spectra from both the alloy and co-deposition fabrication showed little to no τ phase formation, where samples needed a minimum of 450°C to change phase within the film. The reasoning behind this is still unknown, but can be assumed that energy barriers of the phases present in the system have a minimum activation point before they will make way for other phase growth.

The roughness of films plays a key role in their implementation in devices, where the surface roughness of MnAl films was improved from ≈ 2 nm to 0.6 nm by lowering the working pressure of sputter gas from 3 mTorr to 1 mTorr. The surface roughness also plays a key role in sample measurements, where it was discovered that sample with a roughness >2 nm would come out tarnished from heated XRD measurements due to limited vacuum within the graphite dome. The low pressure deposition has the added benefit of depositing much faster, therefore reducing risk of contamination during the fabrication procedure.

The formation of the $L1_0$ τ phase is notoriously difficult, where the various XRD measurements have shown that just being in the correct composition does not correlate to $L1_0$ ordering. The magnetometry measurements shown in figure 7.31 indicate that some ordering is being achieved within the film structure but not enough to give XRD signals. To encourage further growth within the system the film could be grown on choice seed layers/substrate to lattice match the τ phase.

Chapter 8

Conclusion and Discussion

This chapter summarises the results presented in this thesis for the fabrication of $L1_0$ ordered FePt and MnAl thin films using magnetron sputtering. These two materials have applications in spintronic devices, where they have the potential to offer enhanced functionality for next generation of magnetic data storage devices. However, the properties of these materials must be optimised and their growth methods fully understood. The studies reported in this thesis investigated; 1) the growth of both perpendicular and in-plane uniaxial magnetic FePt films using magnetron sputtering and 2) MnAl $L1_0$ ordering fabrication using magnetron sputtering of an alloy target and co-sputtering Al and Mn.

Significant progress has been made with both objectives with new results obtained as detailed in the following paragraphs. However, a PhD project has a finite time and, in large part due to the pandemic, the goals were not fully realised. The work reported here does provide a very clear path forward and a future plan for investigations of the materials discussed within this thesis is given.

8.1 Fabrication of Uniaxial FePt films

$L1_0$ ordered FePt was studied in depth in chapter 6 with focus given to creating a fabrication procedure that produced uniaxial in-plane magnetic alignment in FePt thin films using magnetron sputtering. The production of perpendicular magnetic anisotropy for FePt is widely reported, where a well-defined uniaxial magnetic alignment is needed

for the proposed exchange spring structure. A series of FePt samples of varying thickness (5, 10, 20 and 30 nm) were characterised by XRR, XRD and SQUID magnetometry to understand the film structure and magnetic properties. It was determined that 10 nm of FePt produces the best uniaxial alignment for further study.

There are very few reports on the fabrication of uniaxial in-plane FePt thin films. A notable report using MBE deposition for in-plane FePt by Farrow et al. [20] was taken as a starting point for magnetron sputter growth of uniaxial in-plane FePt. A series of deposition temperatures for FePt on MgO (110) substrate, with a thin (1 nm) Pt seed layer, was investigated to further the understanding of $L1_0$ growth. XRD measurements were performed with in-situ annealing for samples deposited at 300 and 500°C. These results demonstrated that an annealing temperature of 625°C produced the best ordered film. This findings produced by heated XRD analysis were confirmed by sputtering a 10 nm FePt film at 500°C and annealing at 625°C, where characterisation showed $L1_0$ ordering with preferential growth of the (110) plane. VSM measurements of both hysteresis loop and dc demagnetising curves showed uniaxial alignment of the magnetic properties in-plane, where fine rotation measurements showed large differences for a 90 degree rotation in-plane. However, the applied field available was insufficient to saturate the sample. SQUID magnetometry measurements were used to fully saturate the 10 nm FePt film with in-plane uniaxial alignment, where the magnetic properties were determined to be M_s 1100 emu/cm^3 and K_U 3.6x10^7 erg/cm^3. The magnetic properties produced in this work was compared to literature values, shown in table 6.3, where the in-plane magnetic properties of the FePt films produced in this work exceed literature values.

The time available for this project allowed only perpendicular exchange spring structures to be characterised, where 10 nm of FePt was deposited onto MgO substrates and a soft permalloy layer exchange coupled. The magnetic and structural properties of the FePt layer were investigated to ensure the structure does not have an adverse effect on the fabrication of the $L1_0$ phase. It was determined through XRD analysis that the order parameter achieved was consistent with previously made single film samples, thus confirming that the use of magnetron sputtering fabrication for FePt can be readily implemented into the exchange spring structure.

8.1.1   Future Plan

The fabrication of uniaxial in-plane FePt has a large deposition temperature parameter space yet to be explored, where only 300 and 500°C have been covered in this work. The novel approach of using post deposition annealing combined with XRD gave new insight into the growth of the (110) FePt crystal phase. Exploring additional deposition temperature could allow a more refined fabrication procedure, where the aim would be optimisation of the crystal structure while maintaining the magnetic properties. The temperature range of 300 to 500°C could hold the key to forming better crystal structure for (110) FePt films. Once deposited the samples would be subject to a similar study using XRD to monitor the formation of the $L1_0$ phase with annealing temperature, as was shown in figure 6.5. The purpose of this optimisation would be to simplify the fabrication process, potentially improving the integration into larger multilayer stacks. In terms of magnetic anisotropy, the value obtained in this work is close to the highest values reported for perpendicularly oriented FePt thin films although this is a factor of two less than that found in the bulk.

8.2   Fabrication of $L1_0$ MnAl films

The challenges faced when fabricating $L1_0$ ordered MnAl using magnetron sputtering were described in chapter 7, where two approaches were taken (i) alloy target deposition and (ii) co-deposition from elemental Mn and Al targets. The first method used values quoted in literature for the composition of the alloy target. In this work HAXPES was used to determine composition and for the sputtering system employed here it was found that substantial Mn content is lost during the fabrication process. That is, the composition of the deposited films was significantly different from that of the target. Whilst small differences (typically a few at.%) between target and film composition are common, the very large difference (a Mn deficiency of 30%) shown here was unexpected and likely accounts, at least in part, for the lack of progress in developing MnAl as a viable thin film material.

In order to determine if this was a feature of the alloy target co-deposition from elemental Mn and Al targets was also investigated. The rate of deposition for both the Mn and Al target was measured separately, where the samples were capped with Ta to ensure no oxidation. XRR measurements over a series of deposition powers allowed

the ratio of Mn and Al to be varied by changing the rate of deposition from their respective target. Predictions for composition were made and a series of thin films were fabricated to test these values, where the sputtering power used were 20, 30 and 40 W Mn and a relative power ratio for Al between 1 and 2 times the Mn power, which covered the 50-60 at.% Mn window in the MnAl phase diagram. The compositional measurements, shown in figure 7.16, were lower than predicted values. A correction factor was applied to the prediction, where it was determined that the obtained value was 75% of the predicted. Comparison can be made between values expected and obtained values for Mn content, with 75% for co-deposition and 72% for alloy target sputtering, where it is proposed that for both cases Mn is being lost due to poor adhesion to the substrate during deposition. This raises the question of how to better understand the physical phenomena of the film growing on the substrate. One possible route to progress is computational modelling of the arrival of atoms in the sputtering chamber which could help further the understanding of experimental results, where a feedback between experiment and simulation would allow the material achieve be better implemented.

The results presented here show that a consistent percentage loss of Mn was observed independent of whether an alloy or co-deposition from Mn and Al targets was used. The origin behind this loss of Mn was proposed to be due to adhesion issues but additional work is needed to explore this hypothesis further.

The use of an additional Mn target to co-sputtering with the alloy target allowed composition within the desired 50 to 60 at.% Mn region to be realised. The fabrication procedure produced films with high surface roughness which is undesirable in that it both adversely affect the properties of the film and makes integration into a multilayer structure impossible. In order to address this problem, the effect of lowering the working gas pressure used for sputtering was explored. This study investigated a 1 to 10 mTorr region, where deposition times and power were kept constant and the thickness, density and roughness of films measured by XRR. It was determined that by lowering the pressure from 3 mTorr to 1 mTorr the roughness of the films deposited at room temperature would reduce from $\approx$1.8 nm to $\approx$ 1 nm. In order to achieve L1$_0$ ordering there needs to be additional energy at the deposition stage, where increasing temperature also increases the surface roughness. The lower working pressure for sputtering helps to reduce this effect, where it was shown that samples deposited at 200°C with 3

and 1 mTorr had a roughness of 4.3 and 2.4 nm respectively.

The final sections of chapter 7 focused on optimising the fabrication procedure for MnAl films by investigating the phase formation as a function of deposition temperature, where room temperature (RT), 150, 300, 450 °C temperature depositions were carried out using co-deposition of Mn and Al. The samples were characterised by XRR and XRD, where as-deposited RT and 150°C showed no XRD peaks, 300°C showed γ phase formation and 450°C showed the equilibrium state of γ and β phase formation. These samples were then further annealed, with XRD measurements taken during in-situ heating from 150 to 600°C. For the RT and 150°C samples that showed no initial XRD peaks a temperature of 450°C was needed to induce phase changes, whereas the higher deposition temperatures of 300 and 450°C showed no change with annealing up to 600°C. The magnetic properties of the films as deposited at temperature was investigated by VSM, where it was determined that the lower temperature deposited samples had a larger magnetic signal. The hysteresis loops shown in figure 7.31 in conjunction with the XRD measurements indicate that as β and γ phases form in the material the small fraction of τ phase is removed and magnetic signal is lost.

8.2.1   Future Plan

The fabrication of MnAl films in the desired composition has been described for both alloy and co-deposition methods. The transition from Si/SiO$_2$ to MgO (001) substrates would see the optimisation of L1$_0$ phase growth at lower temperatures, where the lattice matching between the L1$_0$ phase and the substrate is increased. The best magnetic properties found in literature for L1$_0$ ordered MnAl thin films uses a Cr (001) ordered seed layers on a MgO (001) substrate using magnetron sputtering [64]. This further minimises the lattice mismatch between MnAl and MgO (001) substrates. The lattice matching helps encourage lower temperature ordering for both deposition and annealing temperatures. One challenge for this work has already been undertaken, which is the formation of the Cr seed layer with (001) orientation as shown in figure 8.1.
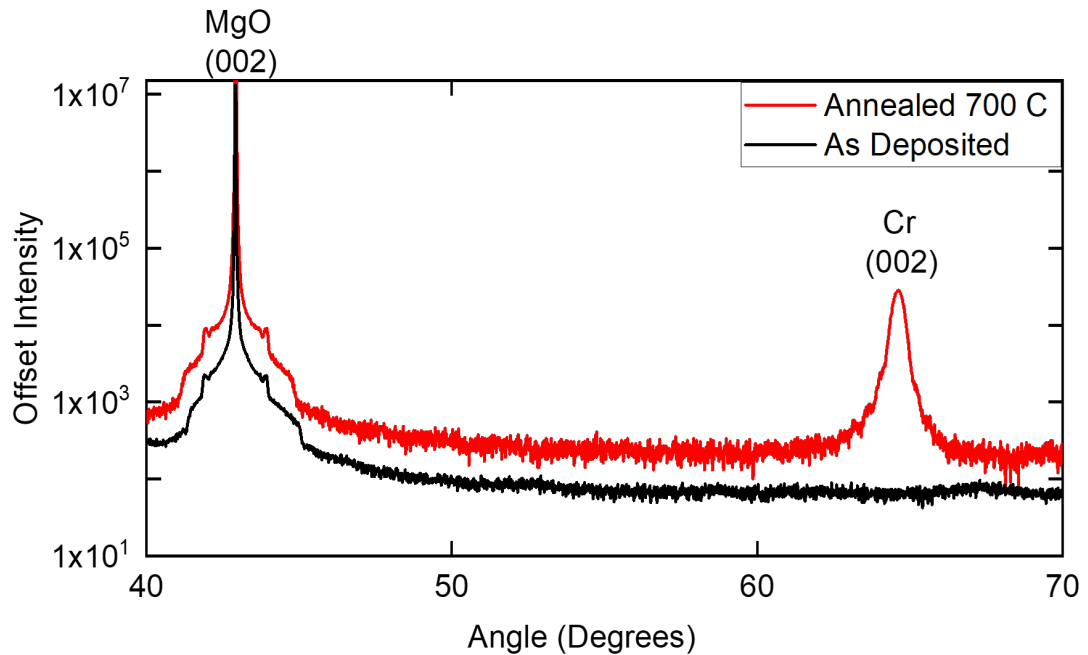
Figure 8.1: Phase transition to an ordered state for Cr seed layer after annealing for 1 hour at 700°C.

Exploring how the growth of MnAl on an optimal surface such as this Cr seed layer could give indication into how the adhesion of Mn plays a role in composition throughout the film. This potential avenue of research would include an in-depth study of composition on various seed layers/substrates, where the distance between substrate and target for sputtering could also be change to alter the energy of arrival of atoms.

The work described in this thesis has opened two avenues for further research of MnAl using magnetron sputtering (i) optimisation of magnetic/structural parameters for fabrication conditions and (ii) an in depth understanding behind variation of Mn content for different deposition systems.

References

[1] G. E. Moore, "Cramming more components onto integrated circuits," *Proceedings of the IEEE*, vol. 86, no. 1, pp. 82–85, 1998.

[2] M. Kief and R. Victora, "Materials for heat-assisted magnetic recording," *MRS Bulletin*, vol. 43, no. 2, 2018.

[3] D. Reinsel, J. Grantz, and J. Rydning, *The Digitization of the World*, 2018. Avaiable at `https://www.seagate.com/files/www-content/our-story/trends/files/idc-seagate-dataage-whitepaper`.

[4] S. Zygridou, C. Barton, P. Nutter, and T. Thomson, "Exploring the potentail of remote plasma sputtering for the production of $L1_0$ ordered thin films," *Journal of Physics D*, vol. 50, no. 27, 2017.

[5] C. Mellor, *Western Digital's 18TB and 20TB microwave-energy hard drives out soon*, 2019. Avaiable at `https://www.theregister.co.uk/2019/09/04/wd_mamr_drives/`.

[6] G. T. S, *Western Digital stuns storage industry with MAMR breakthrough for next-gen HDD's*, 2018. Avaiable at `www.anandtech.com/show/11925/western-digital-stuns-storage-industry-with-mamr-breakthrough-for-nextgen-hdds`.

[7] O. Kmia, *HAMR and MAMR: The technologies that will unlock hard drive capacity this year*, 2019. Avaiable at `fstoppers.com/originals/hamr-and-mamr-technologies-will-unlock-hard-drive-capacity-year-326328`.

[8] J. Thielsch, F. Bittner, and T. Woodcock, "Magnetisation reversal processes in hot-extruded τ-MnAl-C," *Journal of Magnetism and Magnetic Materials*, vol. 426, pp. 25–31, March 2017.

[9] B. Zhou, B. Varaprasad, E. Zhang, D. E. Laughlin, and J.-G. Zhu, "Microstructure analysis on size distribution during film growth in hamr media," *IEEE Transactions on Magnetics*, vol. 54, no. 11, pp. 1–4, 2018.

[10] H. Zhao, X. Li, Z. Zhang, B. Ma, and Q. Y. Jin, "Study of spin valves with $L1_0$-fept pinning layer and different pinned layers," *IEEE Transactions on Magnetics*, vol. 43, pp. 2839–2841, June 2007.

[11] S. D. Granz, K. Barmak, and M. H. Kryder, "Granular L10 FePt-B and FePt-B-Ag (001) thin films for heat assisted magnetic recording," *Journal of Applied Physics*, vol. 111, no. 7, p. 07B709, 2012.

[12] O. Mitsuru, O. Shouhei, K. Fumiyoshi, and F. Masaaki, "L10 ordered phase formation in fept, fepd, copt, and copd alloy thin films epitaxially grown on mgo(001) single-crystal substrates," *Journal of Applied Physics*, vol. 111, no. 7, p. 07A708, 2012.

[13] E. Alexander, C. Jonathan, J. Adam, B. Anders, and R. Jan, "Electronic structure and magnetic properties of $l1_0$ binary alloys," *Phys. Rev. B*, vol. 90, p. 014402, Jul 2014.

[14] LJ Zhu, L. Brandt, J. H. Zharo, and G. Woltersdorf, "Composition-tuned magneto opitcal Kerr effect in $L1_0$ Mn_xGa films with giant perpendicular anisotropy," *Journal of Physics D:Applied Physics*, vol. 49, pp. 1–5, May 2016.

[15] M. S. Parvin, M. Oogane, M. Kubota, M. Tsunoda, and Y. Ando, "Epitaxial l10-mnal thin films with high perpendicular magnetic anisotropy and small surface roughness," *IEEE Transactions on Magnetics*, vol. 54, pp. 1–4, Nov 2018.

[16] M. Oogane, K. Wantanabe, H. Saruyama, M. Hosoda, P. Shahnaz, Y. Kurimoto, M. Kubota, and Y. Ando, "$L1_0$-Ordered MnAl thin films with high perpendicular magnetic anisotropy," *Japanese Journal of Applied physics*, vol. 56, June 2017.

[17] A. Cebollada, R. Farrow, and M. Toney, "Structure and magnetic properties of chemically ordered magnetic binary alloys in thin film form," *Magnetic nanostructures*, pp. 93–122, 2002.

[18] B. Varaprasad, M. Chen, Y. K. Takahashi, and K. Hono, "L1$_0$-Ordered FePt-based perpendicular magnetic recording media for heat-assisted magnetic recording," *IEEE Transactions on Magnetics*, vol. 49, pp. 718–722, Feb 2013.

[19] R. Farrow, D. Weller, R. Marks, M. Toney, A. Cebollada, and G. Harp, "Control of the axis of chemical ordering and magnetic anisotropy in epitaxial fept films," *Journal of applied physics*, vol. 79, no. 8, pp. 5967–5969, 1996.

[20] R. Farrow, D. Weller, R. F. Marks, and M. Toney, "Magnetic anisotropy and microstructure in molecular beam epitaxial FePt110 MgO110," *Journal of applied physics*, vol. 84, pp. 934–939, 1998.

[21] D. Huskisson, S. Zygridou, J. Haigh, C. Barton, P. Nutter, and T. Thomson, "Analysis of grain size in FePt films fabricated using remote plasma deposition," *Journal of Magnetism and Magnetic Materials*, vol. 443, no. 67-72, 2017.

[22] Q.-f. Zhan, S. Vandezande, C. Van Haesendonck, and K. Temst, "Manipulation of in-plane uniaxial anisotropy in fe/ mg o (001) films by ion sputtering," *Applied Physics Letters*, vol. 91, no. 12, p. 122510, 2007.

[23] K. Koh, K. O'Brien, D. Gardner, N. Tayebi, C. Yang, and L. Lin, "Magnetically aligned 2d rectangular micro magnets with uniaxial in-plane anisotropy for high frequency magnetic devices," in *2015 Transducers-2015 18th International Conference on Solid-State Sensors, Actuators and Microsystems (TRANSDUCERS)*, pp. 1275–1278, IEEE, 2015.

[24] G. Heldt, P. Thompson, R. V. Chopdekar, J. Kohlbrecher, S. Lee, L. J. Heyderman, and T. Thomson, "Characterisation of size distribution and positional misalignment of nanoscale island by small-angle X-ray scattering," *Journal of Applied Physics*, vol. 125, p. 014301, Jan. 2019.

[25] R. B. Goldfarb and F. R. Fickett, "Comments on units in magnetism," *U.S. Department of Commerce National Bureau of Standards*, 1985.

[26] D. Jiles, *Introduction to magnetism and magnetic materials*. Boca Raton: CRC Press, third edition. ed., 2015.

[27] L. Shu-hua, "Origine de la boussole ii. animant et boussole," *Isis*, vol. 45, 1954.

[28] W. Gilbert, *On The Magnet*. excvdebat P. Short, 1600.

[29] H. C. Oersted, "Experiment on the effects of a current on the magnetic needle," *Annals of Philosophy*, vol. 16, 1820.

[30] M. D. Graef and M. E. Mchenry, eds., *Structure of Materials: An introduction to Crystallography, diffraction and symmetry*. Cambridge University press, 2012.

[31] M. M. Reventós, J. Rius, and J. M. Amigó, "Mineralogy and geology: The role of crystallography since the discovery of x-ray diffraction in 1912," *Revista de la Sociedad Geológica de España*, vol. 25, no. 3-4, pp. 133–143, 2012.

[32] "Lattice planes and miller indices." `https://www.doitpoms.ac.uk/tlplib/miller_indices/index.php`, 2008.

[33] J. M. D. Coey, ed., *Magnatism and Magnetic Materials*. Cambridge University Press, 2010.

[34] B. D. Cullity and C. D. Graham, *Introduction to Magnetic Materials*. Wiley, 2008.

[35] D. P. A. Maurice, "The quantum theory of the electron," *Proceedings of the Royal Society London*, vol. 117, pp. 610–624, 1928.

[36] D. J. Griffiths and J. Challice, *Introduction to Quantum Mechanics*. Pearson Education, 2005.

[37] R. Skomski, *Simple Models of Magnetism*. Oxford University Press, 2008.

[38] V. Sechovsky, *Magnetism in Solids: General Introduction*. Elsevier, 2001.

[39] G. Bertotti, *Hysteresis in Magnetism*. Academic Press, 1998.

[40] J. C. Mallinson, *The Foundation of Magnetic Recording*. Academic Press, 1993.

[41] S. Wilson, I. P. Grant, and B. L. Gyorffy, *The Effects of Relativity in Atoms, Molecules and the Solid State*. Plenum Press, 1991.

[42] E. F. Kneller and R. Hawig, "The exchange-spring magnet: a new material principle for permanent magnets," *IEEE Transactions on Magnetics*, vol. 27, no. 4, pp. 3588–3560, 1991.

[43] E. E. Fullerton, J. S. Jiang, C. Sowers, J. Pearson, and S. Bader, "Structure and magnetic properties of exchange-spring sm–co/co superlattices," *Applied physics letters*, vol. 72, no. 3, pp. 380–382, 1998.

[44] L. Dzemiantsova, G. Meier, and R. Röhlsberger, "Stabilization of magnetic helix in exchange-coupled thin films," *Scientific reports*, vol. 5, no. 1, pp. 1–7, 2015.

[45] E. E. Fullerton, J. Jiang, C. Rehm, C. Sowers, S. Bader, J. Patel, and X. Wu, "High coercivity, epitaxial sm–co films with uniaxial in-plane anisotropy," *Applied physics letters*, vol. 71, no. 11, pp. 1579–1581, 1997.

[46] D. Keavney, E. E. Fullerton, J. Pearson, and S. Bader, "Magnetic properties of c-axis textured nd/sub 2/fe/sub 14/b thin films," *IEEE Transactions on Magnetics*, vol. 32, no. 5, pp. 4440–4442, 1996.

[47] G. Ballentine, "Precessional switching of sub-micrometer magnetic elements with a perpendicular applied field," *Journal of Magnetism and Magnetic Materials*, vol. 451, pp. 29–31, 2018.

[48] L. Landau and E. Lifshitz, "On the theory of the dispersion of magnetic permeability in ferromagnetic bodies," in *Perspectives in Theoretical Physics*, pp. 51–65, Elsevier, 1992.

[49] B. Dieny, R. B. Goldfarb, and K.-J. Lee, *Introduction to Magnetic Random-Access Memory*. John Wiley and Sons, 2016.

[50] H. Liu, D. Bedau, J. Sun, S. Mangin, E. Fullerton, J. Katine, and A. Kent, "Dynamics of spin torque switching in all-perpendicular spin valve nanopillars," *Journal of Magnetism and Magnetic Materials*, vol. 358, pp. 233–258, 2014.

[51] M. Khan, A. K. Pathak, M. R. Paudel, I. Dubenko, S. Stadler, and N. Ali, "Magnetoresistance and field-induced structural transitions in ni50mn50- xsnx heusler alloys," *Journal of magnetism and magnetic materials*, vol. 320, no. 3-4, pp. L21–L25, 2008.

[52] J. Katine and E. E. Fullerton, "Device implications of spin-transfer torques," *Journal of Magnetism and Magnetic Materials*, vol. 320, no. 7, pp. 1217–1226, 2008.

[53] E. Y. Huang and M. H. Kryder, "L1$_0$-ordered mnal thin films with high perpendicular magnetic anisotropy using tin underlayers on si substrates," *IEEE Transactions on Magnetics*, vol. 51, no. 11, pp. 1–4, 2015.

[54] R. Rowan-Robinson, A. Hindmarch, and D. Atkinson, "Enhanced electron-magnon scattering in ferromagnetic thin films and the breakdown of the mott two-current model," *Physical Review B*, vol. 90, no. 10, p. 104401, 2014.

[55] S. Shen, P. Ohodnicki, S. Kernion, and M. E. McHenry, "Two-current model of the composition dependence of resistivity in amorphous (fe100- xcox) 89-yzr7b4cuy alloys using a rigid-band assumption," *Journal of Applied Physics*, vol. 112, no. 10, p. 103705, 2012.

[56] N. Farzad and N. Alain, *Nanomagnetism and spintronics: fabrication, materials, characterization and applications*. World Scientific, 2010.

[57] J. Bass and W. P. Pratt Jr, "Spin-diffusion lengths in metals and alloys, and spin-flipping at metal/metal interfaces: an experimentalist's critical review," *Journal of Physics: Condensed Matter*, vol. 19, no. 18, p. 183201, 2007.

[58] H. Draaisma, F. Den Broeder, and W. De Jonge, "Perpendicular anisotropy in pd/co multilayers," *Journal of applied physics*, vol. 63, no. 8, pp. 3479–3481, 1988.

[59] V. G. Harris, K. D. Aylesworth, B. N. Das, W. T. Elam, and N. C. Koon, "Structural origins of magnetic anisotropy in sputtered amorphous tb-fe films," *Phys. Rev. Lett.*, vol. 69, pp. 1939–1942, Sep 1992.

[60] A. Kaidatzi, S. Sidorenko, I. Vladymyrsky, and D. Niarchos, *Modern Magnetic and Spintronic Materials*. Springer, 2020.

[61] T. Hasegawa, K. Sasaki, C. W. Barton, and T. Thomson, "Fabrication and magnetization reversal of 110 femnpt dots surrounded by paramagnetic a1 phase formed by ion irradiation," *Scripta Materialia*, vol. 142, pp. 6–9, 2018.

[62] G. Giannopoulos, G. Barucca, A. Kaidatzis, V. Psycharis, R. Salikhov, M. Farle, E. Koutsouflakis, D. Niarchos, A. Mehta, M. Scuderi, *et al.*, "L1 0-feni films on au-cu-ni buffer-layer: a high-throughput combinatorial study," *Scientific reports*, vol. 8, no. 1, pp. 1–9, 2018.

[63] S. Zhao, T. Hozumi, P. LeClair, G. Mankey, and T. Suzuki, "Magnetic anisotropy of τ -MnAl thin films," *IEEE Transactions on Magnetics*, vol. 51, pp. 1–4, Nov 2015.

[64] M. Oogane, K. Watanabe, H. Saruyama, M. Hosoda, P. Shahnaz, Y. Kurimoto, M. Kubota, and Y. Ando, "L1$_0$-ordered MnAl thin films with high perpendicular magnetic anisotropy," *Japanese Journal of Applied Physics*, vol. 56, p. 0802A2, jun 2017.

[65] L.-J. Zhu, S.-H. Nie, and J.-H. Zhao, "Recent progress in perpendicularly magnetized Mn-based binary alloy films," *Chinese Physics B*, vol. 22, p. 118505, nov 2013.

[66] C. Chappert, A. Fert, and F. N. Van Dau, "The emergence of spin electronics in data storage," in *Nanoscience And Technology: A Collection of Reviews from Nature Journals*, pp. 147–157, World Scientific, 2010.

[67] A. Wu, Y. Kubota, T. Klemmer, T. Rausch, *et al.*, "Hamr1. 0 t/in2 demo," *IEEE Transactions on Magnetics*, vol. 49, no. 2, pp. 779–782, 2013.

[68] C.-B. Rong, D. Li, V. Nandwana, N. Poudyal, Y. Ding, Z. L. Wang, H. Zeng, and J. P. Liu, "Size-dependent chemical and magnetic ordering in l10-fept nanoparticles," *Advanced Materials*, vol. 18, no. 22, pp. 2984–2988, 2006.

[69] O. Hovorka, S. Devos, Q. Coopman, W. Fan, C. Aas, R. Evans, X. Chen, G. Ju, and R. Chantrell, "The curie temperature distribution of fept granular magnetic recording media," *Applied Physics Letters*, vol. 101, no. 5, p. 052406, 2012.

[70] S. Okamoto, N. Kikuchi, M. Furuta, O. Kitakami, and T. Shimatsu, "Microwave assisted magnetic recording technologies and related physics," *Journal of Physics D: Applied Physics*, vol. 48, no. 35, p. 353001, 2015.

[71] J.-G. Zhu, X. Zhu, and Y. Tang, "Microwave assisted magnetic recording," *IEEE Transactions on Magnetics*, vol. 44, no. 1, pp. 125–131, 2007.

[72] S. I. Kiselev, J. Sankey, I. Krivorotov, N. Emley, R. Schoelkopf, R. Buhrman, and D. Ralph, "Microwave oscillations of a nanomagnet driven by a spin-polarized current," *nature*, vol. 425, no. 6956, pp. 380–383, 2003.

[73] J.-G. Zhu and Y. Wang, "Microwave assisted magnetic recording utilizing perpendicular spin torque oscillator with switchable perpendicular electrodes," *IEEE Transactions on Magnetics*, vol. 46, no. 3, pp. 751–757, 2010.

[74] Y. Sato, K. Sugiura, M. Igarashi, K. Watanabe, and Y. Shiroishi, "Thin spin-torque oscillator with high ac-field for high density microwave-assisted magnetic recording," *IEEE transactions on magnetics*, vol. 49, no. 7, pp. 3632–3635, 2013.

[75] O. V. Shamis, I. A. Vladymyrskyi, Y. M. Makogon, and S. I. Sidorenko, "Materials science aspects of FePt-based thin films' formation," *Uspehi Fiziki Metallov*, vol. 19, pp. 337–363, sep 2018.

[76] T. Burkert, O. Eriksson, S. I. Simak, A. V. Ruban, B. Sanyal, L. Nordström, and J. M. Wills, "Magnetic anisotropy of l 1 0 fept and fe 1- x mn x pt," *Physical Review B*, vol. 71, no. 13, p. 134411, 2005.

[77] T. B. Massalski, "Binary alloy phase diagrams," *ASM international*, vol. 3, p. 2874, 1992.

[78] C. Creemers, S. Helfensteyn, J. Luyten, and M. Schurmans, "Synergy between material, surface science experiments and simulations," in *Applied Computational Materials Modeling*, pp. 109–169, Springer, 2007.

[79] M. Visokay and R. Sinclair, "Direct formation of ordered copt and fept compound thin films by sputtering," *Applied Physics Letters*, vol. 66, no. 13, pp. 1692–1694, 1995.

[80] C. B. Ndao, "Direct method for qualitative assessment of the fraction of ordered and disordered phases in thick fept films," *Journal of Magnetism and Magnetic Materials*, vol. 403, pp. 86–89, 2016.

[81] H. Su, N. Tang, R. Wang, B. Nie, S. Tang, L. Lv, and Y. Du, "Chemical synthesis of face-centered-tetragonal fept film using sol–gel method," *Chemistry letters*, vol. 36, no. 1, pp. 180–181, 2007.

[82] B. Wang and K. Barmak, "Re-evaluation of the impact of ternary additions of ni and cu on the a1 to l10 transformation in fept films," *Journal of Applied Physics*, vol. 109, no. 12, p. 123916, 2011.

[83] T. Seki, T. Shima, and K. Takanashi, "Fabrication of in-plane magnetized fept sputtered films with large uniaxial anisotropy," *Journal of magnetism and magnetic materials*, vol. 272, pp. 2182–2183, 2004.

[84] T. Shima, T. Seki, K. Takanashi, Y. Takahashi, and K. Hono, "Fabrication of l10 ordered fept thin films with a canted easy magnetization axis on mgo (1 1 0) substrate," *Journal of Magnetism and Magnetic Materials*, vol. 272, pp. E557–E559, 2004.

[85] M. Yu, H. Ohguchi, A. Zambano, I. Takeuchi, J. Liu, D. Josell, and L. A. Bendersky, "Orientation and magnetic properties of fept and copt films grown on mgo (1 1 0) single-crystal substrate by electron-beam coevaporation," *Materials Science and Engineering: B*, vol. 142, no. 2-3, pp. 139–143, 2007.

[86] S. D. Granz and M. H. Kryder, "Granular l10 fept (0 0 1) thin films for," *Journal of Magnetism and Magnetic Materials*, vol. 324, no. 3, pp. 287–294, 2012.

[87] Y. Yu, H.-B. Li, W. Li, M. Liu, Y.-M. Zhang, and W. Fei, "Structure and magnetic properties of magnetron-sputtered fept/au superlattice films," *Journal of Physics D: Applied Physics*, vol. 41, no. 24, p. 245003, 2008.

[88] J. Chen, Y. Zhou, C. Sun, S.-W. Han, and G. Chow, "Where is the ag in fept–ag composite films?," *Applied Physics Letters*, vol. 98, no. 13, p. 131914, 2011.

[89] P. Ho, K.-H. Tu, J. Zhang, C. Sun, J. Chen, G. Liontos, K. Ntetsikas, A. Avgeropoulos, P. M. Voyles, and C. A. Ross, "Domain configurations in co/pd and 11 0-fept nanowire arrays with perpendicular magnetic anisotropy," *Nanoscale*, vol. 8, no. 9, pp. 5358–5367, 2016.

[90] C. Brombacher, H. Schletter, M. Daniel, P. Matthes, N. Jöhrmann, M. Maret, D. Makarov, M. Hietschold, and M. Albrecht, "Feptcu alloy thin films: Morphology, l10 chemical ordering, and perpendicular magnetic anisotropy," *Journal of Applied Physics*, vol. 112, no. 7, p. 073912, 2012.

[91] Y. Ding, J. Chen, B. Lim, J. Hu, B. Liu, and G. Ju, "Granular l 1 0 fe pt: Ti o 2 (001) nanocomposite thin films with 5 nm grains for high density magnetic recording," *Applied Physics Letters*, vol. 93, no. 3, p. 032506, 2008.

[92] Y. En, H. Hoan, D. E. Laughlin, and Z. Jiangang, "Columnar grain growth of fept (l1 {sub 0}) thin films," *Journal of Applied Physics*, vol. 111, no. 7, 2012.

[93] X. Zhang, L. L. Tao, J. Zhang, S. H. Liang, L. Jiang, and X. F. Han, "First-principles study of MnAl for its application in MgO-based perpendicular magnetic tunnel junctions," *Applied Physics Letters*, vol. 110, p. 252403, June 2017.

[94] S. Sato, S. Irie, Y. Nagamine, T. Miyazaki, and Y. Umeda, "Antiferromagnetism in perfectly ordered 11 0-mnal with stoichiometric composition and its mechanism," *Scientific Reports*, vol. 10, no. 1, pp. 1–10, 2020.

[95] T. C. Dublin, *The Cost Periodic Table*. https://www.tcd.ie/Physics/research/groups/magnetism/facts/cost-periodic-table.php (Accessed: 01/08/2021).

[96] J. Cui, M. Kramer, L. Zhou, F. Liu, A. Gabay, G. Hadjipanayis, B. Balasubramanian, and D. Sellmyer, "Current progress and future challenges in rare-earth-free permanent magnets," *Acta Materialia*, vol. 158, pp. 118–137, 2018.

[97] O. Andersen, "Simple approach to the band-structure problem," *Solid State Communications*, vol. 13, no. 2, pp. 133–136, 1973.

[98] K. Anand, J. Pulikkotil, and S. Auluck, "Study of ferromagnetic instability in τ-mnal, using first-principles," *Journal of alloys and compounds*, vol. 601, pp. 234–237, 2014.

[99] J. Park, Y. Hong, S. Bae, J. Lee, J. Jalli, G. Abo, N. Neveu, S. Kim, C. Choi, and J. Lee, "Saturation magnetization and crystalline anisotropy calculations for mnal permanent magnet," *Journal of Applied Physics*, vol. 107, no. 9, p. 09A731, 2010.

[100] A. Koch, P. Hokkeling, M. vd Steeg, and K. De Vos, "New material for permanent magnets on a base of mn and al," *Journal of Applied Physics*, vol. 31, no. 5, pp. S75–S77, 1960.

[101] H. Kōno, "On the ferromagnetic phase in manganese-aluminum system," *Journal of the Physical Society of Japan*, vol. 13, no. 12, pp. 1444–1451, 1958.

[102] A. J. McAlister and J. L. Murray, eds., *Al-Mn (Aluminium-Maganese - ASM Handbook: Alloy Phase Diagrams*. ASM International, 1987.

[103] Z. Liu, C. Chen, Z. Zheng, B. Tan, and R. V. Ramanujan, "Phase transitions and hard magnetic properties for rapidly solidified mnal alloys doped with c, b, and rare earth elements," *Journal of Materials Science*, vol. 47, no. 5, pp. 2333–2338, 2012.

[104] J. Harbison, T. Sands, R. Ramesh, L. Florez, B. Wilkens, and V. Keramidas, "Mbe growth of ferromagnetic metastable epitaxial mnal thin films on alas/gaas heterostructures," *Journal of crystal growth*, vol. 111, no. 1-4, pp. 978–983, 1991.

[105] J. Shen, R. D. Kirby, and D. J. Sellmyer, "The structure and magneto-optic properties of mnal-based thin films," *Journal of applied physics*, vol. 67, no. 9, pp. 4929–4931, 1990.

[106] M. Ellner, "The structure of the high-temperature phase mnal (h) and the displacive transformation from mnal (h) into mn 5 al 8," *Metallurgical Transactions A*, vol. 21, no. 6, pp. 1669–1672, 1990.

[107] S. Thimmaiah, Z. Tener, T. N. Lamichhane, P. C. Canfield, and G. J. Miller, "Crystal structure, homogeneity range and electronic structure of rhombohedral γ-mn5al8," *Zeitschrift für Kristallographie-Crystalline Materials*, vol. 232, no. 7-9, pp. 601–610, 2017.

[108] C. B. Shoemaker, D. P. Shoemaker, T. Hopkins, and S. Yindepit, "Refinement of the structure of β-manganese and of a related phase in the mn–ni–si system," *Acta Crystallographica Section B: Structural Crystallography and Crystal Chemistry*, vol. 34, no. 12, pp. 3573–3576, 1978.

[109] J. Thielsch, F. Bittner, and T. Woodcock, "Magnetization reversal processes in hot-extruded τ-mnal-c," *Journal of Magnetism and Magnetic Materials*, vol. 426, pp. 25–31, 2017.

[110] C. Yanar, J. Wiezorek, W. Soffa, and V. Radmilovic, "Massive transformation and the formation of the ferromagnetic l1 0 phase in manganese-aluminum-based alloys," *Metallurgical and Materials Transactions A*, vol. 33, no. 8, pp. 2413–2423, 2002.

[111] R. D. James, "Displacive phase transformations in solids," *Journal of the Mechanics and Physics of Solids*, vol. 34, no. 4, pp. 359–394, 1986.

[112] P.-Z. Si, H.-D. Qian, C.-J. Choi, J. Park, and H.-L. Ge, "A novel method for measuring the phase transformation temperature and enhanced coercivity in cold-rolled mnalcx (x= 0–5) alloys," *Journal of Magnetism and Magnetic Materials*, vol. 451, pp. 540–545, 2018.

[113] E. Fazakas, L. Varga, and F. Mazaleyrat, "Preparation of nanocrystalline mn–al–c magnets by melt spinning and subsequent heat treatments," *Journal of Alloys and Compounds*, vol. 434, pp. 611–613, 2007.

[114] S. Kontos, A. Ibrayeva, J. Leijon, G. Mörée, A. E. Frost, L. Schönström, K. Gunnarsson, P. Svedlindh, M. Leijon, and S. Eriksson, "An overview of mnal permanent magnets with a study on their potential in electrical machines," *Energies*, vol. 13, no. 21, p. 5549, 2020.

[115] A. Chaturvedi, R. Yaqub, and I. Baker, "A comparison of τ-mnal particulates produced via different routes," *Journal of Physics: Condensed Matter*, vol. 26, no. 6, p. 064201, 2014.

[116] H.-D. Qian, P.-Z. Si, J. Park, K. M. Cho, and C.-J. Choi, "Structure and magnetic properties of nanocrystalline mnal-c prepared by solid-state reaction and high-pressure compaction," *Journal of Electronic Materials*, vol. 48, no. 3, pp. 1395–1399, 2019.

[117] T. Ohtani, N. Kato, S. Kojima, K. Kojima, Y. Sakamoto, I. Konno, M. Tsukahara, and T. Kubo, "Magnetic properties of mn-al-c permanent magnet alloys," *IEEE Transactions on Magnetics*, vol. 13, no. 5, pp. 1328–1330, 1977.

[118] O. Koylu-Alkan, G. C. Hadjipanayis, and R. Madugundo, "Bulk mn-al-c permanent magnets prepared by various techniques," *AIP Advances*, 2016.

[119] R. Madugundo and G. C. Hadjipanayis, "Anisotropic mn-al-(c) hot-deformed bulk magnets," *Journal of Applied Physics*, vol. 119, no. 1, p. 013904, 2016.

[120] J. Huang and P. Kuo, "Sintered mnal and mnalc magnets," *Materials Science and Engineering: B*, vol. 14, no. 1, pp. 75–79, 1992.

[121] T. Rosier, Y. He, and N. El-Masry, "Ferromagnetic τ-mnal epitaxially grown on (100) gaas substrates by pulsed laser deposition," *Materials Letters*, vol. 26, no. 4-5, pp. 227–231, 1996.

[122] J. De Boeck, C. Bruynseraede, H. Bender, A. Van Esch, W. Van Roy, and G. Borghs, "Epitaxial ferromagnetic (τ mnalco) and (cocoal) multilayers on gaas (001) grown by molecular beam epitaxy," *Journal of crystal growth*, vol. 150, pp. 1139–1143, 1995.

[123] W. Van Roy, H. Bender, C. Bruynseraede, J. De Boeck, and G. Borghs, "Degree of order and magnetic properties of τ-mnal films," *Journal of magnetism and magnetic materials*, vol. 148, no. 1-2, pp. 97–98, 1995.

[124] P. Kuo, Y. Yao, W. Chen, and J. Huang, "Preparation and magnetical studies of mn 50 al 50/al bilayer films," *Journal of applied physics*, vol. 81, no. 8, pp. 5253–5255, 1997.

[125] E. Y. Huang and M. H. Kryder, "Thin films with high perpendicular magnetic anisotropy using TiN underlayers on Si substrates," *IEEE Transactions on Magnetics*, vol. 51, pp. 1–4, nov 2015.

[126] Z. Yan, Y. Huang, Y. Zhang, G. Hadjipanayis, W. Soffa, and D. Weller, "Magnetic and structural properties of mnal/ag granular thin films with l10 structure," *Scripta materialia*, vol. 53, no. 4, pp. 463–468, 2005.

[127] P. Kuo, K. Ker, Y. Yao, and J. Huang, "Magnetic properties and microstructure of mn–al–c thin films," *Journal of applied physics*, vol. 85, no. 8, pp. 4892–4894, 1999.

[128] M. Matsumoto, A. Morisako, and J. Ohshima, "Properties of ferromagnetic mnal thin films with additives," *Journal of applied physics*, vol. 69, no. 8, pp. 5172–5174, 1991.

[129] J. Huang, P. Kuo, and S. Shen, "High coercivity and high saturation magnetization mn-al thin films," *IEEE transactions on magnetics*, vol. 31, no. 5, pp. 2494–2498, 1995.

[130] P. Kuo, Y. Yao, J. Huang, S. Shen, and J. Jou, "Microstructural and magnetic studies of mn–al thin films," *Journal of applied physics*, vol. 81, no. 8, pp. 5621–5623, 1997.

[131] G. Fischer and M. Rudee, "Effect of magnetic annealing on the τ-phase of mnal thin films," *Journal of magnetism and magnetic materials*, vol. 213, no. 3, pp. 335–339, 2000.

[132] W. Van Roy, J. De Boeck, H. Bender, C. Bruynseraede, A. Van Esch, and G. Borghs, "Structural and magnetic investigations of epitaxial ferromagnetic τ mnal films grown on gaas/alas by molecular-beam epitaxy," *Journal of applied physics*, vol. 78, no. 1, pp. 398–404, 1995.

[133] P. B. Braun and J. A. Goedkoop, "An x-ray and neutron diffraction investigation of the magnetic phase al0. 89mn1. 11," *Acta Crystallographica*, vol. 16, no. 8, pp. 737–740, 1963.

[134] J. Cotton, "Properties: Magnesia - magnesium oxide MgO properties and applications," Sep 2021. https://www.azom.com/properties.aspx?ArticleID=54.

[135] Y. Touloukian, R. Kirby, E. Taylor, and T. Lee, "Thermophysical properties of matter-the tprc data series. volume 13. thermal expansion-nonmetallic solids," tech. rep., THERMOPHYSICAL AND ELECTRONIC PROPERTIES INFORMATION ANALYSIS CENTER . . . , 1977.

[136] E. Y. Huang and M. H. Kryder, "Fabrication of mnal thin films with perpendicular anisotropy on si substrates," *Journal of Applied Physics*, vol. 117, no. 17, p. 17E314, 2015.

[137] Y. Cui, W. Yin, W. Chen, J. Lu, and S. A. Wolf, "Epitaxial tau phase MnAl thin films on MgO (001) with thickness-dependent magnetic anisotropy," *Journal of Applied Physics*, vol. 110, p. 103909, nov 2011.

[138] M. Hosoda, M. Oogane, M. Kubota, T. Kubota, H. Saruyama, S. Iihama, H. Naganuma, and Y. Ando, "Fabrication of $l1_0$-MnAl perpendicularly magnetized thin films for perpendicular magnetic tunnel junctions," *Journal of Applied Physics*, vol. 111, p. 07A324, apr 2012.

[139] H. Saruyama, M. Oogane, Y. Kurimoto, H. Naganuma, and Y. Ando, "Fabrication of l10-ordered mnal films for observation of tunnel magnetoresistance effect," *Japanese Journal of Applied Physics*, vol. 52, no. 6R, p. 063003, 2013.

[140] C. Navío, M. Villanueva, E. Céspedes, F. Mompeán, M. García-Hernández, J. Camarero, and A. Bollero, "Ultrathin films of l10-mnal on gaas (001): A hard magnetic mnal layer onto a soft mn-ga-as-al interface," *APL Materials*, vol. 6, no. 10, p. 101109, 2018.

[141] S. Nie, L. Zhu, J. Lu, D. Pan, H. Wang, X. Yu, J. Xiao, and J. Zhao, "Perpendicularly magnetized τ-mnal (001) thin films epitaxied on gaas," *Applied Physics Letters*, vol. 102, no. 15, p. 152405, 2013.

[142] C. Duan, X. Qiu, B. Ma, Z. Zhang, and Q. Jin, "The structural and magnetic properties of τ-mnal films prepared by mn/al multilayers deposition plus annealing," *Materials Science and Engineering: B*, vol. 162, no. 3, pp. 185–188, 2009.

[143] G. Ertl, H. Luth, and D. L. Mills, eds., *Auger- and X-Ray Photoelectron Spectroscopy in Materials Science*. Springer Series in Surface Science, 2013.

[144] D. G. Stinson and S.-C. Shin, "Magnetization and anisotropy of co/pd multilayer thin films," *Journal of applied physics*, vol. 67, no. 9, pp. 4459–4461, 1990.

[145] K. Günther, "Aufdampfschidhten aus halbleitenden iii-v-verbindungen," *Zeitschrift für Naturforschung A*, vol. 13, no. 12, pp. 1081–1089, 1958.

[146] A. Adeyeye and G. Shimon, "Growth and characterization of magnetic thin film and nanostructures," in *Handbook of Surface Science*, vol. 5, pp. 1–41, Elsevier, 2015.

[147] K. Wasa, M. Kitabatake, and H. Adachi, *Thin Film Materials Technology*. William Andrew Publishing, 2004.

[148] E. Särhammar, E. Strandberg, N. Martin, and T. Nyberg, "Sputter rate distribution and compositional variations in films sputtered from elemental and multi-element targets at different pressures," *International Journal of Materials Science and Applications*, vol. 3, no. 2, pp. 29–36, 2014.

[149] A. C. Levi and M. Kotrla, "Theory and simulation of crystal growth," *Journal of Physics: Condensed Matter*, vol. 9, pp. 299–344, jan 1997.

[150] J. T. Gudmundsson, "Physics and technology of magnetron sputtering discharges," *Plasma Sources Science and Technology*, vol. 29, no. 11, p. 113001, 2020.

[151] N. Nikitenkov, ed., *Modern Technologies for Creating the thin-film Systems and coatings*. IntechOpen, 2017.

[152] J. A. Thornton, "Structure-Zone Models Of Thin Films," in *Modeling of Optical Thin Films* (M. R. Jacobson, ed.), vol. 0821, pp. 95 – 105, International Society for Optics and Photonics, SPIE, 1988.

[153] A. Anders, "A structure zone diagram including plasma-based deposition and ion etching," *Thin Solid Films*, vol. 518, no. 15, pp. 4087–4090, 2010.

[154] R. Pöttgen, ed., *Zeitschrift für Kristallographie - Crystalline Materials*. Berlin, Boston: Oldenbourg Wissenschaftsverlag, 5 Feb. 2018.

[155] L. Borgese, F. Bilo, E. Bontempi, L. Seralessandri, A. Cinosi, G. Siviero, and L. E. Depero, "Total reflection x-ray fluorescence (TXRF) spectroscopy for environmental and biological analysis.-réflexion spectroscopie des rayons x de fluorescence totale dans l'analyse biologique et de l'environnement," in *16th International Congress of Metrology*, p. 10010, EDP Sciences, 2013.

[156] M. Abd Mutalib, M. Rahman, M. Othman, A. Ismail, and J. Jaafar, "Scanning electron microscopy (sem) and energy-dispersive x-ray (edx) spectroscopy," in *Membrane characterization*, pp. 161–179, Elsevier, 2017.

[157] H.-J. Fitting, H. Glaefeke, and W. Wild, "Electron penetration and energy transfer in solid targets," *Physica status solidi (a)*, vol. 43, no. 1, pp. 185–190, 1977.

[158] H. Konno, "X-ray photoelectron spectroscopy," *Materials Science and Engineering of Carbon*, 2016.

[159] A. Regoutz, M. Mascheck, T. Wiell, S. K. Eriksson, C. Liljenberg, K. Tetzner, B. A. Williamson, D. O. Scanlon, and P. Palmgren, "A novel laboratory-based hard x-ray photoelectron spectroscopy system," *Review of Scientific Instruments*, vol. 89, no. 7, p. 073105, 2018.

[160] D. Want and S. Ikram, "Quantum design mpms 3 magnetometer." https://qd-uki.co.uk/material-characterisation/quantum-design-mpms3-magnetometer/.

[161] D. Rugar and P. Hansma, "Atomic force microscopy," *Physics today*, vol. 43, no. 10, pp. 23–30, 1990.

[162] G. Binnig, C. F. Quate, and C. Gerber, "Atomic force microscope," *Physical review letters*, vol. 56, no. 9, p. 930, 1986.

[163] W. H. Bragg and W. L. Bragg, "The reflection of x-rays by crystals," *Proceedings of the Royal Society of London. Series A, Containing Papers of a Mathematical and Physical Character*, vol. 88, no. 605, pp. 428–438, 1913.

[164] M. Yasaka, "X-ray thin film measurement techniques," *The Rigaku Journal*, vol. 26, no. 2, pp. 1–9, 2010.

[165] K. Inaba, S. Kobayashi, K. Uehara, A. Okada, S. Reddy, and T. Endo, "High resolution x-ray diffraction analyses of (la,sr)mno¡sub¿3¡/sub¿/zno/sapphire(0001) double heteroepitaxial films," *Advances in Materials Physics and Chemistry*, vol. 3, pp. 72–89, 01 2013.

[166] S. D. Granz, K. Barmak, and M. H. Kryder, "Granular 110 FePt:x (x = ag, b, c, SiOx, TaOx) thin films for heat assisted magnetic recording," *The European Physical Journal B*, vol. 86, mar 2013.

[167] A. Khajehnezhad and S. Sebt, "Order parameter in 11 0 fept nanocrystals," *Transactions of the Indian Institute of Metals*, vol. 67, no. 6, pp. 903–907, 2014.

[168] E. Yang, D. E. Laughlin, and J.-G. Zhu, "Correction of order parameter calculations for fept perpendicular thin films," *IEEE transactions on magnetics*, vol. 48, no. 1, pp. 7–12, 2011.

[169] A. Gibaud, M. S. Chebil, , and T. Beuvier, *X-Ray Reflectivity*. Berlin, Heidelberg: Springer Berlin Heidelberg, 2013.

[170] L. G. Parratt, "Surface studies of solids by total reflection of x-rays," *Phys. Rev.*, vol. 95, pp. 359–369, Jul 1954.

[171] A. L. D. Róz, M. Ferreira, F. de Lima Leite, and O. N. Oliveira, eds., *Nanocharacterisation Techniques*. Micro and Nano Technologies, William Andrew Publishing, 2017.

[172] B. Matts and A. Gabriella, "*GenX*: an extensible X-ray reflectivity refinement program utilizing differential evolution," *Journal of Applied Crystallography*, vol. 40, pp. 1174–1178, Dec 2007.

[173] L. G. Parratt, "Surface studies of solids by total reflection of X-rays," *Physical Review*, vol. 95, pp. 359–369, July 1954.

[174] A. J. Ying, C. E. Murray, and I. Noyan, "A rigorous comparison of x-ray diffraction thickness measurement techniques using silicon-on-insulator thin films," *Journal of Applied Crystallography*, vol. 42, no. 3, pp. 401–410, 2009.

[175] T. Seki, K. Utsumiya, Y. Nozki, H. Imamura, and K. Takanash, "Spin wave-assisted reduction in switching field of highly coercive iron-platinum magnets," *Nature communications*, vol. 4, Apr 2013.

[176] J. Fischbacher, A. Kovacs, H. Oezelt, M. Gusenbauer, D. Suess, and T. Schrefl, "Effective uniaxial anisotropy in easy-plane materials through nanostructuring," *Applied Physics Letters*, vol. 111, no. 19, p. 192407, 2017.

[177] S. T., S. T., and K. Takanashi, "Fabrication of in-plane magnetized FePt sputtered films with large uniaxial anisotropy," *Journal of Magnetism and Magnetic Materials*, vol. 272-276, p. 2182–2183, 2004.

[178] T. Shima, T. Moriguchi, S. Mitani, and K.Takanashi, "Low-temperature fabircation of $L1_0$ ordered FePt alloy by alternate monatomic layer deposition," *Applied Physics Letters*, vol. 80, pp. 288–290, 2002.

[179] T. Shima, T. Seki, K. Takanashi, Y. K. Takahashi, and K. Hono, "Fabrication of $L1_0$ ordered FePt thin films with a canted easy magnetisation axis on MgO(110) substrate," *Journal of Magnetism and Magnetic Materials*, vol. 272-276, pp. E557–E559, 2004.

[180] M. M. Schwickert, K. A. Hannibal, M. F. Toney, M. Best, L. Folks, J. U. Thiele, A. J. Kellock, and D. Weller, "Temperature dependent chemical ordering in fept(001) and fept(110) films," *Journal of Applied Physics*, vol. 87, pp. 6956–6958, 2000.

[181] A. Cimino, P. Porta, and M. Valigi, "Dependence of the lattice parameter of magnesium oxide on crystallite size," *Journal of the American Ceramic Society*, vol. 49, no. 3, pp. 152–156, 1966.

[182] C. J. Engberg and E. H. Zehms, "Thermal expansion of al2o3, beo, mgo, b4c, sic, and tic above 1000° c.," *Journal of the american ceramic society*, vol. 42, no. 6, pp. 300–305, 1959.

[183] M. A. Durand, "The coefficient of thermal expansion of magnesium oxide," *Physics*, vol. 7, no. 8, pp. 297–298, 1936.

[184] A. V. Da Rosa and J. C. Ordóñez, *Fundamentals of renewable energy processes*. Academic Press, 2021.

[185] J. Walton, P. Wincott, N. Fairley, and A. Carrick, *Peak fitting with CasaXPS: a casa pocket book*. Accolyte Science, 2010.

[186] M. Panjan, "Self-organizing plasma behavior in rf magnetron sputtering discharges," *Journal of Applied Physics*, vol. 125, no. 20, p. 203303, 2019.